

**SYNTHESIS AND CHARACTERIZATION OF MOLYBDATE
BASED HETRONANOSTRUCTURES FOR ENERGY
STORAGE APPLICATION**

DOCTOR OF PHILOSOPHY

**in
Physics**

By

Shakra Jabeen

Registration Number: 11919654

Supervised By

Dr. Kawaljeet Singh Samra (16468)

Physics (Professor)

Lovely Professional University



**LOVELY PROFESSIONAL UNIVERSITY, PUNJAB
2025**

DECLARATION

I, hereby declare that the presented work in the thesis entitled “**Synthesis and Characterization of Molybdate-based Hetro-nanostructures for Energy Storage Application**” submitted for the award of the degree of Doctor of Philosophy in physics, Lovely Professional University, Phagwara is my original work conducted under the supervision of Dr. Kawaljeet Singh Samra(Supervisor), professor in Department of physics at school of Chemical Engineering and Physical Sciences, Lovely Professional University, Phagwara, Punjab, India. I further declare that the thesis does not contain any part of any work that has been submitted for the award of any degree in this university or in any other university/Deemed University without proper citation.

Shakra

Name of the scholar: Shakra Jabeen

Registration No: 11919654


Department/School: Physics/School of Chemical Engineering and Physical Sciences

Lovely Professional University,

Punjab, India.

CERTIFICATE

This is to certify that the work reported in the Ph. D. thesis entitled "Synthesis and Characterization of Molybdate based Heteronanostructures for Energy Storage Application" submitted in fulfillment of the requirement for the award of degree of **Doctor of Philosophy (Ph.D.)** from physics department, is a research work carried out by Shakra Jabeen, 11919654, is bonafide record of his/her original work carried out under my supervision and that no part of thesis has been submitted for any other degree, diploma or equivalent course.



Name of Supervisor: Dr Kawaljeet Singh Samra

Designation: Professor

Department/School: Physics/School of Chemical Engineering and Physical Sciences.

University: Lovely Professional University, Phagwara, Punjab

India-144411.

Abstract

During this modernization, the expeditious growth of urbanization, the global economy, and a remarkable increase in the caliber of living standards give rise to some major issues like expenditure of non-renewable resources (Fossil fuel reserves), and increased emission of greenhouse gas, air pollution, and water pollution that is very dangerous for the environment. The most promising alternative for this is sustainable energy resources like water, wind, and solar. So, the rapid increase in energy utilization and the environmental impact of traditional energy resources has led to tremendously increased research activities on clean and renewable energy sources during the last decades. The reliability of supply to an electric grid is a serious issue because of the variability and irregularity of these renewable energy sources. This challenge can be overcome by developing devices like rechargeable batteries and supercapacitors. Compared with batteries, supercapacitors as energy storage are a priority because of their elevated power density, quick charging or discharging, good cycling strength, environmental friendliness, security and work as a link for the power-energy difference between capacitors and batteries. The choice of electrode material is crucial for the performance of supercapacitors. RuO_2 as an electrode material yields an elevated specific capacitance value. However, its high cost limits its extensive use in the field of supercapacitors. Alternative resources like carbonaceous material, transition metal dichalcogenides/oxides (TMD/O), metal molybdates, and polymers have been studied extensively.

The Thesis entitled **“Synthesis and Characterization of Molybdate based Heteronanostructures for Energy Storage Application”** is a research work that aims at the synthesis, characterization, and optimization of molybdate based heteronanostructure for energy storage application. The present work consists of nine chapters and each chapter is described briefly. The content of each chapter has been briefly discussed below.

Chapter 1 provides a general introduction to energy storage devices specifically supercapacitors their historical background, types, and components of Supercapacitor.

Chapter 2 deals with a literature review including the introduction to metal molybdate specifically MnMoO_4 with its synthesis methods and Structural, morphological, and Electrochemical Properties.

Chapter 3 This chapter emphasizes the materials and chemicals used in synthesis and characterization techniques such as XRD, FTIR, Raman, X-ray photoelectron spectroscopy, Brunauer-Emmett-Teller (BET) method, and electrochemical techniques including CV, EIS, and galvanostatic charge-discharge (GCD) are employed to determine the desired material characteristics.

Chapter 4 This chapter describes the synthesis and characterization of MnMoO_4 nanoribbons prepared by hydrothermal technique to study the electrochemical properties of In situ electrodes at different mass loadings. XRD, Raman, and FESEM confirmed the structure and morphology of the prepared material. The electrochemical performance of in situ electrodes at different mass loading was analysed using CV, EIS, and GCD. The XRD and Raman confirm pure α - MnMoO_4 monoclinic phase synthesis without any impurity. FESEM reveals nanoribbon-like structure. The electrochemical achievement has been examined through CV, GCD, and EIS analysis. The binder-free electrode with a mass loading of 0.1mg shows a specific capacity of 1050mAhg^{-1} (9000Fg^{-1}) at 5Ag^{-1} . After 1000 cycles, the electrode shows stability of 72.5% at 50Ag^{-1} current density.

Chapter 5 This chapter describes the calcination temperature effects on the electrochemical-achievements of MnMoO_4 nanoparticles synthesized by microwave annealing technique. The prepared samples were calcinated at 300°C , 500°C and 700°C . XRD, Raman, and FESEM confirmed the structural and morphology of the synthesized material. The surface area of synthesized nanoparticles was analysed by the BET technique. The elemental composition and oxidation state of synthesized material was done by XPS study. The electrode electrochemical achievements were analyzed using CV, electrochemical Impedance Spectroscopy, and GCD. The electrode prepared with MnMoO_4 nanoparticles displayed a remarkable capacity of 1613Cg^{-1} and 1549Cg^{-1} at 10mVs^{-1} and 2Ag^{-1} , respectively. An asymmetric device is fabricated by depositing MnMoO_4 nanoparticles and activated carbon on Ni-foam as anode and cathode respectively. The device demonstrated a magnificent energy density of 68Whkg^{-1} at 850Wkg^{-1} and displayed an excellent cycling stability of 139% after 5000 cycles.

Chapter 6 investigation delves into the intricacies of controlled oxidation of graphene oxide (GO) and its influence on electrochemical efficiency of reduced graphene oxide (rGO) and Manganese Molybdate based composites. Further, through a meticulous manipulation of GO composition, we achieved the hydrothermal synthesis of rGO@MnMoO_4 composites, wherein the most optimized configuration displayed a remarkable specific capacity of 1356Cg^{-1} and 1299Cg^{-1} at 10mVs^{-1} and 2Ag^{-1} , respectively. This achievement is ascribed to the intricately

designed microporous microrod morphology of MnMoO_4 , synergistically coupled with the electrical conductivity enhancement facilitated by rGO, attributed to its abundant conjugated carbon bonds. The results further culminate in the development of an asymmetric supercapacitor (ASC) denoted as $\text{rGO@MnMoO}_4/\text{graphite-activated carbon (G-AC)}$, demonstrated altitudinous energy density of 63.5 Whkg^{-1} at a power density of 850 Wkg^{-1} . Notably, this formidable device remained stable at 97% of specific capacity after 9460 cycles, evincing minimal structural and morphological degradation.

Chapter 7 investigation marks a significant stride forward by successfully synthesizing $\text{MoS}_2@\text{MnMoO}_4$ composite material through a streamlined two-step aqua-thermal method. Leveraging the synergistic interplay between MoS_2 and MnMoO_4 , the resultant heterostructures exhibit remarkable enhancements in charge-storage kinetics, bragging a gravimetric capacity of 722.5 Cg^{-1} at 1 Ag^{-1} . Moreover, the non-symmetric supercapacitor assembly, $\text{MoS}_2@\text{MnMoO}_4/\text{graphite mixed activated carbon (AC-G)}$, showcases a formidable energy density of 99.5 Whkg^{-1} at 850 W kg^{-1} , underscored by rugged cyclic stability across 10,000 cycles. Rigorous characterization encompassing surface, morphological, structural, and elemental analysis unveil the mesoporous nature and strong Faradic activity of the composite material, are pivotal factors in its exceptional charge storage efficiency. These revelatory findings herald the boundless potential of $\text{MoS}_2@\text{MnMoO}_4$ heterostructures as resilient and sustainable energy storage solutions, poised to address energy shortages while championing environmental sustainability in the quest for a greener tomorrow.

Chapter 8 focuses on fabricating $\text{Ni}_x\text{Mn}_{1-x}\text{MoO}_4$ ($0 \leq x \leq 1$) as an active material through a straightforward hydrothermal technique. The synthesis method involves the partial substitution of Mn^{2+} with Ni^{2+} ions, yielding the mesoporous $\text{Ni}_{0.25}\text{Mn}_{0.75}\text{MoO}_4$ nanoparticles characterized by varied shapes and sizes in nanoplate morphology. Direct growth of $\text{Ni}_{0.25}\text{Mn}_{0.75}\text{MoO}_4$ on Ni foam demonstrated a remarkable specific capacity of 1297 Cg^{-1} at 1 Ag^{-1} . Moreover, an asymmetric supercapacitor assembled with binder-free $\text{Ni}_{0.25}\text{Mn}_{0.75}\text{MoO}_4@\text{NF}$ and graphitic activated carbon (GAC) as the positive and negative electrode showcased an impressive energy density of 152 Whkg^{-1} at a power density of 840 Wkg^{-1} , alongside exceptional 98.7% retention after 10000 cycles. These outcomes underscore the considerable potential of $\text{Ni}_{0.25}\text{Mn}_{0.75}\text{MoO}_4$ for forthcoming energy storage devices.

Chapter 9 contains the conclusion and future scope of metal molybdates in the energy field.

ACKNOWLEDGEMENT

First and foremost, I would like to express my heartfelt gratitude to the Almighty God for blessing me throughout my research journey. His guidance enabled me to complete my study. I am deeply thankful to my supervisor, Dr. Kawaljeet Singh Samra, Professor of Physics at Lovely Professional University, Punjab. His unwavering support, patience, motivation, enthusiasm, and vast knowledge have been invaluable to me. His guidance has been instrumental at every stage of my research and thesis writing. I am truly privileged to have such an exceptional guide and mentor for my Ph.D. study.

I express my sincere thanks to Prof. Dr. Kailash Juglan, Head of the School and Department, and all the faculty members of the Department of Physics at Lovely Professional University, Punjab, for their support and contributions.

I extend my gratitude to my senior, Mr. Prashant Kumar, for his continuous support and guidance. I am also thankful to the Chemistry Department for their support during my research. I am profoundly grateful to my father, Haji Mohd Aslam, who has been my backbone in every difficult situation. His unwavering support throughout my entire Ph.D. journey has been invaluable. A special thanks to my mother, Smt. Zaitoon Begum has sacrificed her comfort to enable me to achieve success in the academic world and beyond. I will be thankful to my parents throughout my life.

I would also like to express my deep appreciation to my sisters (Nazam Naz, Shazia Kosser, Rozia Kosser, and Fozia Kosser) and my brothers (Mohd Asif and Mohd Saqib) for their constant support and love, without which this achievement would not have been possible. My heartfelt thanks to my brothers-in-law, who have supported me like brothers, for their constant encouragement and guidance during challenging times.

I extend my sincere and profound appreciation to my colleagues: Dr Anjori Sharma, Seema Sharma, Sandeep, Paramjeet, Assima Qureshi, Dr. Dipesh, Sabreen Bashir, Chander Mohan, Khalid Aziz, and Shabina. Your support has been invaluable.

I would like to extend my heartfelt thanks to my roommates, Qurat ul Ain and Mankomal Arora, whose unwavering support and companionship have been instrumental throughout my Ph.D. journey. Your constant encouragement, patience, and understanding have made these years not only bearable but memorable. I am deeply grateful for the late-night discussions, the shared moments of joy and stress, and the unwavering friendship that you have both provided.

Thank you for standing by me in every difficult situation and for making this journey a truly unforgettable experience. Your presence has been a blessing, and I will cherish our memories forever.

Finally, I express my gratitude to my family members for their indispensable support, selfless sacrifices, and unwavering encouragement, which played a significant role in enabling me to complete this research work, directly and indirectly.

Shakra Jabeen

Table of Contents

S.No.	Content	Page No
	Declaration	ii
	Certificate	iii
	Abstract	iv
	Acknowledgement	vii
	Table of Contents	ix-xi
	List of Figures	xii-xv
	List of Tables	xvi
1	Introduction	1
1.1	Background	1
1.2	History of Supercapacitors	3
1.3	What is Inside Supercapacitors?	4
1.3.1	Electrode Materials	4-9
1.3.2	Electrolytes	9
1.3.3	Separator	10
1.4	Types of Supercapacitors	10-13
2	Manganese Molybdate as an Active Electrode Material: A Short Review	14
2.1	Properties of MnMoO ₄	15
2.1.1	Structural Properties	16-21
2.1.2	Morphological Properties	22-24
2.1.3	Electrochemical Properties	24-26
2.2	Impact of Compositing of MnMoO ₄ with Other Materials for Enhanced Electrochemical Performance	26
2.2.1	Carbonaceous Material and MnMoO ₄ -Based Composites	27-29

2.2.2	Metal Oxide and MnMoO ₄ Based Composites	29-30
2.2.3	Other Metal and MnMoO ₄ Based Composites	30
2.3	Motivation and Research Gap	32-33
2.4	Objective of Study	33
3	Materials and Characterizations	34
3.1	Materials and Synthesis Methods	34
3.1.1	Synthesis of MnMoO ₄	34-36
3.1.2	Synthesis of rGO@MnMoO ₄	37-38
3.1.3	Synthesis of MoS ₂ @MnMoO ₄	39
3.1.4	Synthesis of Ni-doped MnMoO ₄ (Ni _x Mn _{1-x} MoO ₄)	40
3.2	Electrode Preparation	41
3.3	Characterization Techniques	42-51
4	Binder-Free MnMoO₄ Nanoribbons on Ni-Foam for High-Performance Electrochemical Energy Storage Devices	52
4.1	Structure and Microstructure Analysis	52-54
4.2	Electrochemical Analysis	55-61
5	Boosting the Electrochemical Characteristics of MnMoO₄ Nanoparticles for Supercapacitor Applications	62
5.1	Structure and Microstructure Analysis	64-68
5.2	Electrochemical Analysis	69-74
5.3	An Asymmetric Device Analysis	74-77
6	Optimizing Electrochemical Performance: Investigating the Influence of Oxidation of Graphene Oxide in rGO@MnMoO₄	78
6.1	Structure and Microstructure Analysis	79-89
6.2	Electrochemical Analysis	89-96
6.3	An Asymmetric Device Analysis	96-98

7	Elevated Charge Storage Kinetics of Mesoporous MoS₂@MnMoO₄ Heterostructures for Advanced Hybrid Supercapacitors	100
7.1	Structural and Microstructural Analysis	103-107
7.2	Electrochemical Analysis	108-110
7.3	An Asymmetric Device Analysis	110-112
8	Mesoporous Ni-doped MnMoO₄ Nanoparticles for High-Performance Asymmetric Supercapacitors.	114
8.1	Structural and Microstructural Analysis	116-120
8.2	Electrochemical Analysis	120-127
8.3	An Asymmetric Device Analysis.	128-131
9	Conclusion and Future Scope	133
	Bibliography	137-154
	List of Publications	155-156

List of Figures

Fig.No.	Title	Page No
1.1	Ragone plot representing the range of different energy storage devices.	2
1.2	Electrochemical Performances of CV and GCD of EDLC, Pseudocapacitive, and rechargeable battery materials.	7
2.1	Properties of MnMoO ₄	15
2.2	Crystal structure of α -MnMoO ₄	16
3.1	Schematic for the synthesis of MnMoO ₄ by hydrothermal method.	36
3.2	Schematic for the synthesis of MnMoO ₄ by microwave method.	36
3.3	Schematic for the synthesis of graphene oxide	37
3.4	Schematic for the synthesis of rGO@MnMoO ₄ by hydrothermal method.	38
3.5	Schematic for the synthesis of MoS ₂ by hydrothermal method	39
3.6	Schematic for the synthesis of MoS ₂ @MnMoO ₄ by hydrothermal method	40
3.7	Schematic for the synthesis of Ni-doped MnMoO ₄ by hydrothermal method	41
3.8	Schematic of Asymmetric supercapacitor device	51
4.1	a) The XRD and b) Raman spectra of MnMoO ₄ nanostructures	53
4.2	a-d) The FESEM micrographs of MnMoO ₄ @NF at different magnifications and e) shows the EDS mapping of MnMoO ₄ @NF.	54
4.3	The CV curves of MnMoO ₄ @NF with different mass loadings, at different scan rates.	55
4.4	a) The variation of specific capacity with scan rate at different mass loadings. b) The variation of the peak current of CV plots with scan rates of MnMoO ₄ @NF at different mass loadings.	57
4.5	The GCD curves of MnMoO ₄ @NF with different mass loadings, at different current densities.	58
4.6	a) The comparison of GCD curves of MnMoO ₄ @NF with different mass loadings at a current of 5A. b) The variation of specific capacity of MnMoO ₄ @NF with current density at different mass loadings.	59

4.7	The variation of retention percentage of specific capacitance of MnMoO ₄ @NF with 0.1mg mass loading. The inset shows the 25 cycles at a certain intermediate time duration.	60
4.8	The EIS curve of MnMoO ₄ @NF with 0.1mg mass loading and the inset represents its equivalent circuit diagram	61
5.1	The XRD spectra of MnMoO ₄ nanoparticles at different calcination temperatures	64
5.2	The Raman spectra of MnMoO ₄ nanoparticles at different calcination temperatures	65
5.3	The FESEM images, of MnMoO ₄ nanoparticles calcinated at a) 300 °C, b) 500 °C, and c) 700 °C. d) The EDS mapping of MnMoO ₄ nano- particles calcinated at 500 °C.	66
5.4	The Nitrogen adsorption-desorption isotherm and the graph between pore volume with pore diameter of MnMoO ₄ nanoparticles calcinated at a) 300°C, b) 500°C and c) 700°C	67
5.5	The XPS spectra of MnMoO ₄ nanoparticles calcinated at 500 °C	69
5.6	a–c) The CV scans of electrodes prepared with MnMoO ₄ nanoparticles calcinated at different temperatures, d) the comparison of CV scans of MnMoO ₄ nanoparticle-based electrodes with bare nickel foam at 10 mV s ⁻¹ , and e) the variation of specific capacity of these electrodes with scan rate.	72
5.7	a–c) The GCD curves of electrodes prepared with MnMoO ₄ nanoparticles calcinated at different temperatures. d) the variation of the specific capacity of these electrodes with current density.	73
5.8	The Nyquist plots of electrodes prepared with MnMoO ₄ nanoparticles calcinated at different temperatures and the equivalent circuit. The inset displays the zoomed view of the high-frequency region	74
5.9	a) The CV curves at different voltage-window (the CV data of bare activated carbon electrode is shown in the inset), b) the CV curves at different scan rates, c) the GCD curves at different current densities, d) the variation of power density and energy density, e) the variation of percentage-specific capacitance retention with cycle number and f) the Nyquist Plots, of the asymmetric device.	76
5.10	The Ragone Plot to compare the present and reported work	77
6.1	XRD spectra of graphene oxide synthesized with different oxidation duration	80
6.2	a) Raman and b) FTIR spectra of graphene oxide synthesized with different oxidation duration.	82
6.3	The diffraction patterns of different rGO@MnMoO ₄ composites.	83
6.4	The Raman a) and FTIR b) spectra of rGO@MnMoO ₄ (A4) composite.	85

6.5	The FESEM images a-d), EDS mapping e), Nitrogen adsorption-desorption isotherm f), and the graph between pore volume with pore radius g) of rGO@MnMoO ₄ (A4) composite.	86
6.6	The Nitrogen adsorption-desorption isotherm a), and the graph between pore volume with pore radius b) of rGO@MnMoO ₄ (A4) composite.	87
6.7	The XPS survey spectrum a) and core spectra b-e) of rGO@MnMoO ₄ (A4) composite.	88
6.8	The CV scans of different rGO@MnMoO ₄ composites a-e) at different scan rates and their comparison f) at scan rate 10mV/s. The variation g) of specific capacity of different rGO@MnMoO ₄ composites with scan rates.	91
6.9	The GCD curves of different rGO@MnMoO ₄ composites a-e) at different current densities and their comparison f) at current density 2A/g. The variation g) of specific capacity of different rGO@MnMoO ₄ composites with current density.	92
6.10	The comparison of CV scans a), the variation of specific capacity b) with scan rate, the comparison of GCD curves c), and the variation of specific capacity d) with the current density of rGO@MnMoO ₄ composites synthesized with different concentrations of GO (G4). The Nyquist Plot e) of the B3 sample and its equivalent circuit.	94
6.11	The CV curves a) at different voltage-window, the CV curves b) at different scan rates, the GCD curves c) at different current densities, the variation d) of power density and energy density, the variation e) of percentage specific capacity retention and Coulombic efficiency with cycle number and the Nyquist plots f) of the asymmetric device.	97
7.1	a) The XRD patterns and b) Raman patterns of MnMoO ₄ , MoS ₂ , and MoS ₂ @MnMoO ₄ respectively.	104
7.2	The FESEM images of MnMoO ₄ a-c), MoS ₂ d-f), and MoS ₂ @MnMoO ₄ g-i), EDS and mapping of MoS ₂ @MnMoO ₄ j -k)	105
7.3	The Nitrogen adsorption-desorption isotherm and the graph between pore volume with pore diameter of a, b) MnMoO ₄ , c, d) MoS ₂ and e, f) MoS ₂ @MnMoO ₄ .	106
7.4	The XPS spectra of MoS ₂ @MnMoO ₄	107
7.5	The CV scans of a) MnMoO ₄ , b) MoS ₂ and c) MoS ₂ @MnMoO ₄ at different scan rates, the GCD of d) MnMoO ₄ , e) MoS ₂ , and f) MoS ₂ @MnMoO ₄ at different current densities, g) the variation of specific capacity of these electrodes with scan rates, h) the variation of specific capacity of these electrodes with current densities and i) EIS spectra of MnMoO ₄ , MoS ₂ and MoS ₂ @MnMoO ₄ and their equivalent circuit.	109
7.6	a) The CV curves at different voltage-window, b) the CV curves at different scan rates, c) the GCD curves at different current densities, d) the variation of power density and energy density with current density, e) the variation of percentage	111

	specific capacity retention and Coulombic efficiency with cycle number and f) the Nyquist plots of the asymmetric device.	
7.7	The Ragone plot for comparison of device performance	113
8.1	The XRD patterns of $\text{Ni}_x\text{Mn}_{1-x}\text{MoO}_4$ at different values of x.	117
8.2	The Raman spectra of $\text{Ni}_x\text{Mn}_{1-x}\text{MoO}_4$ at different values of x.	118
8.3	a-b) The FESEM images, c) EDS mapping, d) Nitrogen adsorption-desorption isotherm, and e) multi-point BET isotherm of $\text{Ni}_{0.25}\text{Mn}_{0.75}\text{MoO}_4$ nanoparticles.	119
8.4	a) The XPS survey spectrum and b-e) and core spectra of $\text{Ni}_{0.25}\text{Mn}_{0.75}\text{MoO}_4$ nanoparticles.	121
8.5	a-d) The CV scans of electrodes prepared with $\text{Ni}_x\text{Mn}_{1-x}\text{MoO}_4$ at different values of x. e) The comparison of the CV scan of all electrodes at 10mV/s. f) The variation of specific capacity of these electrodes with scan rate.	123
8.6	a-d) The GCD curves of electrodes prepared with $\text{Ni}_x\text{Mn}_{1-x}\text{MoO}_4$ at different values of x. e) The comparison of GCD curves of all electrodes at 1A/g. f) The variation of specific capacity of these electrodes with current density.	124
8.7	a) The CV curves at different scan rates, b) the variation of specific capacity with scan rate. c) the GCD curves at different current densities, d) the variation of specific capacity with a current density of binder-free $\text{Ni}_{0.25}\text{Mn}_{0.75}\text{MoO}_4$ nanoparticles-based electrode. e) The EIS curves of binder-enriched and binder-free $\text{Ni}_{0.25}\text{Mn}_{0.75}\text{MoO}_4$ nanoparticles-based electrodes and their equivalent circuit. f) The FESEM images of $\text{Ni}_{0.25}\text{Mn}_{0.75}\text{MoO}_4$ nanoparticles directly grown on the nickel form.	126
8.8	The CV curves at various voltage windows a), different scan rates b), GCD curves at various current densities c), power density and energy density variation d), percentage specific capacitance retention variation e) with cycle number, and Nyquist Plots f) of the binder-enriched $\text{Ni}_{0.25}\text{Mn}_{0.75}\text{MoO}_4@\text{NF} // \text{GAC}$ asymmetric device.	130
8.9	The CV curves at various voltage windows a), different scan rates b), GCD curves at various current densities c), power density and energy density variation d), percentage specific capacitance retention variation e) with cycle number, Nyquist Plots (inset) of the binder-free $\text{Ni}_{0.25}\text{Mn}_{0.75}\text{MoO}_4@\text{NF} // \text{GAC}$ asymmetric device. f) The FESEM image of the binder-free anode after 10000 cycles. g) The equivalent of the device.	131
8.10	The Ragone plot displays the comparison of the present and the previously reported work.	132
9.1	Ragone Plot to compare the energy density of all asymmetric devices.	134

List of Tables

Table No.	Table Captions	Page No.
1.1	The capacitive performance of different electrode materials	8
2.1	The crystal structure of MnMoO ₄ -based materials with different methodologies	17
2.2	Raman characteristics of MnMoO ₄	20
2.3	Different synthesis methods for MnMoO ₄ with their specific capacitances	28
2.4	The comparison of the electrochemical performance of MnMoO ₄ with other composites	31
3.1	Details of chemicals used in research work	36
3.2	Mass loadings of electrodes prepared by in-situ hydrothermal method	42
3.3	The detailing of XPS peaks of elements used in this research work with their binding energies	47
5.1	The fitted values of the equivalent circuit's component of all electrodes.	73
6.1	The structural parameters of GO samples with different levels of oxidation.	81
6.2	The comparison of electrochemical performance of MnMoO ₄ and carbonaceous material-based composites.	95
7.1	The fitted values of the equivalent circuit's component of all electrodes.	111
8.1	Comparative analysis of electrochemical parameters between Ni _{0.25} Mn _{0.75} MoO ₄ and other MoO ₄ -based electrodes.	115
8.2	The fitted values of various components of the equivalent circuit of binder-enriched and binder-free electrodes.	127

Chapter 1

Introduction to Supercapacitors

1.1. Background

The key challenges confronting our global society revolve around health, energy, and the environment. Undoubtedly, most energy requirements are still met by non-renewable resources, including coal, oils, and fossil fuels. These traditional energy foundations are discouraged by their adverse effects on the environment, including pollution and global warming. The continued reliance on nonrenewable energy resources has increased atmospheric CO₂ levels, making it challenging to sustain a healthy way of living on Earth.

To reach zero emissions, sustainable energy resources like hydrothermal, wind, solar, and electrochemical, are one solution to the problem of environmental changes that endanger human survival on the earth [1]. Sources coming from sustainable energy must be harnessed and stored with dependable technologies like batteries and supercapacitors[2]. When comparing the characteristics of various devices, like efficiency, energy density, discharge time, power rating, and cycle life, it is clear that each technology offers unique benefits and drawbacks. It is important to note that no individual energy storehouse or transformative innovation can fulfill all necessities, such as affordability, performance, efficiency, and capability. Therefore, to expand their usage, the development of various technologies can enhance their power while restraining their flaws in conjunction with suitable energy-accumulated systems. Recently, a significant increase in interest and research focused on systems using electrochemical processes like rechargeable batteries and supercapacitors (SCs), which can be used independently or combined to form hybrid systems that can support each other [3]. Battery technology has been extensively utilized and studied as the predominant form of energy storage, particularly in portable electronics and mobile devices. Over the past time, researchers have made noteworthy advancements in enhancing the efficiency and application of batteries with the conversion of alkaline metal ion structures from lead acid. Lithium-ion batteries (LIBs) have emerged as reliable devices in various industries. Nonetheless, LIB systems face significant developmental challenges, including issues related to stability, low power density, and safety [4]. In present-day technology, energy storage devices like fuel cells, are now considered more important than battery devices due to several benefits, including better power density and efficiency, eco-friendliness, fuel variety, flexible configuration, and

quick load reactions, despite the latter being widely used. As electricity-producing devices that transform chemical energy into electrical energy, fuel cells have a higher power output per unit of volume or mass. Consequently, they have greater potential for effective energy conversion [5]. Despite being environmentally friendly, fuel cells fail to meet sustainability goals owing to their slow speed, unreliable hydrogen storage skills, and other obstacles [6]. An electrochemical capacitor, also known as a supercapacitor (SC), has characteristics that lie between those of a conventional capacitor and a battery, as shown in the Ragone Plot in Fig.1.1. The Ragone Plot, is a means of assessing and contrasting the capabilities of different energy storage technologies. The x-axis displays the energy per unit volume (Wh kg^{-1}), while the y-axis displays the power per unit volume (W kg^{-1}). Capacitors although have maximum power density, exhibit the lowest energy density. Conversely, fuel cells have advanced energy density, but require intricate storage mechanisms. Batteries are low in power but high in energy density. Supercapacitors fall between capacitors as well as batteries in both energy and power density. Supercapacitors (SCs), better known as ultracapacitors, have been a topic of extensive research for a decade due to their elevated specific capacitance and specific power.

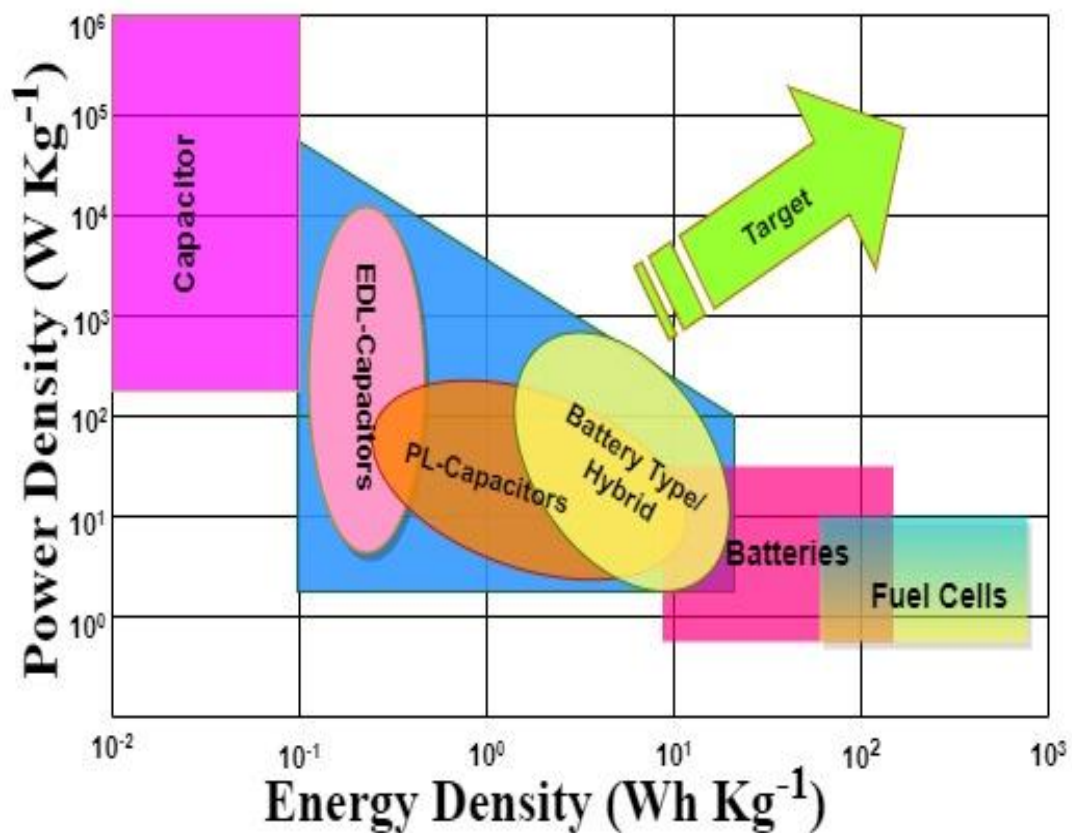


Fig.1.1. Ragone plot representing the range of different energy-storage devices.

Compared with batteries, supercapacitors are these days priority due to their high- specific power, quick charge/discharge, good cycling stability, excellent efficiency rate, function within a warmth range of -40 to -70°C [7], environmental friendliness, safety, and behave as a connection for the power-energy difference that exists between capacitors and batteries [8]. Moreover, SCs are more stable owing to their load capacity during charging and discharging and long-life expectancy. Because they do not use metals of high density and additional chemical compounds that pollute the environment in their manufacturing process, SCs are environmentally friendly and therefore referred to as "green power sources" [9]. Supercapacitors have been researched for numerous energy storage applications, including electric vehicles, power grids, and portable electronics like laptops and cell phones. Consequently, they are becoming increasingly relevant in everyday life [10].

1.2. History of Supercapacitors

The invention of capacitors has a captive history. 1745 Ewald Georg Von Kleist observed the charge storage phenomena in a water-filled handheld glass jar. Subsequently, Dutch physicist Pieter Van discovered a capacitor known as Lyden Jar. Before the invention of supercapacitors, aluminum ceramic capacitors were the most commonly used electrolytic capacitors. In aluminum electrolytic capacitors, one of the two pieces of aluminum foil is etched to form a thin layer of aluminum oxide, which acts as a dielectric. Consequently, they are becoming increasingly relevant in everyday life [10]. The first supercapacitor cell patent application was submitted by Becker to General Electric engineers for an electric double-layer capacitor in 1957 by employing porous carbon as an electrode and an aqueous electrolyte. During its initial stages, it was postulated that energy was stored within the pores of the porous carbon, although the underlying mechanism remains a mystery. Later, the Ohio company(SOHIO) industrialized a new design of an electrochemical condenser, in which activated charcoal was used as an electrode material sandwiched between an insulating separator, and to date, the basic design of a supercapacitor. When supercapacitors were discovered to improve battery and fuel cell performances, they were initially utilized in hybrid electronic automobiles. With time, it revealed that supercapacitors provide the required accelerated power and recoup energy lost during braking, known as regenerative braking. Over time, supercapacitors have become better backup power sources to guard against power outages, and they have replaced fuel cells and batteries as primary energy storage devices [11–13]. SOHIO, unable to commercialize the technology, transferred it to the “National Electrical Code (NEC),” successfully bringing it to the market in 1979.

In 1971, the performance of ruthenium oxide was examined by Tassati and Buzanca, who observed the same electrochemical behavior that as of a capacitor. From 1975-1980, based on ruthenium oxide, lots of research has been conducted on supercapacitors based on ruthenium oxide [14]. Initially, the technology found utility as a power backup for computers. However, from the mid-90s to the present day, companies such as Panasonic, NEC/TOKIN, and Maxwell Technologies have invested in the advancement of electrochemical capacitors. Lux Research conducted a market analysis, revealing that the Electrochemical Capacitor System (ECS) market was valued at approximately \$208 million in 2009. This figure escalated to \$877 million in 2014 and has since continued to surge in recent years owing to its extensive application in devices such as cell phones, digital cameras, and smart grids [14]. Over the past three decades, significant advancements in supercapacitor technology have occurred, encompassing a variety of supercapacitors like flexible, solid-state, aqueous hybrid, healable and stretchable, micro-, paper-based, and bio-inspired pigment-based supercapacitors [10].

1.3. What is Inside Supercapacitors?

A standard supercapacitor elementary cell serving as an energy storehouse device closely resembles a battery in its design, comprising two electrodes (positive and negative), a separator, and an electrolyte.

1.3.1. Electrode Materials

Electrodes are conductive materials that are essential in deciding the efficiency and performance of supercapacitors. For the adsorption and desorption of ions throughout charging and discharging cycles, the electrode materials serve as a base for energy storage. The overall achievements of an electrode material depend on its morphology, redox characteristics, surface area, porosity, surface functional groups, energy density, and charge transfer capabilities [15]. The supercapacitor's specific capacitance profoundly relies on the particular area of material surface used for the electrodes. But in some cases, the measured capacitance doesn't always increase in direct proportion to the superficial area because all parts of the area are not accessible to the electrolyte, limiting the material's effective charge storage capacity. A significant factor that influences the electrochemically active surface area is the size of the pores in the electrode material [16]. The porosity is important for the generation of high specific capacitance. Therefore, if the electrode's superficial area that touches the electrolyte is larger, the capacity of supercapacitors will be higher. This is because a larger surface area allows for more ions to be stored at the electrode-electrolyte interface, thereby increasing the overall capacitance of the supercapacitor. The active materials used as electrodes for supercapacitors

on the basis of charge storage processes can be electric double-layer (EDL) or pseudocapacitive, depending upon their type. A significant feature of an electric double-layer is that it stores an electrical charge which primarily relies on the physical separation of ions in the electrolyte near the surface of the electrode, forming an electric double-layer. This separation creates a voltage across the double layer, which allows EDLCs to store electrical energy without involving any chemical reactions that consume or release electrons. In contrast, pseudocapacitors supply charge via a redox process, characterized by quick and reversible oxidation-reduction occurring at or adjacent to the shallow of the participating component. This process involves modification to the electrode material's valence state brought on by electron transport [17]. The energy storage mechanisms entail not only the cyclic accumulation and depletion of charges through electrostatic processes but also, upon the application of an external potential, rapid and reversible faradaic reduction-oxidation occurs near the boundary of the electrolyte and electrode, facilitating the passage of charges [18].

In supercapacitors, electrode materials are categorized into three types: Electric double-layer capacitive-based, pseudocapacitive-based, and hybrid-based. Carbon-based materials, including carbon aerogels [19], activated charcoal [20], structured carbon [21], and carbon-based nano materials, like carbon nanotubes as well as graphene [22], have been extensively used and investigated for EDLCs. The significant superficial area of carbon-based resources ranges from 1000 to 3000 m²g⁻¹, and the theoretical capacitance ranges from 300 to 550Fg⁻¹ [23,24]. Nevertheless, owing to the limited conductivity as well as inadequate accessibility of all surface sites, the applied explicit capacitance achieved for carbon-based EDLCs in experimental settings has typically been constrained to approximately 100–250 Fg⁻¹ [25]. As a result, commercially available supercapacitors utilizing EDLC electrode materials have an energy storage capacity ranging from 3–10 Whkg⁻¹. Even though these materials exhibit a large specific area, their capacitance is not as high as expected. Therefore, to increase the supercapacitor's specific capacitance a new electrochemically active material, which is pseudocapacitive, was developed.

Electrode materials exhibiting pseudocapacitive behavior generally include transition metal oxides/hydroxides, metal nitrides/sulfides [26], polymers, and metal-organic frameworks (MOFs), which offer alternative options [27]. Examples include ruthenium (IV) oxide, iridium dioxide, iron (II, III) oxide, manganese (IV) oxide, nickel oxide, vanadium oxide, transition metal sulfides, and conductive polymers such as PANI, polyacetylene, polyvinyl alcohol, and polypyrrole. The metal oxides Co₃O₄ (theoretical capacitance 3560Fg⁻¹) [28], MnO₂ (theoretical specific capacitance 1370Fg⁻¹) [28], and ZnO are always abundant and exhibit good

specific capacitance, indicating that they can replace RuO₂. Transition metal oxides (TMOs) can deliver an elevated energy per unit volume and improved electrochemical constancy. Electrodes made from conducting polymers are suitable for use due to their special qualities like superior electrical conductivity, good efficiency/storage capacity, many active redox sites, and low environmental impact [16]. When conductive polymers are present, redox processes take place on the material's surface as well as inside its bulk, increasing the energy density and supercapacitors' ability to store energy. Conducting polymers results in low cycling stability, volume change during the charging-discharging process, and inactive chemical surface area [29]. One major problem with conducting polymers is that at the time of the intercalation/deintercalation process, they become swollen and shrink, which results in electrode destruction and degradation of the electrochemical performance[30,31]. Although pseudocapacitive electrodes can exhibit a higher capacitance than electric double-layer (EDL) electrodes, they generally have disadvantages such as poor cycling stability. No single type of material provided desirable results. Every variety possesses pros and cons of its own.

Therefore, the invention of hybrid materials can improve the electrochemical achievements by combining them to obtain the benefits of each element. The widely observed scenario is to combine conducting polymers or carbon-based materials with metal-based materials to create composites with significantly increased conductivity. This enhances the overall performance, including the cycling life, rate capability, and specific capacitance. The chemical and physical characteristics of electrodes are combined in carbonaceous materials and metal. Carbonaceous materials provide more surface area and charge transfer for non-Faradaic reactions. Comparatively, the electrical charge storage of polymers or metal oxides is via redox reactions [32]. These materials increase the electrode's specific capacitance, thereby enhancing the energy per unit volume of the device [33]. For example, MnO₂/graphene [34], CuO/RuO₂/MWCNT [35], PANI/MWCNT [36], NiMoO₄@MoS₂ [37], MnCo₂O₄/rGO[38], MnO₂@CNT [39], etc. are various types of hybrid electrode as an active materials that are used to enhance the efficiency of device. Thus, increased energy and power per unit volume can be obtained using hybrid materials that are battery-type. For example, MWCNT/LiCo₂O₄ [40], AC-PbO₂ [41], Li₂Mn₄O₉ [42], MnFe₂O₄ [43], CNT/Cu(OH)₂ [44], graphene-V₂O₅ [45] etc. The capacitive performance of various types of electrode materials is detailed in Table 1.1. Hybrid nanomaterials offer superior ionic and electric conductivity compared to other electrode materials. These materials also offer electrochemically active intercalation sites, which results in rapid ion diffusion transport and high specific capacitance. The hybrid electrode materials are operated in a wider potential window. However, work has been done on unitary metal oxide,

metal sulfides, or binary metal oxides as an electrode material as mentioned in Table 1.1. They exhibit limitations such as low energy density or limited cycling stability, and maintaining their morphology can also be challenging.

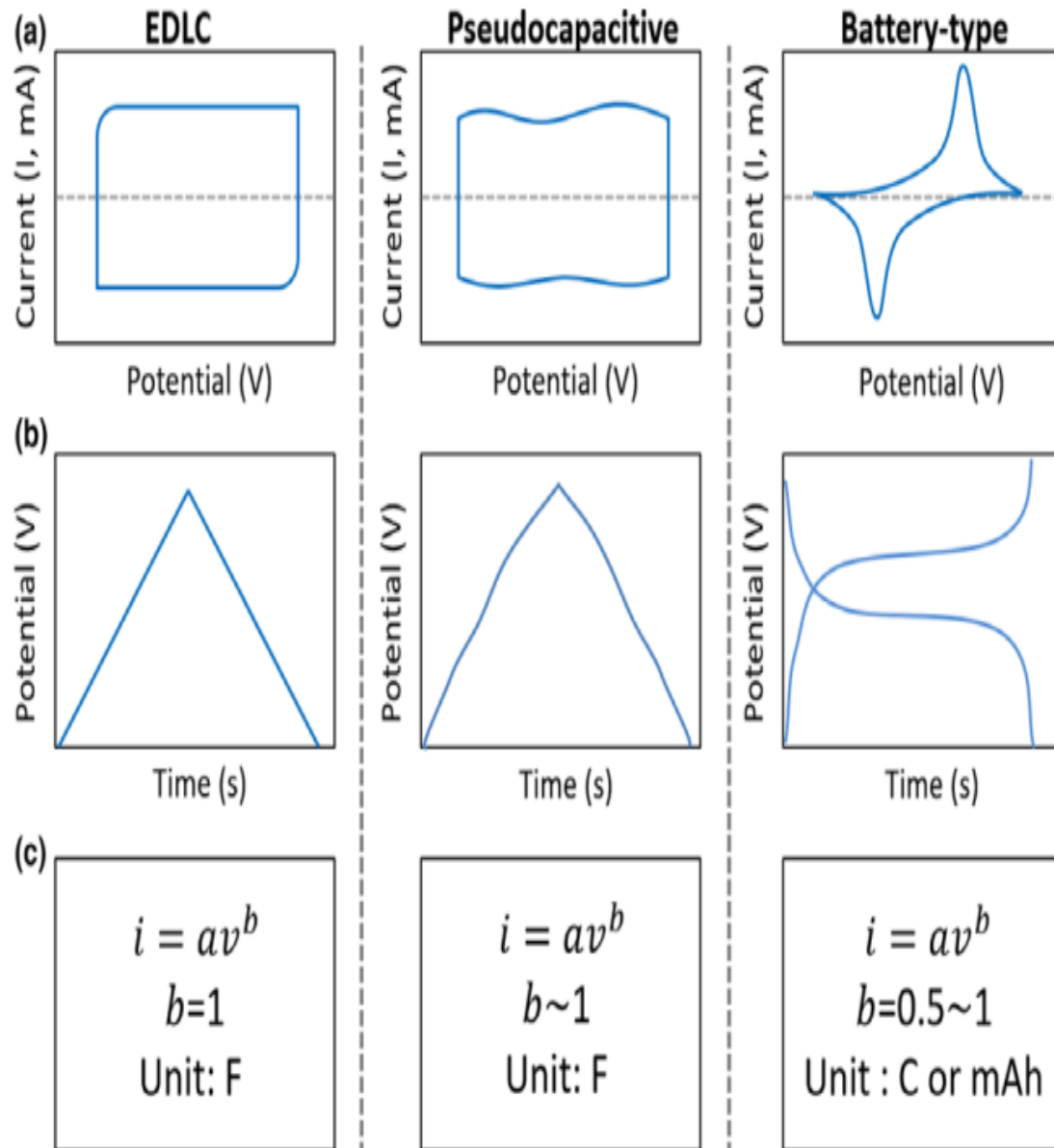


Fig.1.2. Electrochemical performance CV and GCD of EDLC, Pseudocapacitive, and rechargeable battery materials [46].

Table 1.1. The capacitive performance of different electrode materials.

Type	Electrode Materials	Scan Rate /Current Density	Specific Capacitance (Fg^{-1})	Retention	Ref.
Carbon-based materials	Activated Carbon	0.5Ag^{-1}	74	86.5% after 500 Cycles	[20]
	Mesoporous Graphene	5mVs^{-1}	206	96% after 10000 cycles	[46]
	Nitrogen-doped Activated Carbon	0.4Ag^{-1}	115	76.3% after 8000 cycles	[47]
	Graphene CNT composite	0.5Ag^{-1}	290.4	100% after 1300 cycles	[48]
	Carbon spheres	1Ag^{-1}	196.43	90% after 1000 cycles	[49]
Metal oxides/hydroxides	$\text{RuO}_2 \cdot n\text{H}_2\text{O}$	25mVs^{-1}	1340	-	[50]
	MnO_2 micro flowers	5mAcm^{-2}	376	138% after 2500 cycles	[51]
	MnO_2 nanosheet arrays	0.5Ag^{-1}	595.2	89% after 3000 cycles	[52]
	V_2O_5 nanowires	1Ag^{-1}	832	94.6% after 10000 cycles	[53]
	Co_3O_4 nanowires	1Ag^{-1}	1140	93.3% after 5000 cycles	[54]
	NiO nanoflakes	0.5mAcm^{-2}	401	92% after 500 cycles	[55]
	$\text{Ni}(\text{OH})_2$ microrods	1mAcm^{-2}	1018	72.9% after 3000 cycles	[56]
	$\text{Co}(\text{OH})_2$ nanoflakes	2Ag^{-1}	935	82.6% after 1500 cycles	[57]
	Iron oxide nanoneedles	10mVs^{-1}	418.7	93.3% after 5000 cycles	[58]
Conducting Polymers	PEDOT nanoparticles	1Ag^{-1}	284	79% after 5000 cycles	[59]
	PANI nanowires	1Ag^{-1}	950	78% after 500 cycles	[60]
	PANI/CNT	5Ag^{-1}	1030	94.5% after 5000 cycles	[61]
	MnO_2 -embedded PPy nanocomposites	5mVs^{-1}	620	90% after 5000 cycles	[62]
	Graphene/PANI	1Ag^{-1}	763	82% after 1000 cycles	[63]
	PANI/MWCNT nanotubes	1Ag^{-1}	515	94.6% after 1000 cycles	[64]
Metal Sulfides	NiS_2 nanocubes	1.25Ag^{-1}	695	93.4% after 3000 cycles	[65]
	CoS_2 nanocrystals	0.5Ag^{-1}	654	72% after 600 cycles	[66]
	MoS_2 nanosheets	5mVs^{-1}	$\sim 700\text{ Fcm}^{-3}$	97% after 5000 cycles	[67]
	CuS nanosheets	1Ag^{-1}	833.3	75.4% after 500 cycles	[68]

	NiSe nanowire	5Ag^{-1}	1790	70% after 1000 cycles	[69]
	MoS ₂ /rGO	10mVs^{-1}	265	92% after 5000 cycles	[70]
	Ni ₃ S ₂ nanosheets	2Ag^{-1}	1370.4	91.4% after 1000 cycles	[71]
Binary/Ternary metal oxides	NiCo ₂ O ₄ nanostructures	1Ag^{-1}	1650	91.8% after 2000 cycles	[72]
	MnCo ₂ O ₄ @Ni(OH) ₂ core-shell flowers	5Ag^{-1}	2154	90% after 2500 cycles	[73]
	ZnCo ₂ O ₄ nanorods	1Ag^{-1}	1400	97% after 1000 cycles	[74]
	FeMoO ₄ /graphene	1Ag^{-1}	135	70.4% after 500 cycles	[75]
	MnMoO ₄ /CoMoO ₄ nanowires	1Ag^{-1}	187.1	98% after 1000 cycles	[76]
	Co ₃ O ₄ /graphene nanoparticles	1mVs^{-1}	3482	>86.2% after 20000 cycles	[77]
	NiMoO ₄ nanowires	5mAcm^{-2}	1587	76.9% after 4000 cycles	[78]
	NiCo ₂ O ₄ @MnO ₂ core shell nanowire	2mAcm^{-2}	2.24	~113.6% after 8000 cycles	[79]
	MnMoO ₄ -NiWO ₄ Microspheres	1Ag^{-1}	598	82% after 500 cycles	[80]

However, work has been done on unitary metal oxide, metal sulfides, or binary metal oxides as an electrode material as mentioned in Table 1.1. They exhibit limitations such as low energy density or limited cycling stability, and maintaining their morphology can also be challenging. Kinetic information about electrochemical reactions can be provided by the Dunn power law relationships from the b value, where b is an adjustable parameter. GCD and CV of electric double layer, pseudocapacitive, and battery type are shown in Fig.1.2, the cyclic voltammogram curve of the EDLC material is rectangular, the current curve constantly changes linearly over time, and the b value is always 1. The CV curve of pseudocapacitors is quasi-rectangular and contains two inconspicuous peaks and almost linear GCD curves, and the value of b was close to 1. In comparison to EDLC and Pseudocapacitive electrode material, the battery type materials like MnCo₂O₄, NiMoO₄, Co₃O₄, etc. with the CV curve showing obvious redox peaks and the GCD curve has detectable plateaus with a nonlinear curve that shows the faradaic nature of materials and b values lie between 0.5-1 [81, 82].

1.3.2. Electrolytes

Electrolytes are essentially a liquid that acts as a barrier between the electrodes of supercapacitors and allows ions to pass through the surface of the electrode. The selection of the right electrolyte is crucial because it aids charge storage in the electrode while being chemically inert to the electrode. Therefore, the preferred electrode material used in

supercapacitors significantly affects the selection of electrolytes. Different kinds of electrolytes (such as aqueous, solid-state polymer, ionic liquid, and organic) are used in supercapacitors with their benefits and flaws. Supercapacitors (SCs) require a nonvolatile electrolyte with higher electrochemical stability, low viscosity, higher ionic concentration, lower resistance, and reduced ionic radius to expand the range of voltages where they can operate. Organic electrolytes pose handling challenges and are toxic. Ionic liquid electrolytes have low conductivity and are more expensive. Solid-state electrolytes provide low capacitance and poor capability rates. It is claimed that, compared to organic electrolytes, aqueous electrolytes (alkaline and acidic electrolytes) have larger ionic concentrations and lower resistance, which leads to higher capacitance and power density. Moreover, the electrolytes used in supercapacitors should be affordable and non-toxic. Some examples of dissimilar types of electrolytes are basic electrolytes, for example, potassium hydroxide, sodium hydroxide, and sodium chloride, and acidic electrolytes, such as sulfuric acid, electrolytes, and neutral electrolyte PO_4^{3-} buffer [83,84].

1.3.3. Separator

A separator separates the two electrodes from each other and is required for a supercapacitor assemblage to create a barrier. The primary function of a separator is to prevent the short-circuit failure of the system. This permits ions to move freely across the supercapacitor without any chemical modifications. Due to its poor design, the separator can negatively affect the cell and allow it to develop additional resistance. Cellulose paper, glass, ceramics, and polymers are materials used to fabricate separators. Recent developments in separator technology include polymer-based separators, which have the advantages of low cost, flexibility, electrolyte-ion permeability, and porosity. The selected separator must be nonconductive to avoid direct electron transfer between electrodes. [85,86].

1.4. Types of supercapacitors

Supercapacitors can be classified into two groups based on charge-storage mechanisms and the active materials used in their electrodes.

- Symmetric supercapacitors
- Asymmetric supercapacitors

Symmetric supercapacitors are fabricated using identical electrode materials on the cathode and anode. Symmetric supercapacitors use electric double-layer (EDL) or pseudo-capacitance-based electrode materials based on charge storage. Owing to the same electrode materials with equal mass loading on both sides, the operating voltage range for a symmetric supercapacitor

is mostly approximately 1 V, which hinders its energy density. Calvo and colleagues developed a symmetric supercapacitor using activated carbon Xerogel electrodes. The device operates within a 1V potential window and demonstrates a specific capacitance of 35Fg^{-1} . Additionally, it has an energy density of 4.9Whkg^{-1} indicating its capacity to store energy relative to its mass [87]. A thin-film MnO_2 -based symmetric supercapacitor was prepared by Nilesh et al. in a voltage range of 1V. The device displayed a capacitance value of 145Fg^{-1} yielding energy per unit volume of 16Whkg^{-1} and was stable after 2500 cycles [88]. Therefore, spreading the operating voltage range would be additionally effective for aqueous supercapacitors in improving the energy per unit volume rather than increasing the device's capacitance. Bello et al. synthesized an aqueous symmetric supercapacitor based on 3D porous carbon from activated graphene foam using a template-based approach with a voltage of 1.6V. The as-prepared porous material, with a superficial area of $502\text{m}^2\text{g}^{-1}$, makes it a suitable electrode substantial in supercapacitors and it delivers a capacitance of 65Fg^{-1} when tested in 1M Na_2SO_4 achieving an energy per unit volume of 12Whkg^{-1} and a power per unit volume of 0.4kWkg^{-1} [89]. Xie et al developed a sandwiched-like porous carbon/graphene composites enriched with nitrogen by carbonization of Polyacrylonitrile nanofiber paper. The composites showed a superficial area in the range $1957.2 - 2631.8\text{m}^2\text{g}^{-1}$. The supercapacitor delivered a capacitance value of 381.6Fg^{-1} at 0.1Ag^{-1} using an aqueous 6M KOH electrolyte, yielding an energy per unit volume of 13.2Whkg^{-1} at a power per unit volume of 25Wkg^{-1} with a stability of 62.9% [90]. Manuraj et al. fabricated an MoS_2 nanostructure-based symmetric supercapacitor. The shallow area of this material was $18.45\text{m}^2\text{g}^{-1}$. The supercapacitor demonstrates a capacitance of 244Fg^{-1} at 1Ag^{-1} , yielding an energy per unit volume of 12.2Whkg^{-1} and a power per unit volume of 0.6Kwkg^{-1} with a stability of 92% after 9000 cycles [91]. Xia and colleagues reported a RuO_2 symmetric supercapacitor operating within a 1.6V voltage range of 1.6V using an aqueous electrolyte. At 0.625Ag^{-1} , the cell exhibited a capacitance value of 52.66Fg^{-1} . It achieved an energy per unit volume of 18.77Whkg^{-1} at a power per unit volume of 500Wkg^{-1} [92]. A symmetric supercapacitor based on Mn_3O_4 was created by Dubal et al. in a 1M aqueous electrolyte. In the 1V voltage range, the cell provided a capacitance of 72Fg^{-1} . At a power per unit volume of 0.4kWkg^{-1} , it demonstrated an energy per unit volume of 25.4Whkg^{-1} . [92]. Waikar et al. fabricated a PANI-based symmetric supercapacitor. The symmetric supercapacitors achieved a capacitance of 160Fg^{-1} at 5mVs^{-1} with an energy per unit volume of 13.33Whkg^{-1} . After 2000 cycles, the capacitance remained at 47% [93]. Kumar et al. prepared a symmetric supercapacitor using MnO_2 electrodes, operating within a 1.3V potential range. The device exhibited a capacitance of 132Fg^{-1} , achieving an energy per unit volume of

26.4Whkg⁻¹ at a power per unit volume of 36 kWkg⁻¹. After 3000 cycles, the device retained 95.52% of its capacitance [94].

Asymmetric supercapacitors are fabricated using two different electrode materials on the anode and cathode. An asymmetric supercapacitor uses carbon-based material for an electric double layer (EDL) capacitance and a pseudocapacitive electrode material for charge storage. Asymmetric supercapacitors can have both electrodes made from the same material but they can differ in the amount of material used with different mass loadings or can be paired with one “battery-type electrode” with another “supercapacitor-type electrode”. The battery-type electrodes are used as energy reservoirs, whereas capacitor-type electrodes are used as power backups. Ultimately, the demand for elevated energy and power per unit volume can be met. These combinations lead to a rise in the capacitance value of the electrode, thereby enhancing the specific energy. [15,16,95,96]. Asymmetric supercapacitors have larger potential windows owing to their non-identical positive and negative electrodes. Asymmetric supercapacitors are prioritized over symmetric supercapacitors because of their faradaic and non-faradaic behaviors. The EDL-based electrode offers a larger surface area, whereas the pseudo-capacitance-based electrode enhances specific capacitance. The combination yields higher energy and power per unit volume in comparison to symmetric supercapacitors [16]. Kim and colleagues developed an asymmetric supercapacitor using silicon carbide MnO₂ nanoneedles and activated charcoal as anode and cathode in aqueous electrolytes. The supercapacitor displayed a capacitance of 59.9Fg⁻¹ at a scan rate of 2mVs⁻¹ in a voltage range of 1.9V. It delivered an energy per unit volume of 30.06Whkg⁻¹ at a power per unit volume of 113.9 Wkg⁻¹ with a stability of 3.1% after 1000 cycles [97]. Zhang and colleagues created an asymmetric device using Co₃O₄ and activated charcoal as an anode and cathode within a voltage range of 1.15V. The device showed a capacitance value of 81Fg⁻¹, yielding a specific energy of 24.9Whkg⁻¹. After 5000 cycles, the device was 90% stable of its initial capacitance value [98]. Cheng et al. synthesized an asymmetric supercapacitor using CoO@Co₃O₄ and graphene as an anode and cathode, respectively operating within a voltage range of 1.6V using an aqueous electrolyte. The device delivered a capacitance value of 123.9Fg⁻¹ at 1Ag⁻¹, yielding an energy per unit volume of 44.06Whkg⁻¹ at a specific power of 800 Wkg⁻¹. After 6000 cycles, the device was 74.9% stable. [99]. Huang and colleagues synthesized an asymmetric device using β-Ni(OH)₂ nanosheets and activated charcoal as an anode and cathode. The device showed a capacitance value of 105.8Fg⁻¹ in the voltage range of 1.6V and a specific energy of 36.2Whkg⁻¹ with cycling stability of 92% after 1000 cycles [100]. Kim and colleagues developed an asymmetric device in which Li₄Ti₅O₁₂ was wrapped with graphene and activated charcoal as

an anode and cathode. The supercapacitor cell is operated in a voltage range from 1 to 2.5V. The device exhibits a capacitance value of 83.6Fg^{-1} at 0.1mAcm^{-2} and an energy per unit volume of 50Whkg^{-1} at a power per unit volume of 2500Wkg^{-1} [101]. Arian and colleagues synthesized a battery-type electrode $\text{Ni-Mn-Co-S@Co(OH)}_2$ and activated charcoal as an anode and cathode for a hybrid supercapacitor to enhance specific energy. The supercapacitors exhibit a capacitance value of 68.13mAhkg^{-1} at 1Ag^{-1} reflecting an energy per unit volume of 51.1Whkg^{-1} at a power per unit volume of 751.47Wkg^{-1} . The device retains 89.8% of initial capacitance after 1000 cycles [102]. Mixed metal oxides and metal molybdates also show battery-type behavior and have been used as a hybrid supercapacitor. For example, Muzaffar et al. synthesized a hybrid supercapacitor using $\text{FeMoO}_4\text{@MnO}_2$ as both electrodes. Operating within a voltage range of 1.4V, the supercapacitor achieved an energy per unit volume of 56.95Whkg^{-1} at a power per unit volume of 418.46Wkg^{-1} . The device demonstrated excellent stability, retaining 87% of its initial performance after 10000 cycles [103]. Gopi and colleagues synthesized a hybrid supercapacitor using $\text{NiMoO}_4\text{-CoMoO}_4$ and graphene ink as anode and cathode. The device was operated in a voltage range of 1.5V and displayed an energy per unit volume of 27.58Whkg^{-1} at a power per unit volume of 636.06Wkg^{-1} . The device maintained 84.7% initial capacitance after 5000 cycles [104]. Nagaraju and colleagues developed an asymmetric device in which $\text{rGO/V}_2\text{O}_5$ nanosheets and rGO as anode and cathode, respectively. The device exhibited a capacitance value of 195Fg^{-1} at 1Ag^{-1} operating within the voltage range of 1.6V. It achieved an energy per unit volume of 79.5Whg^{-1} at a power per unit volume of 900Wkg^{-1} [105]. Lai and colleagues developed a hybrid device using rGO/Ni(OH)_2 and rGO as the anode and a cathode, respectively operating within a 1.6V voltage window. At a power per unit volume of 1kWkg^{-1} , the device achieved an energy per unit volume of 54.1Whkg^{-1} [106]. A hybrid supercapacitor $\text{NiCo}_2\text{S}_4/\text{RGO//AC}$ displays an energy per unit volume of 41.52Whkg^{-1} at a power per unit volume of 1067Wkg^{-1} with a stability of 82% after 3000 cycles [107].

In this chapter, we have discussed the various components, types, and significance of supercapacitors. It is a well-known fact that the achievements of supercapacitors depend upon the type of active material. So, the selection of efficient electrode material is important. However, the quest for enhanced supercapacitor performance requires an efficient electrode material. One such innovation involves ternary or metal molybdate-based electrode materials, offering a promising avenue for improving energy storage capacity, stability, and cost-effectiveness. In the subsequent chapter, efforts have been made to review the literature on manganese molybdate-based nanocomposites as an electrode material for supercapacitors.

Chapter 2

Manganese Molybdate as an Active Electrode Material: A Short Review

Molybdates with the molecular formula $Z\text{MoO}_4$ (where $Z = \text{Co, Ni, Zn, Mn, Fe, Ba, etc.}$) are an important class of inorganic materials with a tetragonal structure. This structure is stable because the molybdenum ions are surrounded by four O^{2-} ions at the center of the tetrahedral symmetry. Due to their unique structures, molybdates are useful materials with excellent electrical, optical, magnetic, and catalytic properties that others cannot surpass [108]. In industrial applications, molybdate compounds are known for their use as catalysts, corrosion inhibitors, Energy Storage, and other essential chemicals tailored for specialized purposes like nitrogen fixation, calorimetry, etc. [109]. A lot of research has been done on different metal molybdates, including NiMoO_4 , MnMoO_4 , FeMoO_4 , ZnMoO_4 , and CoMoO_4 because of their high stability, quick redox reactions, and excellent conductivity [110].

Based on research interest, NiMoO_4 is the most investigated metal molybdate as an active material for electrodes due to its high theoretical capacity and low toxicity with two redox pairs $\text{Ni}^{2+}/\text{Ni}^{4+}$. Many Ni-based materials have been discussed like NiMoO_4 nanowires [78], 3D porous NiMoO_4 nanoplate arrays [111], NiMoO_4 nanosheets [112], NiMoO_4 nanospheres [113], etc. Despite this, the performance of NiMoO_4 in supercapacitors is hindered because of its weak electrical conductivity, poor ion diffusion, and electron transport leading to performance degradation [26,114–116]. CoMoO_4 is also considered a promising material for supercapacitors and a lot of work has been reported but due to its low toxicity and low cost CoMoO_4 has lower capacity and poorer cyclability than Ni because of cation disorder and low reactivity that hinders its performance [117]. Some Co-based materials have been discussed such as CoMoO_4 nanowires [118], CoMoO_4 nanoparticles [119], CoMoO_4 nanosheets [120], CoMoO_4 nanoclusters [121], CoMoO_4 nanorods [122], etc., other metal molybdates like ZnMoO_4 and FeMoO_4 have lower conductivity and low energy density [123,124].

Among all, MnMoO_4 is a popular researched material for energy storage applications owing to better electrochemical performance providing an elevated specific capacitance arising from multiple reduction-oxidation of Mn ions and excellent electrical conductivity. MnMoO_4 has been widely utilized as an active material in energy storage applications due to its remarkable theoretical specific capacity of 998 mAhg^{-1} . This exceptional performance arises from the synergistic interplay between manganese (Mn) and molybdenum (Mo) ions. The manganese ions primarily contribute to redox activity, which is crucial for efficient energy storage, as they

participate in reversible oxidation-reduction reactions. Meanwhile, molybdenum ions enhance the material's electronic conductivity, facilitating faster electron transport and improving overall electrochemical performance. This unique combination of properties makes MnMoO_4 a promising candidate for advanced energy storage technologies. Other characteristics of manganese molybdate are affordability, environmental friendliness, remarkable stability, high utilization, and wide working voltage[125]. Various methods have been employed to synthesize manganese molybdate (MnMoO_4), each with distinct advantages and limitations including the solid-phase method, Combustion synthesis, The Sonochemical route, The sol-gel method, Coprecipitation method, chemical vapor deposition, Microwave irradiation-assisted techniques, successive ionic layer adsorption and reaction (SILAR), and hydrothermal technique. Among these methods, the hydrothermal technique is the most widely utilized for preparing MnMoO_4 as an electrode material due to its ability to produce materials with exceptional uniformity and reliability, ensuring consistent performance in advanced applications.

2.1. Properties of MnMoO_4

The properties of MnMoO_4 are discussed in Fig.2.1. There is no doubt that structural, morphological, and electrochemical properties play an important role in efficient electrode material. The detailing of these properties is discussed in sections 2.1.1, 2.1.2, and 2.1.3.

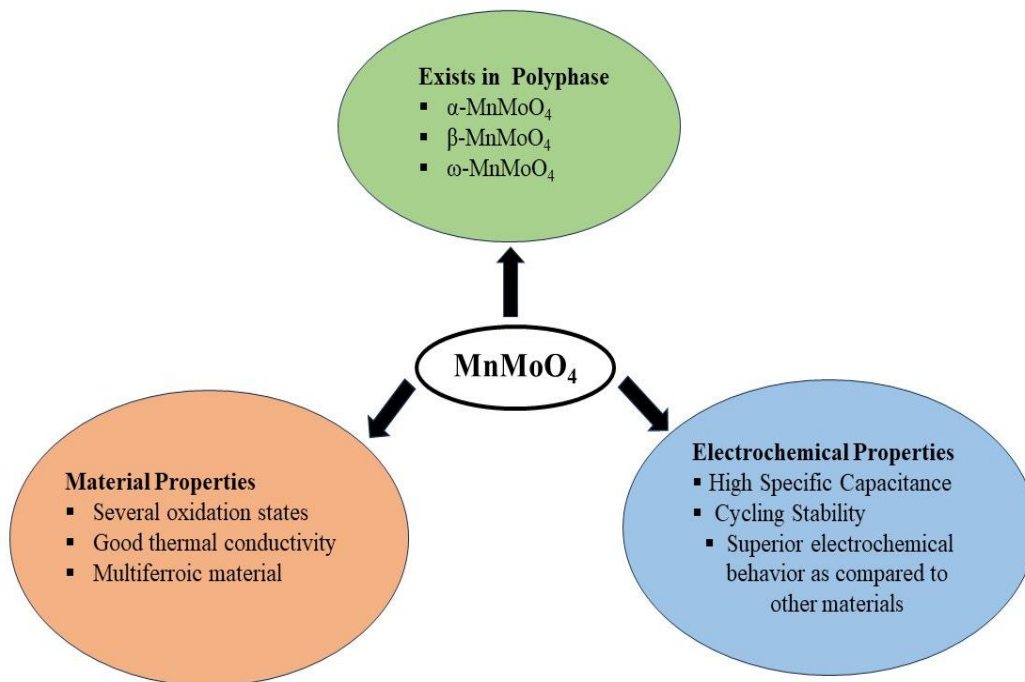


Fig.2.1. Properties of Manganese Molybdate

2.1.1. Structural Properties

MnMoO₄ shows several remarkable structural properties, with X-ray diffraction and Raman spectroscopy as fundamental techniques. XRD analysis provides crucial insights into the crystalline nature of MnMoO₄, including its phase structure, crystallinity, and purity. On the other hand, Raman spectroscopy offers a complementary perspective by revealing the vibrational modes, symmetry, and bonding within the material. It also highlights structural distortions and defects that might be present. XRD and Raman spectroscopy form a powerful duo, providing a comprehensive understanding of MnMoO₄ structural characteristics, essential for its application in various fields. Due to lower adhesion strength and unique structure, MnMoO₄ offers better stability than nickel and cobalt molybdates. Therefore, it exhibits three phases: α -MnMoO₄ shows a monoclinic structure shown in fig.2.2 in which Mn and Mo atoms are coupled to form a tetrahedral crystal structure, β -MnMoO₄ shows a wolframite structure in which the coordination of Mn and Mo shows octahedral sites. The β phase can transform into the α phase when heated at 60 °C for more than 48 hours. ω -MnMoO₄ is the least explored phase and resembles isostructural α -CoMoO₄ with the octahedral spaces occupied by Mn and Mo. It can be converted to α -MnMoO₄ by heating it in air overnight at 600°C [125–129]. Among the three phases, α -MnMoO₄ is the most explored and is stable at room temperature as mentioned in table 2.1. Some literature also found hydrated MnMoO₄ samples and all the reports for this type of material are noted in Table 2.1. From the literature, the synthesized MnMoO₄ with the morphology of nanosheets, nanoplates, nanorods, rhombohedrons, and 3D nanostructures exhibit a triclinic phase, the hydrated phase, and the monoclinic phase, respectively.

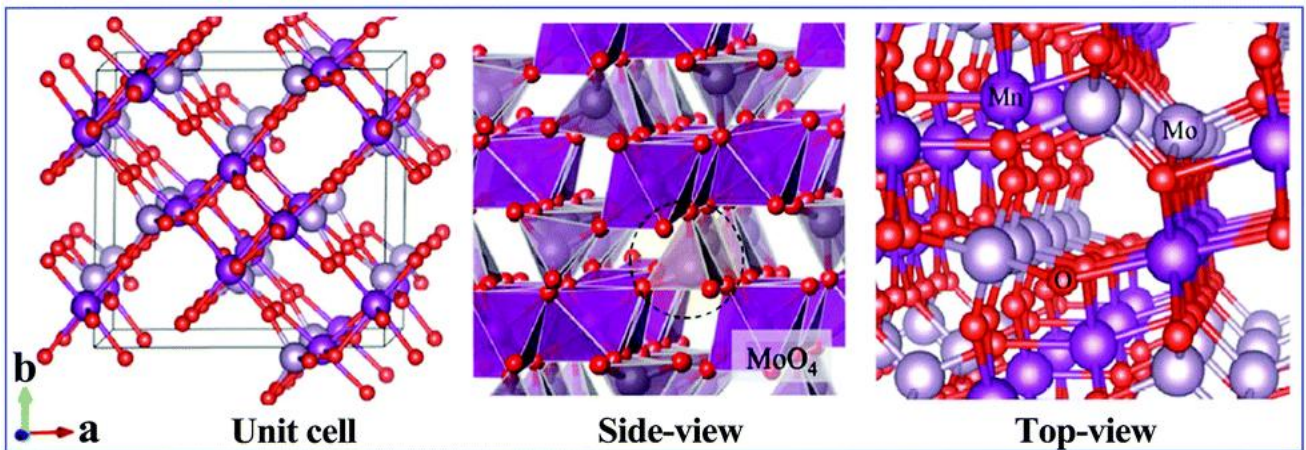


Fig.2.2. Crystal structure of α -MnMoO₄ [130].

Table 2.1. The crystal structure of MnMoO₄-based materials with different methodologies

Compounds	Synthesis Method	Precursors Used	XRD analysis	Crystallite Size	Ref.
α -MnMoO ₄ nanorods	Sol-gel spin coating	MnCl ₂ , MoO ₃ , ethylene glycol, monomethyl ether, ~0.15ml conc. HCl. The film was prepared on FTO substrate at 3000rpm and then calcinated at 300°C for 30 min.	Monoclinic phase	53nm	[131]
3D α -MnMoO ₄	Chemical method	0.1mol/L Na ₂ MoO ₄ , 20ml benzene, Cu foil of 10*1*0.02, 0.1mol/L MnCl ₂ , keep the solution constant for 24hrs at room temperature.	Monoclinic phase	-	[132]
MnMoO ₄ nanorods	Co-precipitation	0.05M MnCl ₂ .4H ₂ O, 0.1M Na ₂ MoO ₄ .2H ₂ O, 10ml PEG, and stirred for 3 hours at room temp. final product was calcinated at 600°C for 3hr.	Monoclinic Phase	26nm	[133]
α -MnMoO ₄ nanorods	Co-precipitation method	0.2M MnCl ₂ .4H ₂ O, 0.2M Na ₂ MoO ₄ , 2M NaOH to maintain pH 7 and stir for 2 hours. Calcinated for 500°C for 3hr.	Monoclinic Phase	43nm	[134]
α -MnMoO ₄ nanorods	Microwave Hydrothermal method	0.2M MnCl ₂ .4H ₂ O, 0.2M Na ₂ MoO ₄ .2H ₂ O, 2M NaOH to maintain pH 7. Transfer solution to quartz vessel at 180°C for 15min and then calcination at 500°C for 3hr	Monoclinic Phase	26nm	[134]
α -MnMoO ₄ rhombohedron	Precipitation method	10ml MnCl ₂ .4H ₂ O, 10ml Na ₂ MoO ₄ .2H ₂ O, 2M NaOH to maintain pH 7 stirred for 1hr. Calcinated at 600°C for 5hrs.	Monoclinic phase	-	[135]
α -MnMoO ₄ nanorods	Microwave-assisted method	0.1M MnCl ₂ .4H ₂ O 0.014M (NH ₄) ₆ Mo ₇ O ₂₄ .4H ₂ O 4ml EG. Stir for 5 min. transfer in the microwave at 150°C for 1,3,5,10,30 and 50 min and then calcinated at 500°C for 4hr.	Monoclinic Phase	-	[65]
MnMoO ₄ nanorods	Solid State chemical synthesis	10mM MnCl ₂ .4H ₂ O, Na ₂ MoO ₄ .2H ₂ O Calcinated at 400°C for 2hr.	MnMoO ₄ .0.9H ₂ O without calcination and MnMoO ₄ after calcination	-	[136]
MnMoO ₄ nanostructures	Hydrothermal method	10mM MnCl ₂ .4H ₂ O and Na ₂ MoO ₄ .2H ₂ O, Diluted HCl and NaOH to vary pH 2,4 and 7. Transfer solution in an autoclave at 150°C for 3hr	Monoclinic phase	-	[137]

Mesoporous MnMoO ₄ nanorods	Hydrothermal method	1:1 Na ₂ MoO ₄ .2H ₂ O, (CH ₃ COO) ₂ Mn.4H ₂ O, polyethylene glycol 400. Hydrothermal reaction at 200°C for 6 hrs.	Monoclinic phase	-	[138]
MnMoO ₄ .4H ₂ O nanoplates	Hydrothermal method	2mmol MnCl ₂ .4H ₂ O and Na ₂ MoO ₄ .2H ₂ O. Hydrothermal reaction at 150°C for 8hrs.	Hydrated phase	-	[139]
MnMoO ₄ nanorods	Solvothermal method	0.1M MnSO ₄ .4H ₂ O, 0.1 M Na ₂ MoO ₄ , 0.3M Na(NO ₃) ₂ , ethanol, 1g PVP as surfactant, ammonia solution. Solvothermal reaction at 180°C for 7hr.	Monoclinic phase	38.3nm	[140]
MnMoO ₄ nanorods	Sonochemical method	1M Na ₂ MoO ₄ .4H ₂ O, 1M (Mn(CH ₃ COO) ₂ .4H ₂ O), ethanol. Calcinated 500°C for 3hr.	Monoclinic phase	21nm	[140]
MnMoO ₄ nanosheets	Hydrothermal method	0.05M Na ₂ MoO ₄ .2H ₂ O and MnCl ₂ .4H ₂ O, Ni foam. Hydrothermal reaction at 150°C for 8hrs.	Triclinic phase	50nm	[141]
MnMoO ₄ nanorods	Microwave-assisted method	1:1(Mn(CH ₃ COO) ₂ .4H ₂ O and Na ₂ MoO ₄ .2H ₂ O, isopropanol, NaOH. Calcinated at 300°C for 3hr. microwave treatment 20,40, 60 and 80 min.	Monoclinic phase	-	[106]
P-doped MnMoO ₄ nanosheets	Hydrothermal method	MnSO ₄ .H ₂ O, Na ₂ MoO ₄ .2H ₂ O and NaH ₂ PO ₄ .H ₂ O. Hydrothermal reaction at 150°C for 8hrs.	Triclinic phase	-	[142]
MnMoO ₄ nanorods	Electrospinning Method	1:1 Na ₂ MoO ₄ .2H ₂ O and MnC ₄ H ₆ O ₄ .4H ₂ O, 0.4g PVP, 4mL DMF, HCl. Calcinated at 500°C for 2hr	Monoclinic Phase	-	[143]

In Raman spectroscopy, certain vibrational modes of material can scatter light, producing a Raman signal. These are known as Raman active modes. The number of Raman active modes depends upon the symmetry and structure of the material. α -MnMoO₄ according to reported results exhibits 13 such vibrational modes that are Raman active based on group theory and the vibrational modes are 3A_g+5B_g+5E_g. The Raman spectrum of MnMoO₄ exhibits stretching and bending vibrations. The stretching and bending vibrations of MnMoO₄ are due to MoO₄⁴⁻. The contribution of the MoO₄ unit in MnMoO₄ significantly stabilizes the structure because the tetrahedral MoO₄ unit is the source of electron contribution in the energy range of -6 to -3.9eV which indicates a significant interaction between the Mo-3d and O-2p. The large transfer charge in manganese molybdate is due to less electronegativity than Ni and Co molybdate. The electronegativity for Mn (1.55) is less than Ni (1.88) and Co (1.91). Thus, the Mn²⁺ ion exhibits

ionic bonding with its nearby oxygen ions in molybdate compounds due to its tendency to transfer its valence electrons to neighboring atoms rather than the other two cations (Ni and Co) [144]. The Raman peaks of MnMoO₄ and its composites are detailed in Table, 2.2. From the literature, the purity of samples, their bonding, and the defects introduced due to the addition of carbonaceous material are mentioned in Table 2.2. For example, Appiagyei et al synthesized Su-GC MnMoO₄ [124], and the Raman analysis showed that the peaks from 200-1000cm⁻¹ represent MnMoO₄ stretching vibrations and Peaks present at 1348 cm⁻¹ and 1586 cm⁻¹ represent D and G bands that are due to disordered and graphitic carbons with their I_D/I_G ratio 0.96. The low D/G intensity ratio reveals highly symmetric G and D band peaks. These observations indicate a low concentration of defects in the graphitic carbon layer, which implies a more carbon-ordered structure that enhances electrical conductivity and mechanical stability. Gosh et al. synthesized Gr-MnMoO₄ [145], peaks from 300-1000 cm⁻¹ represent the stretching vibrations of MnMoO₄ but the extra peaks at 1340, 1580 and 2682 cm⁻¹ are due to disordered graphitic structure, the motion of Sp² carbon bounded atoms i.e., plane stretching of C=C bonds within the graphitic lattice and 2D band because of symmetrical vibration mode characteristics of hexagonal structure of graphite with D/G intensity ratio 0.25. This low ratio indicates a high-quality graphene structure with minimal basal plane defects and a moderate level of edge defects. The small edge defect concentration enhances the material's electronic properties. These characteristics are advantageous for energy storage devices where efficient electron transport and structural integrity are paramount.

MnMoO₄ and its composites exhibit different Raman active modes corresponding to different vibrational activities in the crystal lattice. Stretching vibrations of MoO₄ were observed in the higher wavenumber region i.e., 780-944cm⁻¹, and bending vibrations of MoO₄ were observed in the lower wavenumber region i.e., 287-402cm⁻¹. From Table 2.2. it is clear that MnMoO₄ materials reveal distinct vibrational modes that correspond to the stretching and bending of MoO₄ and Mn-O bonds. Variations in the Raman shift and mode assignments indicate different structural and bonding environments in the nanorods, nanosheets, and composites. Overall, the crystal phase of MnMoO₄ is crucial in determining its electrochemical achievements. By controlling the crystallite size and morphology, specific capacitance can be improved. Small crystallite size can increase in active sites and morphology can increase surface area and consequentially, increase the specific capacitance.

Table 2.2. Raman Characteristics of MnMoO₄

Compounds	Excitation Wavelength (nm)	Raman Peaks (cm ⁻¹)	Vibrations mode	Ref.
3D-MnMoO ₄	785	928-811 350-287	Stretching Vibrations of MoO ₄ ⁴⁻ Bending Vibrations of MoO ₄ ⁴⁻	[132]
MnMoO ₄ nanorods	632	926 817 351	Mo(1)O(2) symmetric stretching Mo(1)O(1)symmetric stretching A _g mode of Mo-O group	[146]
α-MnMoO ₄ nanorods	785	944 933 822 883 343 402 372 and 279	A _g mode A _g mode of M(1)O(2) symmetric stretching A _g mode of M(1)O(1) symmetric stretching B _g (+A _g) mode A _g (+B _g) mode B _g mode A _g ^b (B _g)	[133]
MnMoO ₄ nanorods	500	923 823 and 886 352 630	A _g mode of Mo(1)O(2) symmetric stretching B _g (+A _g) mode of Mo(1)O(1)symmetric stretching A _g mode of Mo-O group impurity	[146]
MnMoO ₄ nanorods	514	944 933 884 820 402 353 and 279 343	A _g mode A _g mode of Mo(1)O(2) symmetric stretching B _g (+A _g) mode A _g mode of M(1)O(1) symmetric stretching B _g mode A _g ^b (B _g) B _g (+A _g) mode	[140]
MnMoO ₄ nanosheets	532	924, 842 and 801 331 and 518	Stretching Vibrations of MoO ₄ ⁴⁻ Bending Vibrations of MoO ₄ ⁴⁻	[141]
MnMoO ₄ nanorods	532	943 – 810 400-250	Stretching Vibrations of MoO ₄ ⁴⁻ Bending Vibrations of MoO ₄ ⁴⁻	[147]
MnMoO ₄ nanorods	-	943-820 400-250	Stretching Vibrations of MoO ₄ ⁴⁻ Bending Vibrations of MoO ₄ ⁴⁻	[143]
Su-GC@MnMoO ₄ microcubes	-	1586 1348 930 807	G band of graphitic carbon D band disordered carbon Mo=O stretching vibration Mo-O stretching vibration	[15]
Gr-MnMoO ₄ hybrid	-	2682 1580 1340 926,862,820, 796, 363 and 328	2D band of graphene G band corresponds to the E _{2g} mode of graphite D band due to graphitic disorder Stretching vibrations of MnMoO ₄	[141]

MnMoO ₄ @CNF	-	1593 1337 928 877 821 250-400	G band due to carbon D band due to graphitic disorder A _g mode symmetrical vibration of Mo-O band A _g ⁻ asymmetrical mode B _g ⁻ asymmetrical mode Bending vibrations of tetrahedral MoO ₄ ⁻	[148]
MnMoO ₄ /G nanocomposites	-	1588 1350 926 873 and 819 662 331	G band corresponds to the E _{2g} mode of graphite D band graphitic disorder Symmetric stretching of Mo-O Asymmetric stretching mode of O-Mo-O Mn-O-Mo bond MoO ₄ Vibrations	[149]
MnMoO ₄ /CoMoO ₄ nanowires	-	100- 1200 872	MnMoO ₄ stretching vibrations Co-O-Mn stretching vibration	[76]
MnMoO ₄ /MnCO ₃ hybrid	-	1085 926 862 820 659 288	A _{1g} (v ₁) mode of Co ₃ ²⁺ symmetric stretching A _g mode of Mo(1)O(2) symmetric stretching B _g (+A _g) mode A _g mode of M(1)O(1) stretching vibration Mn-O stretching vibration E _g (L) mode	[150]

The available literature highlights that MnMoO₄, when used as an electrode material in energy storage applications, including supercapacitors, has been synthesized using various methods. One promising approach can be the in-situ growth of MnMoO₄ on conductive metal substrates, which offers several advantages. This method promotes strong adhesion between the material and the substrate, reducing the likelihood of detachment during operation. It also ensures a uniform distribution of manganese and molybdenum components, resulting in a stable and defect-free structure. Furthermore, in-situ growth facilitates precise control over particle size and surface area, which are critical factors for enhancing redox activity and overall electrochemical performance. The particle size of MnMoO₄ plays a pivotal role in determining ion diffusion kinetics. Smaller particles enable better utilization of the internal active space within the electrode, facilitate rapid ion diffusion, and significantly improve reaction kinetics and electrochemical performance. Despite the material's reported high surface area in literature, MnMoO₄ has often failed to deliver optimal results, which could be attributed to factors such as particle agglomeration or improper mixing during synthesis. These issues can hinder the accessibility of active sites and reduce the material's effectiveness.

2.1.2. Morphological Properties

The MnMoO_4 morphology has a major impact on determining the electrochemical characteristics of supercapacitors. The size and structural properties of the material affect the charge transport, electrolyte accessibility, active site availability, and mechanical stability, ultimately affecting the electrode material's capacitance and cycling stability. Therefore, carefully designed and controlled morphology is important to optimize the electrochemical efficiency of MnMoO_4 electrodes for supercapacitors. The morphology of MnMoO_4 -based materials can be divided into three groups depending upon their synthesis route.

➤ *One-dimensional morphology:* The benefits of 1D MnMoO_4 structures such as nanofibers, nanorods, and nano chains lie in their stable architecture and easy strain relaxation, facilitating axial stretch electron transport and short ion dispersal paths. For example, MnMoO_4 was produced by Lu and his coworkers using a single electrospinning spinneret technique [143]. The morphology of the material before and after calcination was examined. Before calcination, the material behaves as nanofibers with a smooth surface, non-porous or hierarchical nanostructure with 200 nm diameter. When the material calcined at 500°C , the nanofibers turn into a tubular structure containing many pores with a thickness of 120 nm. When the temperature rises to 600°C , the porous nanotubes turn into nano chains with a particle size of 65 nm. Therefore, by calcination, the morphology of the material can be controlled. The surface area of MnMoO_4 nanotubes and nanochains was examined. While the area of small and large mesoporous nanotubes is $155\text{m}^2\text{g}^{-1}$, the area of mesoporous nanochains is only $68\text{m}^2\text{g}^{-1}$. Therefore, the MnMoO_4 nanotube electrode displays a capacitance value of 620Fg^{-1} at 1Ag^{-1} whereas the nanochain MnMoO_4 electrode demonstrates a capacitance value of 452Fg^{-1} at 1Ag^{-1} . The nanotube MnMoO_4 electrode showed 91% cycling stability even after 10000 cycles. Jayasubramaniyan et al. produced $\alpha\text{-MnMoO}_4$ nanorods by precipitation and microwave hydrothermal (MW-HT) method [134]. The morphology of MnMoO_4 prepared by the precipitation process is uniform nanorods with a width of 200 nm, while the shallow morphology of MW-HT MnMoO_4 is a tube-shaped construction with a width of 600 nm. The exact capacity of the electrode prepared by the precipitation method at 1Ag^{-1} current is 142Fg^{-1} , and the specific capacitance of the electrode equipped by MW-HT at 1Ag^{-1} current is 551Fg^{-1} with cycling stability of 89% after 1000 cycles.

➤ *Two-dimensional morphology:* By providing additional active sites on a surface and maximizing the consumption of the entire active planar material, the charge-transfer processes become significantly faster improve the capacitance value, and enhance the material cycling constancy. For example, Saravanakumar and his colleagues synthesized MnMoO_4 by

solvothermal process at different pHs [93]. The pH of the solution was checked by adding ammonia solution. At different pH values, variable forms were obtained. At pH 7 the particles do not resemble nanoparticles. As the pH of the mixture upsurges, the nanoparticles transform into nanorods with different orientations. At pH 11, the nanorods change into irregular shapes like nanoplates due to the increase in ammonia solution. The electrode made from pH 9 showed good electrochemical efficiency with a capacitance value of 697.4Fg^{-1} at 0.5Ag^{-1} . Cao and colleagues developed $\text{MnMoO}_4 \cdot 4\text{H}_2\text{O}$ nanoplates directly on nickel foam by hydrothermal reaction [139]. At a current density of 4mAcm^{-2} , the nanoplates achieved a specific capacitance of 2300Fg^{-1} and retained 92% after 3000 cycles. Two-dimensional ultra-thin nanosheets were synthesized by Mu and colleagues using the hydrothermal reaction grown on nickel foam [141]. The specific capacitance presented by these nanosheets was 1271Fg^{-1} at 5mVs^{-1} scan rate. The electrode was stable at 84.5% after 2000 cycles.

➤ *Three-dimensional morphology:* According to previous studies, three-dimensional nanostructures are more beneficial while maintaining their exceptional characteristics over one-dimensional and two-dimensional morphologies. These include a robust structure, superior permeability, and multiple channels for Faraday reactions, making them a subject of considerable interest. A three-dimensional interconnected MnMoO_4 nanosheet arrays were synthesized by Xu et al. equipped on Ni foam by hydrothermal technique [142]. The nanosheet arrays demonstrate a capacitance value of 4609Fg^{-1} at 1Ag^{-1} . The electrode stability was analyzed by running it for 20000 cycles with a stability of 92% at 20Ag^{-1} current density.

In summary, the results indicate that the series of stability of electrodes at different morphologies along with their specific capacitance, from best to normal, is three dimensions > two dimensions > one dimensions when focusing solely on the microstructures of MnMoO_4 -based materials, without taking into account variations in electrolyte types. The electrochemical performance of MnMoO_4 nanostructures is highly dependent on their dimensional morphology, with each structure offering distinct advantages and limitations. One-dimensional (1D) structures, such as nanorods, nanotubes, and nanochains, exhibit efficient electron transport and strain relaxation but suffer from limited active sites and lower capacitance compared to higher-dimensional counterparts. Two-dimensional (2D) nanostructures, including nanosheets and nanoplates, provide enhanced charge transfer and greater active site exposure, leading to superior capacitance, though they exhibit lower cycling stability. Three-dimensional (3D) architectures, such as MnMoO_4 nanosheet arrays on Ni foam, demonstrate the highest specific capacitance and excellent long-term stability due to their hierarchical structure, which promotes an effective superficial part for ion/charge transport,

reduce conductor separation, and reduce volume expansion/contraction. This results in unparalleled capacitance and excellent cycle safety, providing great potential for supercapacitor applications. Despite their superior performance, challenges related to complex synthesis methods and potential structural degradation over prolonged use must be addressed for practical applications. Therefore, optimizing the synthesis and structural stability of MnMoO_4 across different morphologies is crucial for advancing their use in high-performance energy storage devices. Finally, changing the morphology of electrode materials holds promise for further research on improving electrochemical performance.

2.1.3. Electrochemical Properties

MnMoO_4 proved an interesting material from a practical point of view due to the redox potential of $\text{Mn}^{2+/3+}$ which improved its capacitive performance. In this section, we discussed the electrochemical achievements of MnMoO_4 , also work done by various research groups on the electrochemical achievements of MnMoO_4 is summarized in Table 2.3.

Senthilkumar et al. synthesized alpha manganese molybdate using the precipitation method and prepared an electrode material for symmetric devices. The XRD and FTIR studies confirmed the material synthesis. The micrograph of SEM shows the rhombohedron-like structure of 10-20 μm range. The capacitance of the prepared electrode has been measured at 1.6 Ag^{-1} current density achieving capacities around 200 Fg^{-1} . To study the electrochemical properties, 2M NaOH as an electrolyte has been used to calculate the specific capacitance. CV showed pseudocapacitive conduct due to the $\text{Mn}^{2+}/\text{Mn}^{3+}$ Faradaic reaction. Electrochemical Impedance Spectroscopy (EIS) has been studied to know the internal resistance, the solution resistance, and the capacitive behavior of synthesized electrodes. The electrode had a solution resistance of 1.2 Ω . Symmetric supercapacitor device using MnMoO_4 rhombohedron as anode and cathode delivers an energy per unit volume of 11 Whkg^{-1} at a power per unit volume of 100 Wkg^{-1} . The device retained 91% stability with Columbic efficiency >95% after 1000 cycles [135]. Lu et al. fabricated manganese molybdate nanotubes with hollow interiors and porous structures with a diameter of 120nm. The electrode from the prepared material achieved a capacitance value of 640 Fg^{-1} at 1 Ag^{-1} . After 1000 cycles, the electrode was stable. Further, an asymmetric supercapacitor device has been developed using an active electrode based on MnMoO_4 nanotubes with activated charcoal as a cathode. The energy per unit volume of the synthesized asymmetric device is 31.7 Whkg^{-1} at a power per unit volume of 797 Wkg^{-1} . The asymmetric device displays the pseudocapacitive and Electric double-layer capacitive behavior has been displayed by the asymmetric device confirmed from the CV profile, which confirms

the capacitive behavior [143]. Sheng et al. synthesized one-dimensional MnMoO_4 nanorods by solid-state chemical method. The electrode prepared from MnMoO_4 nanorods proved very stable and retained at 112.6% after 10000 cycles. The morphology of the material before cycling and after cycling was almost the same which also confirms its stability. An asymmetric supercapacitor device has been developed in which MnMoO_4 electrode as active electrode and reduced graphene oxide as cathode attains specific energy of 23.5 Wh kg^{-1} at 187.4 W kg^{-1} power density 0.25 A g^{-1} with retention of 77.2% after 10000 cycles [136]. Mu et al. developed MnMoO_4 nanosheets using a binder-free deposition strategy hydrothermally. The MnMoO_4 nanosheets displayed a capacitance of 1271 F g^{-1} at 5 mV s^{-1} . The electrode was stable at its initial capacitance of 84.5% after 2000 cycles. With an activated carbon anode and MnMoO_4 nanosheets as the cathode, an aqueous asymmetric supercapacitor at 935 W kg^{-1} power density produced 31.6 Wh kg^{-1} energy density. Binder-free MnMoO_4 nanosheets exhibit outstanding performance on Ni foam, indicating its potential application as an active electrode for efficient devices [141]. Prabakaran et al. synthesized MnMoO_4 nanostructures on Ni foam using the hydrothermal technique. The electrode showed a capacitance value of 428.7 mF cm^{-2} at 2 m A cm^{-2} . The hybrid asymmetric supercapacitor with rGO and active material as the negative and the positive electrode showed an energy per unit volume of 0.41 mWh cm^{-3} with a power per unit volume of 40.9 mW cm^{-3} [143]. Cao et al. synthesized MnMoO_4 as an electrode material by a simple wet chemical method. Polyvinylpyrrolidone was used as a surfactant to control the morphology and size of the material during synthesis. At low magnification SEM images rod-like structures of length $5\text{-}10 \mu\text{m}$ with a diameter of $0.5\text{-}1 \mu\text{m}$. Concurrently, two-dimensional nanoflakes are present on the surface of the rod-like structure at higher magnifications. To study the electrochemical properties of material 2 M KOH as an electrolyte has been used. TEM study confirms the crystallization nature and rod-like structure of the material. The cyclic voltammogram curves show the faradaic behavior of the material and that behavior is because of the transformation of $\text{Mn}^{2+}/\text{Mn}^{3+}$ ionic species. The GCD study displayed a capacity of 112.8 C g^{-1} at 0.5 A g^{-1} . The EIS has been noted at a frequency range of $0.01\text{-}10 \text{ kHz}$ with a solution resistance of 0.7Ω . The electrode was stable after 2000 cycles with a cycling stability of 86% [151]. MnMoO_4 nanorods were created by Zhang and colleagues via microwave-assisted hydrothermal reaction with different microwave reaction times (1, 3, 5, 8, 10, 30, and 50 min). The solution was washed, filtered, dried, and calcined at 500°C for 4 hours to obtain the desired results. The MnMoO_4 shows different morphologies for different reaction times. when microwave time was 1min, MnMoO_4 did not have a clear shape, but with increase in reaction time, the rod-like morphology was clear. The nanorods with surface areas of 5.09 m^2

g^{-1} , $10.04\text{m}^2\text{g}^{-1}$, and $3.83\text{m}^2\text{g}^{-1}$ for 10min, 30min, and 50 min reaction times respectively [148]. The reaction time affects the sample's electrochemical performance. The MnMoO_4 nanorods with a reaction time of 10 min showed better results and exhibited a capacitance value of 446.7Fg^{-1} at 1mAcm^{-2} with 81.12% stability after 3000 cycles. Therefore, this synthesis method has great potential in supercapacitor applications [152]. Purushothaman et al. by using the sol-gel method synthesized $\alpha\text{-MnMoO}_4$ in which the precursors (MoO_3 and MnCl_2 with 3 drops of HCl) and 2-methoxy ethanol were coated on Fluorine Tin oxide glass (FTO) a conducting substrate. The nanorods of width 109nm were aligned in one direction indicating uniform growth on FTO which is favorable for electron transport and diffusion. The electrodes electrochemical performance was analyzed using different electrolyte solutions (para toluene sulfonic 7 acid p-TSA, hydrochloric acid HCl , and sulfuric acid H_2SO_4). The material displays a capacitance value of 998Fg^{-1} , 784Fg^{-1} , and 530Fg^{-1} at 5mVs^{-1} in H_2SO_4 , p-TSA, and HCl electrolyte solution, respectively [131]. G.K. Veerasubramani et al. synthesized $\alpha\text{-MnMoO}_4$ nanorods of length 1-2 μm with a diameter of 100-400nm using a facile Sonochemical method and the capacitance of the $\alpha\text{-MnMoO}_4$ nanorods was 168.32Fg^{-1} at of 0.5mAcm^{-2} . The electrode showed 96% cycling stability after 2000 cycles [140]. Babulal and colleagues used polyethylene glycol as a surfactant to synthesize MnMoO_4 using the precipitation method. The surfactant improved the material with better crystallinity, more consistent composition, and purity of phase. The material exhibits nanorods morphology with a rod length of 2.3 μm and a diameter of 160nm. The electrode prepared by synthesized material delivers a capacitance value of 424Fg^{-1} at 1Ag^{-1} by using 1M Na_2SO_4 electrolyte [131]. Saravankumar et al. synthesized MnMoO_4 nanorods at pH7,9 and 11 using the solvothermal method. The electrode with pH 9 showed an increased capacitance value of 697.4Fg^{-1} at 0.5Ag^{-1} [145].

From the above literature, MnMoO_4 prepared from different techniques provides different morphology and that morphology has a direct effect on their electrochemical performance. Also, it has been seen that the electrode prepared from insitu growth (binder-free) shows better electrochemical properties as compared to materials with binder because of the direct growth of MnMoO_4 on a conductive substrate that avoids agglomeration and dead volume due to polymer binder at the nanoscale. Table 2.3 explains the electrochemical performances of MnMoO_4 -based electrodes.

2.2 Impact of Compositing of MnMoO_4 with Other Materials for Enhanced Electrochemical Performance

Although the MnMoO_4 electrode is stable and provides better electrochemical results, we are still not getting the desired energy density of the device. So, numerous works have been done on MnMoO_4 -based composites to get the desired energy density and stable electrode material as mentioned below:

2.2.1. Carbonaceous Material and MnMoO_4 Based Composites

From the literature, it is clear that EDLC-based electrodes are stable and have a higher superficial zone but the value of specific capacitance is very low. However, pseudocapacitors have greater specific energy as well as specific capacitance but poor stability and low power density hinder their performance. In this case, researchers synthesize composites that show the advantage of both. For example, Appiagyei et al synthesized MnMoO_4 coated with sucrose anchored on graphitic carbon by hydrothermal method. The composite holds micro cubic morphology with surface area of $48.2\text{m}^2\text{g}^{-1}$ nearly two times of pure MnMoO_4 . The specific capacitance attained by the composite is 528Fg^{-1} at 2Ag^{-1} in 2M KOH electrolyte. An asymmetric supercapacitor has been developed using su-GC@ MnMoO_4 and activated charcoal as an anode and cathode, yielding an energy per unit volume of 35.4Whkg^{-1} at 223Wkg^{-1} power per unit volume maintained cycling stability after 10,000 cycles of 96.7% [124]. Ahmad et al. synthesized the MnMoO_4 nanoarray hybrid by introducing carbon nanofibers as a binder-free growth directly on nickel foam by simple carbonization, thermal annealing, and electrospinning methods. The hybrid carbon nanofibers on manganese molybdate demonstrated a maximum capacitance value of 389.7Fg^{-1} at 0.1Ag^{-1} , which is a triplet of carbon nanofibers capacitance value i.e., 123.4Fg^{-1} . An asymmetric solid-state supercapacitor was developed, the negative electrode was made of activated charcoal cloth, while the positive electrode consisted of a MnMoO_4 @CNF hybrid mat. The polymer - gel electrolyte, consisting of PVA and KOH, served as both an electrolyte and a separator. The as-synthesized asymmetric cell yields 37.46Whkg^{-1} energy per unit volume at 278Wkg^{-1} power per unit volume [55]. Li and colleagues developed a composite of manganese molybdate encased with cobalt sulfide and reduced graphene oxide (CoS/MMO/rGO) by in-situ hydrothermal method. The hybrid electrode (CoS/MMO/rGO/NF) displayed a capacitance value of 3074.5Fg^{-1} at 1Ag^{-1} using a 2M KOH electrolyte. An asymmetric supercapacitor in which a hybrid electrode and activated carbon are taken as anode and cathode respectively, delivers an energy per unit volume of 50.3Whkg^{-1} at a power per unit volume of 415.8Wkg^{-1} . After 8000 cycles, the material reserved 96% [102].

Table 2.3. Different synthesis methods for MnMoO₄ with their specific capacitances

Material	Synthesis Method	Electrolyte	Specific Capacitance (Fg ⁻¹)	Mass Loading (mg)	Current Density/ Scan Rate	Cyclic Stability	Ref.
α -MnMoO ₄ nanorods	Sol-gel Spin coating method	0.06M p-CH ₃ C ₆ H ₄ SO ₃ H	784	129 μ g	5mVs ⁻¹	Not given	[131]
α -MnMoO ₄ nanorods	Sol-gel Spin coating method	0.06M HCl	530	129 μ g	5mVs ⁻¹	Not given	[131]
α -MnMoO ₄ 3D fan like nanostructures	Precipitation	2M KOH	562	-	1Ag ⁻¹	99.8% after 1000 cycles (at 1A/g)	[132]
MnMoO ₄ .4H ₂ O	Hydrothermal reaction	1M NaOH	2300	0.5	4mAcm ⁻²	92% after 3000 cycles (at 5mV/s)	[139]
α -MnMoO ₄ nanorods	Sonochemical Method	2M NaOH	168.32	1.7	0.5mA cm ⁻²	96% after 2000 cycles (at 100mV/s)	[140]
Rhombohedral like α -MnMoO ₄	Precipitation	2M NaOH	200	-	1.6Ag ⁻¹	91% after 1000 cycles (at 2mV/s)	[135]
MnMoO ₄ .nH ₂ O	Hydrothermal reaction	1M NaOH	1271	0.34	5mVs ⁻¹	84.5% after 2000 cycles (at 10A/g)	[141]
Rod-like MnMoO ₄	Precipitation	2M KOH	112.8	1.5	0.5Ag ⁻¹	109C/g after 2000 cycles (at 1A/g)	[151]
α -MnMoO ₄ nanorods	Microwave Hydrothermal method	2M NaOH	551	-	1Ag ⁻¹	89% after 1000 cycles (at 5A/g)	[134]
MnMoO ₄ .0.9H ₂ O nanorods	Precipitation	1M KOH	215	1.7	1mAcm ⁻²	Not given	[153]
Tube-like MnMoO ₄	Spinneret electrospinning technique	2M KOH	620	6	1Ag ⁻¹	91% after 10000 cycles (at 1A/g)	[145]
MnMoO ₄ nanorods	Solvothermal method	2M KOH	697.4	3.2	0.5Ag ⁻¹	84% after 500 cycles (at 5 A/g)	[143]
α -MnMoO ₄ nanorods	Microwave-assisted method	2M KOH	446.7	0.97	1mAcm ⁻²	81.12% after 3000 cycles (at 8mA cm ⁻²)	[152]
MnMoO ₄ nanorods	Microwave-assisted method	1M KOH	836	2	5mVs ⁻¹	84% after 3000 cycles (at 100 mV/s)	[146]
MnMoO ₄ nanorods	Solid State Chemistry reaction	2M NaOH	210.2	-	1Ag ⁻¹	112.6% after 10000 cycles (at 5A/g)	[136]
MnMoO ₄ nanosheets	Hydrothermal reaction	3M KOH	4609	0.5	1Ag ⁻¹	92.4% after 20000 cycles (100 mV/s)	[141]

A 3D composite contains CNT, reduced graphene oxide (rGO), and manganese molybdate synthesized by Mu et al. by using a binder-free approach (CNT/rGO/MnMoO₄) nanosheets to increase the superficial area in addition to the fast ion electron transmission during

electrochemical reaction. The electrode displays a capacitance value of 2374.9Fg^{-1} at 2mVs^{-1} using an electrolyte of 2M NaOH . The formation of an asymmetric device by using activated charcoal/ carbon nanotubes on nickel foam (CNT-AC) and CNT/rGO/MnMoO₄ as the electrode materials, displays an energy per unit volume of 59.4Whkg^{-1} at a power per unit volume of 1367.9Wkg^{-1} [153].

From the reviewed literature, it is evident that MnMoO₄ can be combined with various carbon-based materials. Among these combinations, the pairing of MnMoO₄ with reduced graphene oxide stands out as the most prevalent and offers superior electrochemical performance, high cycling stability, and good energy density.

2.2.2. Metal Oxide and MnMoO₄ Based Composites

MnMoO₄-based electrode has low conductivity as well as poor cycling stability. So, to enhance the MnMoO₄ electrode efficiency, the introduction of various methods come into existence such as a combination of two or three metal oxide nanomaterials. For example, A simple and convenient synthesis of NiCo₂O₄@MnMoO₄ flower-shaped microparticles by using hydrothermal technique formation of an asymmetric device using activated charcoal and NiCo₂O₄@MnMoO₄ as a cathode and anode, yielding an energy per unit volume of 44.16Whkg^{-1} at a power per unit volume of 0.8kWkg^{-1} . [154]. Wei et al. synthesized NiCo₂S₄ encapsulated with MnMoO₄ by hydrothermal treatment. The composite displayed a capacitance value of 1186.44Fg^{-1} at 1Ag^{-1} with 90.1% stability. The symmetric device displays an energy per unit volume of 47.8Whkg^{-1} at a power per unit volume of 699.9Wkg^{-1} with stability of 88.3% after 5000 cycles [155]. A composite of MnMoO₄ nanosheets with MnCo₂O₄ nanosheets directly on Ni foam using a hydrothermal technique has been synthesized [123]. The electrode displayed a capacitance value of 885Cg^{-1} at 3Ag^{-1} with 95% stability after 5000 cycles. An asymmetric device in which activated charcoal and MnCo₂O₄@MnMoO₄ as electrode materials deliver an energy per unit volume of 49.4Whkg^{-1} at a power per unit volume of 815Wkg^{-1} [156]. Chen et al. synthesized CuCo₂O₄@MnMoO₄ nanosheet arrays by using a binder-free approach on nickel foam using hydrothermal treatment. The binder-free CuCo₂O₄@MnMoO₄ as active material demonstrates a capacitance of 1327.5Fg^{-1} using 6M potassium hydroxide solution at 1Ag^{-1} with cycling stability of 92.8% after 6000 cycles. When current density increases at 20Ag^{-1} , the specific capacitance reaches 1055.3Fg^{-1} . An asymmetric supercapacitor in which graphene hybrids as cathode and composite as anode delivers an energy per unit volume of 58.9Whkg^{-1} at a power per unit volume of 670Wkg^{-1} [157]. Li et al. synthesized Nickel molybdate with the doping of Manganese (MNMO) by

hydrothermal method. The merged MNMO nanostructures deliver a capacitance of 1262.6Fg^{-1} at 1Ag^{-1} . An asymmetric supercapacitor by using activated carbon on carbon cloth with carbon nanotubes as cathode and composite as anode delivers an energy per unit volume of 64.96Whkg^{-1} at a power per unit volume of 864.5Wkg^{-1} with 77% stability after 5000 cycles[158]. Moreover, to increase capacitance, the composite of MnMoO_4 with different materials also improves conductivity, cycling stability, and energy density. Table 2.4 explains the electrochemical performance of MnMoO_4 with other composites.

2.2.3. Other Metal Oxides and MnMoO_4 Based Composites

Xie et al. synthesized arrays of core-shell nanosheets of $\text{Ni}_3\text{S}_2@\text{MnMoO}_4$ using a two-step hydrothermal technique. MnMoO_4 nanosheets were grown on the arrays of Ni_3S_2 nanosheets at various hydrothermal reaction times. When hydrothermal was maintained for 2 hours, Ni_3S_2 nanosheets with small nanoparticles of MnMoO_4 were observed. When reaction time increases for 4 hours, MnMoO_4 is completely grown on Ni_3S_2 nanosheets and is conductive. When reaction time increases to 6 hours, Ni_3S_2 nanosheets are completely enveloped by MnMoO_4 nanosheets. The extensively grown MnMoO_4 nanosheets in Ni_3S_2 6h hindered electrolyte penetration and thus negatively affected the electrochemical efficiency of the electrode. The $\text{Ni}_3\text{S}_2@\text{MnMoO}_4$ electrode 4h displayed a capacity of 979.3Cg^{-1} at 2mAcm^{-2} . An asymmetric device was developed by using active material and activated charcoal as the positive and the negative electrode, yielding an energy per unit volume of 31.4Whkg^{-1} at a power per unit volume of 399.9Wkg^{-1} with a retention rate of 91.3% [159]. A polymer-based composite of MnMoO_4 nanorods has been synthesized. The embedded core-sheath polypyrrole with MnMoO_4 nanorods of diameter 150-200nm showed a capacitance value of 462.9Fg^{-1} at 5mVs^{-1} using 2M KCl electrolyte. The symmetric supercapacitor showed an energy per unit volume of 34.4Whkg^{-1} at a power per unit volume of 500Wkg^{-1} with cycling stability of 80.6% after 1000 cycles [91]. A ppy@ MnMoO_4 and cellulose fibers by a double in situ deposition method. The active material displays a capacitance of 440.1Fg^{-1} at 2Ag^{-1} . After 1000 cycles, the material retained 83% of the initial capacitance value [160].

Table 2.4. The comparison of electrochemical performance of MnMoO₄ with other composites.

Electrodes	Synthesis Process	Electrolyte	Current Density (A/g) or Scan rate (mV/s)	Specific Capacitance (Fg ⁻¹)	Ref.
CNT/rGO/MnMoO ₄	Hydrothermal	2M NaOH	2mVs ⁻¹	2374.9	[153]
MnMoO ₄ /Graphene	Hydrothermal	1M Na ₂ SO ₄	2 Ag ⁻¹	364	[144]
MnMoO ₄ @MWCNT	Hydrothermal	1M KOH	1Ag ⁻¹	1017	[161]
Mn _{0.63} Ni _{0.37} MoO ₄ -RGO	Sonochemical	2M KOH	2Ag ⁻¹	161.1 mAhg ⁻¹	[140]
MnMoO ₄ /G	Hydrothermal	1M Na ₂ SO ₄	0.1Ag ⁻¹	302.08	[162]
Mn _{1/3} Ni _{1/3} Co _{1/3} /rGO	Hydrothermal	3M KOH	1Ag ⁻¹	1750	[163]
MnMoO ₄ @CNF	Electrospinning carbonization thermal annealing	1M KOH	0.1Ag ⁻¹	389.7	[164]
Ni(OH) ₂ /MnMoO ₄ /rGO/NF	Hydrothermal	3M KOH	1Ag ⁻¹	1329.1Cg ⁻¹	[165]
Ni ₃ S ₂ @MnMoO ₄ nanosheets	Hydrothermal	2M KOH	2mAcm ⁻²	979.3 Cg ⁻¹	[102]
NiCo ₂ O ₄ @MnMoO ₄ core shell nanoarrays	Hydrothermal	3M KOH	2.5mAcm ⁻²	1169	[156]
NiCo ₂ S ₄ @MnMoO ₄ core shell	Hydrothermal	3M KOH	1Ag ⁻¹	1186.4	[166]
NiCo ₂ O ₄ @MnMoO ₄ Core shell	Hydrothermal	6M KOH	5Ag ⁻¹	1821	[167]
Co ₂ O ₄ @MnMoO ₄	Hydrothermal	6M KOH	5mAcm ⁻²	2603.9	[154]
MnMoO ₄ @NiMoO ₄ @Mn ₂ O ₃	Hydrothermal	2M KOH	1mAcm ⁻²	2048.2 Cg ⁻¹	[168]
PCNS@Co _{0.21} Ni _{0.79} MoO ₄ nanospheres	Hydrothermal Method	2M KOH	1Ag ⁻¹	954	[169]
Mn _{0.1} Ni _{0.9} MoO ₄ /rGO nanorods	Hydrothermal	6M KOH	0.5Ag ⁻¹	688.9	[170]
Ni _{0.85} Co _{0.15} MoO ₄ /NF	Co-Precipitation	3M KOH	1Ag ⁻¹	1301	[171]

In Conclusion, MnMoO₄ has demonstrated significant potential as an electrode material for electrochemical applications due to its redox-active Mn²⁺/Mn³⁺ transitions, which enhance its capacitive performance. Various synthesis methods, including precipitation, hydrothermal, solvothermal, microwave-assisted, and Sonochemical techniques, have been employed to optimize its morphology, directly influencing electrochemical properties such as capacitance, cycling stability, and energy density. Binder-free approaches have shown superior performance by eliminating inactive polymer binders, leading to better conductivity and reduced resistance. To further enhance energy density and stability, MnMoO₄ has been composited with carbonaceous materials like reduced graphene oxide (rGO), carbon nanofibers (CNF), and carbon nanotubes (CNT), which improve surface area and electron transport, resulting in superior capacitance and power density. Additionally, the incorporation of transition metal oxides and sulfides such as NiCo₂O₄, CoS, and MnCo₂O₄ has been explored to enhance conductivity and cycling stability. These composite materials exhibit high specific

capacitances, improved rate performance, and stable long-term cycling, making MnMoO_4 -based electrodes promising candidates for high-performance energy storage devices. The synthesis of MnMoO_4 requires precise control over reaction conditions, posing challenges for large-scale production. While MnMoO_4 demonstrates promising electrochemical properties, its long-term stability remains a concern, as structural degradation under specific conditions can impact efficiency. Achieving optimal performance necessitates careful doping and structural modifications, further complicating material optimization. Also, transitioning MnMoO_4 from laboratory-scale research to industrial applications requires extensive investigation into its practical feasibility and economic viability.

2.3. Motivation and Research Gap

MnMoO_4 , due to its superior specific power, abundant oxidation states of molybdenum, and excellent cycling efficiency, has garnered significant attention as an active material for energy storage devices. However, MnMoO_4 as active materials in supercapacitors still lag behind in energy density i.e., energy per unit volume. This shortfall is mainly due to its low electronic conductivity which results in limited rate capability and accelerated capacity degradation [124,171]. Therefore, there is substantial potential for further enhancement of MnMoO_4 electrodes to improve their electrochemical performance. Varying the morphology and synthesis mechanisms can play a crucial role in this enhancement. From the literature, it is clear that several parameters have not yet been thoroughly explored:

- **Mass Loading:** Varying the mass loading can reveal how different loadings affect the capacitance and energy density of the electrode. Investigating the optimal mass loading of MnMoO_4 on the electrode will ensure more consistent performance.
- **Calcination Conditions:** Studying the effects of different calcination temperatures and durations on the crystalline structure, morphology, and electrochemical performance can lead to better and more optimized results.
- **Development of Multicomponent Composites:** One effective approach to overcoming the limitations of MnMoO_4 is the development of multicomponent composites. This can be achieved by incorporating carbonaceous materials, transition metal dichalcogenides, or by doping MnMoO_4 with other metal oxides.
 - **Carbonaceous Materials:** Incorporating materials such as graphene oxide, reduced graphene oxide, and multi-walled carbon nanotubes into MnMoO_4 can significantly enhance its conductivity and stability. A detailed study of the optimal ratios and types of these carbonaceous materials will provide insights

into their impact on the performance of MnMoO₄ composites. Additionally, research should explore the influence of the structural properties of these carbon sources on the overall performance of the composites.

- ***Transition Metal Dichalcogenides:*** The effects of combining MnMoO₄ with various transition metal dichalcogenides need to be examined. These studies could lead to the creation of novel composite materials with superior electrochemical properties.
- ***Doping with Metal Oxides:*** Investigating the effects of doping MnMoO₄ with different metal oxides will help to recognize the variations in the electronic structure and their influence on capacitance and stability. This research aims to identify the most effective dopants and optimal doping levels to enhance the performance of MnMoO₄ electrodes.

2.4. Research Objectives

The main objectives of the study of the present research are:

1. A facile synthesis of metal molybdate nanostructures and their characterization.
2. Synthesis of heteronanostructures of metal-molybdate and dichalcogenides/carbonaceous material and their optimization.
3. Development of hetero-nanostructures-based electrodes and their relevant characterization.

Chapter 3

Material and Characterizations

In this chapter, details of the chemicals used in our research have been detailed and enlisted. The synthesis mechanisms of MnMoO_4 and its composites, including rGO@MnMoO_4 , $\text{MoS}_2\text{@MnMoO}_4$, and Ni-doped MnMoO_4 , have been detailed. In addition, various techniques like X-ray diffraction (XRD), Fourier transform infrared (FTIR), Raman, and X-ray photoelectron spectroscopies (XPS), with Field emission scanning electron microscopy, and Brunauer-Emmett-Teller (BET) used to characterize the structures, morphology, elemental composition, and electrochemical behavior of synthesized materials are elaborated. Electrodes were prepared and analyzed from the synthesized materials using CV, GCD, and electrochemical impedance spectroscopy techniques. In addition to this, prepared electrodes were used as active materials for the assembly of asymmetric supercapacitors. Techniques like CV, EIS, and galvanostatic charge- discharge (GCD) were also used for device testing.

3.1. Materials and Synthesis Methods

In this section, the synthesis mechanisms of MnMoO_4 , rGO@MnMoO_4 , $\text{MoS}_2\text{@MnMoO}_4$, and Ni-doped MnMoO_4 are discussed in detail. All chemicals used for the synthesis process of MnMoO_4 , rGO@MnMoO_4 , $\text{MoS}_2\text{@MnMoO}_4$, and Ni-doped MnMoO_4 are listed in Table 3.1. The chemicals utilized in this research work were of research quality and were not further purified.

3.1.1. Synthesis of MnMoO_4

The synthesis of manganese molybdate has been done by hydrothermal and microwave-assisted methods.

a). Synthesis by the hydrothermal method: MnMoO_4 was grown on Ni foam directly by using two primary homogeneous solutions of 0.3mmol of $\text{MnCl}_2 \cdot 4\text{H}_2\text{O}$ and $\text{Na}_2\text{MoO}_4 \cdot 2\text{H}_2\text{O}$ in 30ml deionized water, separately, stir them for 10 minutes at 500 rpm. Both solutions were mixed by constant magnetic stirring for 1hr, and the pH of the solution was maintained at 7 by adding 2M NaOH constantly. The autoclave was kept at 150°C for 12 hours in an electric oven, as shown in Fig. 3.1. Once the reaction was completed, the autoclave was left to cool naturally to room temperature; the sample on the nickel foam was carefully cleaned with water

Table 3.1. Details of chemicals used in research work.

S. No	Chemicals	Formula	Purity	Supplier	Country
1	Manganese Chloride Tetrahydrate	$\text{MnCl}_2 \cdot 4\text{H}_2\text{O}$	Extra pure	Himedia Lab. Ltd.	India
2	Sodium Molybdate dihydrate	$\text{Na}_2\text{MoO}_4 \cdot 2\text{H}_2\text{O}$	99%	Sigma Aldrich Ltd.	United State
3	Nickel Nitrate hexahydrate	$\text{Ni}(\text{NO}_3)_2 \cdot 6\text{H}_2\text{O}$	99%	Loba Chemie Pvt. Ltd.	India
4	Ammonium Fluoride	NH_4F	95%	Loba Chemie Pvt. Ltd.	India
5	Thiourea	$\text{CH}_4\text{N}_2\text{S}$	99%	Sigma Aldrich	United State
6	Urea	NH_2CONH_2	99%	Sigma Aldrich	United State
7	Graphite Powder	C	-	Sigma Aldrich	United State
8	Potassium Permanganate	KMnO_4	99%	CDH Pvt. Ltd.	India
9	Potassium Hydroxide	KOH	85%	Loba Chemie Pvt. Ltd.	India
10	Sodium Hydroxide	NaOH	97%	Loba Chemie Pvt. Ltd.	India
11	Ethylene Glycol	$\text{C}_2\text{H}_6\text{O}_2$	99%	Loba Chemie Pvt. Ltd.	India
12	N-Methyl-2-Pyrrolidone (NMP)	$\text{C}_5\text{H}_9\text{NO}$	98%	Loba Chemie Pvt. Ltd.	India
13	Polyvinylidene Fluoride (Pvdf)	$(\text{C}_2\text{H}_2\text{F}_2)_n$	-	Loba Chemie Pvt. Ltd.	India
14	Acetylene Black	$\text{ClCH}=\text{CHCl}$	98%	Sigma Aldrich	United State
15	Activated carbon	C	-	Loba Chemie Pvt. Ltd.	India
16	Sulphuric Acid	H_2SO_4	97%	Loba Chemie Pvt. Ltd.	India
17	Hydrochloric Acid	HCl	-	Loba Chemie Pvt. Ltd.	India
18	Sodium Nitrate	NaNO_3	99%	Loba Chemie Pvt. Ltd.	India
19	Hydrogen Peroxide	H_2O_2	Extra pure	Loba Chemie Pvt. Ltd.	India
20	Polyvinyl Alcohol (PVA)	$(\text{C}_2\text{H}_4\text{O})_x$	-	Loba Chemie Pvt. Ltd.	India
21	Ethanol	$\text{C}_2\text{H}_5\text{OH}$	-	AR China	India
22	Acetone	$\text{C}_3\text{H}_6\text{O}$	99%	Loba Chemie Pvt. Ltd.	India

DI and pure ethanol numerous times and dried in an oven at 60°C for 24 hours.

b). Synthesis by microwave-assisted method: MnMoO_4 was synthesized by using 0.3 M $\text{MnCl}_2 \cdot 4\text{H}_2\text{O}$ with 0.3 M $\text{Na}_2\text{MoO}_4 \cdot 2\text{H}_2\text{O}$ in 60ml DI water, followed by the dropwise addition of 0.15 M urea and 10 ml ethylene glycol, sequentially. The solution was stirred for 1 h to get a regular mixture. The pH was maintained at 8 by the insertion of 2 M NaOH. The final solution

was then annealed in a household microwave at 400 W for 8 min as shown in Fig. 3.2. The precipitates collected after filtration were washed, dried, and calcinated at 300, 500, and 700 °C for 3 h.

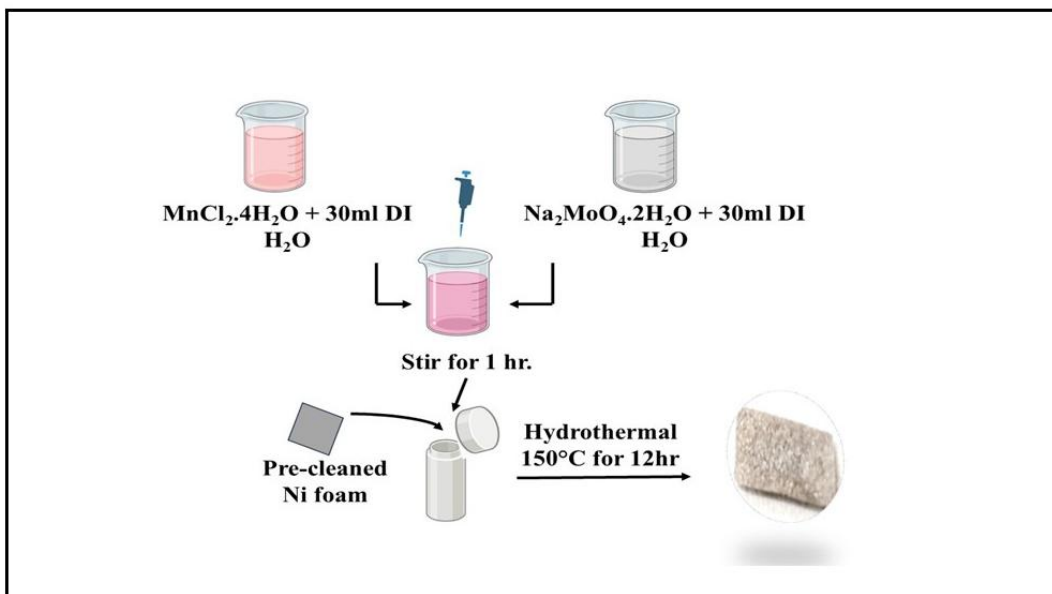


Fig.3.1. Schematic for the synthesis of MnMoO_4 by hydrothermal method.

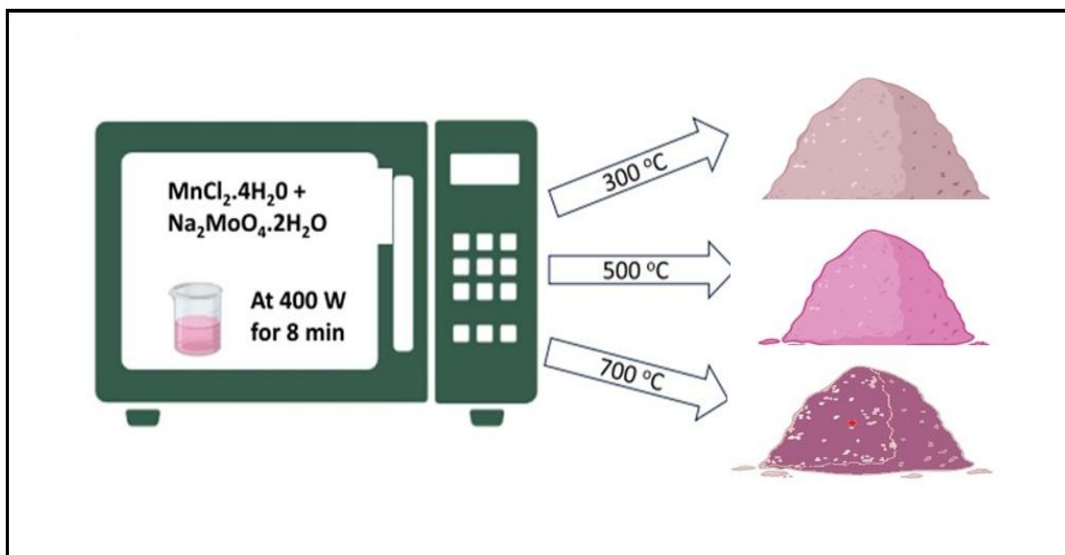


Fig.3.2. Schematic for the synthesis of MnMoO_4 by microwave method.

3.1.2. Synthesis of $rGO@MnMoO_4$

The synthesis of $rGO@MnMoO_4$ involves two steps. Firstly, graphene oxide (GO) was synthesized by Hummer's Process after that the graphene oxide with various concentrations was added to the $MnMoO_4$ solution to get $rGO@MnMoO_4$.

3.1.2.1 Synthesis of Graphene Oxide

Graphene oxide was synthesized by using Hummer's method [162]. Initially, graphite powder was introduced into sulfuric acid and stirred for 10 minutes, followed by sequential addition of sodium nitrate and potassium permanganate maintaining a temperature below 5°C with continuous stirring. Subsequently, the resulting solution was transferred into separate beakers and subjected to varying stirring durations: 1 hour, 2 hours, 4 hours, 6 hours, and 8 hours, designated as G1, G2, G4, G6, and G8, respectively. After the addition of DI water, the temperature was maintained at 50°C . To arrest the reactions, hydrogen peroxide was added and stirred for 15 minutes until the color of the solution changed to yellowish brown as shown in Fig.3.3. Throughout the entire process, an ice bath was employed to maintain the optimal temperature for the synthesis.

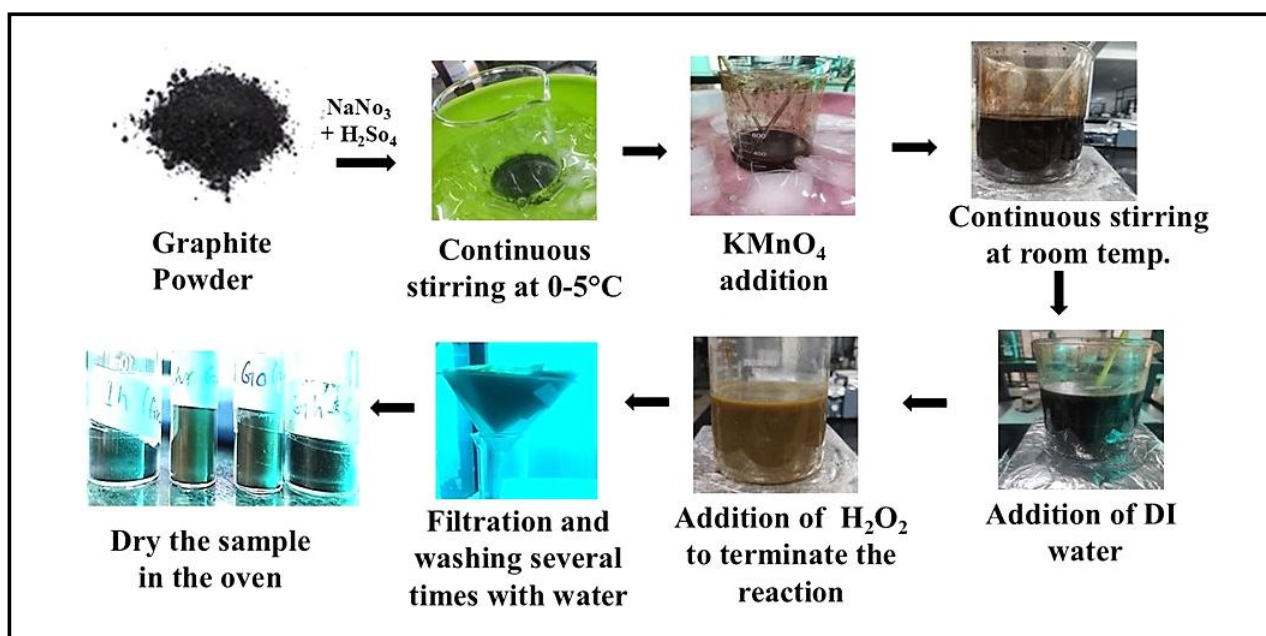


Fig.3.3. Schematic for the synthesis of graphene oxide.

3.1.2.2. Synthesis of $rGO@MnMoO_4$

The composites of $rGO@MnMoO_4$ were skillfully synthesized and grown on nickel foam via a straightforward hydrothermal reaction. Two separate homogeneous solutions were taken in which 15mM of $MnCl_2 \cdot 4H_2O$ and $Na_2MoO_4 \cdot 2H_2O$ in 20ml deionized water, were prepared. The two solutions were then mixed using constant magnetic stirring, and a suspension of 1.6mg of GO in deionized water was drop-wise added to the mixture. Along with this addition of GO, the pieces of Ni-foam were also introduced into the solution. The pH of the solution was carefully maintained at 8.5 by constant addition of 2M NaOH. After that, the prepared solution was put into a 150 ml autoclave with a Teflon lining as shown in Fig.3.4., which was placed in an electric oven, maintaining a temperature of 150°C for 12 hours. Once the reaction was completed, the autoclave was left to naturally cool to room temperature. The resulting composites grown on the nickel foam were meticulously cleaned and then dried in an oven at 60°C for 24 hours. These $rGO@MnMoO_4$ composites, synthesized with GO of varying oxidation durations, were designated as A1, A2, A4, A6, and A8, respectively. Furthermore, the composites grown on Ni-foam with different concentrations of GO (G4) – namely 0.4mg, 0.8mg, 1.6mg, and 3.2mg – were individually labeled as B1, B2, B3, and B4.

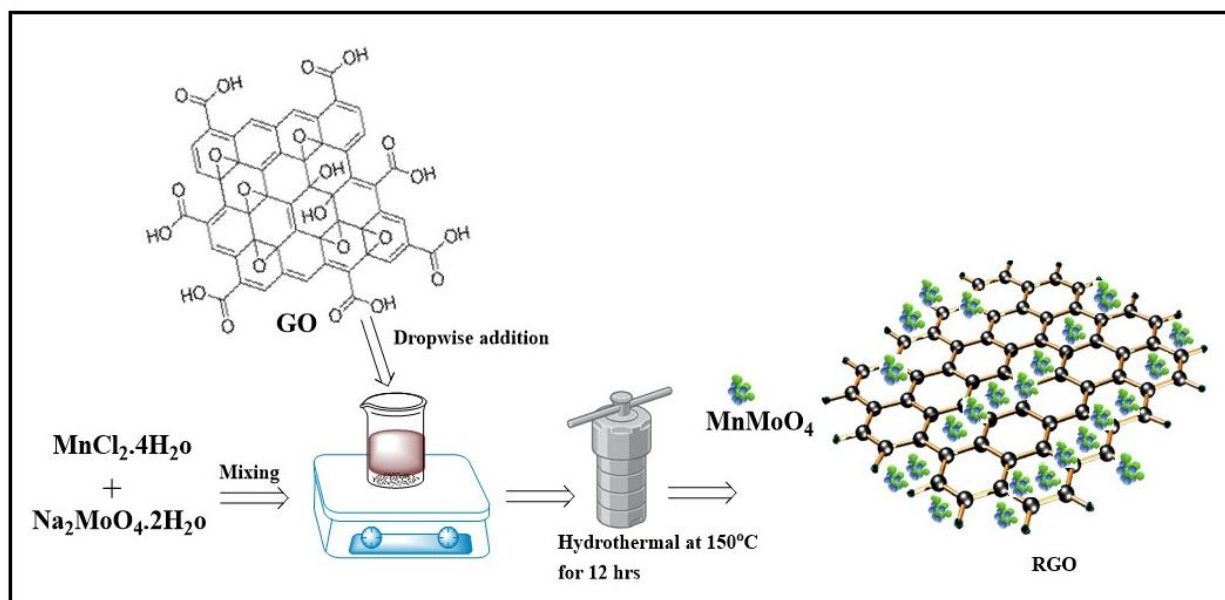


Fig.3.4. Schematic for the synthesis of $rGO@MnMoO_4$ by hydrothermal method

3.1.3. Synthesis of $\text{MoS}_2@\text{MnMoO}_4$

The synthesis of $\text{MoS}_2@\text{MnMoO}_4$ involves a two-step hydrothermal reaction. First MoS_2 was synthesized from the hydrothermal method and then poured into MnMoO_4 solution to get $\text{MoS}_2@\text{MnMoO}_4$.

3.1.3.1. Synthesis of MoS_2

MoS_2 was synthesized by taking 0.5M $\text{Na}_2\text{MoO}_4 \cdot 2\text{H}_2\text{O}$ mixed in 20 ml of DI water, and 2M $\text{CH}_4\text{N}_2\text{S}$ was dissolved in another 20 ml of DI water. Both solutions were combined and stirred for 1 hour to achieve a homogeneous mixture. The final solution was then poured into a hydrothermal reactor and kept at 180°C for 18 hours as shown in Fig.3.5. After natural cooling, the resulting black MoS_2 was rinsed multiple times with ethanol and acetone and then dried at 60°C for 12 hours.

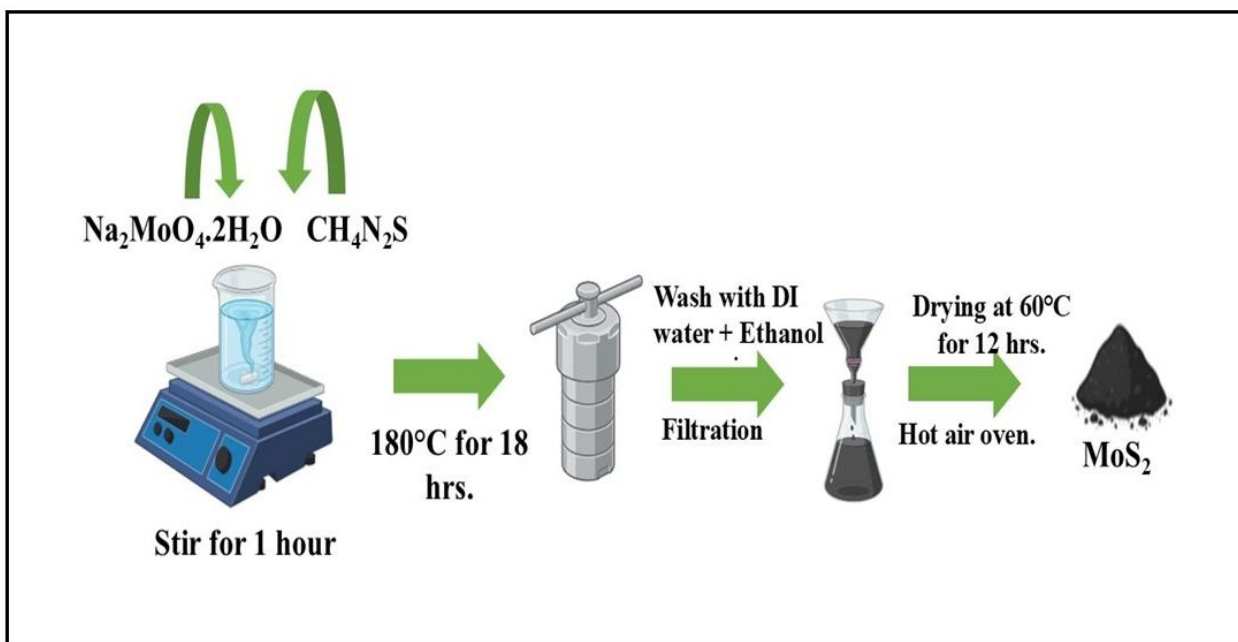


Fig. 3.5. Schematic for the synthesis of MoS_2 by hydrothermal method.

3.1.3.2. Synthesis of $\text{MoS}_2@\text{MnMoO}_4$

$\text{MoS}_2@\text{MnMoO}_4$ was synthesized by taking 130mg of the as-prepared MoS_2 powder poured into 20 ml of DI water and ultrasonicated for 30 minutes. Simultaneously, 0.1M $\text{MnCl}_2 \cdot 4\text{H}_2\text{O}$ was placed in 30 ml of DI water and stirred for 10 minutes. Afterward, 0.1M $\text{Na}_2\text{MoO}_4 \cdot 2\text{H}_2\text{O}$ was mixed in MnCl_2 solution, and the mixture was agitated for 1 hour to attain a homogeneous mixture. The MoS_2 solution was then added dropwise to the mixture and stirred for an additional hour to ensure homogeneity while maintaining the pH of the solution at 8.5 by adding 2M

NaOH. The solution was subsequently transferred to a reactor and heated to 160°C for 16 hours. The final solution was filtered, washed multiple times with ethanol and acetone, and then dried at 80°C for 8 hours as shown in Fig.3.6.

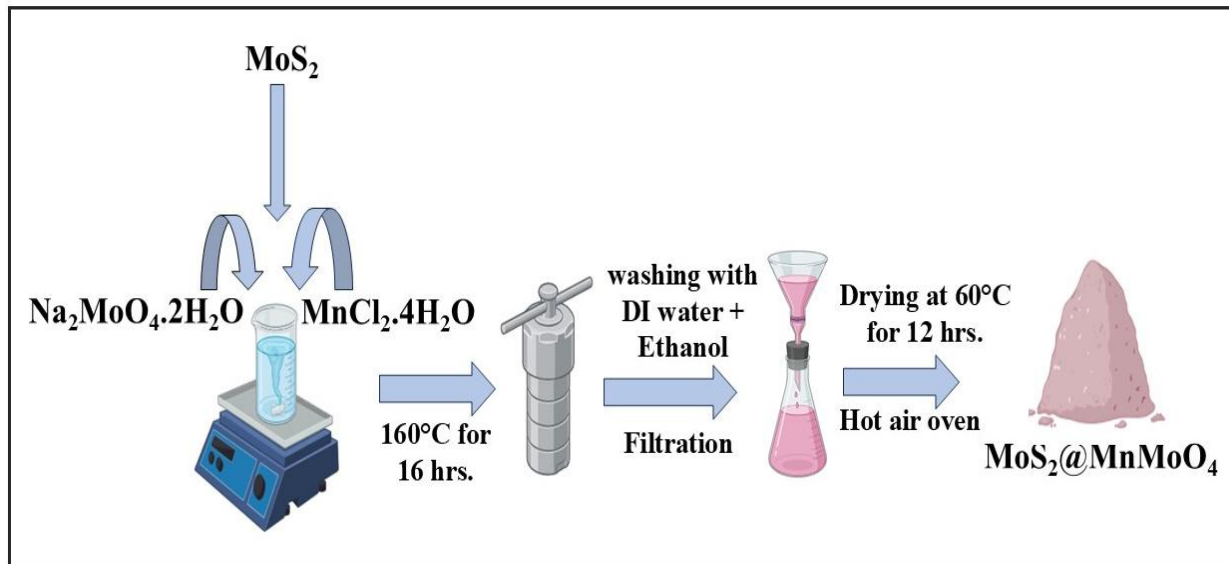


Fig.3.6. Schematic for the synthesis of MoS₂@MnMoO₄ by hydrothermal method.

3.1.4. Synthesis of Ni-doped MnMoO₄ (Ni_xMn_{1-x}MoO₄)

Ni-doped MnMoO₄ was synthesized using a straightforward single-step hydrothermal process. In a solution of 60 ml deionized (DI) water, 1M of Na₂MoO₄·2H₂O and 1M MnCl₂·4H₂O were combined. In specific proportions, MnCl₂·4H₂O was substituted by Ni(NO₃)₂·6H₂O to achieve different fractions. The molar ratios between MnCl₂·4H₂O and Ni(NO₃)₂·6H₂O were 0.9:0.1, 0.8:0.2, 0.75:0.25, and 0.7:0.3, respectively, producing distinct samples. Subsequently, 0.2M urea and 0.13M ammonium fluoride were dispersed in the solution. The mixture was stirred at 70°C with 550 rotations per minute for 1 hour to ensure a homogeneous blend. Following this, 10ml of ethylene glycol was inserted to the solution and mixed for an additional 2 hours. The solution's pH was maintained at 8.5 by adding 2M NaOH. The resulting mixture was transferred to an autoclave and maintained at 160°C for 6 hours as shown in Fig.3.7. The samples were then filtered using ethanol and acetone, and those samples, labeled as Ni_{0.1}Mn_{0.9}MoO₄ (A1), Ni_{0.2}Mn_{0.8}MoO₄ (A2), Ni_{0.25}Mn_{0.75}MoO₄ (A3), and Ni_{0.3}Mn_{0.7}MoO₄ (A4), were calcinated at 600°C for 6 hours. For in-situ synthesis, Ni foam was introduced into the autoclave for the Ni_{0.25}Mn_{0.75}MoO₄ (A3-Insitu) sample. The remaining procedure remained consistent across all samples.

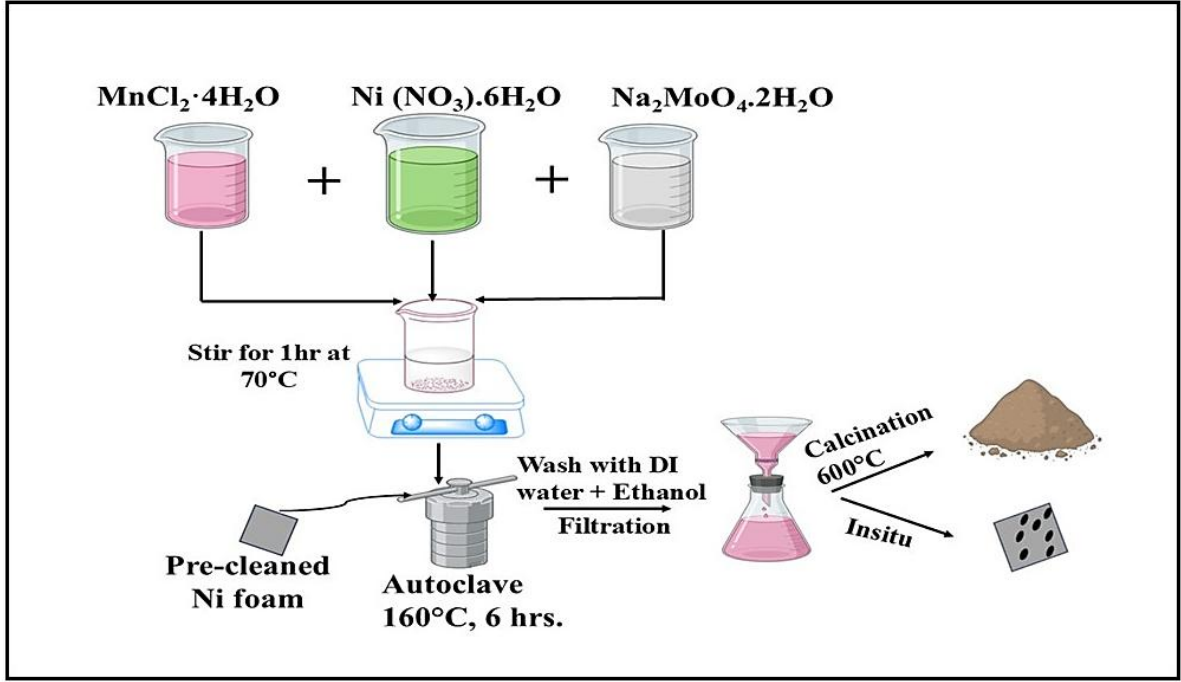


Fig.3.7. Schematic for the synthesis of Ni-doped MnMoO_4 by hydrothermal method.

3.2. Electrode Preparation

The slurry was prepared with 8:1:1 weight-percentage of active material, PVDF and acetylene black, respectively, in 1-Methyl-2pyrrolidinone (NMP). The electrode was prepared by depositing the slurry on $\sim 1 \text{ cm}^2$ of nickel foam and kept in a hot air oven at 60°C for 12 hrs to get dried. Similarly, the negative electrode was prepared by considering the 8:1:1 weight of AC, acetylene black, and PVDF, respectively.

The slurry for the graphite-activated carbon GAC-based negative electrode was prepared with a percentage ratio of 6:2:1:1 of activated carbon, graphite fine powder, PVDF, and acetylene black in 1-Methyl-2-pyrrolidinone (NMP). The cathode was developed by depositing the slurry on approximately 1 cm^2 of nickel foam and dried for 12 hours at 60°C . In addition to attaining optimal performance, there should be charge-balancing computation between positive and negative electrodes.

To obtain charge balance $Q_+ = Q_-$, the mass balance equation is required and can be calculated as:

$$\frac{m_+}{m_-} = \frac{C_{\text{cathode}} \times \Delta V_{\text{cathode}}}{C_{\text{anode}} \times \Delta V_{\text{anode}}} \quad (i)$$

where m_+ is the mass of the positive electrode and m_- is the mass of the negative electrode.

Insitu electrode has been prepared for hydrothermally synthesized MnMoO₄, rGO@MnMoO₄, and Ni-doped MnMoO₄ nanoparticles. A few pieces of pre-cleaned nickel foam were put into a 150ml stainless-steel autoclave with Teflon lining. Before the synthesis, pieces of nickel foam (1cm×1.5cm) were washed with 2M HCl aqueous solution in an ultrasound bath for 20 minutes to remove the impurities on the surface and then rinsed with deionized water and ethanol many times. The autoclave was maintained at a different temperature for different hours in an electric oven. Once the reaction was completed, the autoclave was allowed to cool down to room temperature on its own; the sample on the nickel foam was cautiously cleaned multiple times using ethanol and deionized water and dried in an oven at 60°C for 24 hours. The mass loading of electrodes was different for different materials as shown in Table 3.2.

Table 3.2. Mass loadings of electrodes prepared by in-situ hydrothermal method.

Electrode Material	~Mass Loading (mg)
MnMoO ₄ ,	0.1
	0.4
	0.6
	1.2
	1.4
rGO@MnMoO ₄ (A1, A2, A4, A6 and A8)	0.5
Ni-doped MnMoO ₄	1

3.3. Characterization Techniques

Synthesized material is characterized by various techniques which are detailed below:

3.3.1. X-Ray Diffraction

X-ray diffraction is a non-destructive, non-contact, and versatile technique used to analyze the various properties of materials including crystalline phases, lattice constants, atomic arrangement, and other structural characteristics like average grain size, crystallinity, strain, and crystal defects of solid, powder, or liquid samples. It interferes with the atomic planes of crystals with another caused by an incident beam of X-rays as they leave the crystal. X-rays are electromagnetic radiation within a range of $10^{-3} - 10^1$ nm wavelength produced by the electronic transitions of electrons in the inner orbital of atoms. It is based on constructive interference of monochromatic X-rays and a crystalline sample at specific angles. The interaction of incident rays with the sample produces constructive interference when Bragg's law is satisfied. The material phases can be identified when the X-ray diffraction pattern of the unknown sample is

compared with reference database patterns and this database is maintained by the International Centre of Diffraction data.

As a result, the X-ray diffraction pattern represents the unique fingerprint of the material's periodic atomic groupings. The crystallite size of any material can be measured by using the Debye Scherrer formula and is given as:

$$D = \frac{k\lambda}{\beta \cos\theta} \quad (ii)$$

where D belongs to crystallite size, K represents the proportionality constant, λ corresponds to the wavelength of radiation used, β represents the full-width half maxima and θ is the Bragg diffraction angle [172],[173].

Technical Details: XRD data of MnMoO₄, graphene oxide, rGo@MnMoO₄, MoS₂, MoS₂@MnMoO₄, and Ni_xMn_{1-x}MoO₄ composites were recorded at 2 θ by using Bruker D8 Advance X-ray diffractometer with Cu radiation of wavelength 1.54Å between scanning range of 10-70° with scanning rate of 0.5°/min and scanning step of 0.02.

3.3.2. Raman Spectroscopy

Raman spectroscopy is a powerful analytical technique that measures sample vibrational energy modes using scattered light. In addition to providing structural and chemical information, it can identify substances based on their unique Raman “fingerprint”. This information is extracted by detecting Raman Scattering in the sample and that is due to an inelastic scattering of photons that results in a change in photon energy. The foundation of Raman spectroscopy is the idea that polarizability changes during vibrations. A shift in the polarizability of molecules is required for a molecular vibration to be Raman active. The process of obtaining a Raman spectrum involves subjecting a sample to visible or near-infrared monochromatic light from a strong laser source. The benefits of using lasers are their high intensity, high monochromaticity, limited bandwidth, coherence, and high resolution. The intensity of Raman spectra depends on the shift in polarizability. Raman spectrum can be obtained by plotting the intensity of Raman scattered radiation against its frequency difference from the incident radiation, which is often expressed in units of cm⁻¹. This difference is known as the Raman shift. By analyzing the frequency shifts and intensities of these scattered photons, researchers can extract valuable information about a material's chemical composition, bonding, symmetry, and electronic properties. This non-destructive and sensitive technique finds widespread applications in chemistry, physics, materials science, and biology, offering insights into diverse phenomena ranging from molecular structure elucidation to chemical reaction monitoring and biomedical diagnostics [174].

Technical Details: For our Raman data, the Renishaw In Via Reflex Raman Spectrometer was utilized to record the Raman spectrum within the range of 170-2000 cm^{-1} by using an excitation of 532 nm. The Raman spectrum of MoS_2 was recorded using an excitation of 785 nm.

3.3.3. Fourier Transform Infrared Spectroscopy

Fourier Transform Infrared Spectroscopy is a powerful systematic method to identify particular functional groups present in a molecule. It works on the principle that molecules vibrate at specific frequencies. These frequencies fall in the electromagnetic spectrum's IR range of 4000 – 200 cm^{-1} . The vibrations that fall in the 4000-1000 cm^{-1} IR range are stretching and bending. When IR light is incident on samples. The sample absorbs some of the infrared light, while some passes through (transmits). A molecular fingerprint of the material is produced by the resultant spectrum, which shows the molecular absorption and transmission. No two distinct molecule configurations produce the same infrared spectrum, much like fingerprints. For IR activity, a change in electric dipole moment is required. The intensity of IR mainly depends on the magnitude of change in the dipole moment. It identifies functional groups and chemical bonding details, thereby offering insights into the structure and molecular composition. The elementary principle of FTIR is the interaction of material with infrared radiation, and at different wavelengths, the absorption of IR light energy is noted to evaluate the molecular characteristics of the sample [175],[176].

Technical Details: Fourier Transform Infrared Spectra (FTIR) of samples were acquired in the range of 400-4000 cm^{-1} in transmittance mode by using a Perkin Elmer FTIR spectrometer.

3.3.4. Field Emission Electron Microscopy

The field emission scanning electron microscope is a tool used by biologists, chemists, and physicists to study microscopic structures on the surface of cells and other materials. These structures can be as small as 1 nanometer. With a spatial resolution as fine as 1.5 nm, FESEM offers images with three to six times more clarity and less electrostatic distortion than typical SEM. The field emission scanning electron microscope is a cutting-edge analytical tool extensively employed by scientists across various disciplines to investigate the intricate structures of materials at nanoscale resolutions. Unlike traditional scanning electron microscopes (SEM), FESEM offers enhanced imaging capabilities, producing remarkably crisp and high-resolution images of sample surfaces. By utilizing field emission electron sources, FESEM

achieves superior imaging performance with significantly reduced electrostatic distortions, enabling researchers to study minute features with unparalleled clarity.

Different components' characteristics are isolated and arranged into an energy spectrum using an energy-dispersive X-ray detector. This spectrum is subsequently analyzed using software to determine the abundance of individual elements within the sample [177],[178].

Technical Details: In our study, the synthesized materials underwent thorough morphological characterization using FESEM from Hitachi SU8000 and JEOL JSM7900F, made in Japan.

3.3.5. Brunauer-Emmett-Teller (BET) Technique

The analytical technique known as BET is employed to determine the specific surface area, pore size, and pore volume of samples. BET is the extension of the Langmuir method that provides a method to calculate surface area by considering the adsorptive monolayer coverage on the solid surface. Adsorption-desorption isotherms, typically utilizing inert gases like N₂ and Ar/He, are used to evaluate the physical adsorption which incorporates multilayer coverage on the sample surface. The Brunauer-Emmett-Teller equation is utilized to calculate the sample's surface area and total pore volume:

$$S_t = \frac{V \times N \times S}{v \times a} \quad (iii)$$

$$V_{liq} = \frac{P \times V \times W}{T \times R} \quad (iv)$$

In these equations, V represents the volume of the monolayer adsorbent gas, N is Avogadro's number, S denotes the absorption cross-section of the sample, v stands for the molar volume of the adsorbent gas, a represents the mass of the sample, P represents the ambient pressure, V represents the volume of adsorbed gas, W represents the volume of liquid in N₂ pore and T represents the ambient temperature. The pore volume and pore diameter of a porous material can be estimated by the Barrett-Joyner-Halenda (BJH) method. This method is utilized to determine pore size distributions from experimental isotherms, employing the Kelvin model of pore filling. It specifically pertains to pores within the mesopore and small macropore size range. The total pore volume is determined by measuring the quantity of vapor adsorbed at a relative temperature nearing unity, assuming that the pores are filled with liquid adsorbate. Five types of isotherms can be seen in BET analysis, depending on the sample type. Type I isotherms are seen in microporous solids with a porosity of order 2 nm, which have relatively small external surfaces. Type II and III isotherms are primarily seen in nonporous/microporous samples. Interestingly, the mesoporous sample (size: 2 nm-50 nm) displays Type IV and V

isotherms, which are formed by the multilayer adsorption of the molecules followed by capillary condensation [179].

Technical Details: Brunauer-Emmett-Teller (BET) characterization of MnMoO₄, rGO@MnMoO₄, MoS₂, and MoS₂@MnMoO₄ samples has been done on Quanta chrome Instruments. For the sample Ni_xMn_{1-x}MoO₄ BET characterization was done on Belsorp Max, making Microtrac instrument. The samples were analyzed in nitrogen gas for 3 hours.

3.3.6. X-ray Photoelectron Spectroscopy

X-ray Photoelectron Spectroscopic analysis is mostly used in material science, chemistry, and chemical engineering. It's a go-to method for analyzing the surface chemistry, elemental composition, and bonding structure of various surfaces and interfaces. XPS acts like a magnifying glass, peering into a vacuum-compatible solid material's top few nanometers (depending on the sample). It is a high-resolution electron spectrometer with a finding limit of 40 μ m diameter circles used to determine the energy range of the photoemitted electrons. X-ray Photoelectron Spectroscopy (XPS) is a powerful technique for determining the oxidation states of materials. The oxidation states are identified by deconvoluting the XPS data, a critical step in extracting accurate and meaningful information from complex spectra. XPS spectra often feature overlapping peaks from multiple chemical states, background noise, and instrumental broadening. Deconvolution facilitates the separation and identification of these individual contributions. An empirical approach was utilized to determine the oxidation states, fitting the XPS peaks with Gaussian/Lorentzian peak sets derived from reference standards. The distinct peaks in the observed spectrum represent the electronic energy levels of the material under investigation. Since each element is known to have a distinct set of binding energies, as shown in Table 3.3, the concentration of the elements present on the surface may be identified and ascertained using XPS. The peaks between 370 and 455 eV represent nitrides due to the argon supply leakage during sputtering profiling to remove sample surface contamination if the sample has any. The peak at 655 eV represents the different chemical state of manganese. Determining the chemical condition of the substance under investigation is another benefit of XPS. The chemical shift, a little change in the elemental binding energy caused by the various chemical environments of the constituent elements in compounds, is what determines the chemical state. This information can be used to analyze the bonding of polymers, proteins, and even the oxidation status of metals [180],[181],[182].

Technical Details: In our study, X-ray Photoelectron Spectroscopy was conducted with the Thermo Scientific NEXA Surface-Analyzer.

Table 3.3. The detailing of XPS peaks of elements used in this research work with their binding energies is mentioned below: [183]

The Chemical state of Mn 2p	Binding Energies (eV)
Mn metal	638.7
MnO	641.4
Mn ₂ O ₃	641.4
MnO ₂	641.8
The chemical state of Mo 3d	Binding Energies (eV)
Mo metal	228 eV
MoO ₂	229.5
MoO ₃	233.1
The Chemical state of O1s	Binding Energies (eV)
Metal oxides	529- 530
Metal CO ₃	531.5 – 532
SiO ₂	532.9
Organic C=O	531.5 – 532
Organic C-O	533
The chemical state of Ni 2p	Binding Energies (eV)
Ni Metal	852.6
NiO	853.7
Ni (OH) ₂	855.6
The chemical state of C1s	Binding Energies (eV)
C-C	284.8
C-O-C	286
O-C=O	288.5
The Chemical state of S 2p	Binding Energies (eV)
Metal sulphide	~161.5
Metal SO ₄	~ 169
Na ₂ (SO ₃) ₂	166.5
Thiol bound to gold, Au-S	162.5

3.3.7. Electrochemical measurements

The prepared electrode electrochemical performance and the device were assessed on an electrochemical workstation, Metrohm Multi Autolab/M204. Three electrode setups and two electrode setups, respectively, were used to test the electrochemical characteristics of the constructed electrode and supercapacitor device.

The three-electrode setup contains a working electrode (WE), reference electrode (RE), and counter electrode (CE). The primary function of the counter electrode is to adjust the potential during the measurements by providing the required current to balance the reaction happening on the active electrode. A reference electrode is used to measure the potential on the active electrode, and due to material stability, it is considered that the reference electrode has an almost constant half-reaction potential. Ag/AgCl electrode was utilized as a reference electrode, platinum wire served as a counter electrode, and 3 M KOH was employed as an electrolyte.

CV was carried out in the constant potential window between 0.01 and 0.7 V at different scan rates. The GCD test was operated in the potential window 0 to 0.42 V at different current densities. EIS was carried out at a voltage of 10 mV in the frequency range of 0.01 Hz to 100 kHz.

▪ *Cyclic Voltammetry*

CV is a powerful electrochemical technique for studying various aspects of electrochemical systems. It allows researchers to probe a range of parameters, including electrode potential, diffusion coefficients, and the reduction and oxidation processes of molecules. CV is particularly useful for investigating electron transfer reactions, which are fundamental to many catalytic processes.

The core principle of CV involves cycling the voltage applied to a working electrode immersed in a stable electrolyte solution. The voltage changes drive current flow across the electrode. To ensure a stable reference point, a separate reference electrode is used. By measuring the current response at the working electrode as the voltage is swept back and forth, CV generates a characteristic "cyclic voltammogram." This voltammogram essentially depicts the current response of the system to the applied voltage variation. In CV analysis, researchers typically optimize and fix the range of voltages applied (potential window) to obtain meaningful information. This allows them to assess the capacitance value of the prepared electrode under various scanning rates, which control the speed at which the voltage is cycled. [183],[184].

The specific capacitance of the electrode from the CV curve can be calculated by using this equation:

$$C_s = \frac{\int IdV}{2 \times m \times V \times K} \quad (v)$$

where $\int IdV$ is the area under the curve, m is the mass of the electrode, V is the potential window, and k is the scan rate.

▪ **Galvanostatic Charge Discharge**

GCD is a standard electrochemical testing technique to evaluate the efficiency and durability of batteries and supercapacitors. In GCD testing, a material or system undergoes charging/discharging within predetermined potential limits. The GCD plot can be linear or of triangular symmetry, depending upon the type of material. A triangular symmetric charge-discharge plot signifies good reversibility and fast redox activity. GCD profiles not only identify irreversible faradaic processes but also help in assessing specific capacitance, specific capacity, energy density, power density, and Coulombic efficiency of materials. The specific capacitance value increases with decreases in current density due to longer discharging time. In low current density, the discharging time is longer, which permits the electrolyte ions to penetrate the surface and into the inner layer of electrode material, thereby causing a good insertion/exertion process, which causes an increased capacitance value.

The following relations from GCD data are used to calculate the technical terms

$$\text{Specific Capacitance } (F\ g^{-1}) = \frac{I\Delta t}{m\Delta V}, \quad (vi)$$

$$\text{Specific Capacity } (C\ g^{-1}) = \frac{I\Delta t}{m} \quad (vii)$$

$$\text{Coulombic Efficiency}(\eta) = \frac{t_d}{t_c} \times 100 \quad (viii)$$

where I (A) is the discharging current, Δt (s) is the discharging time, m (g) is the weight of active material on the electrode, ΔV (V) is the potential window, t_d is the discharging time, and t_c is the charging time.

▪ **Electrochemical Impedance Spectroscopy**

EIS is a popular technique for calculating a system's impedance in response to the frequency of an alternating current (AC) potential. Compared to other electrochemical testing methods, EIS offers three main advantages. Firstly, it is a minimally invasive technique, which means it does not significantly alter the device's characteristics during measurement. EIS provides information on capacitance and voltage relationships without pushing the supercapacitor device beyond its equilibrium point. Secondly, EIS provides insights into the device's resistance, which is crucial for understanding power consumption. Thirdly, EIS results are not influenced by time or current, adding to its reliability.

EIS measurements can be done by applying a potential of 5mV to 10mV over a wide frequency f range, for example, 1mHz to 1MHz. It can also provide a relationship between the imaginary part of impedance $|Z|$ and the real part f. Like CV and GCD, specific capacitance can be

calculated using a linear portion of the $\log |Z|$ vs $\log f$ curve, known as the Bode Plot. Specific capacitance can be calculated by using the formula given below:

$$C = \frac{1}{2\pi f|Z|} \quad (ix)$$

From the Bode plot, we can find that with increasing frequency, the capacitance decreases, and at high-frequency regions, supercapacitors behave like pure resistance, suggesting that high frequencies are probably too high for electrolyte ions to enter micropores.

The EIS can also be expressed as a Nyquist plot where the actual and imaginary part of the impedance is plotted on the x and y-axis, respectively. From the Nyquist plot, a plane semicircle section in the high frequency (10^4 Hz) range indicates the low resistance or charge transfer resistance that the boosted electrical conduction of the sample. Pseudo charge transfer resistance is observed in the high to medium frequency (10^4 Hz- 1Hz) range and is linked to the porous structure of the electrodes. At a low frequency (<1Hz) range, the impedance plot shows pure capacitive behavior. Theoretically, the Nyquist plot of a pure capacitor shows a parallel line to the imaginary axis. But in actual cases, a line with an inclination angle across the real axis between 45° and 90° is there, which represents the ion diffusion process operating between Warburg diffusion and ideal capacitive ion diffusion. The EIS data can be interpreted by using equivalent circuit models. These models consist of elements like resistors, inductors, and capacitors with distributed elements such as constant phase elements and Warburg impedance. The Warburg diffusion is an element in the equivalent circuit that models the diffusion process. The Warburg impedance element is always associated with charge transfer resistance and is difficult to recognize. The square root of the frequency has an inverse relationship with the magnitude of the Warburg impedance[185],[186],[187].

3.3.8. Asymmetric Supercapacitor

The asymmetric supercapacitors consist of positive and negative electrodes with a separator or electrolyte solution as shown in Fig. 3.8. In our work, MnMoO_4 , rGO@MnMoO_4 , $\text{MoS}_2\text{@MnMoO}_4$, and $\text{Ni}_x\text{Mn}_{1-x}\text{MoO}_4$ as positive electrodes whereas activated carbon, graphite activated carbon as a negative electrode and 3M potassium hydroxide (KOH) electrolyte were used. CV, GCD, and EIS techniques have been characterized to know about the optimization, specific capacitance, energy density, cycling stability, as well as the power density of the device.

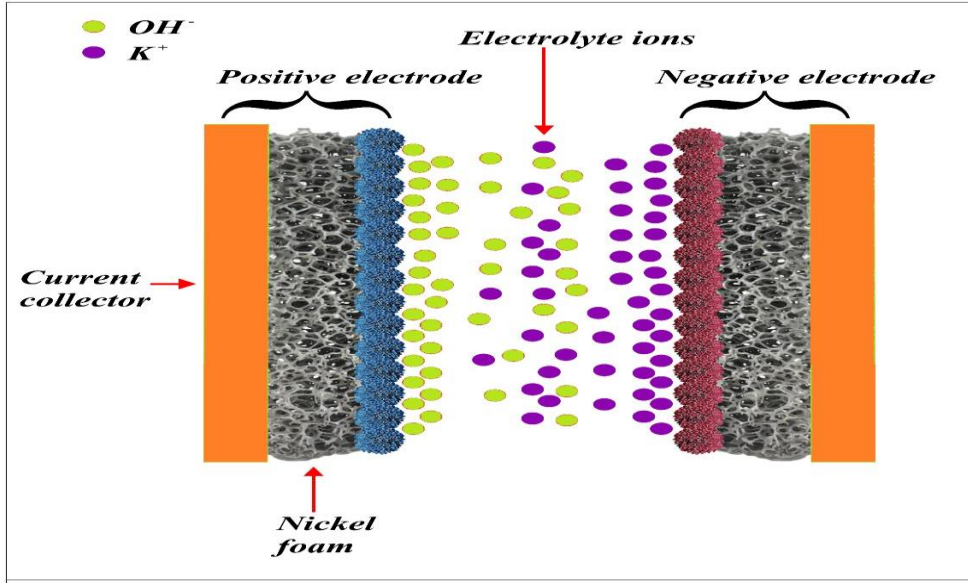


Fig. 3.8. Schematic of asymmetric supercapacitor device.

The energy density is energy per unit volume, and power density, which is energy released per unit time, are the essential parameters for assessing the overall achievements of supercapacitors. The integral and general energy and power densities of an asymmetric supercapacitor can be determined using the following equations:

$$\text{Integral Energy density (Wh kg}^{-1}\text{)} = I \int_0^t V(t) dt \quad (x)$$

$$\text{General Energy density (Wh kg}^{-1}\text{)} = \frac{\text{Specific capacity} \times \Delta V}{7.2} \quad (xi)$$

$$\text{Power density (W kg}^{-1}\text{)} = \frac{3600 \times \text{Energy density}}{\Delta t} \quad (xii)$$

where Δt (s) is the discharging time and ΔV (V) is the potential window.

Chapter 4

Binder-free MnMoO₄ nanoribbons on Ni-foam for high-performance electrochemical energy storage devices

Manganese Molybdate (MnMoO₄) has attracted considerable research courtesy because of its outstanding catalysis, good redox activity, environmental-friendliness, inexpensive and great electrochemical behavior [140],[188]] due to the synergistic result of Mn and Mo ions as the first contribute towards redox activity and the later offer electronic conductivity [130]. The MnMoO₄/CoMoO₄ nanowires exhibit a capacitance value of 187.1 Fg⁻¹ at 1 Ag⁻¹ [76] due to the high surface/volume ratio. Jayasubramaniyan et al. reported 551 Fg⁻¹ at 1 Ag⁻¹ for the α -MnMoO₄ nanorods synthesized by microwave hydrothermal method [134]. Ghosh et al. synthesized an α -MnMoO₄/graphene-based hybrid composite, which displayed outstanding cyclic stability [144], ascribed to the three-dimensional (3D) graphene network and its strong bonding with MnMoO₄. Purushothaman et al. developed 129 μ g of MnMoO₄ nanorods on the substrate and obtained 784 Fg⁻¹ at 5 mVs⁻¹ in 0.06 M Para toluene sulfonic acid [131]. Another group synthesized MnMoO₄·4H₂O and obtained 2300 Fg⁻¹ with 0.5 mg cm⁻² mass-loading at 4 mA cm⁻² in 1 M NaOH [139]. More recently, Xu et al. grew 0.5 mg cm⁻² MnMoO₄ on the nickel foam and reported 4609 Fg⁻¹ at 1Ag⁻¹ and decent energy as well as power densities of 107.38 Whkg⁻¹ and 801.34 Wkg⁻¹, respectively [189]. It has been observed from the review of literature that MnMoO₄ is accomplished of being used as an efficient material and can perform well even at lower mass loadings, an attempt has been made to carry forward this work to explore the consequence of mass-loading on its electrochemical achievements. In the present study, MnMoO₄ nanostructures have been synthesized and deposited on Ni foam directly, by the one-step hydrothermal treatment. Without any binder, it is applied directly as an electrode, for the electrochemical assessment.

4.1. Structure and Microstructure Analysis

The X-ray diffraction pattern of MnMoO₄@NF nanostructures is displayed in Fig. 4.1 (a). The appeared diffraction peaks reveal the presence of (001), (201), (021), (201) (220), (112), (-221), (-202), (112), (002), (-222), (400), (040), (-132), (222), (-332), (113) and (241) planes in the studied range *i.e.*, between 10 to 50 degrees, are exactly mapping with the JCPDS card number 01-72-0285, which indicated the presence of monoclinic α -MnMoO₄ crystal structure [145]. Further, the absence of any impurity peak suggests the formation of high-quality

MnMoO₄ nanoribbons. Figure 4.1(b) displays the Raman spectrum of MnMoO₄ nanostructures. The bands at the high wave number region *i.e.*, 800 to 950 cm⁻¹, are attributed to stretching vibrations, and those at the low wavenumber region *i.e.*, 200 to 400 cm⁻¹ represent the bending vibrations of MoO₄ ions [190]. The characteristic Raman active A_g and B_g vibrations of α -MnMoO₄ are distinctly evident from the appearance of required bands between 200 to 1000 cm⁻¹.

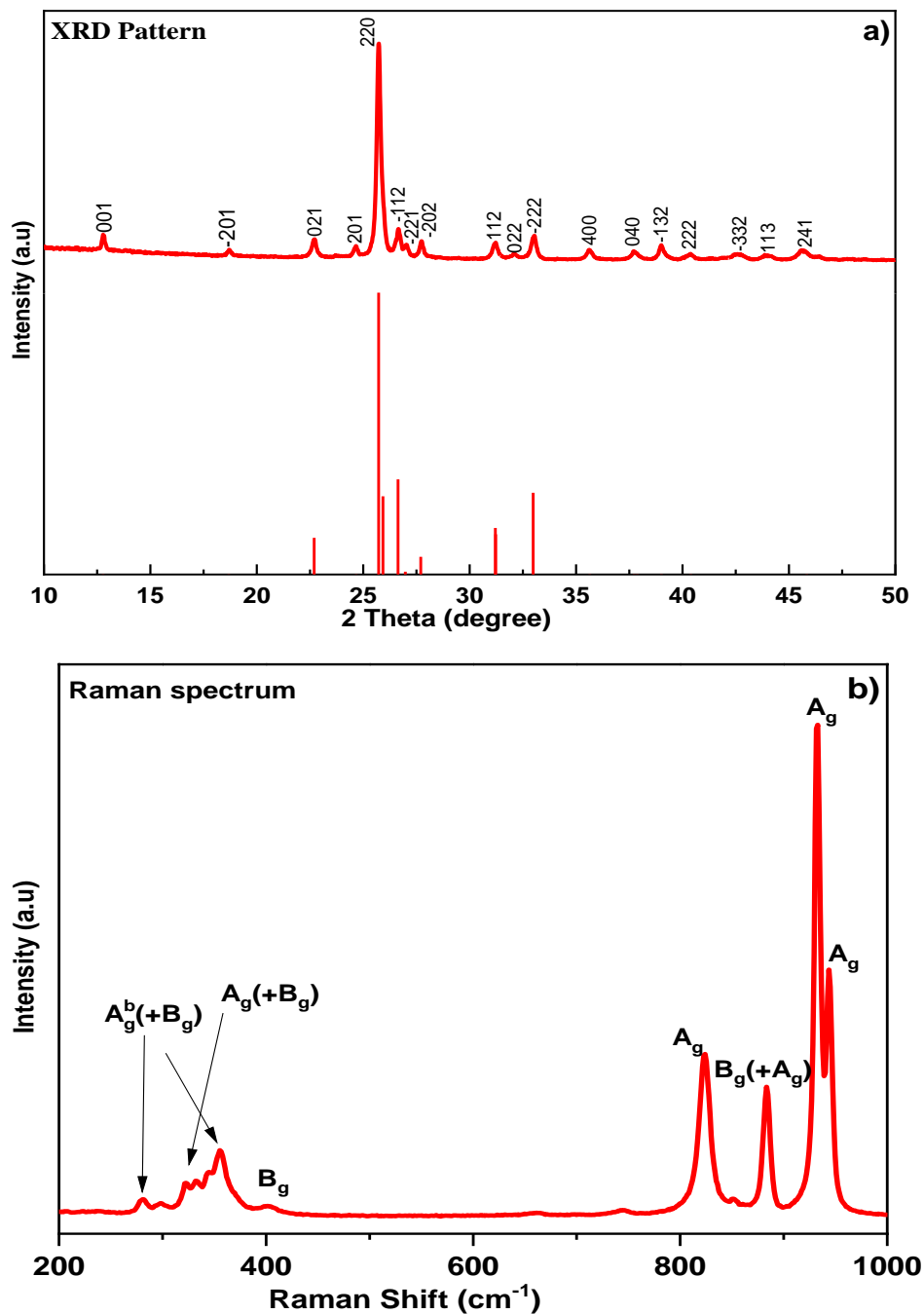


Fig. 4.1: a) The X-ray diffraction pattern and b) Raman spectrum of MnMoO₄ nano-structures.

The A_g vibrations are prominently visible at 944, 933, and 824 cm^{-1} , B_g vibrations are displayed at 402 cm^{-1} , $B_g(+A_g)$ and $A_g(+B_g)$ vibrations are present at 884 cm^{-1} and 343 cm^{-1} , respectively, and the bands at 353 and 279 cm^{-1} are ascribed to $A_g^b(+B_g)$ vibrations [191],[192].

FESEM was used to assess the morphological features of the synthesized nanostructures. Uniform deposition of MnMoO_4 nanostructures on the nickel form is visible at lower magnification in Fig.4.2 (a-d). At higher magnification, it is revealed that the synthesized nanostructures have ribbon-like shapes and are uniformly grown on the mesh. The strong

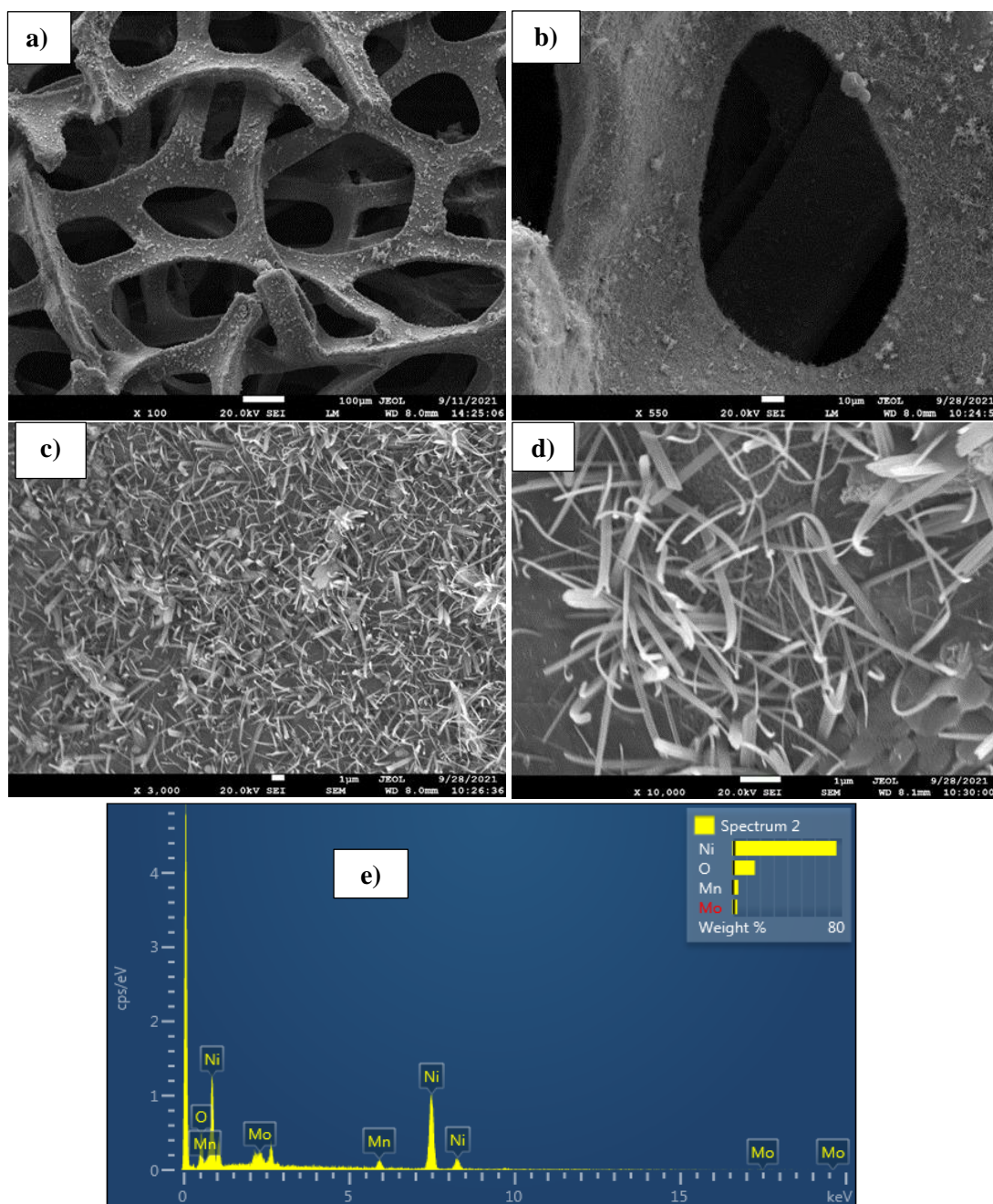


Fig. 4.2: a-d) The FESEM micrographs of MnMoO_4 @NF at different magnifications and e) shows the EDS mapping of MnMoO_4 @NF.

bonding seen in nickel nanoribbons could potentially be attributed to their elevated surface energy and thermodynamic instability [134]. The high density of MnMoO_4 nanoribbons on Ni-foam suggests a higher probability of ion diffusion in the electrochemical cell. The EDS mapping of MnMoO_4 nanoparticles is shown in Fig.4.2 (e), which confirms the uniform distribution of Mn, Mo, and O atoms in the synthesized sample.

4.2. Electrochemical Analysis

The electrochemical achievements of $\text{MnMoO}_4@\text{NF}$ have been evaluated by CV, EIS, and GCD measurement with three electrode setups, by using 3M potassium hydroxide as electrolyte.

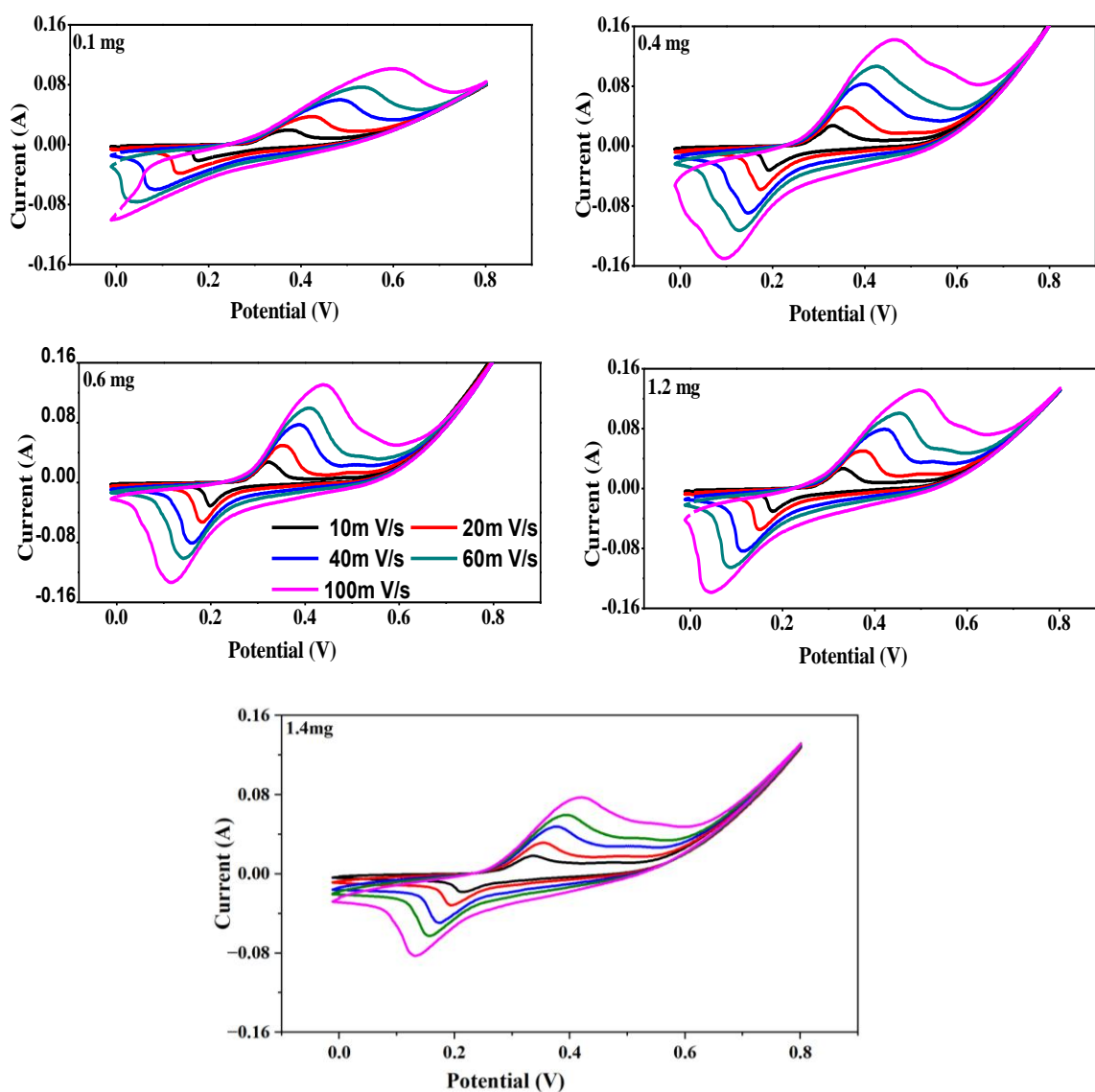


Fig. 4.3. The CV curves of $\text{MnMoO}_4@\text{NF}$ with different mass loadings, at different scan rates.

The CV curves of MnMoO₄@NF at different mass loadings *i.e.*, 0.1mg, 0.4mg, 0.6mg, and 1.2mg, are plotted in Fig. 4.3. The potential window was kept between -0.01V to 0.8V and the sweeping rates were varied from 10mVs⁻¹ to 100mVs⁻¹. In the CV curves of all mass loadings, the appearance of a pair of distinct redox peaks illustrates their faradaic behavior. As scan rates increased, the anodic and cathodic peaks were seen to migrate towards higher and lower potential for oxidation and reduction, respectively. The rapid ionic and electronic propagation at the electrode-electrolyte interface at higher scan rates is responsible for this behavior at high scan rates.

On comparison of CV plots of MnMoO₄@NF with different mass loadings at all scan rates, it is observed that the area within the CV graphs increased first up to a mass loading of 0.4mg but then decreased with further increase of the amount of MnMoO₄ on nickel foam. Among all the investigated cases, an electrode with 0.1mg mass loading had the minimum CV area. At first glance, it can be interpreted that the electrodes with higher mass loading have better charge storage capability but interestingly, the calculated values of specific capacity displayed the opposite trend, as depicted in Fig. 4.4(a) [193]. The electrode with minimum mass loading *i.e.*, 0.1 mg can show a magnificent Faradic behavior with a specific capacity of 830 mAhg⁻¹ (3695 Fg⁻¹) at the scan rate of 10 mVs⁻¹, which is manifold higher than the values of specific capacity of electrodes with higher mass loadings, which is attributed to inverse relation of specific capacitance with the loaded mass on the electrode. It can also be interpreted that lesser mass loading can provide a greater electrochemical active superficial area on electrodes for interaction with electrolytes and dense nanoribbons offer better opportunities for ion diffusion [194]. Agglomeration at higher mass loadings might have resulted in reduced surface area and consequently deteriorated their electrochemical performance. The calculated values of the specific capacity of 0.1 mg of MnMoO₄@NF at all investigated scan rates are significantly at par as compared to high mass-loaded electrodes.

With the increase of scan rate, the values of specific capacity, at all mass loadings were decreasing. This may be due to incomplete ion diffusion process or availability of lesser time for interaction between electrode and electrolyte at higher scan rates and hence results in reduced charge transport.

Further, the charge storage kinetics was investigated by exploring the following relation between peak current, *I*, and scan rate, *V* of the CV curves [189]:

$$I = AV^X \quad (xiii)$$

where X is linked to a surface-controlled process if its value is close to 1 and a diffusion-controlled process if its value is close to 0.5, where A is constant and is dependent upon the electrode material's composition and the exponent. The exponent X can be calculated from the slope of straight lines plotted between \log_{10} of peak current and \log_{10} of scan rate. Figure 4.4(b) is showing the variation of peak current of CV plots with scan rates of $\text{MnMoO}_4\text{@NF}$ at different mass loadings. The calculated values of X were 0.64, 0.65, 0.64, and 0.63 for 0.1mg, 0.4mg, 0.6mg, and 1.4mg loaded $\text{MnMoO}_4\text{@NF}$, respectively, which strongly suggests the dominance of diffusion-controlled process in all the studied electrodes. The nanoribbons-based morphology as observed in the FESEM micrographs firmly supports this finding.

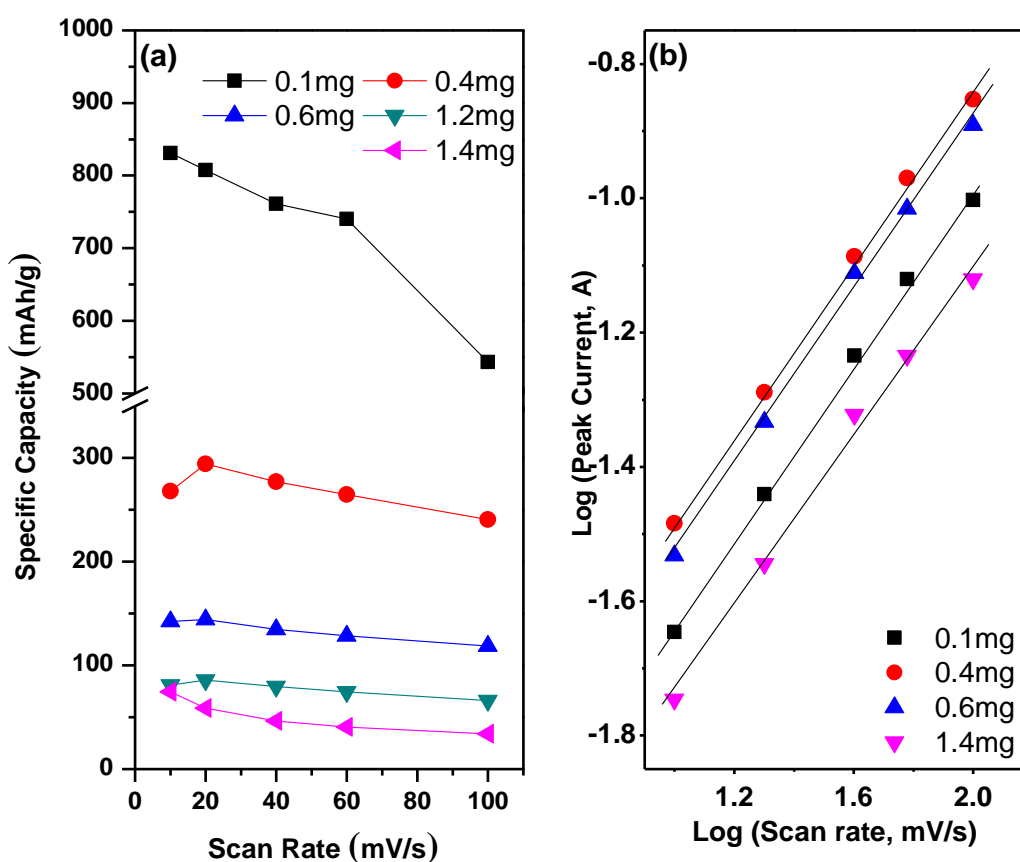


Fig. 4.4. a) The variation of specific capacity with scan rate at different mass loadings. **b)** The variation of the peak current of CV plots with scan rates of $\text{MnMoO}_4\text{@NF}$ at different mass loadings.

The charging and discharging behavior of $\text{MnMoO}_4\text{@NFs}$ was explored in the potential window 0 to 0.42V to further understand the effect of mass loading on their charge storage capability. The GCD curves of $\text{MnMoO}_4\text{@NF}$ with different mass loadings, at different currents are presented in Fig. 4.5. The current density was varied from 2 Ag^{-1} to 50 Ag^{-1} . Similar and symmetrical GCD curves are observed for all mass loadings and at all current densities, which confirms their pseudocapacitive behavior. It is noticed that the discharging

time at all current densities was longer for 0.1 mg loaded $\text{MnMoO}_4\text{@NF}$, suggesting its better electrochemical performance. The comparison of GCD curves of $\text{MnMoO}_4\text{@NF}$ with different mass loadings, at the current density of 5Ag^{-1} is also compared in Fig. 4.6(a). The difference in discharging time of differently loaded $\text{MnMoO}_4\text{@NF}$ is distinctly visible. The values of specific capacitance of all studied electrodes at different current densities are calculated and plotted in Fig. 4.6(b). It revealed the spectacular specific capacities of 1050, 943.05, 886.11, and 722.08 mAhg^{-1} of $\text{MnMoO}_4\text{@NF}$ with 0.1mg mass loading, at 5, 10, 20, and 50 Ag^{-1} , respectively, and thus perspicuously outperformed the heavily loaded electrodes and till date other reported results on the same material, as shown in Table 2.3. The uniform array of nanoribbons vertically grown on nickel form offers more active sites to facilitate Faradic reaction and deeper electrically conducting pore channels to enhance the ion diffusion process.

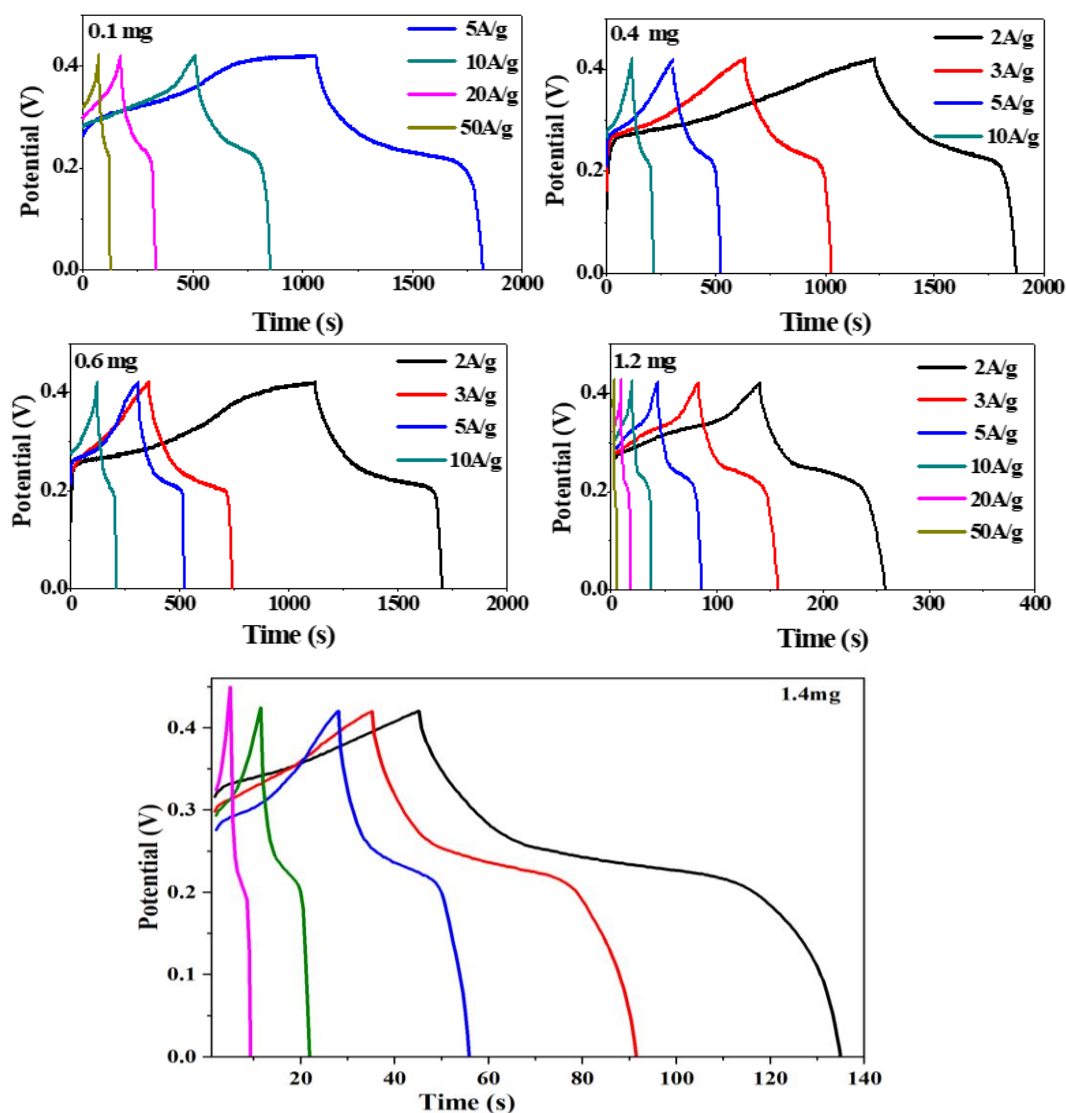


Fig. 4.5. The GCD curves of $\text{MnMoO}_4\text{@NF}$ with different mass loadings at different current densities.

It can be seen from Fig. 4.5 and 4.6 that charge-discharge time duration and the values of specific capacity, respectively, of MnMoO₄@NF for all mass loadings decreases with the increase of current densities. At lower current density, more electrolyte ions can interact with the reaction sites available on the electrode, which leads to higher specific capacity and vice-versa [141]. Further, to investigate the enduring stability of MnMoO₄@NF with 0.1mg mass loading, cyclic charge- discharge measurement at a high current density of 50 A g⁻¹ has been done for 1000 cycles as shown in Fig.4.7. Apparently, the electrode with 0.1mg mass loading has shown a noteworthy retention of specific capacitance of almost 72.5 % of its initial value at such a high current density, which is further revealing its good cyclability.

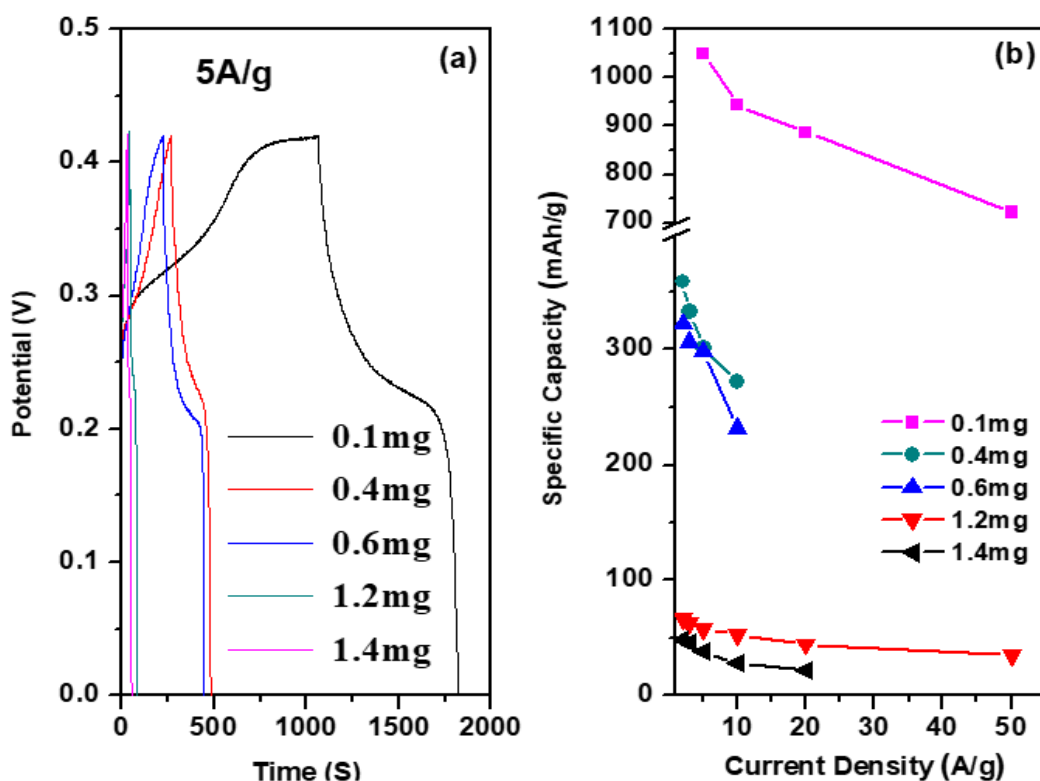


Fig. 4.6. **a)** The comparison of GCD curves of MnMoO₄@NF with different mass loadings at a current of 5 A/g. **b)** The variation of specific capacity of MnMoO₄@NF with current density at different mass loadings.

The EIS plot of the best sample of MnMoO₄@NF was recorded in the frequency range 0.01 Hz to 100 kHz at 10 mV amplitude and displayed in Fig. 4.8 to explore its charge transfer kinetics. Its equivalent circuit diagram portrayed in the inset was drawn based on a discrete-component circuit model. The equivalent circuit contains a series resistance, R_s , an impedance element, and a Warburg, W connected in series. The impedance component consists of a charge

transfer resistance, R_{CT} , and a capacitor, C_P connected in parallel with a constant phase element, CPE. It is assumed that the W , C_P , and CPE are responsible for the diffusion process, pseudo-capacitance, and double-layer capacitance, respectively. Our proposed circuit is carrying an additional component *i.e.*, Warburg, as compared to that reported by Xu *et.al.* [189]. The following relation portrays the impedance of the constant phase element:

$$Z(CPE) = A^{-1}(\omega)^{-n} \quad (xiv)$$

where n is a distributing factor whose value varies between 0 to 1 and ω is the imaginary component of angular frequency [141]. The fitted values of R_s and R_{CT} were 2.62 Ω and 2.33 m Ω , respectively, due to better charge propagation with minimal resistance, are responsible for the high charge transfer rate and rapid kinetics of $MnMoO_4@NF$ with 0.1mg mass loading. This finding is consistent with the results of cyclic voltammetry and GCD analysis. The presence of the Warburg element further confirms the presence of a diffusion process as observed in the CV analysis. The estimated value 0.94 of the exponent, n revealed the capacitive nature of the constant phase element present in the equivalent circuit [131].

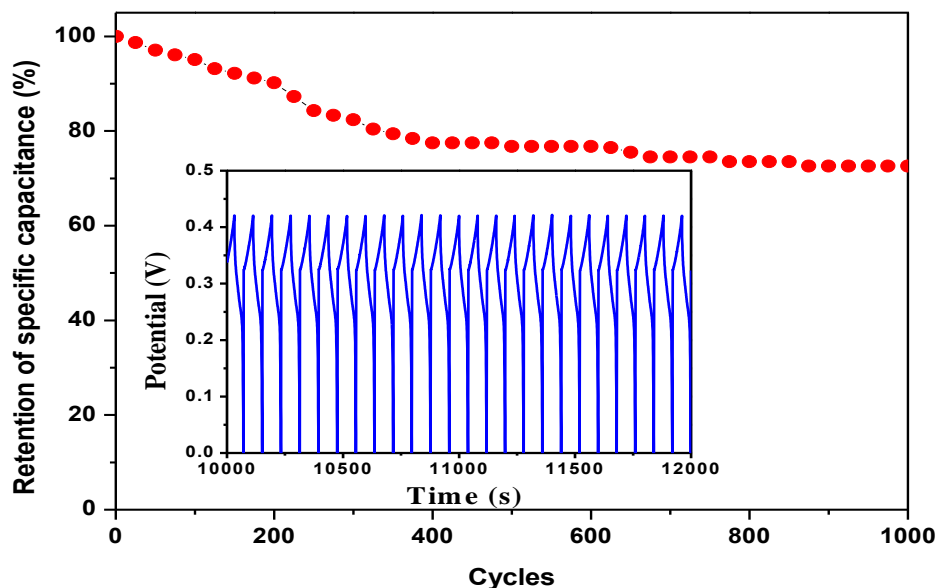


Fig. 4.7. The variation of retention percentage of specific capacitance of $MnMoO_4@NF$ with 0.1mg mass loading. The inset shows the 25 cycles at a certain intermediate time duration.

The electrochemical performance of previously reported results of $MnMoO_4$ has been compared with that of the best sample of the present work and is summarized in Table 2.3. After comparison, it is revealed that the supercapacitor performance of $MnMoO_4@NF$ with 0.1mg mass loading prepared by hydrothermal technique in the present work has superior electrochemical behavior.

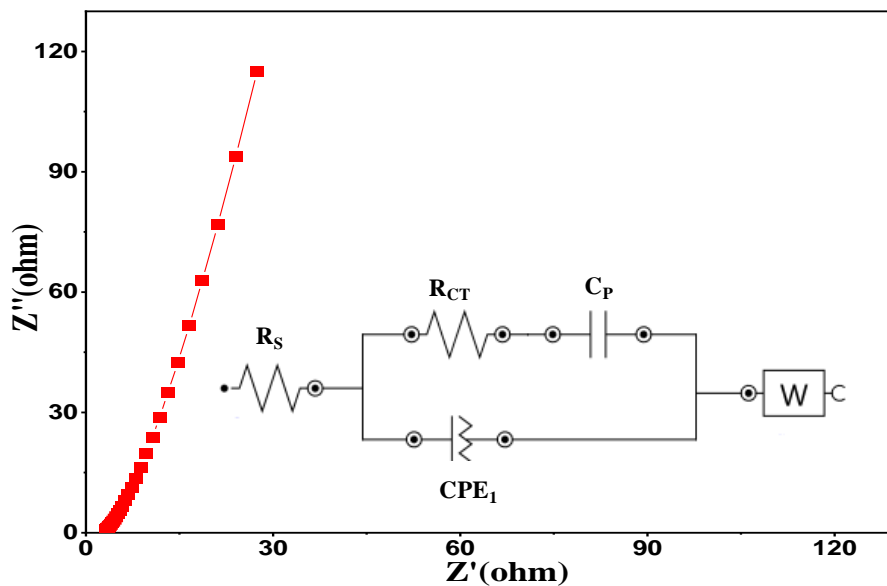


Fig. 4.8. The EIS curve of MnMoO₄@NF with 0.1mg mass loading and the inset is representing its equivalent circuit diagram.

Conclusion

The nanoribbons of α -MnMoO₄ nanoribbons are successfully grown on the nickel foam by one-step hydrothermal method. It is confirmed by FESEM micrographs and EDS mapping. Analysis of X-ray diffraction and Raman graphs confirmed the formation of a monoclinic α -MnMoO₄ crystal structure. It is revealed that the electrode with minimum mass loading outperformed the heavily loaded electrodes in term of specific capacitance and retention rate capability. The binder-free electrodes with 0.1 mass loading exhibited a magnificent specific capacity of 1050mAhg⁻¹ (9000 Fg⁻¹) at the high current density of 5 Ag⁻¹. After 1000 galvanostatic charge-discharge cycles, decent retention of 72.5% was maintained even at a very high current density of 50 Ag⁻¹. The presence of abundant active sites and the dominance of diffusion-based processes are made accountable for the higher charge storage capability of MnMoO₄@NF. The results of electrochemical evaluation strongly suggest the potential candidature of MnMoO₄ on nickel foam for high-performance supercapacitor application, specifically at low mass loading.

Chapter 5

Boosting the electrochemical characteristics of MnMoO₄ nanoparticles for supercapacitor applications

The energy-related research has witnessed a notable surge of interest in binary metal molybdates. These binary metal molybdates (MMoO₄, where M = Ni, Co, Zn, Mn, etc.) have attracted considerable attention as compared to other materials like metal oxides, metal hydroxides, and metal sulfides [195] due to their eco-friendliness, low cost, favorable electrical and electrochemical properties [133]. Among binary metal molybdates, Manganese Molybdate (MnMoO₄) has captured significant focus due to its remarkable catalytic properties, excellent redox activity, environmentally friendly nature, cost-effectiveness, and impressive electrochemical behavior. The synergistic effects of manganese (Mn) and molybdenum (Mo) ions i.e., the former contribute to the redox activity, while the latter enhances electronic conductivity, resulting in a highly desirable combination of properties [196]. The electrochemical properties of energy storage systems are significantly influenced by the synthesis route employed because the morphology and surface area of electrode materials primarily depend on the fabrication conditions [197]. Several techniques like solid-phase method, precipitation method, liquid state method, microwave irradiation-assisted technique, etc., have been employed widely to prepare the nano-scaled MnMoO₄ [130]. Sheng and his coworkers prepared MnMoO₄ nanoparticles by solid-state reaction and reported a specific capacitance of 210 F g⁻¹ at 1 A g⁻¹ and cycling stability of 112.6% after 10,000 cycles. Their asymmetric device with reduced graphene oxide (rGO) as a negative electrode demonstrated an energy density of 23.5 W h kg⁻¹ at 187.4 W kg⁻¹ [136]. The 3D fan-like nanostructures of α -MnMoO₄ were synthesized by Wang et al. via precipitation method and stated a specific capacitance of 562 F g⁻¹ at 1 A g⁻¹ with cycling stability of 99.8% [132]. Senthilkumar et al. prepared rhombohedral-like α -MnMoO₄ by precipitation method and quantified the specific capacitance of 200 F g⁻¹ at 1.6 A g⁻¹ and cycling stability of 91% [135]. Using the same method, Nti and coworkers prepared MnMoO₄·4H₂O nanoparticles and testified the specific capacitance of 215 F g⁻¹ at 1 mA cm⁻² [198]. In the precipitation method, it is challenging to prevent the agglomeration of nano-particles due to significant variations in local concentration and temperature within the reactant solutions [199]. The liquid state synthesis method can control morphology and can overcome agglomeration. Purushothaman and his coworkers prepared α -MnMoO₄ nanoparticles by sol-gel method and reported the specific capacitance of

784 F g⁻¹ at 5 mV s⁻¹ [131]. Cao et al. synthesized MnMoO₄·4H₂O nanoplates by hydrothermal method and testified its specific capacitance of 2300 Fg⁻¹ at 4 mA cm⁻² and cycling stability of 92% after 3000 cycles[139]. The same technique was used by Mu et al. to develop MnMoO₄·nH₂O and stated the specific capacitance of 1271 Fg⁻¹ at 5 mV s⁻¹ and cycling stability of 84.5% after 2000 cycles. Their asymmetric device delivered an energy density of 31.6 Wh kg⁻¹ at 935 W kg⁻¹ [141]. Saravanakumar and his coworkers prepared MnMoO₄ nanoparticles by solvothermal method, and their electrode delivered a specific capacitance of 697.4 Fg⁻¹ at 0.5 Ag⁻¹ [145]. Xu et al. prepared MnMoO₄ nanosheets by hydrothermal reaction and reported the specific capacitance of 4609 Fg⁻¹ at 1 Ag⁻¹, and their asymmetric device i.e., MnMoO₄//AC, delivered 107.38 Whkg⁻¹ at 801.34 Wkg⁻¹ [189]. The nanoparticles of α-MnMoO₄ nanoparticles synthesized by Veerasubramani et al. via the Sonochemical method exhibited a specific capacitance of 168.32 Fg⁻¹ at 0.5 mAcm⁻² and cycling stability of 96% after 2000 cycles at 100 mVs⁻¹ [140]. Though the MnMoO₄ nanoparticles prepared via the liquid state synthesis method delivered better and stable results, this process is time-consuming and in certain cases, there is an issue with the reproducibility of results[200]. Thus, the microwave irradiation-assisted technique has been utilized for the swift synthesis of MnMoO₄ nanoparticles. This method is favored for its notable advantages, including a high penetration depth, minimal thermal gradient effect, and rapid synthesis [201]. For example, Jayasubramaniyan et al. prepared α-MnMoO₄ nanoparticles by microwave hydrothermal method and reported the specific capacitance of 551 Fg⁻¹ at 1 Ag⁻¹ and cycling stability of 89% after 1000 cycles at 5 Ag⁻¹ [134]. Zhang et al. prepared α-MnMoO₄ nanoparticles by the same technique and stated the specific capacitance of 446.7 Fg⁻¹ at 1 mAcm⁻² and cycling stability of 81.1% after 3000 cycles at 8 mAcm⁻² [152]. Similarly, Harichandran et al. prepared MnMoO₄ nanoparticles by microwave-assisted method and testified its specific capacitance of 836 Fg⁻¹ at mVs⁻¹ and cycling stability of 84% after 3000 cycles at 100 mVs⁻¹ [202]. Based on the literature survey above, it can be concluded that while MnMoO₄ nanoparticles have been synthesized using various techniques, only a few reports are available on the microwave-assisted synthesis of MnMoO₄ nanoparticles. Therefore, our present investigation focuses on the specific use of the facile and time-saving microwave-assisted synthesis technique, followed by the calcination of the obtained nanoparticles. Notably, the impact of calcination temperature on the electrochemical performance of MnMoO₄ nano-particles obtained through the microwave-assisted synthesis route has not been studied before.

5.1 Structure and Microstructure Analysis

The X-ray diffraction patterns of MnMoO_4 nanoparticles calcinated at different temperatures are plotted in Fig.5.1. It is observed that the samples calcinated at 500 and 700 °C were crystallized as evidenced by their sharp, intense, and well-defined peaks. On the other hand, it was noticed that the calcination of 300 °C was not enough to crystallize MnMoO_4 nanoparticles. The presence of (001), (20-1), (02- 1), (002), (11-2), (13-1), (31-2), (400), and (11-3) planes at their respective positions are well-mapped with the JCPDS: 98-000-4001, which confirmed the formation of monoclinic $\alpha\text{-MnMoO}_4$. It is perceived that the intensity and sharpness of the peak assigned to the (002) plane increased with the increase of calcination temperature, indicating the growth of crystallite size. The computed values of the crystallite size of MnMoO_4 nanoparticles calcinated at 300, 500, and 700°C were 6.9, 45.5, and 52.2 nm, respectively.

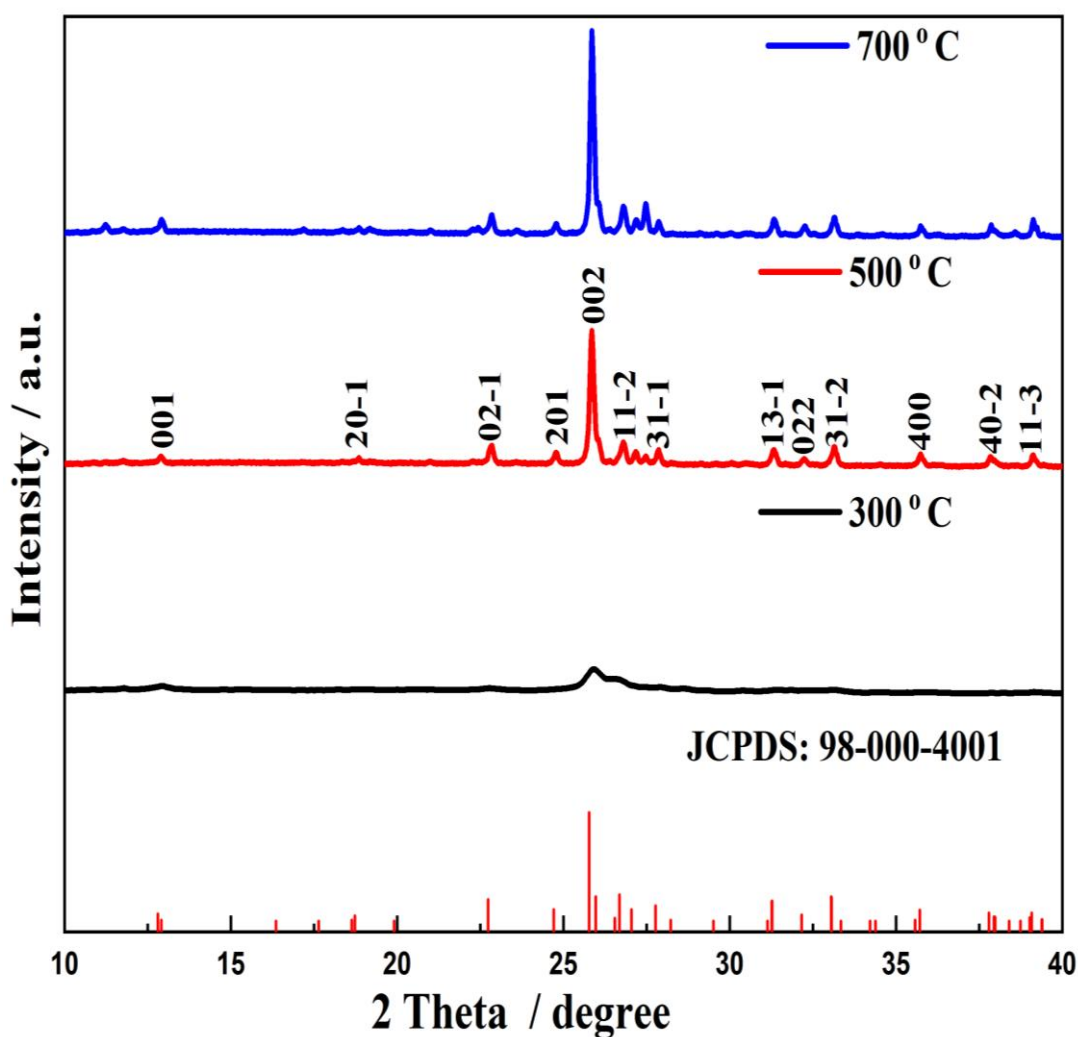


Fig. 5.1. The XRD spectra of MnMoO_4 nanoparticles at different calcination temperatures.

The Raman spectra of the calcinated nanomaterial are displayed in Fig. 5.2. The Raman spectrum of MnMoO_4 nanoparticles calcinated at 300°C , endorsed the finding of XRD analysis regarding the incomplete crystallization of the nanomaterial. However, the distinctive and well-defined bands in the Raman spectra of the nanoparticles calcinated at higher temperatures validated the formation of MnMoO_4 . The band observed at 930 cm^{-1} corresponds to symmetrical O-Mo-O stretching vibrations i.e., A_g mode. The bands at 880 and 820 cm^{-1} infer the presence of B_g (+ A_g) and A_g mode, respectively, ascribed to Mo-O symmetric stretching vibrations.[189] The bending vibrations of tetrahedral MoO_4 ions i.e., A_g and A_g (+ B_g) modes were noticed at 349 and 339 cm^{-1} , respectively[190]. The XRD and Raman results validate the formation of MnMoO_4 nanoparticles.

The FE-SEM micrographs of MnMoO_4 nanoparticles calcined at different temperatures are depicted in Fig. 5.3(a–c). The particle size increases with the rise in calcination temperature. As shown in Fig. 5.3(a, b), the nanoparticles exhibit multiple morphologies, including nanorods of varying sizes. However, at higher calcination temperatures, the nanorod morphology disappears, attributed to an increase in particle size. The EDS mapping of the MnMoO_4 nanoparticles calcined at 500°C , as shown in Fig. 5.3(d), confirms the absence of any impurity in the synthesized sample.

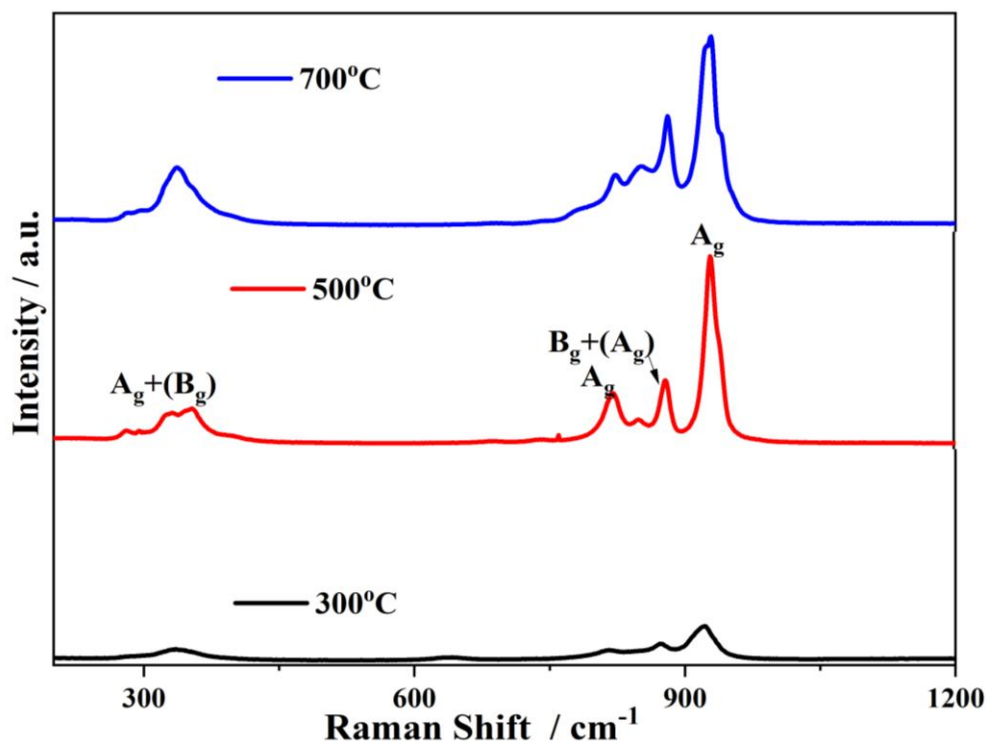


Fig. 5.2. The Raman spectra of MnMoO_4 nanoparticles at different calcination temperatures.

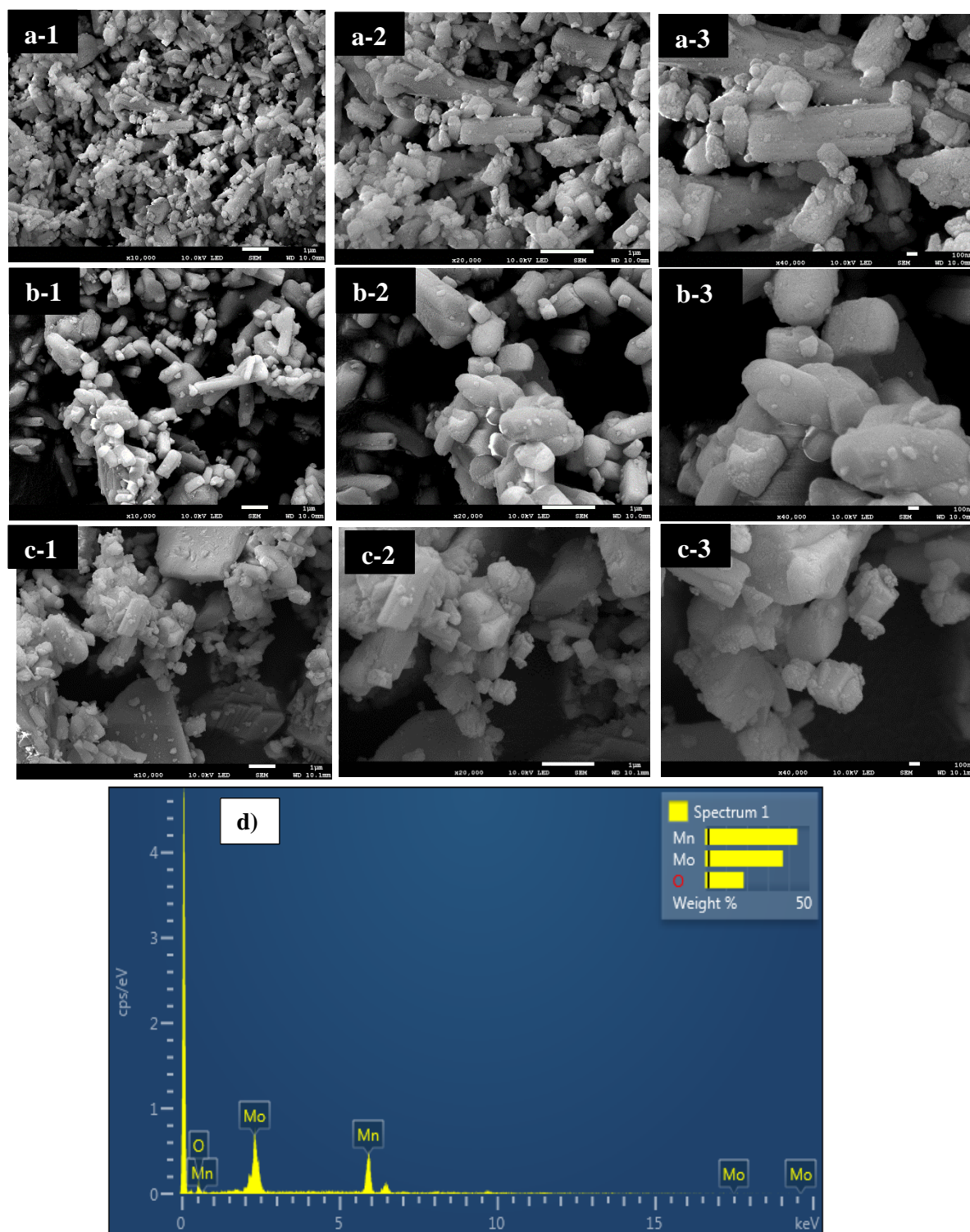


Fig.5.3. The FESEM images, of MnMoO₄ nanoparticles calcinated at **a)** 300 °C, **b)** 500 °C, and **c)** 700 °C. **d)** The EDS mapping of MnMoO₄ nano- particles calcinated at 500 °C.

The BET analysis was done for all three samples to further analyze the surface of nanomaterial. The obtained value of multipoint BET surface area from the N₂ adsorption-desorption isotherm Fig. 5.4 of MnMoO₄ calcinated at 300, 500, and 700 °C are 7.8, 3.1, and 2.3 m² g⁻¹, which are larger than previously reported work [203]. The decreasing trend of the surface area of the synthesized nanomaterial with the increase of calcination temperature is seconding the observation of XRD analysis. The average pore diameters of all samples are ~ 1.8 nm measured from the graphs between the pore volume and pore diameter Fig. 5.4, revealing the microporous nature of the MnMoO₄ nanoparticles. The microporous morphology infers the enlarged surface of the synthesized nanomaterial, which suggests their potential utilization as an efficient electrode material for a high-performance energy storage device.

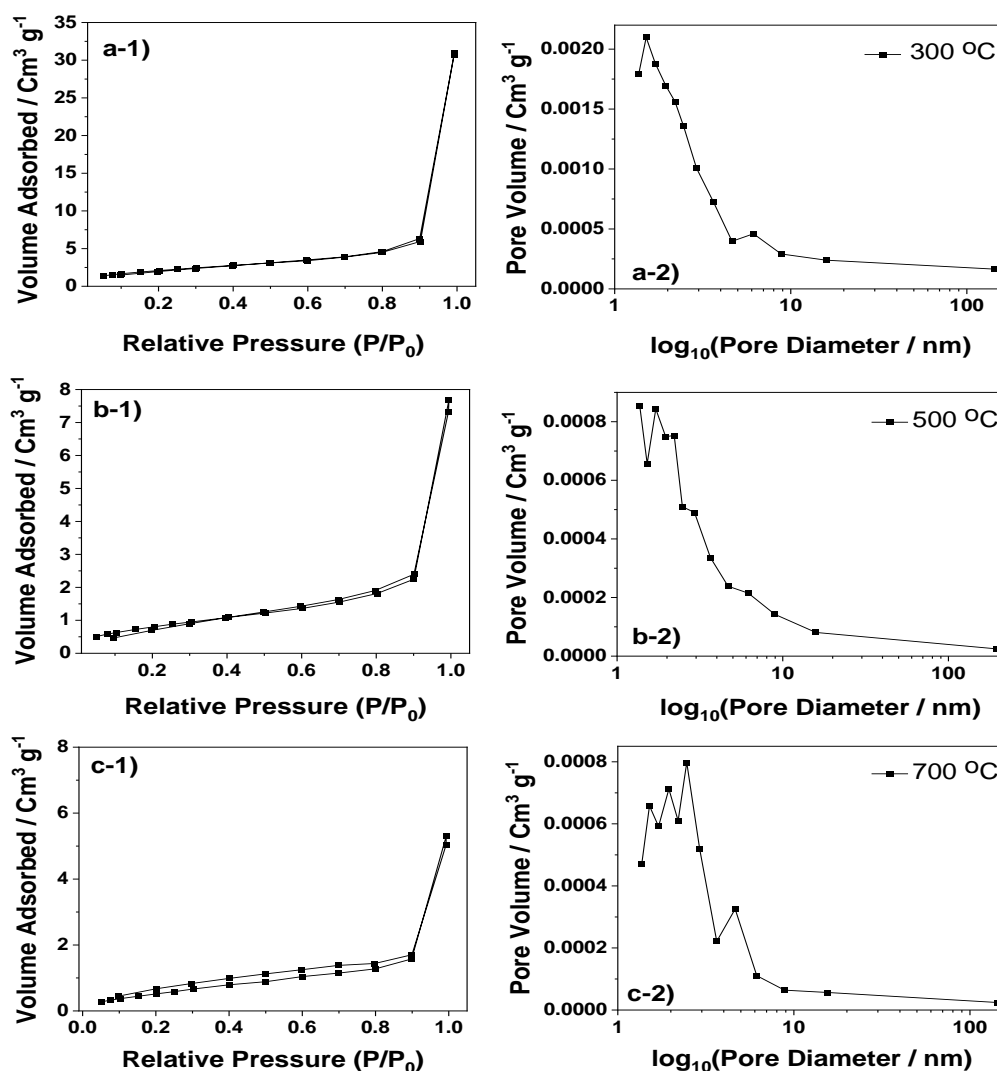


Fig. 5.4. The Nitrogen adsorption-desorption isotherm and the graph between pore volume with pore diameter of MnMoO₄ nanoparticles calcinated at a) 300°C, b) 500°C and c) 700°C.

The XPS spectra of MnMoO₄ nanoparticles calcinated at 500°C are plotted in Fig. 5.5 to explore its elemental composition and oxidation state. The survey spectrum Fig. 5.5(a) displayed three main peaks at 641.18, 231.58, and 529.8 eV, corresponding to Mn 2p, Mo 3d, and O 1s, respectively. However, the peak of C-1s at 284.8 eV was considered for calibration purposes [204]. To analyze the chemical environment and oxidation states of the material, XPS spectra are deconvoluted to separate peaks corresponding to different oxidation states. This process provides valuable insights into the redox behavior of Mn and Mo, enabling the quantification of the Mn/Mo ratio, chemical stoichiometry, and the relative proportions of each oxidation state. The binding energy values obtained from the experimental data closely align with standard reference values from the International XPS Library, confirming the reliability and consistency of the synthesized MnMoO₄ phase. A pair of peaks in the core-level spectrum Fig. 5.5(b) of Mn 2p spectrum at 641.1 eV and 653.04 eV corresponds to 2P_{3/2} and 2P_{1/2}, respectively, and their binding energy difference, i.e., 11.86 eV, confirm +2 oxidation state of Mn. The peak at 647.5 eV in the core spectrum of Mn 2p may be attributed to the shake-up phenomenon. In this process, the outgoing photoelectron interacts with a valence electron, inducing its excitation to a higher energy level. As a result, the energy of the core electron is decreased, and a satellite structure emerges a few electron volts away from the core-level position on the kinetic energy scale. The doublet in Mo 3d spectrum Fig. 5.5(c) at 231.58 and 234.78 eV ascribes to Mo 3d_{5/2} and Mo 3d_{3/2}, respectively. The energy separation between them was 3.2 eV, which infers its +6 oxidation state. The main peak at 529.8 eV in the core-level spectrum of O 1s Fig. 5.5(d) was deconvoluted into three peaks at 529.7, 531.2, and 532.5 eV. The main peak at 529.7 corresponds to lattice oxygen which is essential for maintaining the structural integrity of MnMoO₄, and the other two peaks are ascribed to surface hydroxyl groups, indicating the presence of small moisture in the sample. [145]. In the Mn 2p spectrum, the presence of a shake-up satellite is a distinctive feature of transition metal ions, further confirming the existence of Mn²⁺ in the sample. Similarly, the Mo 3d spectrum indicates that molybdenum primarily exists in its highest oxidation state, as evidenced by the +6 oxidation state. The absence of significant peaks at lower binding energies suggests a negligible presence of Mo⁴⁺ or Mo⁵⁺, reinforcing the high oxidation state stability of molybdenum within the MnMoO₄ lattice. Additionally, in the O 1s spectrum, the presence of hydroxyl groups plays a crucial role in influencing the electrochemical performance of MnMoO₄ by enhancing ion transport and facilitating interfacial charge transfer processes.

5.2. Electrochemical Analysis

The electrochemical behavior of any electroactive material primarily depends upon the size and morphology of the nanomaterial. The electrodes prepared by depositing MnMoO_4 nanoparticles on Ni-foam with the help of a binder were tested by a series of electrochemical measurements to examine their potential application in an asymmetric supercapacitor. The cyclic voltammetry (CV) scans of MnMoO_4 nanoparticles calcinated at different temperatures are shown in Fig. 5.6 (a–d). A pair of distinctly visible redox peaks in the CV curves recorded at different scan rates revealed the Faradaic behavior of all three electrodes. The oxidation of Mn^{2+} to Mn^{3+} and reduction from Mn^{3+} to Mn^{2+} could be the probable cause behind the anodic and cathodic peaks at ~ 0.3 and 0.15 V, respectively. The presence of +2 and +3 oxidation states of Mn has already been revealed in XPS analysis.

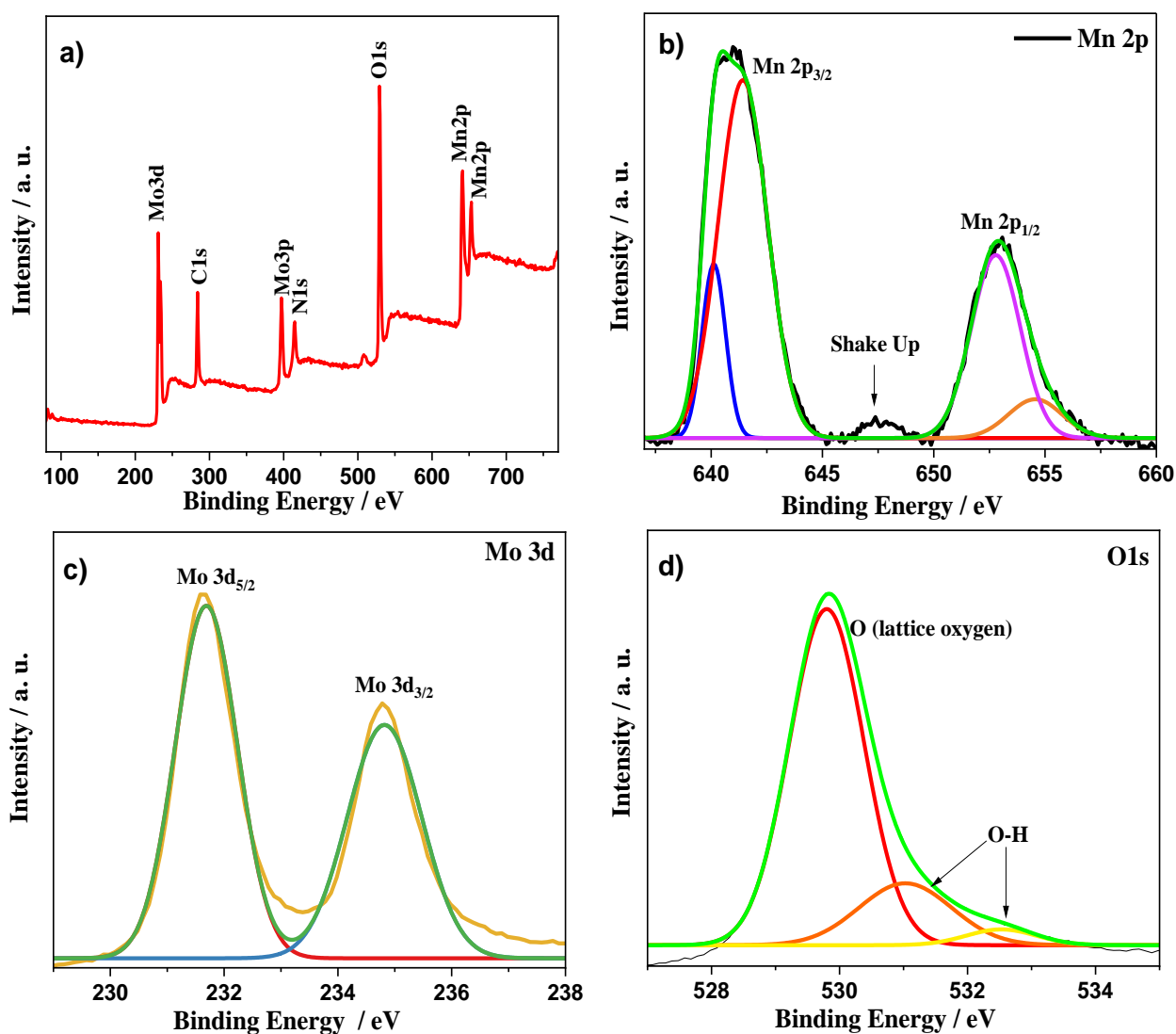
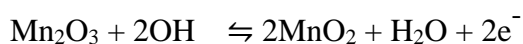
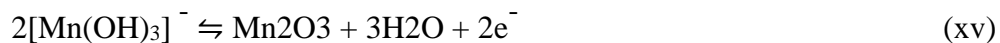


Fig. 5.5. The XPS spectra of MnMoO_4 nanoparticles calcinated at 500°C .

In all the studied electrodes, the shape of the CV curve was retained, however, with the increase of scan rates, the shifting of anodic and cathodic peaks towards positive and negative potential, respectively, suggests the occurrence of swift Faradic reactions at the electrode-electrolyte interface [152]. The suggested electrochemical reactions occurring in KOH involving MnMoO₄ electrodes can be depicted through the subsequent equation:



The increase in current values with higher scan rates during CV measurements can be attributed to the kinetic limitations of the electrochemical reactions occurring at the electrode-electrolyte interface. As the scan rate increases, the electrochemical processes may not have sufficient time to reach equilibrium, resulting in higher current values. The CV curves of electrodes developed with MnMoO₄ nanoparticles calcinated at 500 °C encompass a larger area than other electrodes, at all scan rates, revealing its higher charge-storage capacity. The variation of the specific capacity of all studied electrodes with scan rate is plotted in Fig. 5.6(e). It is inferred that the charge storage capacity of nanomaterials calcinated at 500°C has outperformed other electrodes under investigation, by more than twofold. At 10 mVs⁻¹, the same electrode exhibited an altitudinous-specific capacity of 1613 C g⁻¹ (2272.6 F g⁻¹) ascribed to the enlarged surface area provided by microporous nanorod morphology and electrical conductivity enhancement by Mo ions [134]. The fall of specific capacity of all electrodes at higher scan rates is ascribed to the swift to and fro movement of electrolyte ions, which leads to their limited interaction with the available electroactive surface area.

The galvanostatic charge-discharge (GCD) of electrodes prepared with MnMoO₄ nanoparticles calcinated at 300, 500, and 700 °C is displayed in Fig. 5.7(a–c). The quasi-symmetric GCD patterns reconfirmed the Faradic or battery-type nature of the electrode material. The prolonged discharging time of the electrode prepared with MnMoO₄ nanoparticles calcinated at 500 °C at all current densities inferring its high charge-storage capacity. The comparison of specific capacity of these electrodes at different current densities graphed in Fig. 5.7(d), validated the supremacy of the nanomaterial, which was treated at 500 °C attributed to the synergistic effect of Mn and Mo ions. At the current density of 2 A g⁻¹, this electrode demonstrated a soaring-specific capacity of 1549 C g⁻¹ (3688.09 F g⁻¹), which is more than double the value of other investigated electrodes, under the same conditions. The decrease in the specific capacity of all

electrodes at higher current densities is ascribed to the reduced diffusion of electrolyte ions in the deeper electroactive sites of the electrode material. The Nyquist plots of all studied electrodes are shown in Fig. 5.8, to elucidate their reaction kinetics. The impedance curve of the 500 °C treated electrode material has shown the largest slope at high frequency, among all assessed electrodes. This observation has given the initial indication of the high-rate charge-transfer phenomenon and rapid kinetics of the best-performing electrode. The proposed equivalent circuit is also portrayed in Fig. 5.8. The circuit [141] comprises equivalent resistance (R) linked in series with two other impedance components. The R depends upon interfacial contact resistance between the current collector and active material, Ni foam's internal resistance, and the electrolyte's ionic resistance [204]. The first impedance component has a capacitance (C1) and a Warburg (W) associated with bulk material, and the second impedance component representing grain boundaries contains a capacitance (C2) and a constant phase element (CPE). The impedances of bulk and grain boundaries are here associated with charge-transfer resistance (between the active material and electrolyte) and interfacial or Helmholtz boundaries, respectively. The impedance of constant phase element can be written as $Z_{CPE} = \omega^{-N}/A$, where, ω and N are angular frequency and distributing factor, respectively [205]. The fitted values of the equivalent circuit's component of all electrodes are presented in Table 5.1. The minimum value of R i.e., 623 m Ω suggests the good charge-transfer properties of the electrode prepared with MnMoO₄ nanoparticles calcinated at 500°C, as it was already evident from the CV and GCD analysis. This result is further confirmed by the value of charge-transfer resistance ~585 m Ω of the same electrode as can be seen from the inset of Fig. 5.8. The contribution of capacitances associated with bulk i.e., 926 μ F and grain boundaries i.e., 3.69 mF, are attributed to the enhanced surface area and smooth boundaries of the nanoparticles, respectively. The presence of Warburg i.e., 20.2 mMho, represents the diffusion of electrolyte ions in the microporous surface of the electrode material. Further, the mapped values of N were 0.23, inferring the resistive nature of the phase element. After a comparison of the fitted values of all studied electrodes, from Table 5.1 and from the inset of Fig. 5.8, it is observed that the nanomaterial treated at 500 °C displayed better reaction kinetics. Based on the above microstructural and electrochemical analysis, it can be deduced that the nanoparticles of MnMoO₄ calcinated at 500 °C attain the optimum size ~ 42 nm, which is appropriate to avail the maximum benefits of synergistic effect i.e., the optimized surface area associated with microporous morphology and conductivity enhancement by Mo ions.

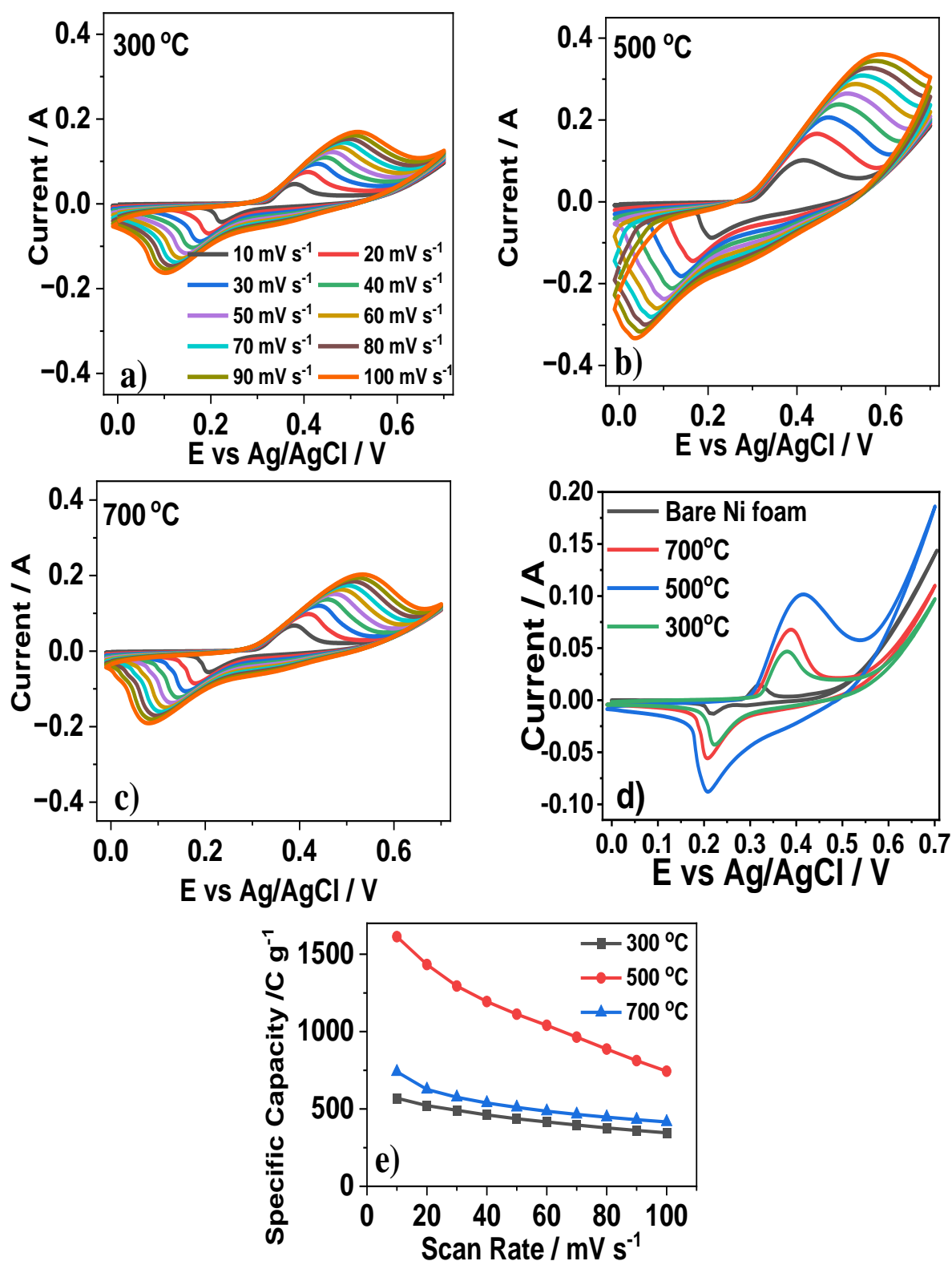


Fig. 5.6 a–c) The CV scans of electrodes prepared with MnMoO₄ nanoparticles calcinated at different temperatures, d) the comparison of CV scans of MnMoO₄ nanoparticle-based electrodes with bare nickel foam at 10 mV s⁻¹, and e) the variation of specific capacity of these electrodes with scan rate.

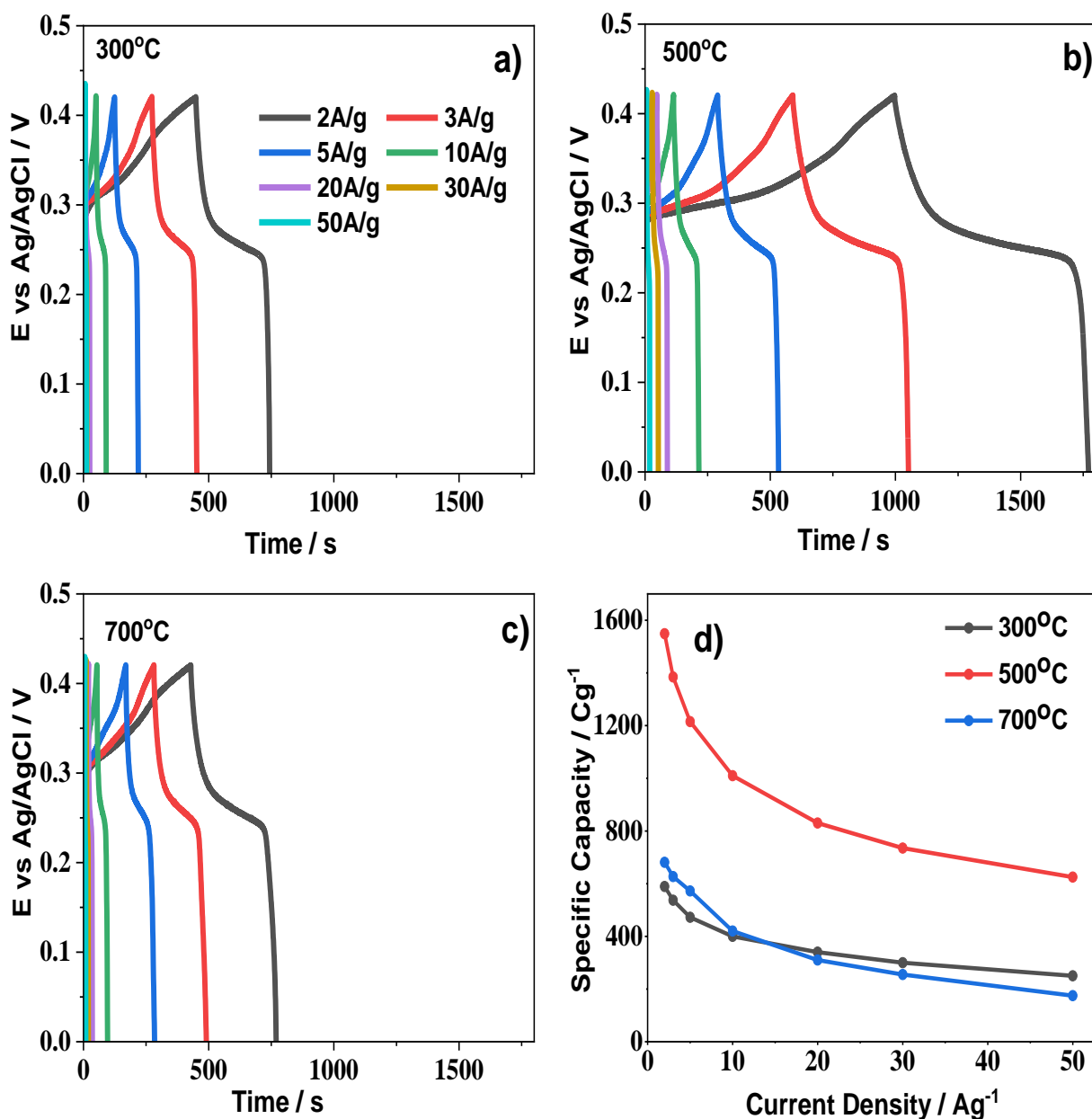


Fig. 5.7 a–c) The GCD curves of electrodes prepared with MnMoO₄ nanoparticles calcinated at different temperatures. d) the variation of the specific capacity of these electrodes with current density.

Table 5.1. The fitted values of the equivalent circuit's component of all electrodes

Sample calcinated at	R	C ₁	W	C ₂	CPE
300°C	816mΩ	1.67mF	6.23mMho	947μF	187mMho, N=0.327
500°C	623mΩ	926μF	20.2mMho	3.69mF	1.55mMho, N=0.236
700°C	897mΩ	557μF	20mMho	3.76mF	6.23mMho, N=0.332

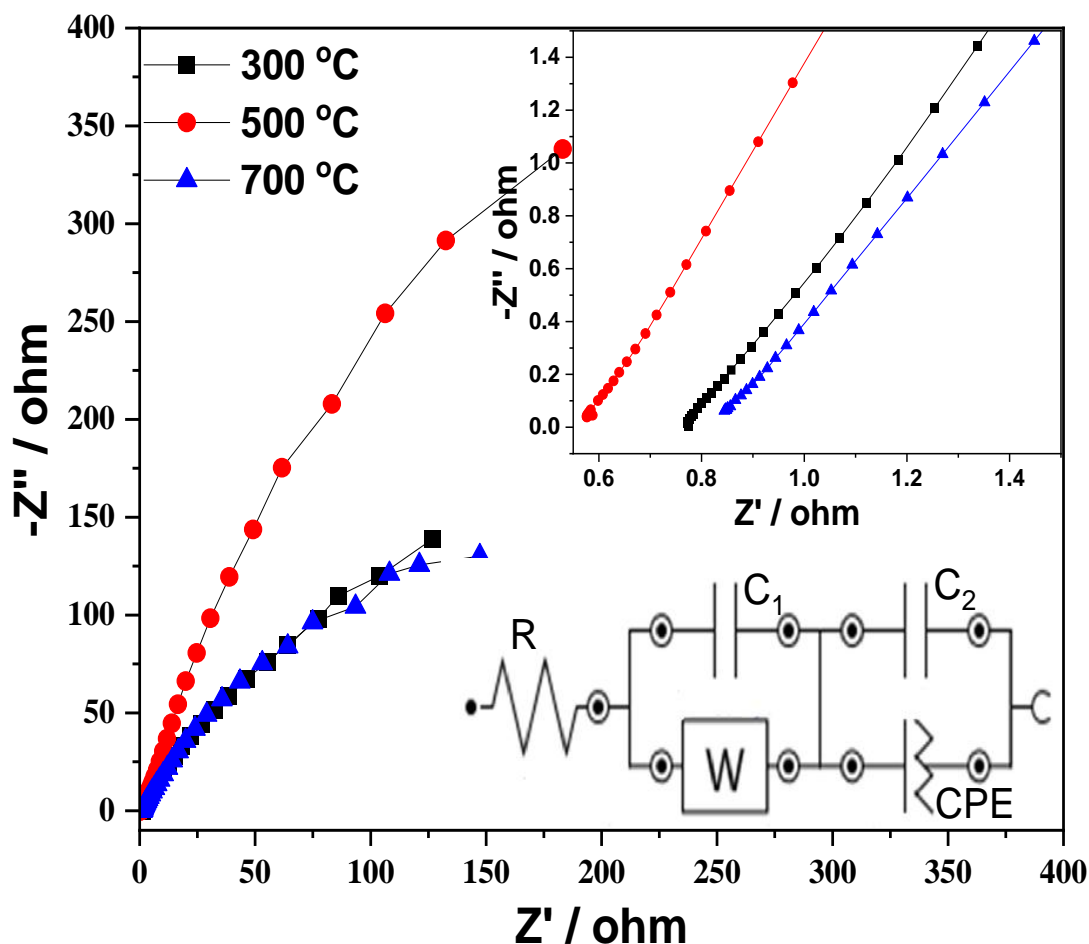


Fig. 5.8. The Nyquist plots of electrodes prepared with MnMoO_4 nanoparticles calcinated at different temperatures and the equivalent circuit. The inset displays the zoomed view of the high-frequency region.

The calcination of 300 °C is not enough to crystallize MnMoO_4 , so results in unevenly distributed smaller crystals with an open network, which restricts the ion/charge transfer. However, at 700 °C calcination, the size of crystals becomes larger, which reduces the electroactive surface area of the electrode material available for electrolyte interaction.

5.3. An Asymmetric Device Analysis

The empirical application of the MnMoO_4 nanoparticles-based electrode was assessed by fabricating an asymmetric supercapacitor device. The MnMoO_4 nanoparticles calcinated at 500 °C and activated carbon (AC) were deposited on Ni-foam (NF) i.e., $\text{MnMoO}_4\text{@NF//AC}$, as positive and negative electrodes, respectively, of the device. The PVA was considered as the separator and 3 M KOH as the electrolyte. The device's optimized potential window, i.e., 1.71 V, was decided from the CV scans recorded at the different potential windows by applying

the constant scan rate of 60 mV s^{-1} , as shown in Fig. 5.9(a). In Fig. 5.9(b), the CV scans of the device in the optimized potential window at different scan rates are displayed. Interestingly, the combination of Faradic and double-layer processes is responsible for the device's energy storage mechanism. The retention of the shape of the CV curves at all scan rates infers the magnificent rate performance of the asymmetric supercapacitor. The GCD curves at different current densities are exhibited in Fig. 5.9(c). The measured values of the specific capacitance from the discharging time of the device at 1, 2, 3, 5, and 10 Ag^{-1} were 167.6, 153.5, 137.6, 107.3, and 73 Fg^{-1} , respectively. Thus, the variation of power density and energy density of the device with current density is plotted in Fig. 5.9(d). The asymmetric device demonstrated an excellent energy density (E_g) of 68 W h kg^{-1} at a power density of 850 W kg^{-1} . To have a more accurate value, we have calculated integral energy density (E_I) as shown in Fig. 5.9(d). It is observed that the device exhibited a maximum energy density (E_I) of 49.3 Whkg^{-1} at a power density of 623 Wkg^{-1} . Additionally, it retained approximately 140% of its specific capacitance after 5,000 cycles, as shown in Fig. 5.9(e), demonstrating its exceptional cyclic stability. The initial rise in capacitance is ascribed to the sluggish activation of a large number of blocked electrochemically active sites. The Nyquist plots Fig. 5.9(f) of the asymmetric supercapacitor recorded before and after 5000 cycles ensured the minimal structural and morphological degradation of the deposited materials. Moreover, it is revealed that after 5000 cycles, the diffusion-based energy storage mechanism was improved considerably as can be seen from the larger slope at the lower frequency region of the Nyquist plot. The Ragone plot is presented in Fig. 5.10, to compare the present and reported work. It can be clearly seen that the fabricated $\text{MnMoO}_4\text{@NF//AC}$ asymmetric device has outperformed many previously reported similar devices.

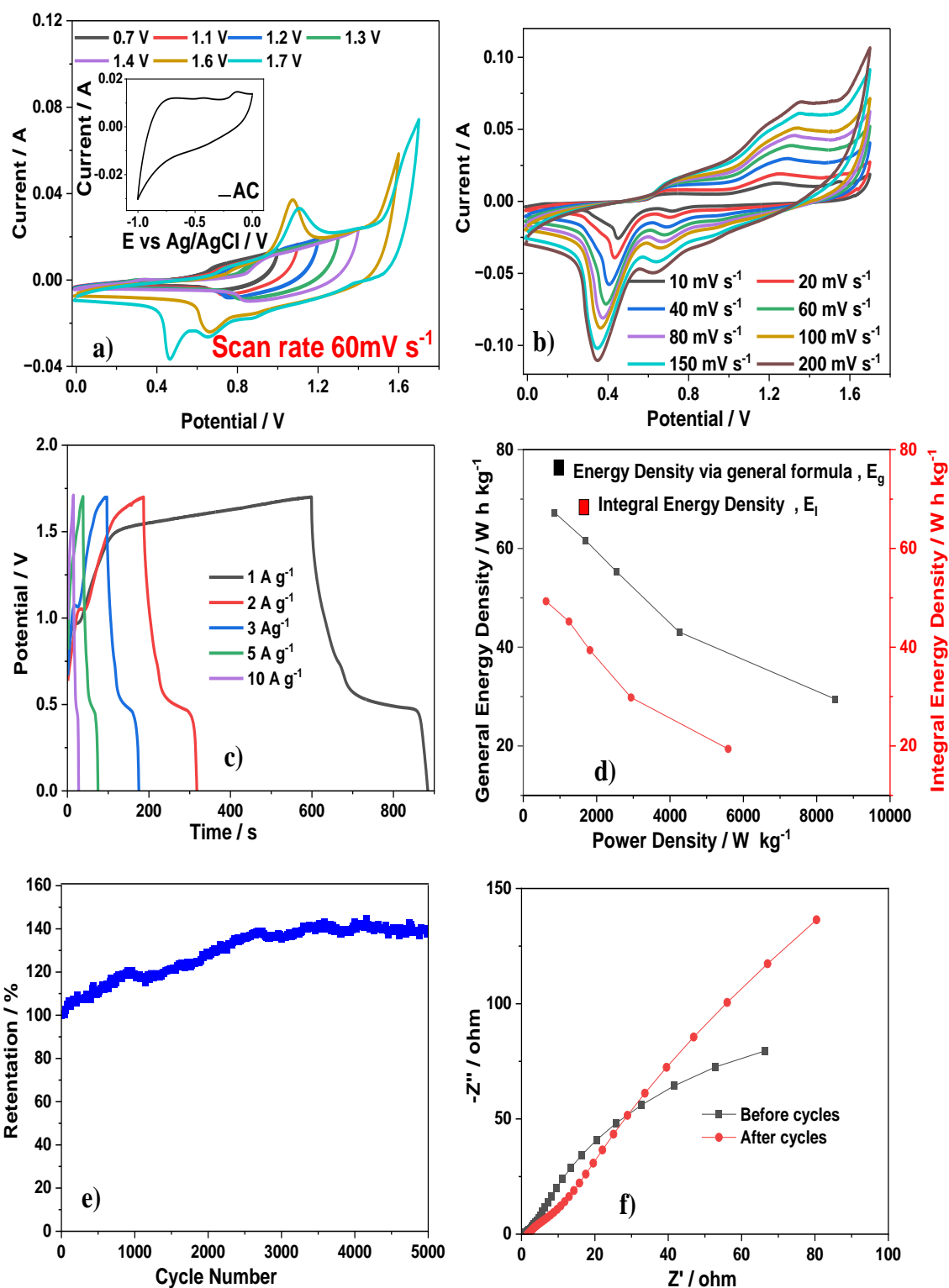


Fig.5.9. **a)** The CV curves at different voltage-widow (the CV data of bare activated carbon electrode is shown in inset), **b)** the CV curves at different scan rates, **c)** the GCD curves at different current densities, **d)** the variation of power density and energy density with current density, **e)** the variation of percentage-specific capacitance retention with cycle number and **f)** the Nyquist Plots, of the asymmetric device.

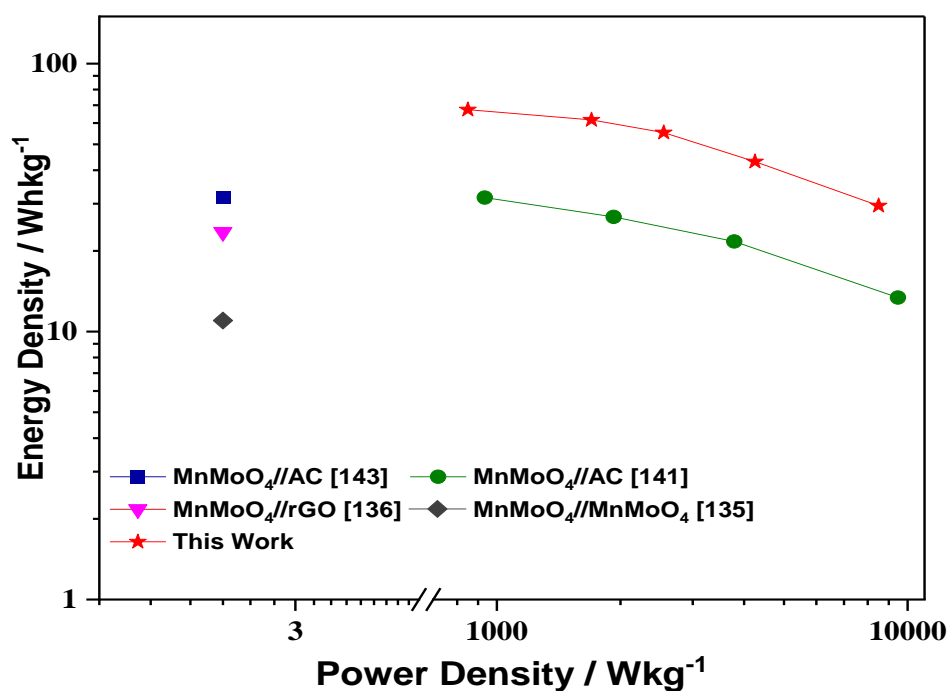


Fig.5.10. The Ragone plot

Conclusion

The MnMoO₄ nanoparticles were synthesized by a microwave-assisted facile and time-saving technique. The synthesized nanoparticles were calcinated at three different temperatures to vary their crystal size and morphology. A strong correlation between the calcination temperature and electrochemical performance of MnMoO₄ nanoparticles was found. The nanoparticles of MnMoO₄ calcinated at 500 °C were appropriate to avail the maximum benefits of synergistic effect i.e., the enlarged surface area associated with microporous morphology and conductivity enhancement by Mo ions. The optimized MnMoO₄ nanoparticles-based electrode demonstrated an altitudinous-specific capacity of 1613 Cg⁻¹ (2272.6 Fg⁻¹) and 1549 Cg⁻¹ (3688.09 Fg⁻¹) at 10 mVs⁻¹ and 2 Ag⁻¹, respectively. The asymmetric supercapacitor MnMoO₄@NF//AC@NF exhibited an excellent energy density of 68 Whkg⁻¹ at 850 Wkg⁻¹ (49.3 Whkg⁻¹ at 623 Wkg⁻¹ from gravimetric calculations) and outstanding cyclic stability even after 5000 cycles.

Chapter 6

Optimizing electrochemical performance: Investigating the influence of oxidation of graphene oxide in rGO@MnMoO₄

In recent decades, supercapacitors have garnered significant attention due to their remarkable long cycling life, high power density, fast charging-discharging rates, and eco-friendly nature [141]. The quest for high-performance supercapacitors hinges on the crucial role of electrode materials [32], which profoundly influences power density, operating voltage, energy density, and specific capacitance [206]. Consequently, an abundance of research has been dedicated to carbonaceous materials [207], including carbon nanotubes (CNT), graphene, reduced graphene oxide (rGO), and more, owing to their exceptional attributes such as high surface area and excellent conductivity. However, CNTs face a notable drawback: the challenge of uniform dispersion in solvents, leading to agglomeration [208]. Conversely, graphene oxide, adorned with diverse oxygen functionalities and wide optical band gap, remains electrically nonconductive [209]. On the other hand, rGO with an optical band gap ranging from 0.02 to 2 eV as reported by Shen et al., boasts high electrical conductivity, mechanical strength, a superior surface-to-volume ratio, and outstanding electrochemical properties [210]. Moreover, intriguing reports suggest that the optical, structural, and electrical properties of rGO can be artfully tailored, either by varying reaction time, reaction-temperature [211],[212],[213],[214],[215] or by employing different oxidizing agents [216]. In the realm of metal molybdates, such as CoMoO₄, NiMoO₄, MnMoO₄, and their composites, attention has surged due to their diverse oxidation states, and commendable thermal and chemical stability [161]. Among these, MnMoO₄ has garnered unique interest, boasting low cost, eco-friendliness, a wide working voltage range, and impressive catalytic and electrochemical characteristics [188]. However, the full potential of MnMoO₄ as an electrode material is restrained by its poor electron conduction [198].

One effective approach to address the limitations of diverse electrode materials is the development of multicomponent composites, capitalizing on synergistic effects to augment redox activity [217],[218],[219]. Thus, extensive research has focused on binary or ternary composites, aiming to tailor materials with desired properties. For instance, Thangapan et al. crafted a nanocomposite of MnMoO₄ and graphene, unveiling an electrode with a specific capacitance of 302 Fg⁻¹ at 0.1 Ag⁻¹

¹ and an energy density of 41.9 Whkg⁻¹ at 208 Whkg⁻¹ [162]. Similarly, Gosh et al. synthesized another captivating composite of MnMoO₄/graphene, revealing a specific capacitance of 364 Fg⁻¹ at 2Ag⁻¹ and a high energy density of 202 Whkg⁻¹ at 2000 Wkg⁻¹ in their half-cell characterization [144]. Meanwhile, Mu et al. ingeniously incorporated CNT/rGO to support MnMoO₄ on Ni foam, resulting in nanosheets with a specific capacitance of 2264.7 Fg⁻¹ at 15 mAcm⁻². Astonishingly, their asymmetric device, featuring CNT/rGO@MnMoO₄ as the positive electrode and activated carbon (AC)/CNT as the negative electrode, attained an impressive energy density of 59.4Whkg⁻¹ at 1367.9Wkg⁻¹ [153]. Furthermore, Rabbani et al. contributed to the frontier, presenting a Mn_{0.67}Ni_{0.37}MoO₄-RGO nanocomposite-based electrode, flaunting a specific capacity of 161.1 mAhg⁻¹ at 2Ag⁻¹ and an energy density of 87 Whkg⁻¹ at 1080 Wkg⁻¹ [207].

Based on the above literature survey, it is evident that the incorporation of carbonaceous materials into MnMoO₄ significantly enhances its electrochemical properties. In the pursuit of advancing this frontier, the present study delves into the impact of oxidation of controlled graphene oxide on the electrochemical performance of rGO@MnMoO₄-based composites. Furthermore, the optimization of the stoichiometric composition of GO in rGO@MnMoO₄-based composites is meticulously investigated and unveiled in this manuscript. Remarkably, to the best of our knowledge, such research has not been done so far. The controlled oxidation of GO significantly boosted the electrochemical performance of the rGO@MnMoO₄ composite. Optimized composition GO also played a vital role in achieving impressive outcomes. The optimized rGO@MnMoO₄ electrode exhibited a remarkable specific capacity of 1356Cg⁻¹ at 10mVs⁻¹ and 1299Cg⁻¹ at 2Ag⁻¹. These exceptional results stem from the synergistic effects between rGO and MnMoO₄. MnMoO₄'s microporous microrod morphology significantly increased electroactive surface area, while rGO improved electrical conductivity through abundant conjugated carbon bonds. Consequently, the asymmetric supercapacitor device demonstrated an impressive energy density of 63.5Whkg⁻¹ at a power density of 850Wkg⁻¹.

6.1. Structure and Microstructure Analysis

The XRD patterns of different GOs, prepared by varying their oxidation duration, are shown in Fig. 6.1. As a reference, the diffraction pattern of graphite powder is also included. The diffraction patterns of graphene oxides synthesized at different varying stirring durations: 1 hour, 2 hours, 4 hours, 6 hours, and 8 hours, designated as G1, G2, G4, G6, and G8, respectively samples exhibited

characteristic peaks of graphene oxide at $2\theta = 9.53^\circ$, 8.27° , 10.31° , 9.12° , and 9.37° . The absence of the distinctive peak of graphite at 26.5° in all these curves suggests the complete transformation of graphite powder into graphene oxide. The positions of these characteristic peaks indicate larger interplanar spacing between the GO layers due to the assimilation of oxygen functional groups and exfoliation of graphitic planes. The structural parameters of GO samples with different levels of oxidation are shown in Table 6.1. It is observed that the crystallite size varied with the oxidation duration of GO, reaching its maximum value of 97.4 \AA after four hours of oxidation [220]. This variation in the crystallite size of the GO can be attributed to the complex interplay of several factors during the oxidation process. In the early stages of oxidation, oxygen-containing functional groups, such as epoxide and hydroxyl groups, might be introduced into the GO structure. These groups disrupt the sp^2 carbon-carbon bonds and introduce disorder into the GO layers. This disorder could be the reason behind the reduced size of crystallites.

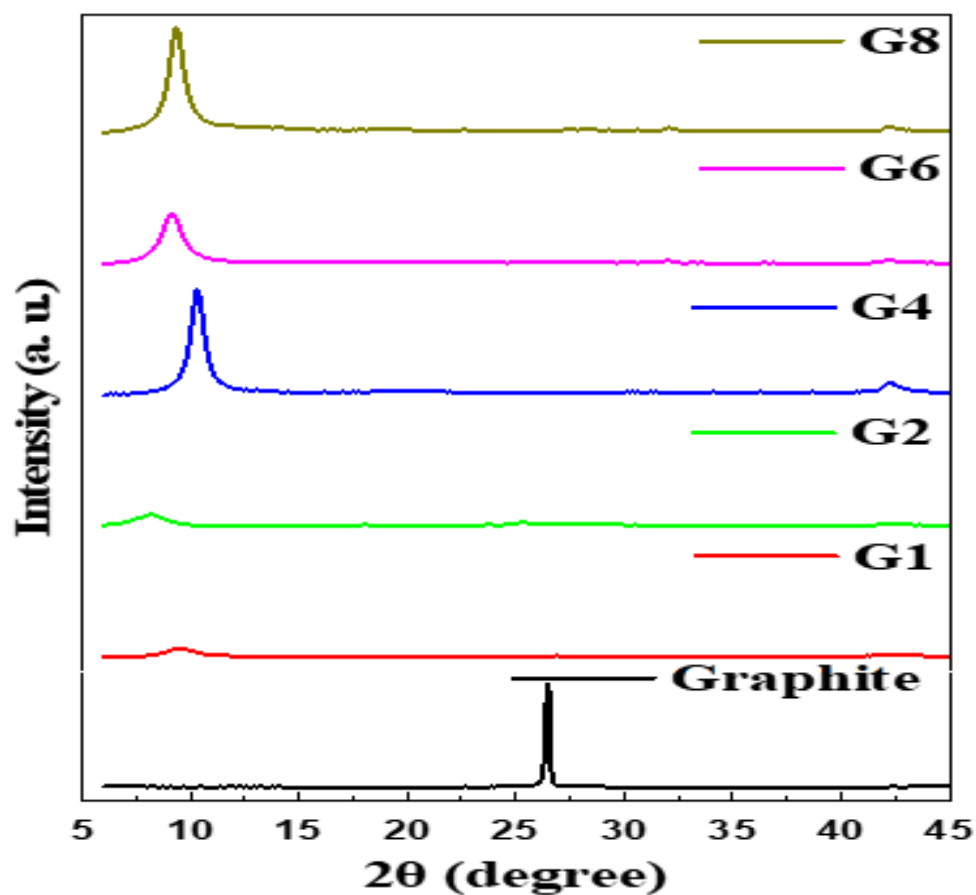


Fig.6.1. XRD spectra of graphene oxide synthesized with different oxidation duration.

Table 6.1. The structural parameters of GO samples with different levels of oxidation.

Sr. No.	Sample	2 Theta (Degree)	Interplanar spacing (nm)	Crystallite Size (Å)
1	G1	9.5	0.93	30.6
2	G2	8.3	1.07	26.1
3	G4	10.3	0.86	97.4
4	G6	9.1	0.97	58.9
5	G8	9.4	0.94	90.3
6	Graphite	26.5	0.34	371.1

At four hours of oxidation, it may have reached a point where some of the introduced defects and disorders begin to heal. This could happen through the removal of oxygen groups and the restoration of sp^2 carbon-carbon bonds. Due to the partial reestablishment of structural order, the crystallite size might have been increased [221]. However, with extended oxidation times, the introduction of excessive oxygen groups can further disrupt the crystalline order, potentially leading to over-oxidation and a decrease in crystallite size. The observed variation in diffraction intensity in the synthesized GO samples could be attributed to structural changes, including alterations in layer thickness, or structural disorder. The weak peaks around 42° in the XRD spectra of GO indicate the presence of turbostratic structures of disordered carbon materials [211].

Fig. 6.2 (a), displays the Raman spectra of all samples of GO. The D and G bands of the G1 sample are located at 1350 cm^{-1} and 1603 cm^{-1} , respectively, confirming the formation of GO. The intensity ratio of D and G bands (I_D/I_G) increased with the increase of oxidation duration, suggesting the addition of defects in GO upon longer oxidation. The G band position of the G1 sample at 1603 cm^{-1} indicates the presence of carbon double bonds ($C=C$) of unmodified graphite contents [222]. The shifting of this G band towards the lower wavenumber side of the spectrum, from 1603 cm^{-1} to 1577 cm^{-1} , is ascribed to the enhanced oxidation of carbon contents with an increase in stirring time.

In Fig. 6.2(b), the FTIR spectra of all GO samples are displayed, validating the successful assimilation of various oxygen-associated functional groups to varying extents on the graphite layers after oxidation. The absorption bands at 570 , 866 , 1041 , 1207 , 1395 , 1614 , and 1710 cm^{-1} , assigned to the stretching vibrations of C-H, C-O-H, C-O-C, C-O, C=O, C=C, and COOH groups, respectively, are characteristic peaks of GO [223],[224]. The presence of considerable C=C groups in the G4 sample is evident from the position of the G band in the Raman spectrum at 1602 cm^{-1}

and the distinctive absorption band in the FTIR spectrum at 1614 cm^{-1} , suggesting its better electrical conductivity compared to other GO samples.

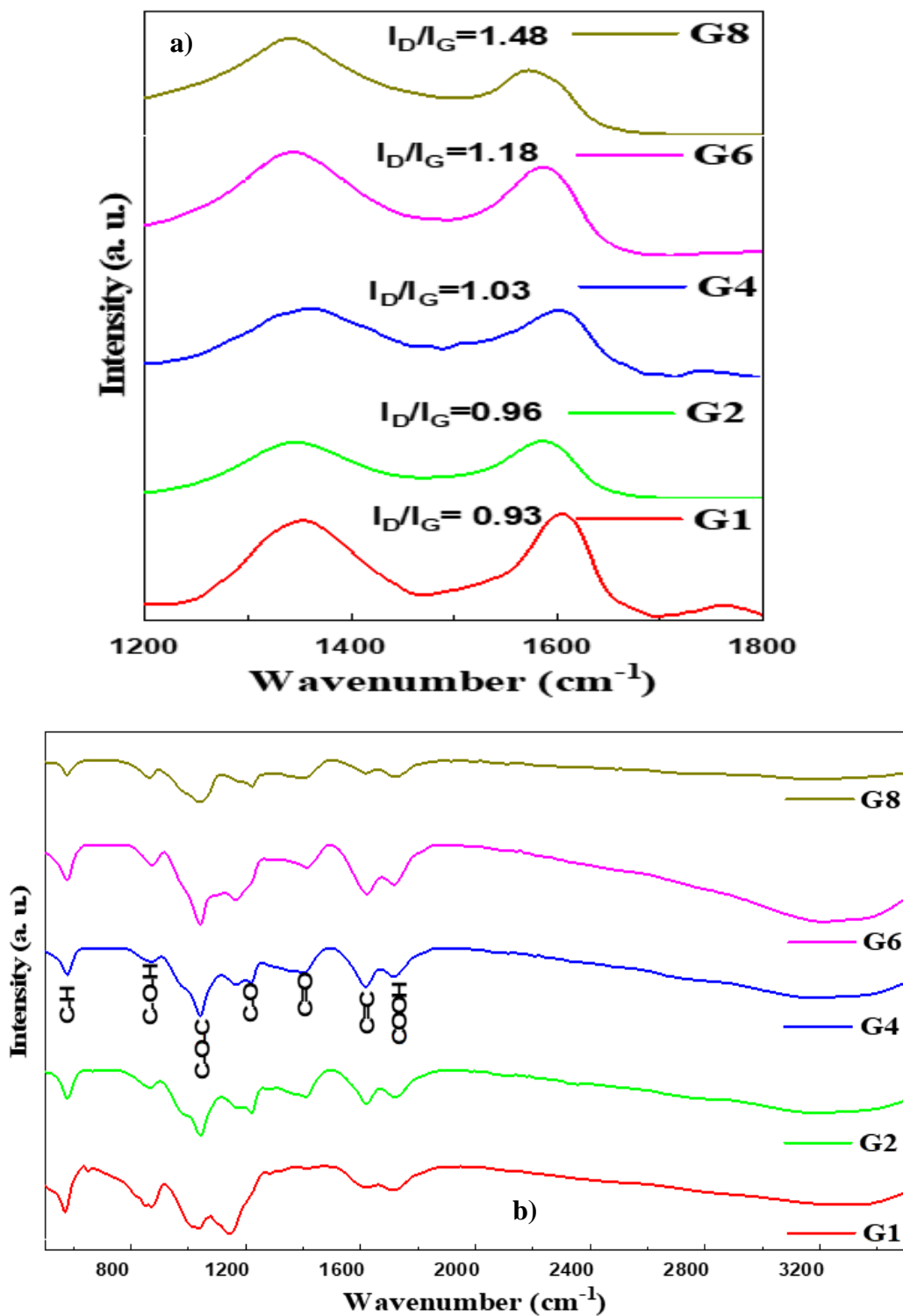


Fig.6.2. a) Raman and b) FTIR spectra of graphene oxide synthesized with different oxidation duration.

All of these GO samples were utilized to prepare composites with MnMoO_4 , referred to as rGO@MnMoO_4 . These rGO@MnMoO_4 composites, synthesized with GO of varying oxidation durations, were designated as A1, A2, A4, A6, and A8, respectively. In Fig. 6.3, the XRD patterns of different rGO@MnMoO_4 composites are presented. The XRD diffraction pattern of all composites closely resembles that of JCPDS: 78-0220, indicating the formation of Manganese Molybdate hydrate, i.e., $\text{Mn}(\text{MoO}_4)(\text{H}_2\text{O})$.

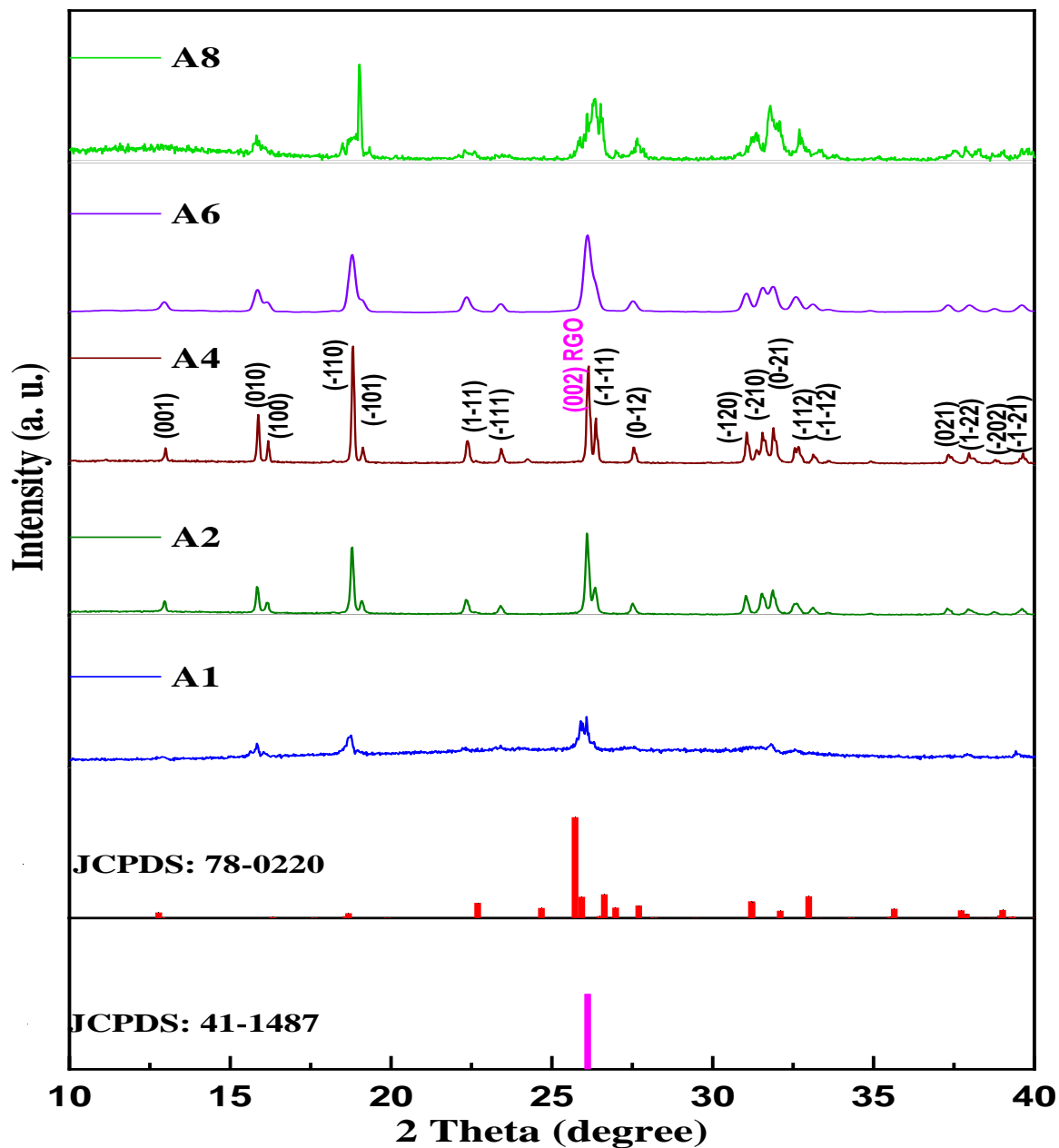


Fig. 6.3. The diffraction patterns of different rGO@MnMoO_4 composites.

The absence of any diffraction peak between 9° to 11° suggests the absence of GO in composites. The high pressure and temperature during the hydrothermal process likely converted the graphene oxide to reduced graphene oxide (rGO). Consequently, a strong diffraction peak appeared at 26.2° , representing the (002) plane of rGO (JCPDS: 41-1487), which overlapped with the (-1-11) plane of MnMoO_4 located at 26.4° [207]. It is observed that all peaks of MnMoO_4 and rGO are noticeable in all the curves, but they are more prominent in those of A2 and A4 samples. Furthermore, the primary peak of rGO at 26.2° in the A4 sample is more intense and prominent, clearly indicating the formation of well-reduced GO in the composite. Here, GO served as a scaffold for the growth of MnMoO_4 microparticles and played a crucial role in determining the properties of the composites. The varying oxidation durations of GO in A1, A2, A4, A6, and A8 led to differences in the structure and properties of the resulting composites. From Fig. 6.3, it can be seen that A4 represents the composite with an oxidation duration of GO that strikes the right balance. It is neither under-oxidized nor over-oxidized. The growth of MnMoO_4 microparticles on the GO scaffold in A4 is likely well-controlled and uniform, with optimized structural integrity, defects, and an appropriate level of oxygen-containing functional groups, which possibly provides a large surface area for electrochemical reactions and efficient charge transport.

In the Raman spectrum Fig.6.4(a) of the rGO@MnMoO_4 composite, the bands between 800 to 950 cm^{-1} are attributed to characteristic A_g and $B_g(+A_g)$ stretching vibrations, respectively, and the band at 337 cm^{-1} represents the $A_g(+B_g)$ bending vibrations of MoO_4 ions [190]. The Raman active D and G bands of rGO were centered at 1347 and 1600 cm^{-1} , respectively. The ID/IG ratio value, i.e., 1.12, suggests the dominance of defects, and the location of the G band at 1600 cm^{-1} indicates the considerable presence of conjugated carbon bonds, implying the better electrical conductivity of rGO. The synthesis of the rGO@MnMoO_4 composite is further evident from its FTIR spectrum as shown in Fig.6.4(b). The absorption bands at 779 , 890 , and 935 cm^{-1} are characteristic bands of MnMoO_4 , attributed to Mo-O stretching, Mo-O-Mo bending, and Mo=O stretching vibrations, respectively, of MoO_4 [144]. However, the absorption bands at 587 , 1072 , 1221 , and 1614 cm^{-1} are attributed to vibrations of C-H, C-O-C, C-O, and C=C groups, respectively, of rGO. These comprehensive characterizations affirm the successful formation of the rGO@MnMoO_4 composite, laying the groundwork for its potential applications in advanced energy storage systems.

The FESEM images of the rGO@MnMoO₄ (A4) composite at different magnifications and its EDS mapping are presented in Fig. 6.5(a-e). It is evident that the composite uniformly covers the Ni-foam substrate, showcasing multiple morphologies of irregular sizes and shapes, including entangled micro rods with distinct edges. These micro rods are likely representative of MnMoO₄, as a similar nanoribbon morphology of the same material was observed in our previous work [196].

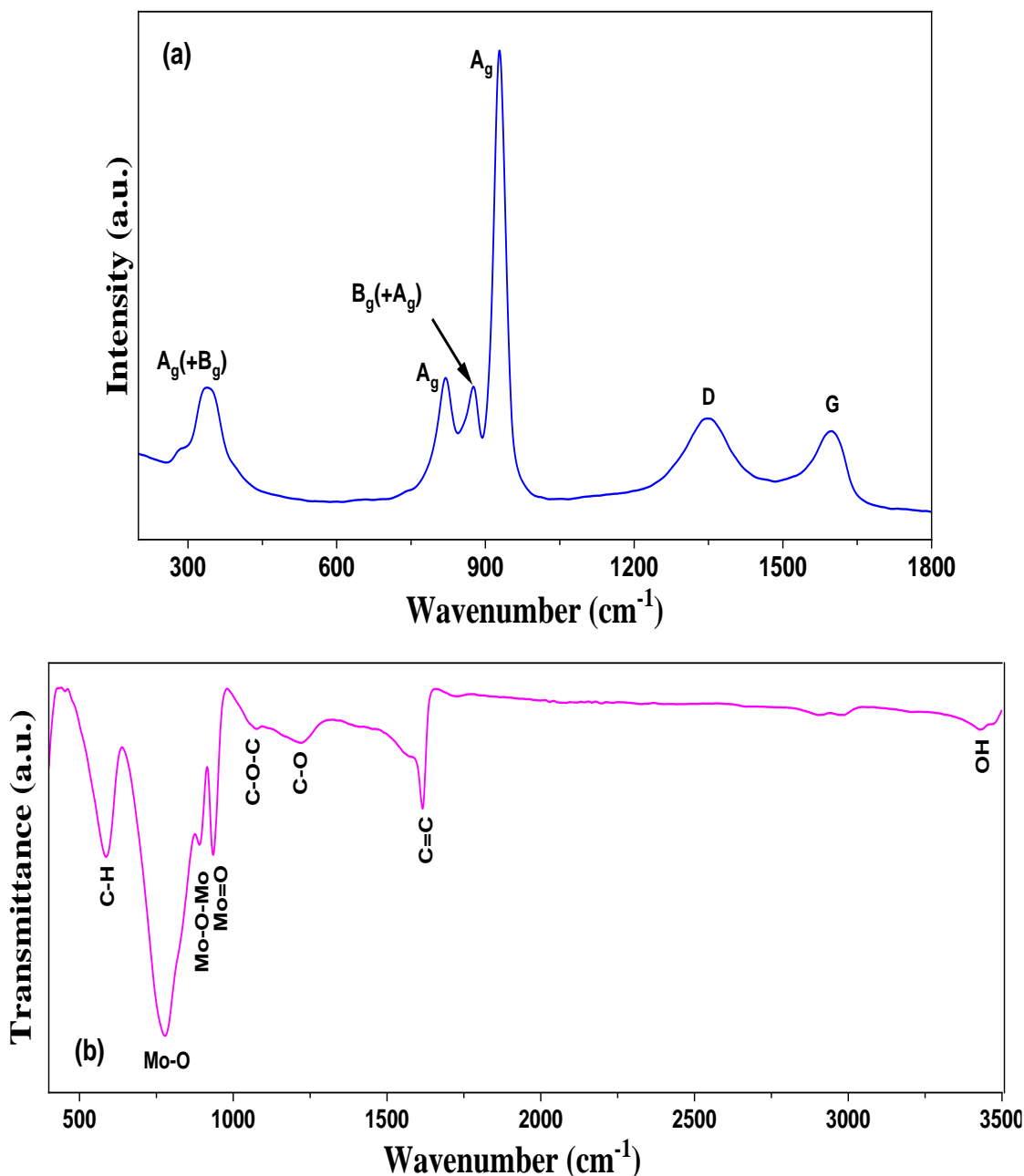


Fig. 6.4. The Raman **a)** and FTIR **b)** spectra of rGO@MnMoO₄ (A4) composite.

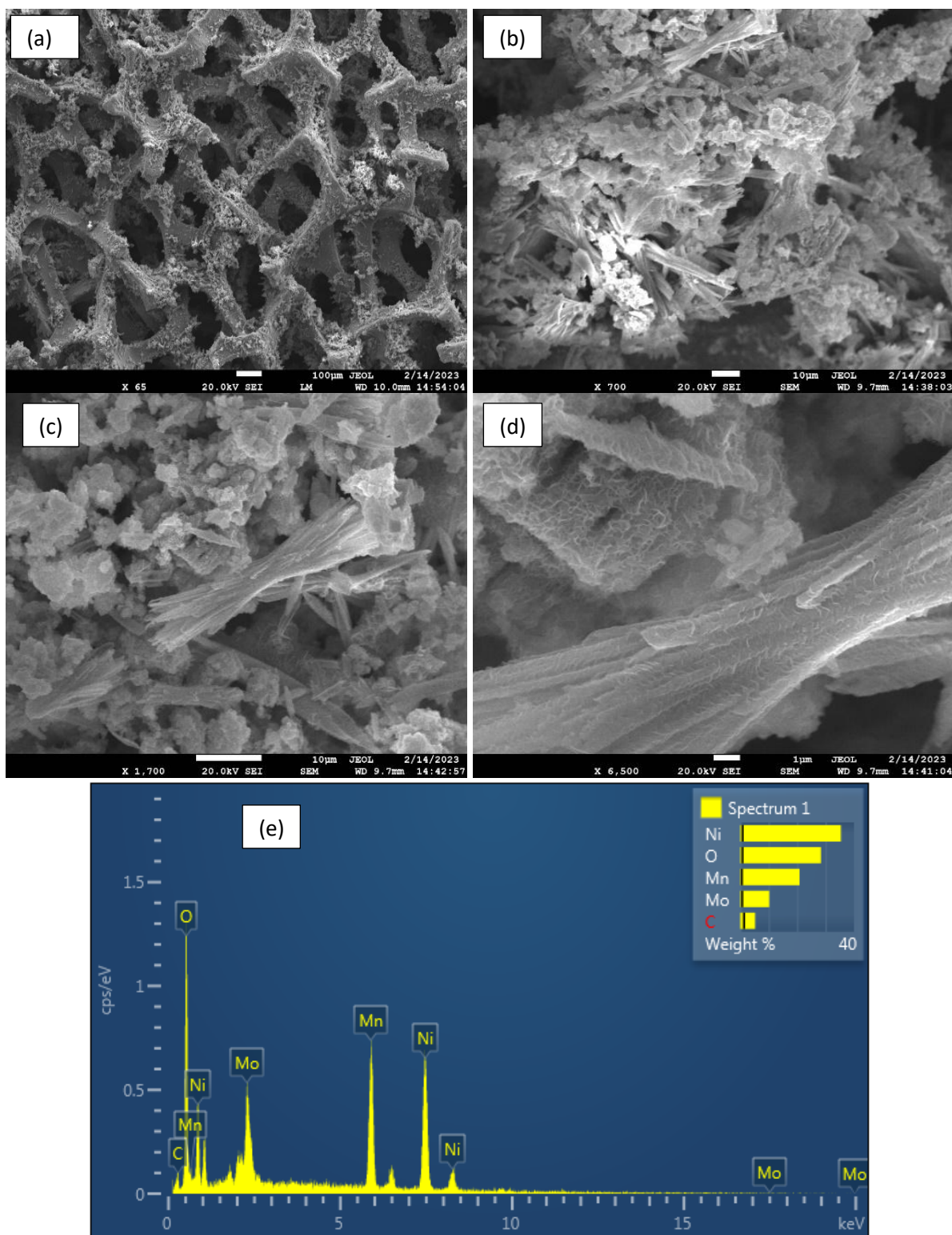


Fig. 6.5. The FESEM images **a-d**), EDS mapping **e**) of rGO@MnMoO₄ (A4) composite.

The surface analysis of the A4 sample was conducted using the Brunauer, Emmett, and Teller (BET) method. The N₂ adsorption-desorption isotherm, as shown in Fig. 6.6(a-b), exhibits a well-defined hysteresis loop. The isotherm resembles the H3-type hysteresis loop. An open end in the hysteresis loop at lower pressures during desorption indicates that the gas molecules exit the pores. The measured BET surface area was 26.3 m²g⁻¹, which exceeds the previously reported result [144]. Furthermore, the Barrett-Joyner-Halenda (BJH) pore size distribution plot of the A4 sample, also displayed in Fig. 6.6(b), reveals an average pore diameter of 1.5nm, indicating its microporous nature. The enlarged microporous surface area, coupled with enhanced conductivity due to the considerable presence of C=C bonds, suggests the immense potential of the rGO@MnMoO₄ composite as an efficient electrode material for enhanced energy storage applications. The unique combination of morphology, surface area, and electrical conductivity makes it a promising candidate as an efficient electrode material for advanced energy storage systems.

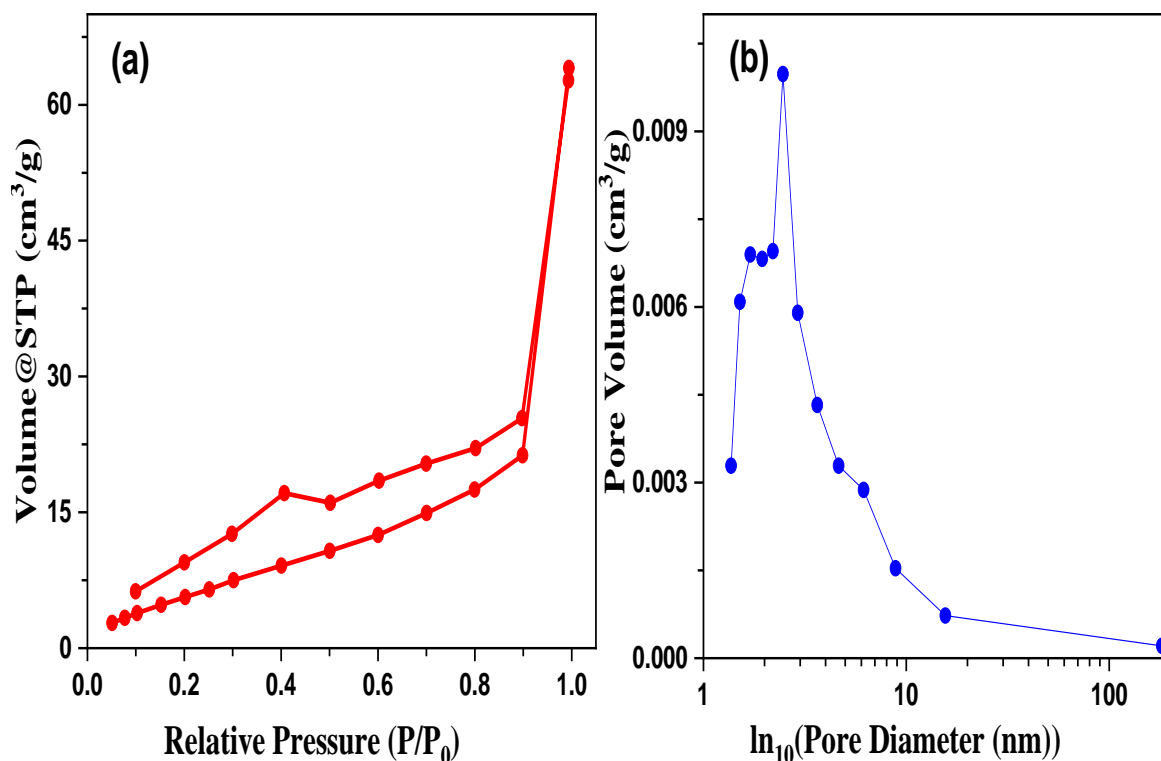


Fig. 6.6. The Nitrogen adsorption-desorption isotherm **a)**, and the graph between pore volume with pore radius **b)** of rGO@MnMoO₄ (A4) composite.

The XPS analysis was conducted to assess the oxidation states and elemental composition of the rGO@MnMoO₄ (A4) composite. To address this, the XPS analysis of the rGO@MnMoO₄ (A4) composite was conducted to thoroughly investigate its oxidation states, elemental composition, and chemical bonding environments. The binding energy values obtained from the experimental data closely align with standard reference values from the International XPS Library, confirming the reliability and consistency of the synthesized MnMoO₄ phase. In the wide-range

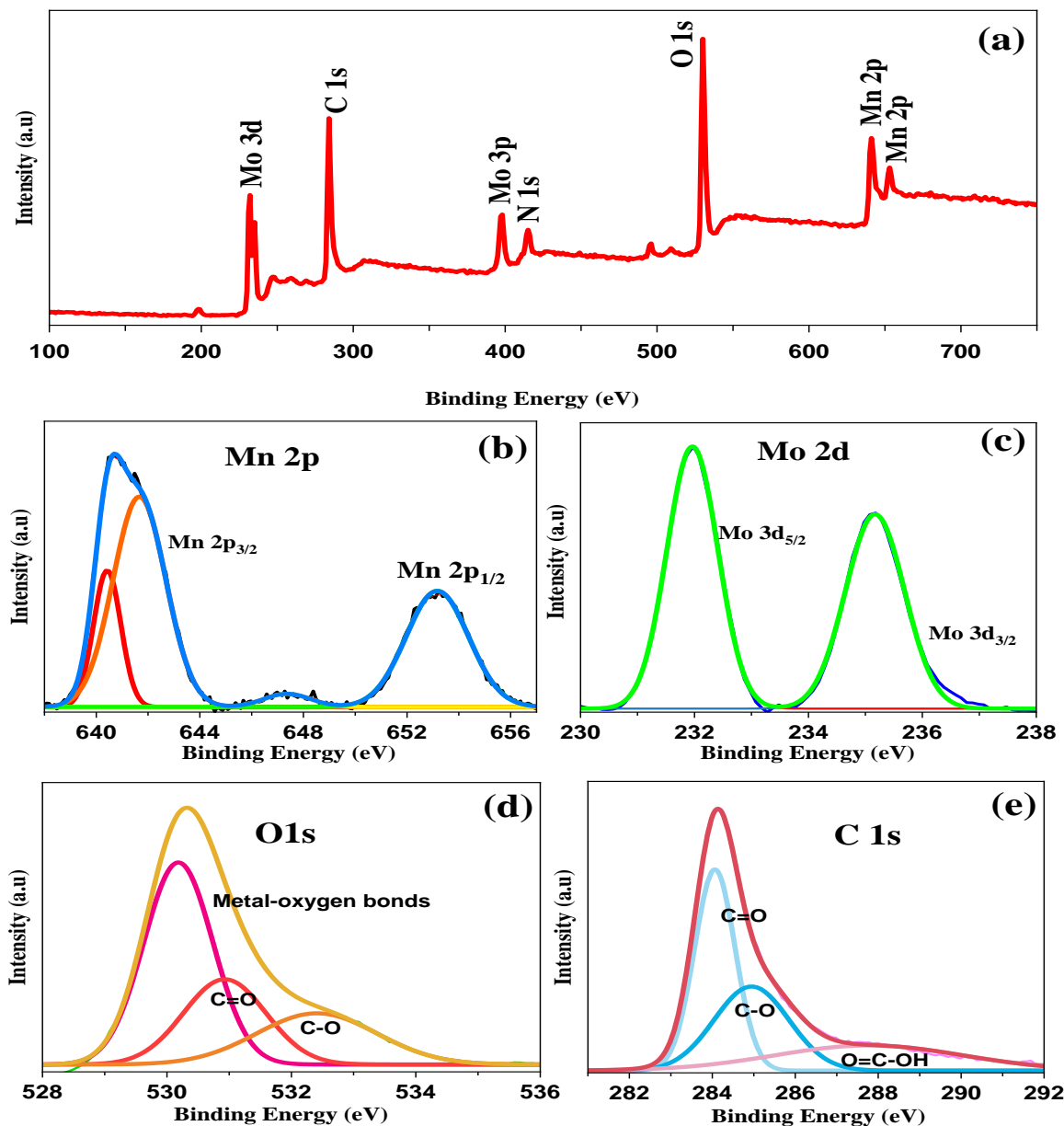


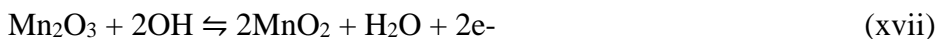
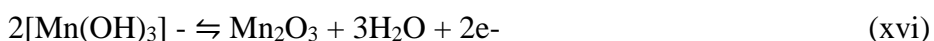
Fig. 6.7. The XPS survey spectrum **a)** and core spectra **b-e)** of rGO@MnMoO₄ (A4) composite.

survey of the A4 sample, displayed in Fig. 6.7(a), four peaks at 640.7, 530.3, 284.1, and 231.9 eV correspond to Mn 2p, O 1s, C 1s, and Mo 3d, respectively. The core-level spectrum of Mn 2p presented in Fig. 6.7(b) exhibits two binding energy peaks at 640.7 and 653.2 eV, corresponding to Mn 2p_{3/2} and Mn 2p_{1/2}, respectively. The separation between the two peaks, 12.5 eV, suggests the '+2' oxidation state of Mn. Another doublet in the core-level spectrum of Mo 3d Fig. 6.7(c), at 231.9 eV and 235.1 eV, is ascribed to Mo 3d_{5/2} and Mo 3d_{3/2}, respectively, indicating the '+6' oxidation state of Mo indicating the structural stability of MnMoO₄. The high-resolution scan of O1s in Fig. 6.7(d) can be deconvoluted into three peaks at 530.1, 531.0, and 532.4 eV, attributed to metal-oxygen bonds, C=O, and C-O bonds of rGO, respectively. The deconvolution of the main peak of C1s Fig. 6.7(e) leads to three peaks at 284.0, 284.9, and 287.7 eV, corresponding to C=O, C-O, and O=C-OH bonds, respectively [225]. According to the semi-quantitative analysis, the carbon-to-oxygen (C/O) ratio of the synthesized composite was found to be 1.9, including the oxygen contents of MnMoO₄. This result further confirms the findings of the XRD analysis regarding the transformation of GO to rGO during the hydrothermal process.

6.2. Electrochemical analysis

The potential of various rGO@MnMoO₄ composites, namely A1, A2, A4, A6, and A8, as efficient electrode materials, was assessed using a three-electrode setup with 3M KOH as the electrolyte. The composites were directly grown on Ni-foam to avoid any adverse effects of binders. The cyclic voltammetry (CV) scans of these samples at different scan rates are presented in Fig. 6.8(a-e).

The suggested electrochemical reactions occurring in KOH involving Rgo@MnMoO₄ electrodes can be depicted through the subsequent equation:



In all CV scans, a pair of redox peaks is observed, indicating their Faradic nature, possibly associated with the reversible electron movement between +2 and +3 oxidation states of Mn. The shifting of reduction and oxidation peaks towards higher and lower potentials, respectively, is attributed to reduced ion diffusion at higher scan rates. Remarkably, all electrodes maintain the shape of the CV curves even at 100mVs⁻¹, indicating their robustness in facilitating rapid charge transfer processes. As shown in Fig. 6.8(f), the area enclosed by the CV curve of the A4 electrode

at a scan rate of 10 mV/s was larger than that of the other electrodes, indicating its higher specific capacity. The comparison of specific capacity variation of these rGO@MnMoO₄ composite-based electrodes at different scan rates is depicted in Fig. 6.8(g). It is evident that the binder-free A4 electrode exhibited significantly superior specific capacity compared to A1, A2, A6, and A8 electrodes. The maximum specific capacity displayed by the A4 electrode through cyclic voltammetry was an impressive 1356Cg⁻¹ at 10mVs⁻¹.

The galvanostatic charge/discharge (GCD) behavior of different rGO@MnMoO₄ composite-based electrodes within the 0 to 0.42V potential window is depicted in Fig. 6.9(a-e). The near-symmetrical charging-discharging profile of all these electrodes, along with the presence of a plateau in the discharging curves, indicates their typical Faradic capacitive nature. Notably, 6.9(f) illustrates that the charging and discharging duration of the A4 electrode is longer than that of the A1, A2, A6, and A8 electrodes. At 2Ag⁻¹, the A4 electrode exhibited a discharging time of 650s, showcasing its impressive specific capacity of 1299Cg⁻¹. The comparison of specific capacities of these electrodes at different current densities, as shown in Fig. 6.9(g), clearly reveals that the A4 electrode outperforms the others. These results, combined with the findings from the CV analysis, lead to the conclusion that the GO prepared with a 4-hour stirring duration is the most suitable graphene oxide for rGO@MnMoO₄-based composites, offering enhanced electrochemical applications. The enhanced electrical conductivity of GO (G4) may have synergistically contributed to the enlarged surface area of microporous MnMoO₄ micro rods, resulting in considerable capacitance improvement of the composite material. Moreover, the decrease in specific capacity of all electrodes at higher scan rates Fig. 6.8 and current densities Fig. 6.9 can be attributed to reduced redox kinetics due to the limited diffusion of electrolyte ions in the active sites of the electrode.

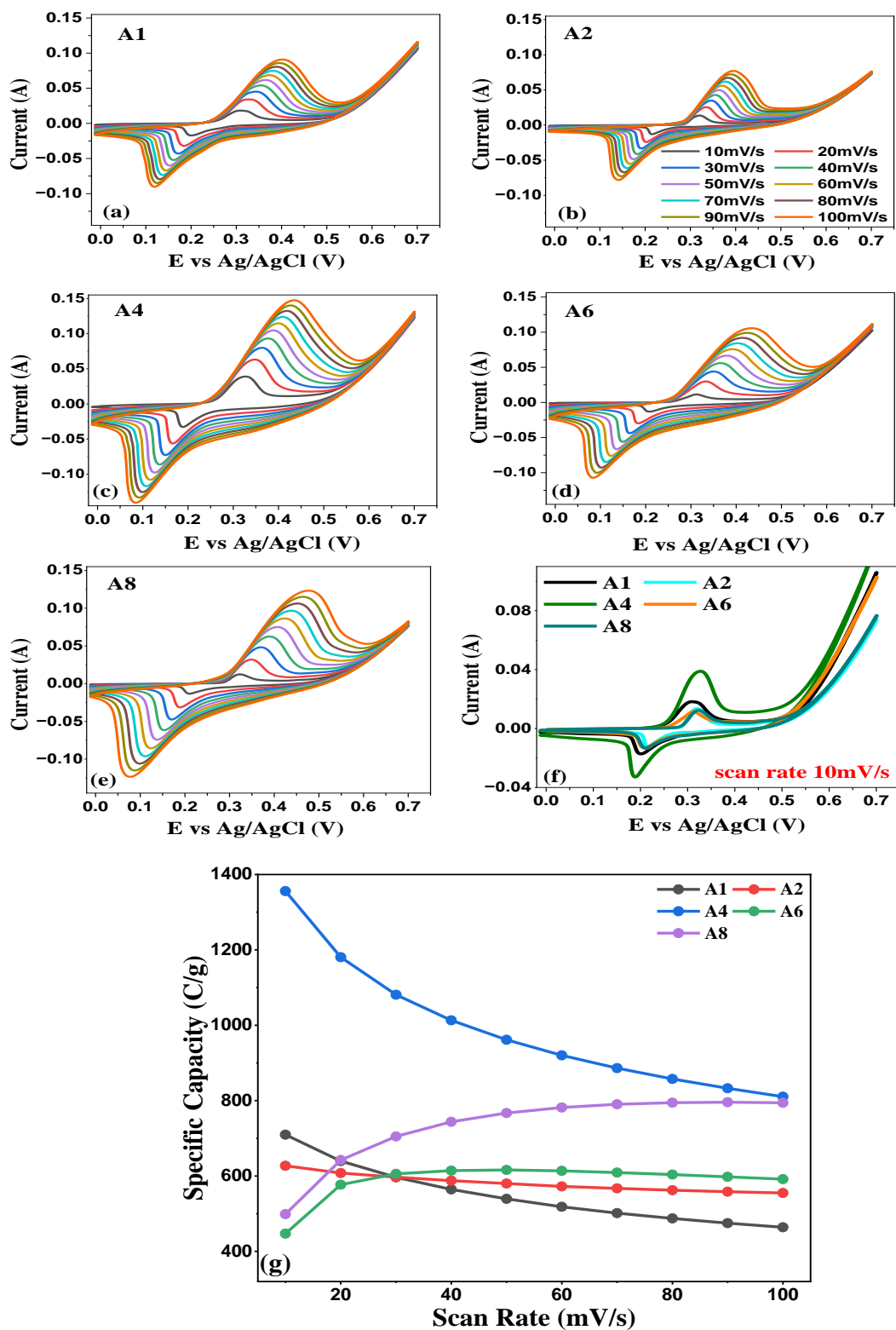


Fig. 6.8. The CV scans of different rGO@MnMoO₄ composites **a-e**) at different scan rates and their comparison **f**) at scan rate 10mV/s. The variation **g**) of specific capacity of different rGO@MnMoO₄ composites with scan rates.

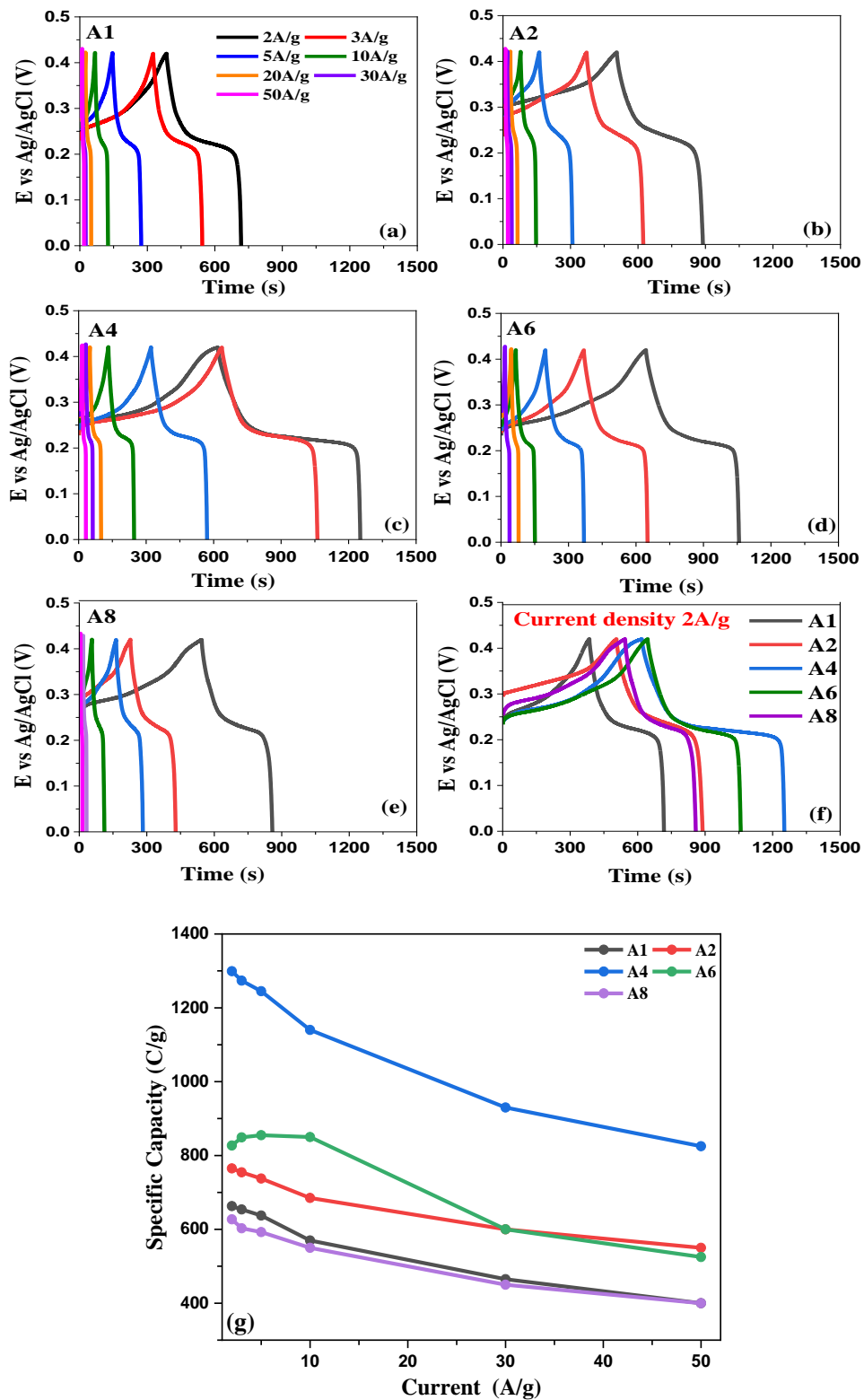


Fig. 6.9. The GCD curves of different rGO@MnMoO₄ composites a-e) at different current densities and their comparison f) at current density 2 A/g. The variation g) of specific capacity of different rGO@MnMoO₄ composites with current density.

6.2.1. Comparative study of rGO@MnMoO₄ at different graphene oxide concentrations

To further enhance the performance of the A4 sample, the effect of GO (G4) composition in the rGO@MnMoO₄ (A4) composite was investigated. The composites grown on Ni-foam with different concentrations of GO(G4) i.e. 0.4, 0.8, 1.6, and 3.2 mg in the reaction mixture of MnCl₂.4H₂O and Na₂MoO₄.2H₂O were separately labeled as B1, B2, B3, and B4, respectively. The comparison of CV scans of rGO@MnMoO₄ composite with varying concentrations of GO(G4) is depicted in Fig. 6.10(a). It is observed that the area under the CV curve of the B3 electrode at 10mVs⁻¹ is larger than that of other B-series electrodes, specifying its higher charge-storing capability. The B3 electrode exhibited a magnificent specific capacity of 1356Cg⁻¹ at 10mVs⁻¹ Fig. 6.10(b). Fig. 6.10(b) further illustrates the variation of the specific capacity of these electrodes with scan rate. Notably, the B3 electrode demonstrated a higher specific capacity at lower scan rates, while at higher scan rates, B2 performed well. The charging and discharging patterns of these B-series electrodes and their variation of specific capacities at different current densities (Fig. 6.10(c) and 6.10(d), respectively) revealed that the B3-electrode displayed the highest specific capacity at all current densities. Specifically, the B3 electrode exhibited an overwhelming specific capacity of 1299Cg⁻¹ at 2Ag⁻¹. These findings suggest that the addition of 1.6mg of GO(G4) in the rGO@MnMoO₄ composite is the most optimized composition. Furthermore, comparing the electrochemical performance of MnMoO₄ and carbonaceous material-based composites in Table 6.2., it becomes evident that the most optimized rGO@MnMoO₄ composite-based electrode in this investigation has outperformed other reported electrodes prepared with similar composition. To comprehend the reaction kinetics, the Nyquist Plot of the most efficient B3-electrode was recorded between 0.01 Hz to 100 kHz and presented in Fig. 6.10(e).

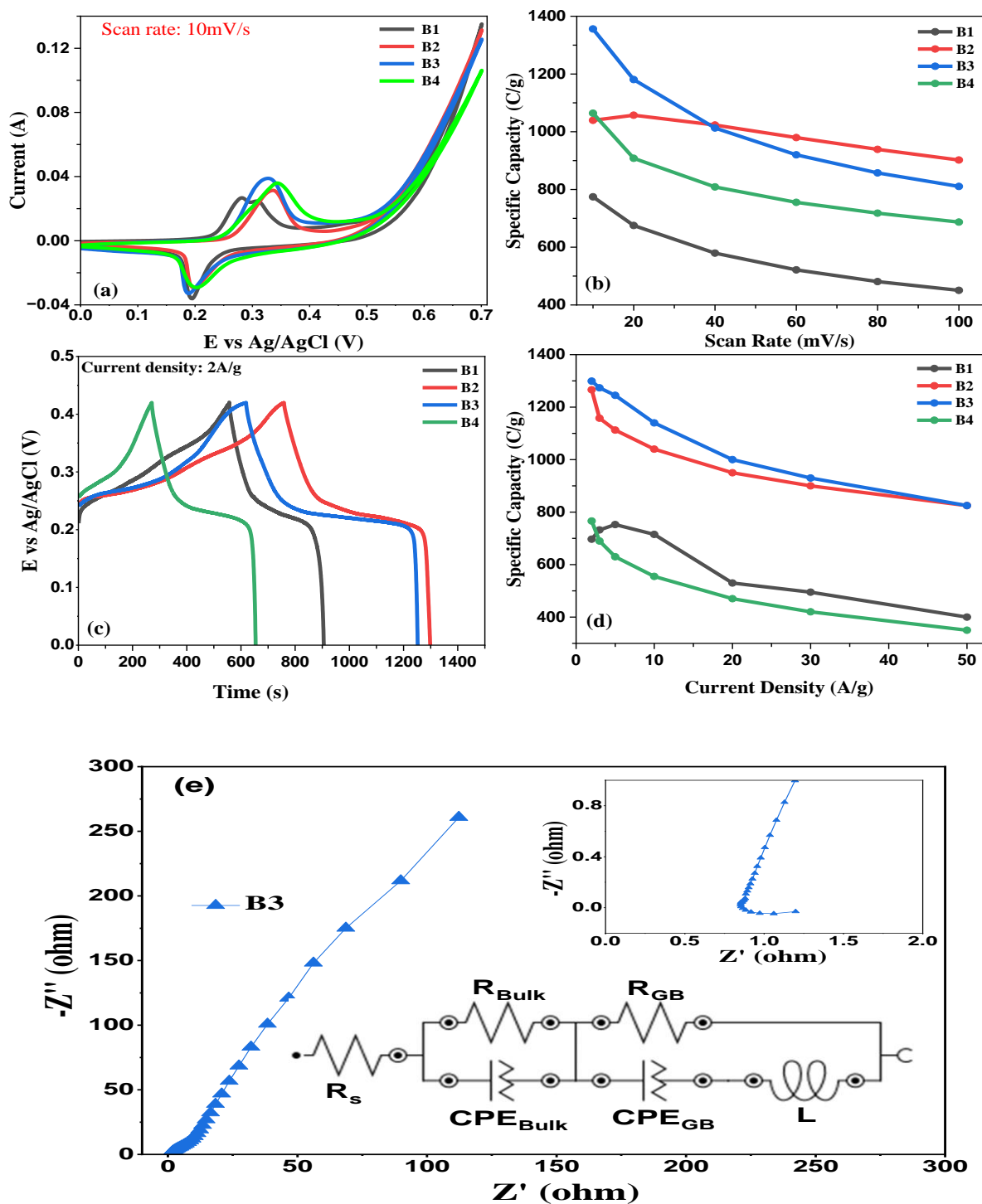


Fig. 6.10. The comparison of CV scans **a)**, the variation of specific capacity **b)** with scan rate, the comparison of GCD curves **c)** and the variation of specific capacity **d)** with current density of rGO@MnMoO₄ composites synthesized with different concentrations of GO (G4). The Nyquist Plot **e)** of the B3 sample and its equivalent circuit.

Table 6.2: The comparison of electrochemical performance of MnMoO₄ and carbonaceous material-based composites.

Electrode & Full Device	Synthesis Process	Electrolyte	Current Density (A/g) or Scan rate (mV/s)	Specific Capacitance (Fg ⁻¹)	Energy Density (Whkg ⁻¹)	Power Density (Wkg ⁻¹)	Ref.
CNT/rGO/MnMoO ₄ <i>CNT/rGO/MnMoO₄/ / CNT-AC</i>	Hydrothermal	2M NaOH	2mVs ⁻¹	2374.9	59.4	1367.9	[153]
MnMoO ₄ /Graphene	Hydrothermal	1M Na ₂ SO ₄	2 Ag ⁻¹	364	-	-	[144]
MnMoO ₄ @MWCNT <i>MnMoO₄/MWCNT// AC</i>	Hydrothermal	1M KOH	1Ag ⁻¹	1017	18.2	362	[161]
Mn _{0.63} Ni _{0.37} MoO ₄ -RGO	Sonochemical	2M KOH	2Ag ⁻¹	161.1 mAhg ⁻¹	-	-	[207]
MnMoO ₄ /G	Hydrothermal	1M Na ₂ SO ₄	0.1Ag ⁻¹	302.08	-	-	[162]
Mn _{1/3} Ni _{1/3} Co _{1/3} /rGO	Hydrothermal	3M KOH	1Ag ⁻¹	1750	-	-	[163]
MnMoO ₄ @CNF	Electrospinning carbonization thermal annealing	1M KOH	0.1Ag ⁻¹	389.7	-	-	[164]
Su-GC@MnMoO ₄ <i>Su-GC@MnMoO₄// AC</i>	Hydrothermal	2M KOH	2Ag ⁻¹	528	35.4	223	[226]
Ni(OH) ₂ /MnMoO ₄ /rGO/NF <i>Ni(OH)₂/MnMoO₄/rGO/NF//AC</i>	Hydrothermal	3M KOH	1Ag ⁻¹	1329.1Cg ⁻¹	61.4	428.4	[165]
rGO@MnMoO ₄ <i>rGO@MnMoO₄// G-AC</i>	Hydrothermal	3M KOH	2Ag ⁻¹	3092 (1299Cg ⁻¹)	63.5	850	This Work

The discrete-component circuit model was used to propose its equivalent circuit, which is also depicted in Fig. 6.10(e). The circuit contains equivalent resistance (R_s) connected in series to two other impedances. R_s depends on the interfacial contact resistance between the current collector and active material, Ni-foam's internal resistance, and the electrolyte's ionic resistance [204]. The first impedance component consists of a bulk resistance (R_{Bulk}) and an associated constant phase-element (CPE_{Bulk}), while the second impedance component contains a resistance (R_{GB}), a constant phase-element (CPE_{GB}), and an inductance (L) associated with grain boundaries. These impedances are associated with charge-transfer resistance (between the active material and electrolyte) and interfacial or Helmholtz boundaries, respectively. The constant phase element's impedance can be written as $Z_{CPE} = \omega^{-N}/A$, where ω and N are the angular frequency and distributing factor, respectively [205]. The fitted value R_{Bulk} , i.e., 7.4Ω , indicates the good charge-transfer properties of the electrode material (B3), as already validated in the CV and GCD analysis. The lower value of bulk resistance may be attributed to the higher C/O ratio i.e., 1.9, and the considerable formation of alternate conjugated carbon bonds in the optimized electrode material during the hydrothermal annealing, leading to its higher electrical conductivity. It can be noted that a very small resistance, i.e., 0.8Ω , is applied by the connecting wires, electrolyte, and Ni-foam. However, the large value of the grain boundary or interfacial resistance, i.e., $1.73k\Omega$, may be associated with bond elongation due to the penetration of electrolyte ions in the microporous composite. The small size of grains is also contributing to the interfacial resistance. The inductance element ($L = 99.8nH$), representing the bending of impedance curve in the fourth quadrant, is ascribed to the leads, test setup, or grain boundaries. Furthermore, the mapped values of N for bulk and interfacial boundaries were 0.83 and 0.85, respectively, inferring the capacitive character of both phase elements.

6.3.An Asymmetric Device Analysis

In order to further assess the electrochemical performance of the optimized electrode for practical applications, an asymmetric supercapacitor device was developed by applying rGO@MnMoO₄ (B3) and graphite-activated carbon (G-AC) on Ni-foam, as the cathode and anode, respectively. The electrolyte used was 3M KOH, and polyvinyl alcohol was used as the separator. The suitable potential window of 1.7V for the device was estimated from the CV profiles Fig.6.11(a) recorded at a scan rate of 60mV/s by varying the potential. The CV scans of the device at different scan

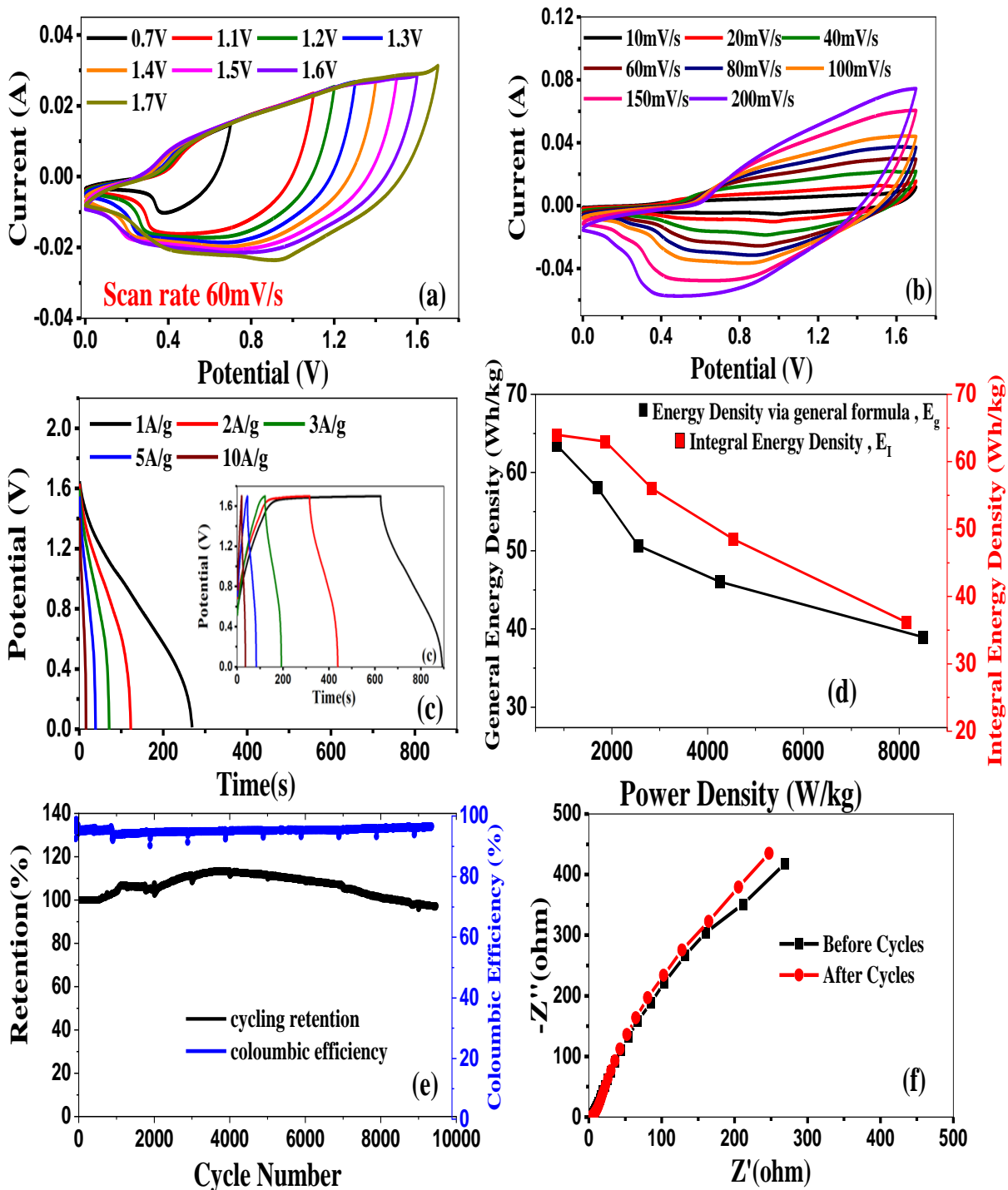


Fig.6.11. The CV curves **a)** at different voltage-widow, the CV curves **b)** at different scan rates, the GCD curves **c)** at different current densities, the variation **d)** of power density and energy density with current density, the variation **e)** of percentage specific capacity retention and Coulombic efficiency with cycle number and the Nyquist plots **f)** of the asymmetric device.

rates are displayed in Fig. 6.11(b). Interestingly, it can be seen that both Faradic and double-layer phenomena contribute to the energy storage mechanism of the device. The non-shifting of redox peaks at all studied scan rates i.e., from 10 to 200 mVs⁻¹, revealed the noteworthy charging or discharging capacity of the asymmetric device [204]. The GCD curves of the device were recorded at different current densities Fig. 6. 11(c) shows a near-symmetrical profile attributed to reversible redox phenomena. Meanwhile, the device demonstrated a specific capacity of 269 Cg⁻¹ at 1 Ag⁻¹, resulting in an impressive energy density of 63.5 Whkg⁻¹ at a power density of 850 Wkg⁻¹ when calculated from the standard formula. The difference between the power density and energy density of the device plotted in Fig. 6.11(d) infers the inverse relation between energy and power density. As shown in Fig. 6.11(e), the asymmetric device displayed a very good cycle lifespan and a fantastic Coulombic efficiency, retaining 97% of specific capacitance through 9460 cycles. The energy density of the asymmetric device was also calculated using the integral energy density (E_I) formula to obtain accurate values, as shown in Fig. 6.11 (d). The device exhibited an energy density (E_I) of 64 Whkg⁻¹ at a power density of 846 Wkg⁻¹. The initial rise in capacity was ascribed to the sluggish initiation of blocked electrochemically available sites. The Nyquist plots Fig. 6.11(f) of the asymmetric supercapacitor recorded before and after 9460 cycles ensured minimal structural and morphologic degradation of the deposited materials. The electrochemical efficiency of the asymmetric rGO@MnMoO₄//G-AC device has outperformed all the recently reported MnMoO₄ and carbonaceous-based devices, as detailed in Table 6.2, which is attributed to the synergistic properties of rGO and MnMoO₄.

Conclusion

Based on the compelling results and in-depth discussions, it is evident that the controlled oxidation of GO has a remarkable impact on the electrochemical achievements of the rGO@MnMoO₄ composite. Among its counterparts, the GO(G4) prepared with a 4-hour stirring duration exhibited superior synergistic effects in the composite, contributing to its exceptional energy-storage capacity. The optimized composition of GO(G4) played a crucial role in achieving such impressive results. The electrode prepared with the most optimized rGO@MnMoO₄ composite demonstrated a truly magnificent specific capacity, reaching an impressive specific capacity of 1356 Cg⁻¹ at 10 mVs⁻¹ and 1299 Cg⁻¹ at 2 Ag⁻¹. These remarkable performances are a direct consequence of the synergistic effects between rGO and MnMoO₄ in the composite. The microporous microrod

morphology of MnMoO_4 significantly increased the electroactive surface area, while rGO enhanced the electrical conductivity by providing an abundance of conjugated carbon bonds. Notably, the asymmetric supercapacitor device demonstrated an altitudinous energy density of 63.5 Whkg^{-1} (64 Whkg^{-1}) at a power density of 850 Wkg^{-1} (846 Wkg^{-1}), showcasing its exceptional capabilities. The device also exhibited a fantastic Coulombic efficiency and retained an outstanding 97% of specific capacitance after 9640 cycles. Even after such a rigorous test, minimal structural and morphological degradation of the deposited materials was observed, revealing the device's long-lasting performance and reliability. In nutshell, the findings of this study reveal the remarkable potential of the rGO@MnMoO_4 composite, highlighting its capabilities for next-generation energy storage applications. The synergistic effects of rGO and MnMoO_4 have paved the way for impressive performance, making this composite a promising candidate for advanced electrochemical devices.

Chapter 7

Elevated Charge-Storage Kinetics of Mesoporous MoS₂@MnMoO₄ heterostructures for Advanced Hybrid Supercapacitors

The ongoing use of non-renewable energy sources, coupled with their adverse ecological impacts has motivated the innovation of new energy storage and conversion systems [227]. Supercapacitors have garnered widespread concentration due to their high power per unit volume, rapid charge-discharge capabilities, and prolonged longevity. The application potential of SCs is reliant upon their energy per unit volume [[228],[161]. Therefore, the progress and creation of electrode materials with superior performance and elevated energy density could enhance the utilization of supercapacitors in the realm of energy preservation [229]. Currently, composite electrode materials based on transition metal molybdate oxides (XMoO₄, where X is Ni, Co, Mn, Fe) have found application in ultracapacitors. This is attributed to their outstanding electrochemical performance, including notable specific capacitance, favorable rate-capability, and anticipated resilience, all achieved without compromising power density [230]. Among these, Manganese molybdate exhibits promising potential as an active material for electrochemical capacitors. This is attributed to its advantages, including cost-effective, eco-friendly, readily available resources, wide potential window, excellent specific capacitance, rich porosity, and robust cycling stability that distinguishes it from other ternary metal-oxides [188]. Manganese molybdates have garnered attention for their potential to enhance the capacitance of supercapacitors. This is attributed to their advantages, including affordability and better conductivity when compared to other binary metal oxides like CoMn₂O₄, NiMn₂O₄, etc., excellent redox performance, as well as its inherent wide working potential window, cost-effectiveness, and environmentally friendly characteristics [153],[151],[231]. For example, Sheng and colleagues synthesized MnMoO₄ nanoparticles through a solid-phase synthesis, revealing 210 Fg⁻¹ at 1 Ag⁻¹ and 112.6% stability after 10,000 cycles. In their device setup, employing graphene-oxide (reduced) as the negative electrode, they achieved 23.5 Whkg⁻¹ at a power per unit volume of 187.4 Wkg⁻¹ [136]. Mu and collaborators synthesized MnMoO₄·nH₂O and reported 1271 Fg⁻¹ at 5 mVs⁻¹, with a stability of 84.5% after 2000 cycles. Their supercapacitor, utilizing this material and activated charcoal as an anode and cathode demonstrated energy per unit volume of 31.6 Whkg⁻¹ at 935 Wkg⁻¹ power per unit volume

[141]. Xu and co-authors synthesized MnMoO_4 nanosheets via hydrothermal route, disclosing 4609 Fg^{-1} at 1 Ag^{-1} . In their device, $\text{MnMoO}_4//\text{AC}$, they achieved 107.38 Whkg^{-1} at 801.34 Wkg^{-1} [189]. In our previous work, we synthesized MnMoO_4 by microwave method. The asymmetric supercapacitor with MnMoO_4 as anode and graphite mixed in activated carbon (AC-G) as cathode showed 68 Whkg^{-1} at 850 Wkg^{-1} and 139 % maintenance after 5000 cycles [232]. Despite its positive attributes, MnMoO_4 demonstrates constrained electrochemical performance and power density attributed to its low direct current conductivity of approximately 10^{-8} Scm^{-1} and slow ionic migration during the electrochemical phenomenon [233]. These issues lead to low energy density [164].

Molybdenum disulfide (MoS_2), similar to graphene, belongs to a growing category of layered two-dimensional (2D) materials that have garnered noteworthy interest. This is due to its remarkable electronic properties and versatile utilization in optical electronics and energy preservation. MoS_2 exhibits the potential for charge storage both within and between layers through the faradaic redox process [234]. It surpasses oxides in terms of electronic and ion-based conductivity [235], presents multiple oxidation states (+2 to +6) [236], features a van der Waals' gap, possesses an elevated theoretical capacity [237], showcases an ample electroactive area, and have different polymorphs (2H and 1T phase), but simultaneously it suffers from restacking, poor rate-capability and storage capacity retention [238]. To address the shortcomings of individual materials, the creation of composite electrodes featuring distinctive nanostructures is viewed as a beneficial approach to improve the charge storage capability of electrochemical capacitors. For example, Chen and collaborators fabricated arrays of hierarchical $\text{NiCo}_2\text{S}_4@\text{NiMoO}_4$ core-shell nanosheets on Ni foam, resulting in an electrode, which demonstrated 1487.6 Fg^{-1} at 1 Ag^{-1} and maintained 89.7% after 8000 cycles [239]. Xie et al. synthesized $\text{Ni}_3\text{S}_2@\text{NiMoO}_4$ core-shell nanoarrays by hydrothermal technique. The assemblage of asymmetric supercapacitor in which $\text{Ni}_3\text{S}_2@\text{NiMoO}_4$ and activated charcoal as an anode and cathode showed 28.4 Whkg^{-1} at 90.8 W kg^{-1} [229]. Asaithambi and colleagues synthesized transition metal doped $\text{SnO}_2@\text{MoS}_2$ composite by hydrothermal method. The Mn-doped $\text{SnO}_2@\text{MoS}_2$ composite showed 242 Fg^{-1} at 0.5 Ag^{-1} with a retention rate of 83.95% after 5000 cycles [240]. Parisa et al. developed $\text{MoS}_2@\text{Fe}_3\text{O}_4@\text{rGO}$ by hydrothermal route. The nanocomposite showed 527 Fg^{-1} at 0.5 mAcm^{-1} with 93% maintenance after 5000 cycles [241]. Wan et al. synthesized $\text{NiMoO}_4@\text{MoS}_2$ nanorods and their electrode showed 2246.7 Fg^{-1} at 1 Ag^{-1} with a cycling stability of 88.4%. A supercapacitor, in which

NiMoO₄@MoS₂ as anode and porous carbon doped with N and S as cathode exhibit 47.5 Whkg⁻¹ at 0.44kWkg⁻¹ with cycling stability of 80.2% after 10000 cycles.[37]. Yang and colleagues assembled an asymmetric device in which Nickel sulfide/Molybdenum disulfide is the anode and the cathode is the negative electrode. The Nickel sulfide/MoS₂ showed 757 Fg⁻¹ at 0.5Ag⁻¹. The supercapacitor manifests 40Whkg⁻¹ at 0.4 kWkg⁻¹ with 100% stability after 10000 cycles.[242] Zhang and colleagues developed a symmetric device in which s-MnO₂/MoS₂ worked as both electrodes. The device showed 0.0036 mWh cm⁻² with cycling stability of 90 % after 3000 cycles [243]. Iqbal and colleagues synthesized a symmetric supercapacitor in which MoS₂@TiO₂ worked as positive as well as cathode. The supercapacitor showed 21 Whkg⁻¹ at 13000 Wkg⁻¹ with cycling stability of 98% after 2000 cycles [244]. Zhao and coworkers synthesized an asymmetric device in which Ni(OH)₂/MoS₂ is an anode and active graphene is the cathode. The device showed an energy per unit volume of 13Wh kg⁻¹ at a power per unit volume of 3500Wkg⁻¹ [245]. Wang and coworkers synthesized an asymmetric supercapacitor in which NiCo₂S₂-C-MoS₂ and activated charcoal as an anode and cathode, respectively. At a power per unit volume of 400Wkg⁻¹, the device yields an energy per unit volume of 27.7Whkg⁻¹ [246]. Mohammadi and coworkers synthesized an asymmetric device in which CuCo₂S₄ is an anode and activated charcoal is a cathode. The device showed an energy per unit volume of 43.65Whkg⁻¹ at a power per unit volume of 16Wkg⁻¹ [247]. Rafique and coworkers synthesized an asymmetric device in which Mn₃O₄ is the anode and MoS₂ is the cathode. The device showed an energy per unit volume of 31Whkg⁻¹ at a power per unit volume of 9000Wkg⁻¹ [248]. Chen and coworkers synthesized an asymmetric device in which NiMoO₄@NiS₂/MoS₂ is an anode and activated charcoal as a cathode. The device showed an energy per unit volume of 26.8Whkg⁻¹ at a power per unit volume of 700 Wkg⁻¹ [249]. Tian et al. synthesized a symmetric supercapacitor in which carbon@MoS₂/MoO₂ was used as an anode and cathode. The device showed an energy per unit volume of 30.8 Whkg⁻¹ at a power per unit volume of 800 Wkg⁻¹ [168]. Yang and coworkers synthesized an asymmetric supercapacitor in which Mn-Co-MoS₂ and activated charcoal as anode and cathode. The device yields 20.51Wh kg⁻¹ at 819.71Wkg⁻¹ [250]. Khawula and coworkers synthesized a symmetric f-MoS₂/CNS-based supercapacitor. The device showed an energy per unit volume of 7.4Whkg⁻¹ at a power per unit volume of 3700Wkg⁻¹ [251].

Motivated by the concept of creating nanocomposites for the development of efficient faradaic electrodes, MoS₂ characterized by elevated ionic conductivity and ample surface area, can be

combined with MnMoO₄, possessing excellent specific capacitance, rich porosity, and outstanding structure stability to compensate for their respective shortcomings. By combining the strengths of both MoS₂ and MnMoO₄, the assembled MoS₂@MnMoO₄ heterostructures demonstrate improved electronic conductivity, structural stability, and enhanced electrochemical performance. In this work, we report a two-step hydrothermal route for the simple synthesis of MoS₂@MnMoO₄ heterostructures. First, MoS₂ was synthesized from the hydrothermal method, and then 130mg of the as-prepared MoS₂ powder poured into MnMoO₄ solution to get MoS₂@MnMoO₄. Remarkably, in comparison to MnMoO₄ and MoS₂ individually, the MoS₂@MnMoO₄ nanocomposite demonstrated significantly improved capacitance (722.5Cg⁻¹ at 1Ag⁻¹). The hybrid device, where MoS₂@MnMoO₄ served as the anode and graphite mixed activated carbon (AC-G) as the cathode, yields an impressive energy density of 99.5Whkg⁻¹ at a power density of 0.85 kWkg⁻¹ by extended cyclic stability and good columbic efficiency.

7.1. Structural and Morphological Analysis

To ascertain the crystal-structure of MnMoO₄, MoS₂, and the MoS₂@MnMoO₄ composite, X-ray diffraction (XRD) technique was employed, as illustrated in Fig. 7.1. Peaks corresponding to pure MnMoO₄ were observed at 12.7° (110), 17.6° (200), 22.6° (02-1), 25.9° (002), 31.2° (112), 33.2° (131), 37.8° (13-2), 40.3° (222), 42.5° (42-2), 45.6° (241), 49.4° (42-3), 55.3° (313), and 57.3° (441) in Fig. 7.1(a), in agreement with JCPDS number 98-003-3459. In Fig.7.1(b), peaks for pure MoS₂ were observed at 13.3°, 34.2°, and 56.5°, corresponding to (002), (130), and (110) planes, respectively, indicating a 1T/2H mixed MoS₂ phase [252]. The XRD pattern of MoS₂@MnMoO₄ distinctly displayed the diffraction peaks of both MnMoO₄ and MoS₂. In Fig. 7.1(a), a slight peak shift was discerned, attributed to the incorporation of MoS₂ in MnMoO₄. The Raman spectra depicted in Fig.7.1(b) illustrate the findings for MnMoO₄, MoS₂, and MoS₂@MnMoO₄. Within the higher wavenumber range (936 – 817 cm⁻¹), stretching vibrations of tetrahedral MoO₄⁴⁻ ions were observed, while in the lower range (351-275 cm⁻¹), bending oscillations of MoO₄⁴⁻ ions were noted [253]. Notably, the most pronounced peaks at 930 and 817 cm⁻¹ are connected with the Ag resonance mode, representing the symmetric extension vibrations of O-Mo-O and Mo-O, sequentially [140]. Additionally, the band at 845 /cm yields the Bg mode [196], and the peak at 321 /cm represents the Ag(+Bg) mode[254]. Furthermore, the peak at 878 cm⁻¹ is ascribed to the Bg(+Ag) mode, indicating the asymmetric extension mode of oxygen in Mo=O[255]. The peaks detected at 275 and 351 / cm correspond to the Ab g(+Bg) mode[196]. Upon analysis, the Raman

spectrum of pure MnMoO_4 confirms its synthesis without any impurities. In the case of MoS_2 , the spectrum reveals peaks at 198 cm^{-1} , signifying the J1 phonon mode associated with 1T- MoS_2 [256], along with peaks at 234 and 332 cm^{-1} , attributed to longitudinal acoustic (LA) vibration modes [257]. Additionally, peaks at 280 and 369 cm^{-1} correspond to $E_1 1g$ and $E_1 2g$, respectively, indicating in-plane Mo-S vibrations characteristic of 2H- MoS_2 [257],[250]. Finally, the Raman spectrum of the $\text{MoS}_2@\text{MnMoO}_4$ composite exhibits prominent peaks of MnMoO_4 , particularly the A_g , B_g , and $B_g(+A_g)$ modes, along with the presence of LA and $E_1 2g$ modes of MoS_2 , confirming the composite's composition.

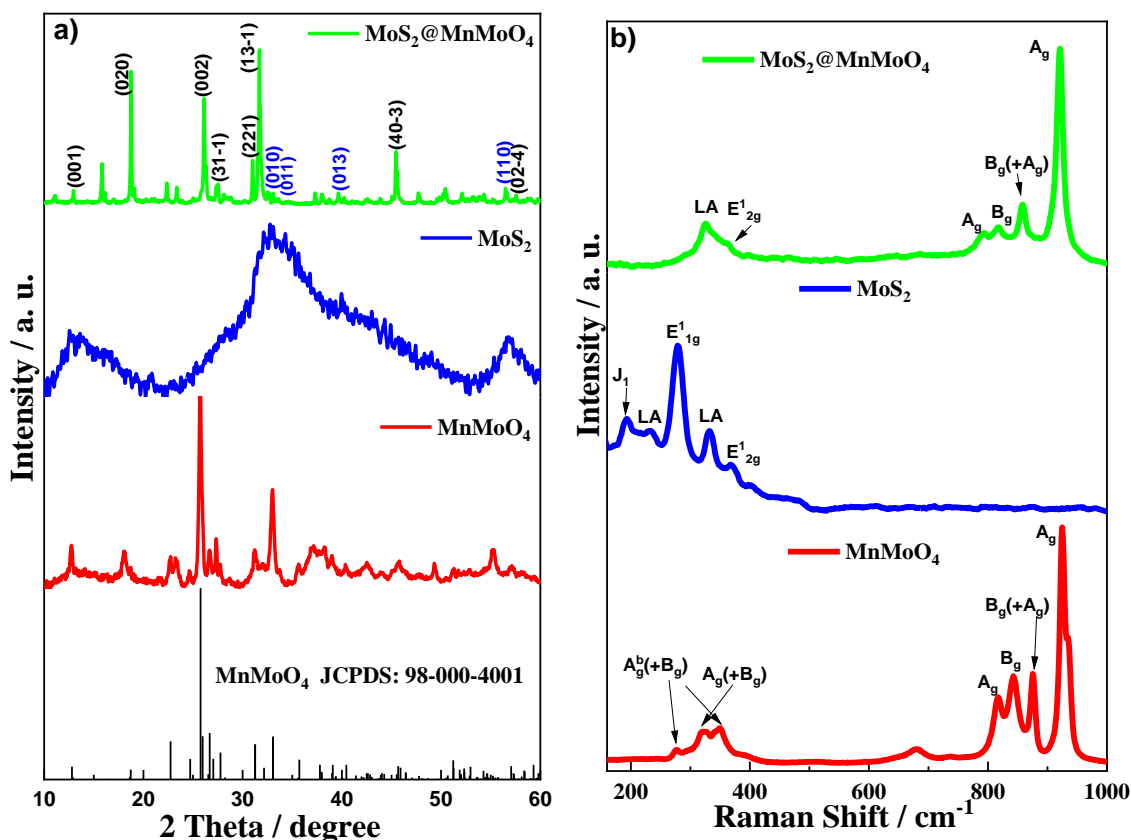


Fig.7.1 a) The XRD patterns and **b)** Raman patterns of MnMoO_4 , MoS_2 , and $\text{MoS}_2@\text{MnMoO}_4$ respectively.

The FE-SEM micrographs presented in Fig. 7.2 illustrate the morphology of MnMoO_4 , MoS_2 , and $\text{MoS}_2@\text{MnMoO}_4$ nanoparticles at different magnifications. Fig. 7.2(a-c) displays the various shapes and sizes of MnMoO_4 , including nanorods and randomly clustered formations. In contrast, Fig. 7.2(d-f) reveals the non-uniform aggregated granular morphology of MoS_2 . Notably, Fig. 7.2(g-i) showcases the distinctive heterostructures of $\text{MoS}_2@\text{MnMoO}_4$ composite material, featuring granules and nanorods. These heterostructures exhibit an augmented surface area, which

is expected to facilitate the electrolyte's ion diffusion rate, potentially enhancing the electrochemical performance. Additionally, EDS charting of $\text{MoS}_2@\text{MnMoO}_4$ validates the uniform distribution of Mn, Mo, O, and S elements throughout the composite material.

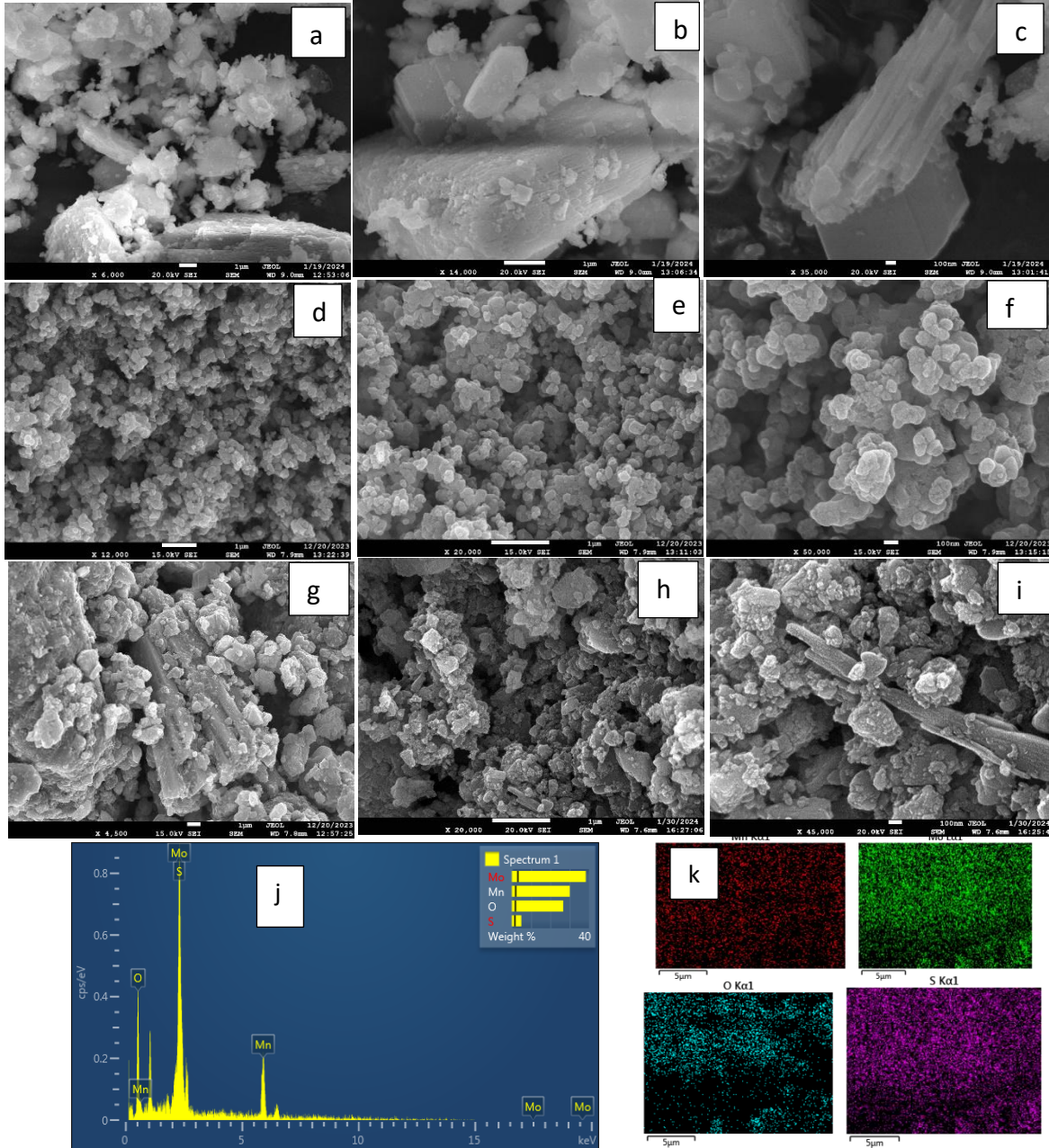


Fig.7.2 The FESEM images of MnMoO_4 **a-c**), MoS_2 **d-f**), and $\text{MoS}_2@\text{MnMoO}_4$ **g-i**), EDS and mapping of $\text{MoS}_2@\text{MnMoO}_4$ **j-k**)

The BET adsorption-desorption technique was utilized to examine the pore details and specific surface area of MnMoO₄, MoS₂, and MoS₂@MnMoO₄. As depicted in Fig. 7.3, all samples exhibited an H3 hysteresis loop. The surface area and pore size according to the BJH distribution for MnMoO₄, MoS₂, and MoS₂@MnMoO₄ samples were found to be 8.4, 10.5, and 17.8 m²g⁻¹, and 3.6, 3.6, and 8.8 nm, respectively. These findings clearly indicate that the composite material, compared to MoS₂ and MnMoO₄, possesses an enhanced surface area, which aligns with the observations from the SEM images. The analysis of pore diameter reveals that the samples exhibit a mesoporous nature. The composite MoS₂@MnMoO₄ exhibits a larger surface area and mesoporous nature, which suggests potential benefits for enhancing electrochemical performance.

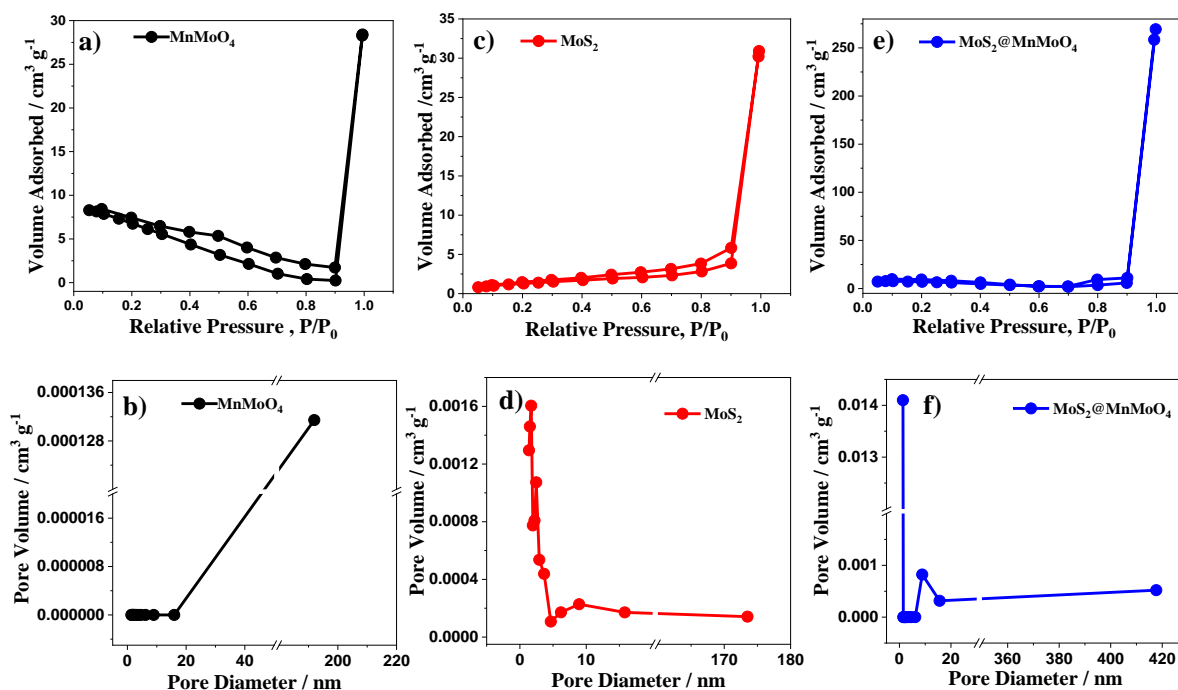


Fig.7.3 The Nitrogen adsorption-desorption isotherm and the graph between pore volume with a pore diameter of **a, b)** MnMoO₄, **c, d)** MoS₂ and **e, f)** MoS₂@MnMoO₄.

The elemental composition of MoS₂@MnMoO₄ was analyzed via XPS survey, as illustrated in Fig. 7.4. Fig. 7.4(a) validated the presence of Mn, Mo, O, and S elements, with the C peak at 284 eV serving for calibration. The Mn 2p core-level spectrum Fig. 7.4(b) displayed four distinct peaks, accurately fitted using Gaussian analysis. The peak at 641.3 eV corresponded to Mn 2p_{3/2}, while Mn 2p_{1/2} was associated with the peak at 653.2 eV. The separation of 11.9 eV between these peaks indicated the Mn²⁺ oxidation state [139]. In the Mo 3d region Fig. 7.4(c), three distinct peaks

were observed, corresponding to Mo 3d_{5/2} of Mo⁴⁺ in MoS₂ and Mo 3d_{5/2} and Mo 3d_{3/2} of Mo⁶⁺ in MnMoO₄ [143],[258]. The S 2p spectrum Fig. 7.4(d) revealed three peaks at 161.01, 162.6, and 168.5 eV, attributed to S²⁻ 2p_{3/2}, S²⁻ 2p_{1/2}, and the sulfate group (SO₃), respectively [259],[260]. The O 1s spectrum Fig. 7.4(e) demonstrated three peaks at 530.2, 531.5, and 536.9 eV, representing lattice O²⁻ and OH groups on the surface [140], [37].

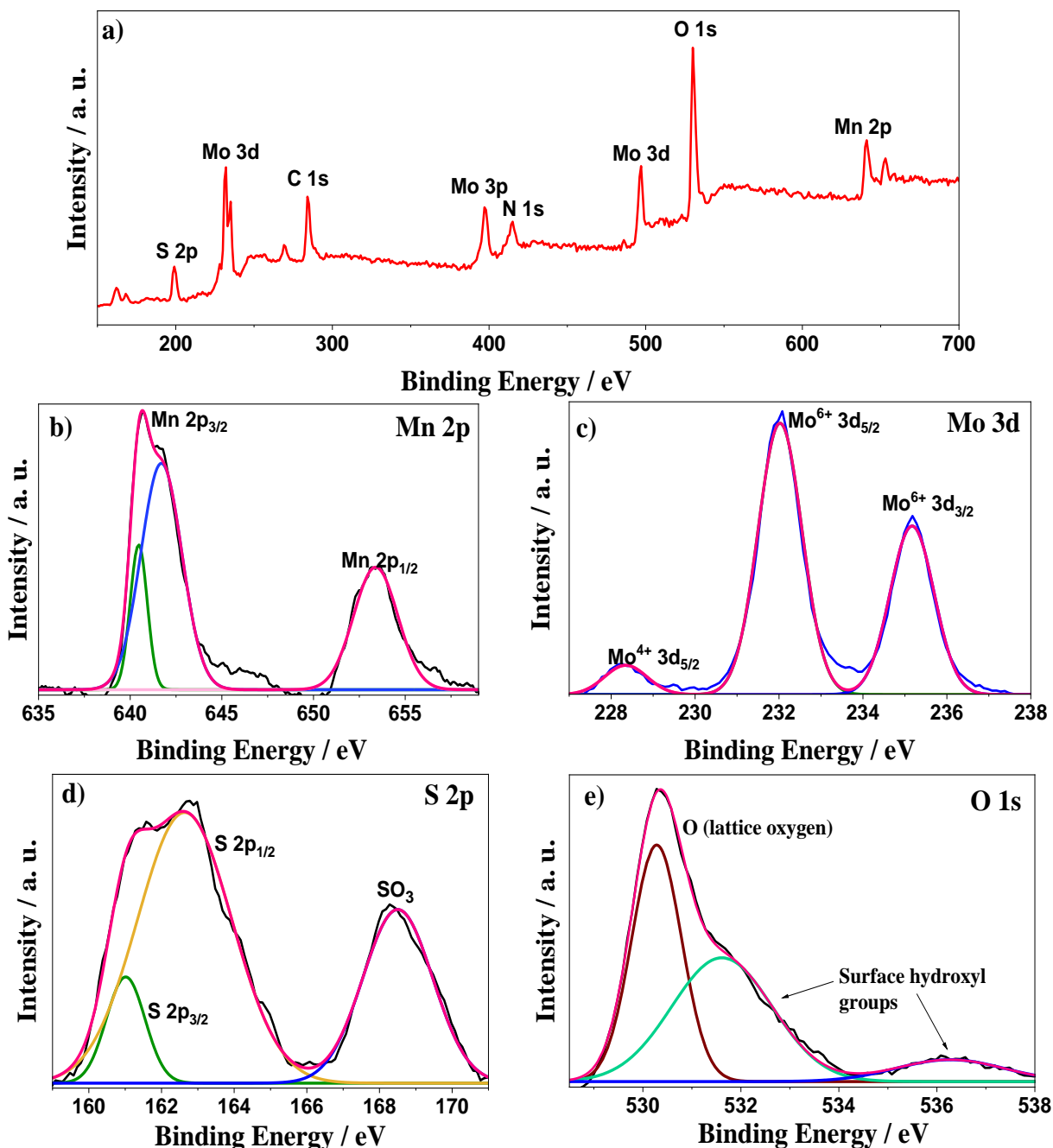
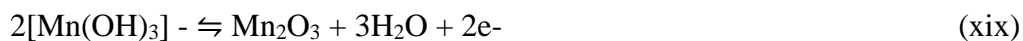


Fig.7.4. The XPS spectra of MoS₂@MnMoO₄.

7.2. Electrochemical Analysis

The charge-storage kinetics of the working electrodes were assessed in a three-electrode setup with 3M KOH as the electrolyte. The cyclic voltammetry (CV) plots of the MnMoO₄, MoS₂, and MoS₂@MnMoO₄ electrodes were examined, as displayed in Fig. 7.5(a-c), within the potential window of -0.01-0.7V at different scan rates ranging from 10-100mVs⁻¹. Each CV scan of MnMoO₄ revealed a pair of redox peaks, suggesting their Faradic nature, potentially ascribed to the to and fro movement of electrons between the +2 and +3 oxidation states of manganese (Mn). The CV profile of MoS₂ displayed oxidation states linked with Mo+4. The shift of redox peaks towards high and low potential scale, sequentially, was ascribed to diffusion limitation at higher scan rates. Notably, all electrodes maintained their CV curve profile even at 100 mV s⁻¹, demonstrating their resilience in enabling swift charge transfer mechanisms. Upon comparison with MnMoO₄ and MoS₂, the composite MoS₂@MnMoO₄ exhibited a larger CV area, indicating a higher specific capacity ascribed to the synergistic effect between MnMoO₄ and MoS₂. Fig. 7.5(g) illustrates the comparison of specific capacity variation of all electrodes at different scan rates. From the graph, it is evident that the composite MoS₂@MnMoO₄ outperformed the pure materials in a specific capacity. The maximum specific capacity obtained at 10 mV s⁻¹ for MnMoO₄, MoS₂, and MoS₂@MnMoO₄ was 236.3, 215.4, and 580.7 Cg⁻¹, sequentially. As the capacitive properties of the electrodes are predominantly governed by Faradaic reactions, so the probable redox reactions can be defined as:



The Galvanostatic charge-discharge (GCD) patterns of MnMoO₄, MoS₂, and MoS₂@MnMoO₄ were examined, as depicted in Fig. 7.5 (d-f), within the potential range of 0-0.42V at various current densities ranging from 1-10 A g⁻¹. The asymmetrical charging and discharging profiles observed in all these electrodes suggested their characteristic Faradic behavior. Fig. 7.5(h) presents the comparison of specific capacity variation of all working electrodes at different current densities. From the graph, it is evident that the MoS₂@MnMoO₄ electrode demonstrated the longest discharging time among the pure materials, suggesting the highest specific capacity, which aligns well with the CV results. The maximum specific capacity of MnMoO₄, MoS₂, and

$\text{MoS}_2@\text{MnMoO}_4$ was 176.5, 505.5, and 722.5 Cg^{-1} at a current density of 1Ag^{-1} . Furthermore, the decrease in the specific capacity of all electrodes under higher scan rates (as depicted in Figure 7.5(g)) and current densities (as shown in Figure 7.5(h)) could be ascribed to diminished redox kinetics caused by the constrained electrolyte's ion diffusion within the pores of the electrode.

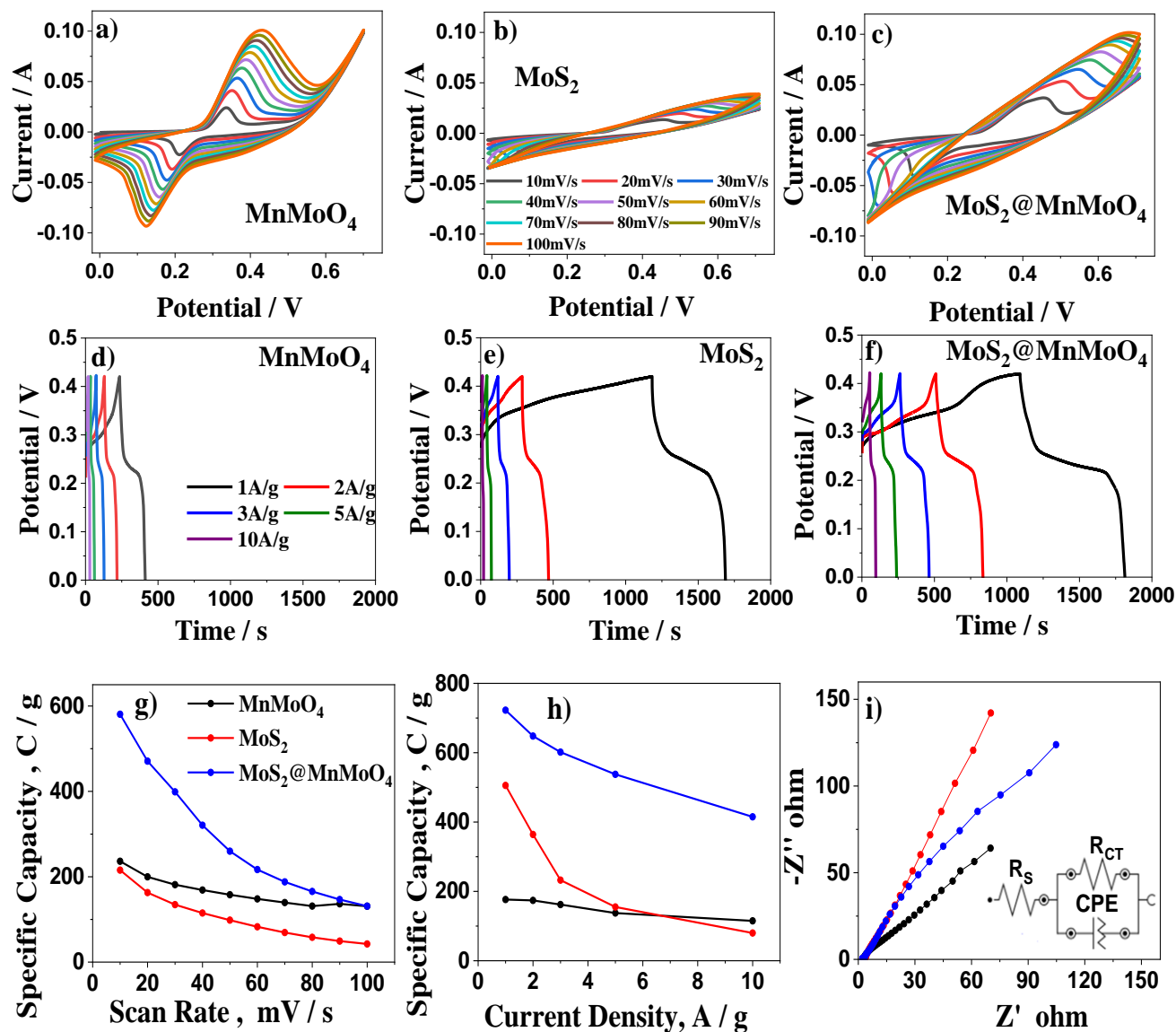


Fig.7.5 The CV scans of a) MnMoO_4 , b) MoS_2 and c) $\text{MoS}_2@\text{MnMoO}_4$ at different scan rates, the GCD of d) MnMoO_4 , e) MoS_2 and f) $\text{MoS}_2@\text{MnMoO}_4$ at different current densities, g) the variation of specific capacity of these electrodes with scan rates, h) the variation of specific capacity of these electrodes with current densities and i) EIS spectra of MnMoO_4 , MoS_2 and $\text{MoS}_2@\text{MnMoO}_4$ and their equivalent circuit.

In further exploration of the charge kinetics of electrode materials, electrochemical impedance spectroscopy (EIS) analysis was conducted. Displayed in Fig. 7.5(i) are the Nyquist plots of all investigated electrodes immersed in a 3M KOH solution across a frequency spectrum of 0.01Hz-100 kHz. The accompanying inset illustrates the equivalent circuit diagram of all examined electrodes. This diagram featured series equivalent resistance (R_S), charge-transport resistance (R_{CT}), and a constant-phase-element (CPE). R_S , influenced by various factors such as interface resistance among the electrode substrate and the deposited material, the inner impedance of Ni foam, and the electrolyte resistance, played a significant role. R_{CT} represented the resistance across the electrode/electrolyte contact area, while CPE accounted for deviations from ideal capacitor behavior due to surface irregularities at the double-layer interface. These deviations, influenced by factors such as surface roughness, chemical variations, and the heterogeneous nature of the electrode-electrolyte interface owing to ion adsorption, were considered. CPE could be expressed as proportional to ω^{-N} , where ω and N represented the angular frequency and distribution factor, respectively, within the range of 0 to 1. In CPE, $N=0$ denoted a pure resistor, while $N=1$ represented ideal capacitors. The fitted parameters of the equivalent circuit elements are presented in Table 7.1. According to the model proposed, the $\text{MoS}_2@\text{MnMoO}_4$ -based electrode exhibited improved reaction kinetics by minimizing resistances, notably R_S (2.2 Ω) and R_{CT} (850 Ω), during the charge/ion transfer process. Additionally, the mapped values of N , with MnMoO_4 at 0.5, MoS_2 at 0.7, and $\text{MoS}_2@\text{MnMoO}_4$ at 0.7, suggested a propensity of CPE towards capacitive behavior. The enhanced reaction kinetics of $\text{MoS}_2@\text{MnMoO}_4$, as evidenced by CV, GCD, and EIS results, can be attributed to the synergetic collaboration between MnMoO_4 and MoS_2 within the composite. This synergy facilitated the enhanced charge-storage kinetics by providing a large electroactive surface area, meso-porosity, and high ionic conductivity.

7.3 An Asymmetric Device Analysis

A hybrid supercapacitor device ($\text{MoS}_2@\text{MnMoO}_4//\text{AC-G}$) was crafted to gauge the electrochemical prowess of our meticulously refined electrode for real-world applications. This setup featured $\text{MoS}_2@\text{MnMoO}_4$ as the positive electrode and AC-G as the negative electrode, utilizing a 3 M potassium hydroxide (KOH) electrolyte. The appropriate voltage range of 1.7 V for the device was determined from the cyclic voltammetry profiles Fig. 7.6(a), obtained at 60 mV s^{-1} , with potential adjustments. Fig. 7.6(b) demonstrates the CV scans of the device conducted at

varying scan rates. Impressively, both Faradic and double-layer mechanisms participate in the device's

Table 7.1. The fitted values of the equivalent circuit's component of all electrodes.

Samples	R_s	R_{CT}	CPE
MnMoO ₄	2.5 Ω	900 Ω	12.5mMho, N=0.529
MoS ₂	3.35 Ω	6.2k Ω	4.45mMho, N=0.727
MoS ₂ @MnMoO ₄	2.2 Ω	850 Ω	7.99mMho, N=0.678

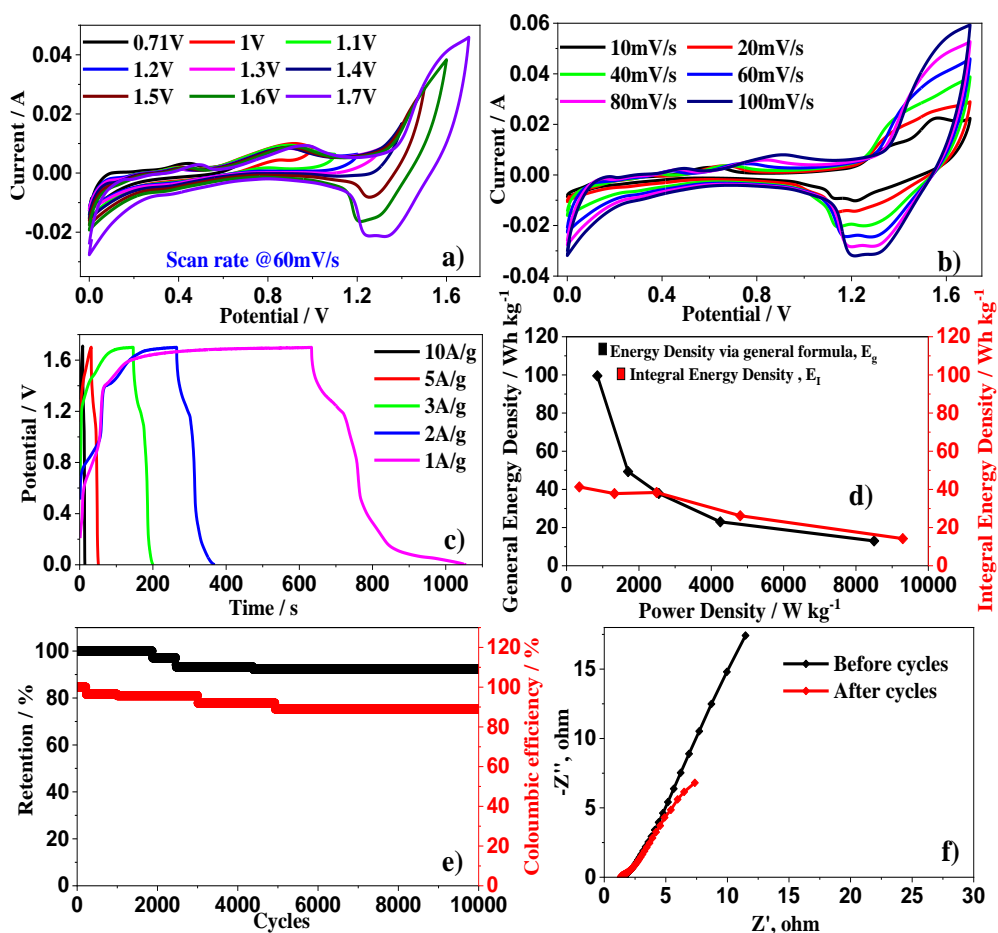


Fig. 7.6. a) The CV curves at different voltage-window, b) the CV curves at different scan rates, c) the GCD curves at different current densities, d) the variation of power density and energy density with current density, e) the variation of percentage specific capacity retention and Coulombic efficiency with cycle number and f) the Nyquist plots of the asymmetric device.

energy storage process. The consistent positioning of reduction/oxidation peaks across all scan rates, spanning from 10 to 100 mVs⁻¹, indicates the fabricated supercapacitor's outstanding charging and discharging capability. The galvanostatic charge- discharge (GCD) profiles, depicted in Fig. 7.6 (c), exhibit an asymmetrical shape attributed to reversible reduction/oxidation phenomena. Furthermore, the specific capacity of the supercapacitor device reaches 247.9 Cg⁻¹ at 1 Ag⁻¹, leading to an outstanding energy density (E_g) of 99.5 Whkg⁻¹ at 850 Wkg⁻¹ by using the general formula. Examination of power and energy density variations with current density, as depicted in Fig. 7.6(d), unveils an inverse correlation between energy and power density, owing to diffusion constraints at higher current densities. Figure 7.6(e) showcases the excellent cycle life and Coulombic efficiency of the hybrid device, maintaining 92.5% and 89%, respectively, of specific capacitance over 10,000 cycles. The energy density of the asymmetric device was also calculated using the integral energy density formula (E_I) as shown in Fig. 7.6 (d) to get a more accurate value. The device exhibited an energy density (E_I) of 41.3 Wh kg⁻¹ at a power density of 352.7 Wkg⁻¹. Nyquist plots (Figure 7.6(e)) inset captured before and after 10,000 cycles indicate negligible structural and morphological deterioration of the coated materials. In the Ragone plot displayed in Fig. 7.7, a comparative analysis of the performance of the MoS₂@MnMoO₄//AC-G device is conducted against other similar works recently reported. It is evident that the current device surpasses all its counterparts, thanks to the synergistic collaboration between MnMoO₄ and MoS₂.

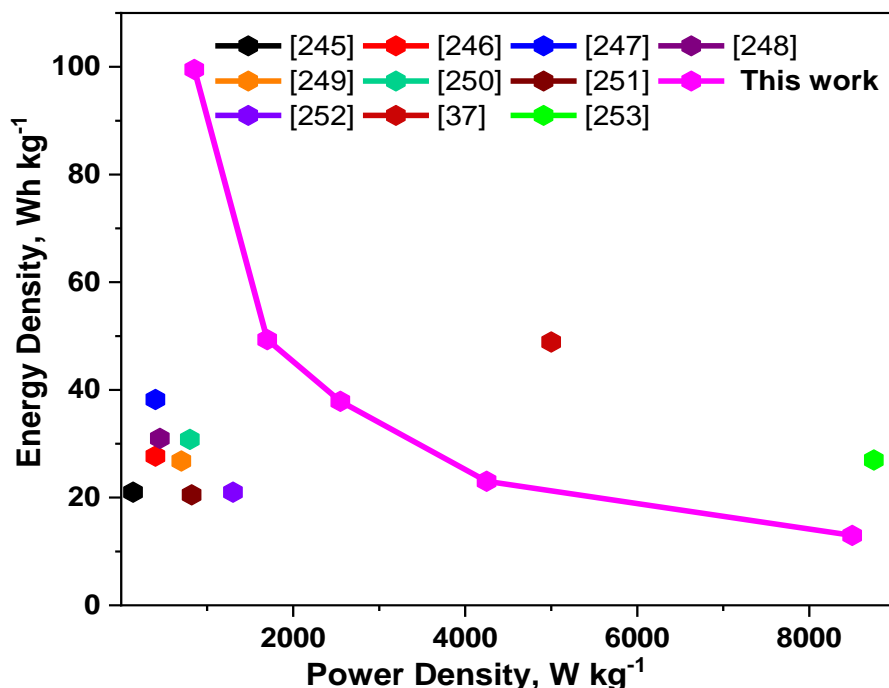


Fig.7.7 The Ragone plot for comparison of device performance.

Conclusion

In nutshell, the successful synthesis of $\text{MoS}_2@\text{MnMoO}_4$ composite through a simple two-step hydrothermal process has yielded significant advancements in energy storage capabilities. By harnessing the beneficial attributes of MoS_2 heightened ionic conductivity and enlarged surface area, alongside MnMoO_4 exceptional electrochemical durability and robust faradic activity, the resultant $\text{MoS}_2@\text{MnMoO}_4$ heterostructures have displayed notably enhanced charge-storage kinetics. With a specific capacity reaching 722.5 Cg^{-1} at 1 Ag^{-1} , the $\text{MoS}_2@\text{MnMoO}_4$ electrode surpasses the performance of both MnMoO_4 and MoS_2 electrodes. Additionally, the asymmetric supercapacitor device $\text{MoS}_2@\text{MnMoO}_4//\text{AC-G}$ demonstrates a remarkable energy density of 99.5 Whkg^{-1} (41.3 Whkg^{-1}) at a power density of 850 Wkg^{-1} (352.7 Wkg^{-1}), while maintaining approximately 92.5% of its specific capacitance over 10,000 cycles. These impressive results underscore the considerable promise of $\text{MoS}_2@\text{MnMoO}_4$ heterostructures for ushering in the advancement of efficient and enduring energy storage solutions.

Chapter 8

Mesoporous Ni doped MnMoO₄ nanoparticles for high-performance asymmetric supercapacitors

In the domain of metal molybdates, manganese molybdate has garnered attention as a capable active material because of its substantial theoretical capacity, the plentiful oxidation states of molybdenum, low operational potential, cost-effectiveness, and environmentally benign nature [261],[233]. Despite these merits, MnMoO₄ encounters challenges such as low electronic conductivity and substantial volume expansion during electrochemical processes, resulting in limited rate capability and accelerated capacity degradation [262]. In addressing this issue, various strategies have been explored, including core-shell heterostructures [263], morphology optimization [264],[265] and heteroatom doping[266],[267], to enhance supercapacitor performance. Particularly, doping molybdates with heteroatoms during their growth process has shown promise in augmenting redox reactions and electrical conductivity, thereby improving overall electrochemical performance. This synergy between the host material and the doped metal ions probably leads to enhanced electrochemical performance [169].

Existing research highlights successful attempts to harness the potential of these materials. For instance, Lin and coworkers synthesized carbon@Co_xNi_{1-x}MoO₄, with porous carbon nanospheres (PCNS) PCNS@Co_{0.21}Ni_{0.79}MoO₄ exhibiting a capacitance of 954 Fg⁻¹ at 1 Ag⁻¹. An asymmetric device was fabricated with PCNS@Co_{0.21}Ni_{0.79}MoO₄ and activated charcoal as the anode as well as the cathode. This device delivers 36.7 Whkg⁻¹ at 346.4 Wkg⁻¹, with cyclic stability of 90.2% after 5000 cycles of charge and discharge[169]. Yuan and coworkers synthesized Mn-doped NiMoO₄ mesoporous nanorods on reduced graphene oxide (Mn_{0.1}Ni_{0.9}MoO₄/rGO) as an electrode material for a symmetric device. The Mn_{0.1}Ni_{0.9}MoO₄/rGO electrode displayed a capacitance value of 688.9 Fg⁻¹ at 0.5 Ag⁻¹. The symmetric device, in which Mn_{0.1}Ni_{0.9}MoO₄/rGO served as both electrodes, delivered 49.2 Whkg⁻¹ at 1800 Wkg⁻¹, with stability of 96.1% after 200 cycles[170]. Zhang and coworkers synthesized Ni_{1-x}Co_xMoO₄ electrodes for an asymmetric device. The Ni_{1-x}Co_xMoO₄ possessed a capacitance value of 755.2 Fg⁻¹ at a current density of 1Ag⁻¹. In the asymmetric supercapacitor configuration, using Ni_{0.85}Co_{0.15}MoO₄/NF and activated charcoal as anode and cathode resulted in an energy per unit volume of 37.26 WhKg⁻¹

Table 8.1. Comparative analysis of electrochemical parameters between $\text{Ni}_{0.25}\text{Mn}_{0.75}\text{MoO}_4$ and other MoO_4 -based electrodes.

Electrode Materials	Method	Specific capacitance of electrode (Fg^{-1})	Energy density of device (Whkg^{-1})	Power density of device (Wkg^{-1})	Cyclic stability of device	Ref.
Ni_3S_2 @ MnMoO_4 nanosheets Ni_3S_2 @ MnMoO_4 //AC	Hydrothermal method at 2M KOH	979.3 Cg^{-1} at 2mAcm^{-2}	31.4	399.9	91.3% after 5000 cycles	[159]
NiCo_2O_4 @ MnMoO_4 core shell nanoarrays NiCo_2O_4 @ MnMoO_4 //AC	Hydrothermal method at 3M KOH	1169 at 2.5mAcm^{-2}	15	6734	96.45% after 10000 cycles	[231]
NiCo_2S_4 @ MnMoO_4 core shell NiCo_2S_4 @ MnMoO_4 // NiCo_2S_4 @ MnMoO_4	Hydrothermal method at 3M KOH	1186.4 at 1Ag^{-1}	47.8	699.9	88.3% after 5000 cycles	[166]
NiCo_2O_4 @ MnMoO_4 Core shell NiCo_2O_4 @ MnMoO_4 // rGO/ Fe_2O_3	Hydrothermal method at 6M KOH	1821 at 5Ag^{-1}	91.87	374.15	68% after 2000 cycles	[167]
Co_2O_4 @ MnMoO_4 NiCo_2O_4 @ MnMoO_4 // AC	Hydrothermal method at 6M KOH	2603.9 at 5mAcm^{-2}	44.16	800	-	[154]
MnMoO_4 @ NiMoO_4 @ Mn_2O_3 MnMoO_4 @ NiMoO_4 @ Mn_2O_3 //AC	Hydrothermal method at 2M KOH	2048.2 Cg^{-1} at 1mAcm^{-2}	49.9	877.8	96.3% after 20000 cycles	[168]
PCNS@ $\text{Co}_{0.21}\text{Ni}_{0.79}\text{MoO}_4$ nanospheres PCNS@ $\text{Co}_{0.21}\text{Ni}_{0.79}\text{MoO}_4$ //AC	Hydrothermal Method at 2M KOH	954 at 1Ag^{-1}	36.7	346.4	90.2% after 5000 cycles	[169]
$\text{Mn}_{0.1}\text{Ni}_{0.9}\text{MoO}_4$ /rGO nanorods $\text{Mn}_{0.1}\text{Ni}_{0.9}\text{MoO}_4$ /rGO // $\text{Mn}_{0.1}\text{Ni}_{0.9}\text{MoO}_4$ /rGO	Hydrothermal Method at 6M KOH	688.9 at 0.5Ag^{-1}	49.2	1800	96.1% after 200 cycles	[170]
$\text{Ni}_{0.85}\text{Co}_{0.15}\text{MoO}_4$ /NF $\text{Ni}_{0.85}\text{Co}_{0.15}\text{MoO}_4$ /NF// AC/NF	Co-Precipitation Method at 3M KOH	1301 at 1Ag^{-1}	37.26	400	-	[171]
MNMO-0.2:1 nanostructure CC/CNTs@MNMO// CC/CNTs@AC	Hydrothermal Method at 2M KOH	1262.6 at 1Ag^{-1}	64.95	864.5	77% after 5000 cycles	[158]
$\text{Ni}_{0.25}\text{Mn}_{0.75}\text{MoO}_4$ nanoplates $\text{Ni}_{0.25}\text{Mn}_{0.75}\text{MoO}_4$ //G- AC	Hydrothermal Method at 3M KOH	1879.7 (789.5 Cg^{-1}) at 1Ag^{-1}	46.7	850	80.7% after 10000 cycles	This Work
$\text{Ni}_{0.25}\text{Mn}_{0.75}\text{MoO}_4$ @N F nanoparticles $\text{Ni}_{0.25}\text{Mn}_{0.75}\text{MoO}_4$ @N F//GAC	Hydrothermal Method at 3M KOH	3164.6 (1297.5 Cg^{-1}) at 1Ag^{-1}	152.01	840	98.7% after 10000 cycles	This work

And a specific power of 400 Wkg^{-1} [171]. Li and colleagues developed Mn-doped nickel molybdate nanostructures, where Mn-doped NiMoO_4 (MNMO) displayed a capacitance value of 1262.6 Fg^{-1} at 1 Ag^{-1} . The asymmetric supercapacitor, employing MNMO and activated carbon on carbon cloth/CNT as anode and cathode, delivered an energy per unit volume of 64.95 Whkg^{-1} at a power per unit volume of 864.5 Wkg^{-1} , with a stability of 77% after 5000 cycles [158]. The electrochemical details of other but relevant molybdate-based electrodes are shared in Table 8.1. The present research problem is to investigate the impact of Ni-doping within MnMoO_4 on its electrochemical performance. The close similarity in ionic radii of Ni^{2+} ions (0.069 nm) and Mn^{2+} ions (0.082 nm), coupled with the near-equivalent electronegativities of Ni (1.91) and Mn (1.55), facilitates the seamless integration of Ni atoms into the lattice structure of MnMoO_4 . This compatibility allowed the formation of a randomized solid solution, denoted as $\text{Ni}_x\text{Mn}_{1-x}\text{MoO}_4$, with x ranging between 0 and 1. The samples are labeled as $\text{Ni}_{0.1}\text{Mn}_{0.9}\text{MoO}_4$ (A1), $\text{Ni}_{0.2}\text{Mn}_{0.8}\text{MoO}_4$ (A2), $\text{Ni}_{0.25}\text{Mn}_{0.75}\text{MoO}_4$ (A3), and $\text{Ni}_{0.3}\text{Mn}_{0.7}\text{MoO}_4$ (A4). The synthesized $\text{Ni}_{0.25}\text{Mn}_{0.75}\text{MoO}_4$ electrode demonstrated superior conductivity and excellent electrochemical performance, showcasing its potential as a promising energy storage material. The results obtained from asymmetric supercapacitor employing binder-enriched $\text{Ni}_{0.25}\text{Mn}_{0.75}\text{MoO}_4$ @nickel foam (NF) as the anode and graphite/activated carbon (GAC)@NF as the cathode, further validate its viability, presenting 46.7 Whkg^{-1} energy at 850 Wkg^{-1} power density. Subsequently, direct growth of $\text{Ni}_{0.25}\text{Mn}_{0.75}\text{MoO}_4$ on nickel foam the same asymmetric device configuration, exhibited even more promising results, demonstrating an impressive 152 Whkg^{-1} energy density at a power density of 840 Wkg^{-1} .

8.1. Structural and Microstructural Analysis

The XRD analysis aimed to explore the crystal structures of $\text{Ni}_x\text{Mn}_{1-x}\text{MoO}_4$ nanoparticles across varying values of x, ranging from 0 to 1. The XRD patterns in Fig 8.1 indicate the presence of distinct diffraction peaks of MnMoO_4 in all the studied samples. Specifically, peaks at 22.6° (021), 24.5° (201), 25.6° (220), 26.5° (-221), 27.6° (-311), 31.1° (-131), 33.0° (-312), 35.6° (400), 37.7° (040) and 38.9° (330) confirm the presence of MnMoO_4 (JCPDS no 98-000-4001). Upon the incorporation of Ni^{2+} into $\text{Ni}_x\text{Mn}_{1-x}\text{MoO}_4$, a discernible shift in the MnMoO_4 diffraction peaks towards higher angles was observed. This shift can be attributed to the smaller ionic radius of Ni^{2+} (0.069 nm) compared to Mn^{2+} (0.082 nm), leading to a reduction in interplanar spacing within the

$\text{Ni}_x\text{Mn}_{1-x}\text{MoO}_4$ nanoparticles. Moreover, the diffraction patterns of $\text{Ni}_x\text{Mn}_{1-x}\text{MoO}_4$ exhibited sharper peaks compared to those of MnMoO_4 . This enhanced sharpness may be indicative of the integration of Ni ions within the intricate $\text{Ni}_x\text{Mn}_{1-x}\text{MoO}_4$ nanostructures. The utilization of the Scherer formula [268] enabled the determination of average crystallite sizes for samples MnMoO_4 , A1, A2, A3, and A4, yielding values of 21, 28, 38, 32, and 36 nm, respectively, manifesting the increase of crystallite size of $\text{Ni}_x\text{Mn}_{1-x}\text{MoO}_4$ after the incorporation of Ni^{2+} .

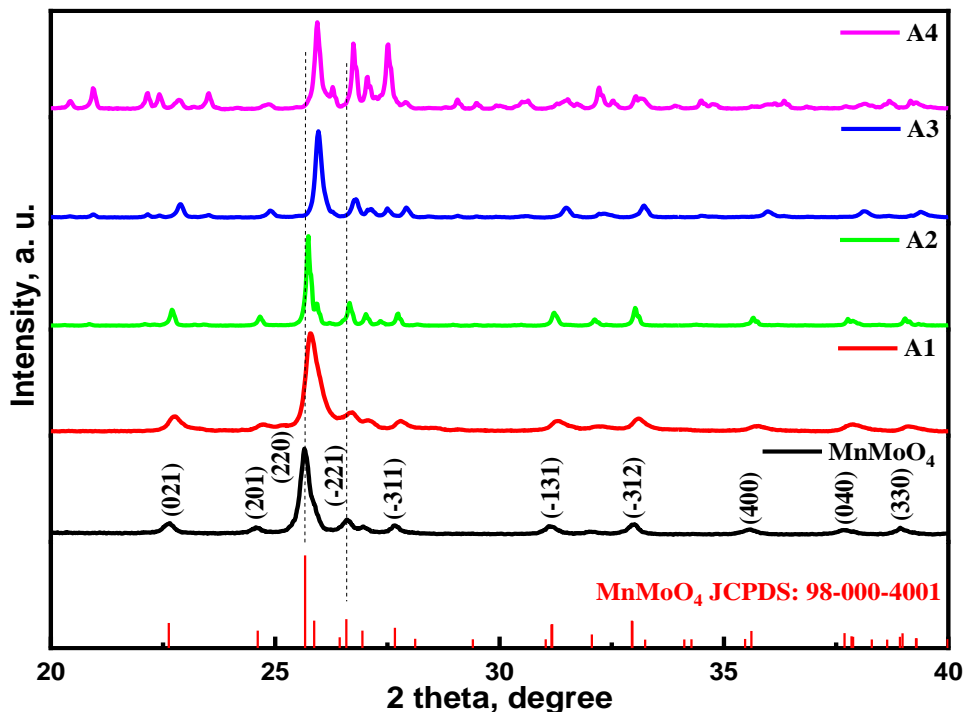


Fig.8 .1 The XRD patterns of $\text{Ni}_x\text{Mn}_{1-x}\text{MoO}_4$ at different values of x .

Raman spectroscopy was employed to conduct a comparative assessment of the structural characteristics exhibited by the $\text{Ni}_x\text{Mn}_{1-x}\text{MoO}_4$ nanoparticles. In Fig.8.2, the Raman spectra of MnMoO_4 , A1, A2, A3, and A4 nanoparticles are presented. The distinct Raman active vibrations of MnMoO_4 , primarily observed between 200 and 1000 cm^{-1} , predominantly stem from the vibrations attributed to MnMoO_4^{2-} ions. Specifically, peaks observed at 944, 933, and 824 cm^{-1} are indicative of symmetric stretching, while the peak at 884 cm^{-1} corresponds to the antisymmetric stretching of the Mo-O bond. Additionally, the peaks detected at 280 and 350 cm^{-1} correspond to the bending vibrations exhibited by MoO_4^{2-} ions [196]. These characteristic vibrational patterns substantiate the presence and formation of MnMoO_4 within the nanoparticle structure. Moreover, the impact of increased Ni content is discerned in the vibrational behavior of MoO_4^{2-} ions. As

depicted in Fig. 8.2, a gradual blueshift of major peaks is observed by the elevation of Ni content, signifying the effective incorporation of Ni into the MnMoO_4 lattice [158].

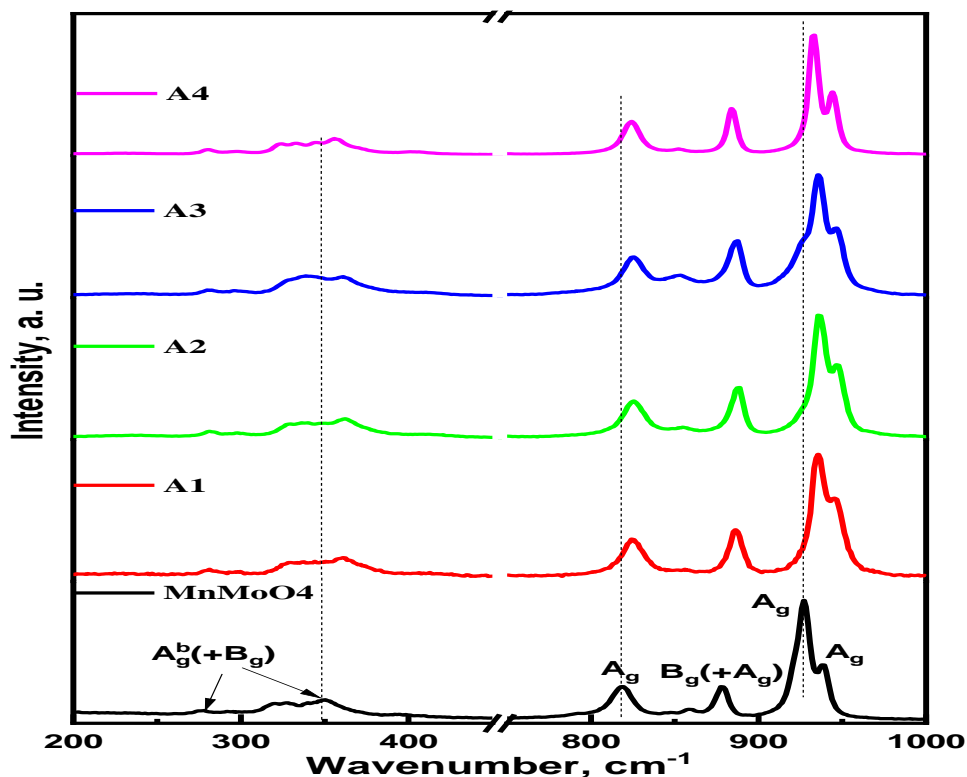


Fig.8.2 The Raman spectra of $\text{Ni}_x\text{Mn}_{1-x}\text{MoO}_4$ at different values of x .

Figures 8.3 (a-b) display FESEM images depicting the $\text{Ni}_{0.25}\text{Mn}_{0.75}\text{MoO}_4$ (A3) powder sample. The micro-images captured at various magnifications reveal a nanoplate morphology exhibiting diverse shapes and sizes. The EDS mapping, as shown in Figure 8.3 (c), confirms the uniform distribution of Ni within the MnMoO_4 lattice. Subsequently, a BET investigation was conducted to additionally scrutinize the superficial characteristics of the $\text{Ni}_{0.25}\text{Mn}_{0.75}\text{MoO}_4$ nanoplates. The N_2 adsorption-desorption isotherm presented in Figure 8.3(d) resembles a type IV isotherm, indicating the formation of multilayers within the synthesized nanoparticles, as also observed in the FESEM image (Fig. 8.3(b)) [269]. The obtained multi-point BET surface area from Fig. 8.3 (e) is $122.6 \text{ m}^2 \text{ g}^{-1}$. The straight-line region between 0.05 to 0.25 of relative pressure was considered for the calculation of various relevant parameters. Additionally, the total pore diameter and pore volume, determined as 2.76 nm and $0.085 \text{ cm}^3 \text{ g}^{-1}$, underscores the mesoporous nature of the A3

sample [270]. These findings strongly suggest that the mesoporous electroactive material could potentially offer an enhanced surface area facilitating electrode-electrolyte interaction and electrolyte penetration, so could probably act as a better electrode material.

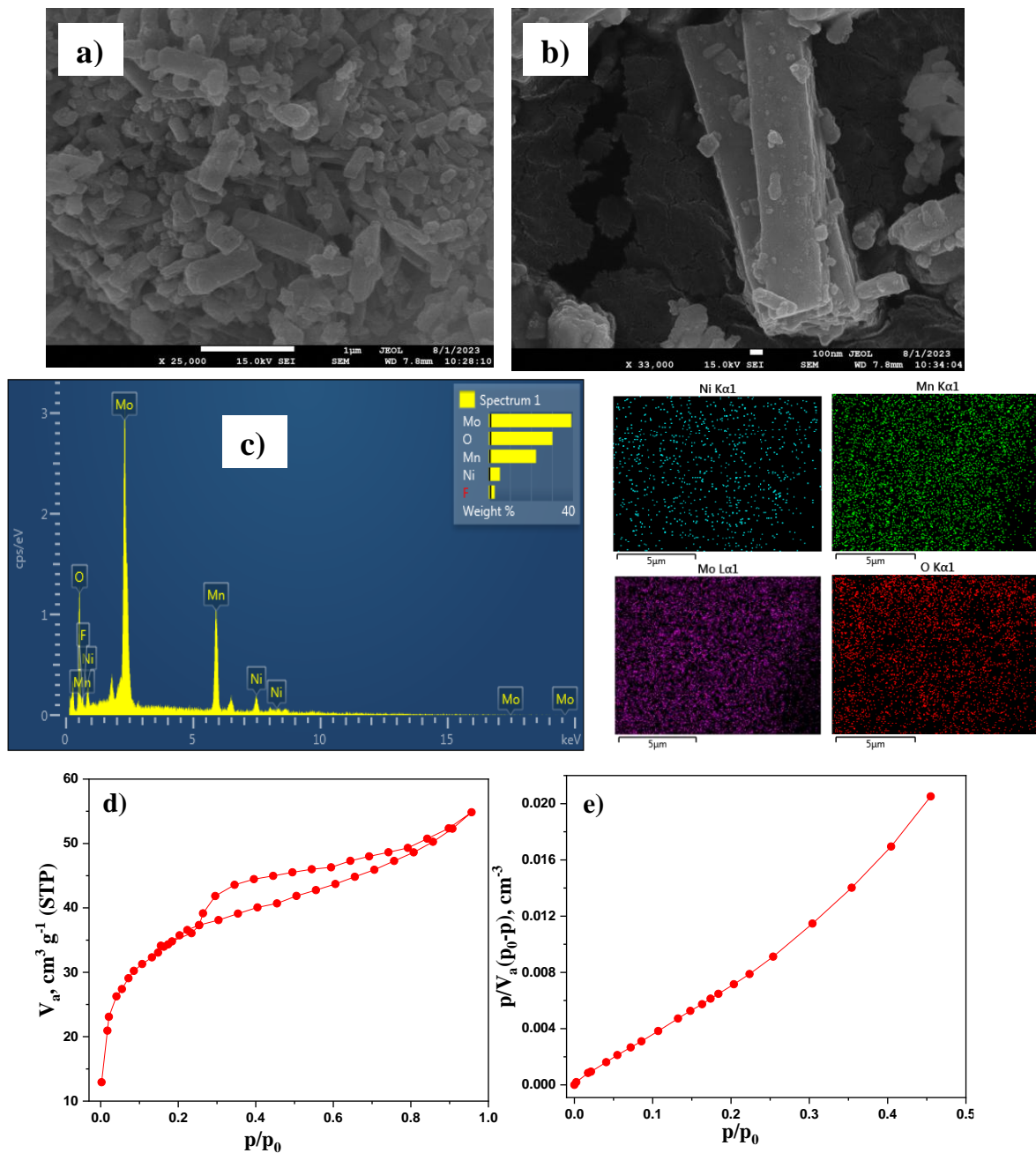


Fig. 8.3 a-b) The FESEM images, c) EDS mapping, d) Nitrogen adsorption-desorption isotherm, and e) multi-point BET isotherm of $\text{Ni}_{0.25}\text{Mn}_{0.75}\text{MoO}_4$ nanoparticles.

Further analysis of the $\text{Ni}_{0.25}\text{Mn}_{0.75}\text{MoO}_4$ (A3) powder sample involved an extensive investigation of oxidation states and elemental composition using X-ray photoelectron spectroscopy. The results presented in Fig. 8.4(a-e) unequivocally reveal the presence of nickel, manganese, molybdenum, and oxygen ions. In the wide-range survey of the A3 sample shown in Fig. 8.4(a), distinct peaks are observed at 232.2, 283.5, 532.4, 641.2, and 857.3 eV, corresponding to Mo 3d, C1s, O1s, Mn 2p, and Ni 2p, respectively. The core level spectrum of nickel, as depicted in Fig. 8.4(b), distinctly displays the Ni 2p_{1/2} and Ni 2p_{3/2} states, exhibiting peaks at 873.6 eV and 855.8 eV, respectively, along with two satellite peaks at 861.3 eV and 879.7 eV [231]. The substantial energy difference of 18.3 eV between the main peaks of Ni 2p_{1/2} and Ni 2p_{3/2} confirms the +2-oxidation state of Ni. Additionally, the peak at 867.08 in the Ni 2p spectrum corresponds to the shake-up peak [271], resulting from a photoelectron departing from a valence electron, inducing its transition to a higher energy state and causing a decrease in the energy of the core electron, thus giving rise to a satellite structure located a few electron volts away from the core level on the kinetic energy scale. Moving to the manganese core level spectrum Fig. 8.4(c), peaks at 640.4 eV and 653.1 eV correspond to 2p_{3/2} and 2p_{1/2}, respectively. Further deconvolution of the Mn 2p spectrum indicates four distinct peaks: two at 640.1 eV and 652.8 eV corresponding to Mn^{2+} ions, while the other two at 641.2 eV and 656.6 eV correspond to Mn^{3+} ions [233]. Consequently, the XPS analysis confirms the coexistence of both +2 and +3 oxidation states of Mn within the $\text{Ni}_{0.25}\text{Mn}_{0.75}\text{MoO}_4$ nanoparticles. The Mo 3d core spectrum Fig. 8.4(d) displays a doublet at 231.58 and 234.78 eV representing Mo 3d_{5/2} and Mo 3d_{3/2}, respectively, with an energy separation of 3.2 eV, inferring a +6-oxidation state. Meanwhile, the core-level spectrum of O 1s Fig.8.4(e) exhibits a main peak at 529.8 eV, deconvoluted into three peaks at 529.8, 531.4, and 533.3 eV. The primary peak at 529.8 eV corresponds to lattice oxygen, while the other two are attributed to surface hydroxyl groups, suggesting the presence of moisture content or the metal hydroxide moieties on the surface of the sample [145],[272].

8.2. Electrochemical Analysis

The assessment of $\text{Ni}_x\text{Mn}_{1-x}\text{MoO}_4$ electrode materials' performance was conducted employing CV, EIS, and GCD, techniques using a three-electrode system. A comprehensive examination of CV profiles for electrodes prepared with A1, A2, A3, and A4 samples is delineated in Fig. 8.5(a-d), utilizing a 3M KOH aqueous electrolyte, an Ag/AgCl reference electrode and a platinum plate

counter electrode within the potential range of 0.01-0.7V and varied scan rates from 10-100 mV/s. The discernible redox peaks observed across all electrode CV profiles indicate the Faradic nature of A1, A2, A3, and A4-based electrodes. The suggested electrochemical reactions occurring in KOH involving $\text{Ni}_x\text{Mn}_{1-x}\text{MoO}_4$ electrodes can be depicted through the subsequent equations [263]:

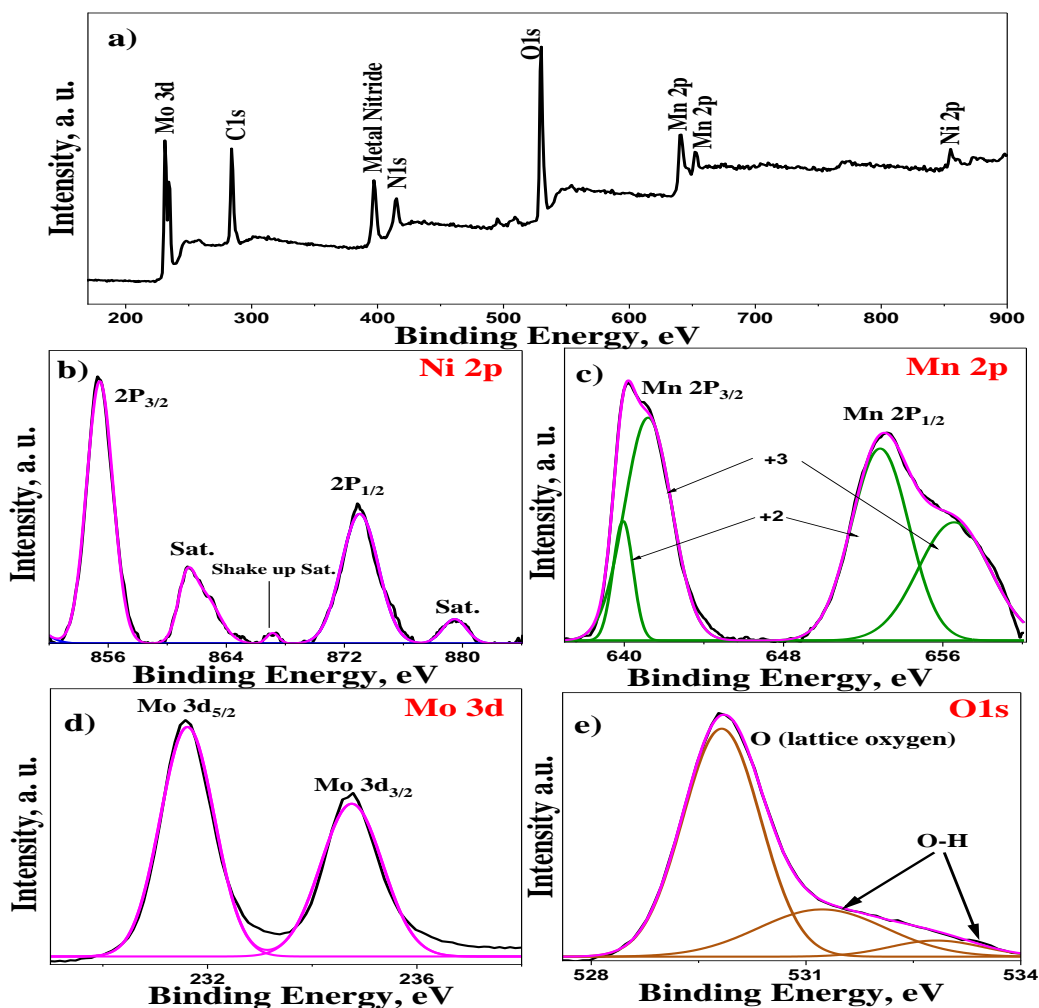
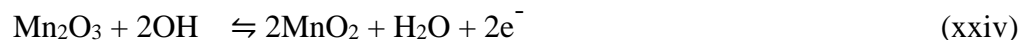
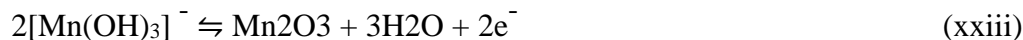
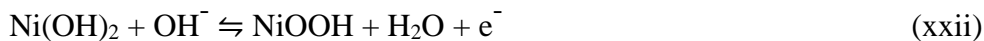


Fig. 8.4. a) The XPS survey spectrum and b-e) and core spectra of $\text{Ni}_{0.25}\text{Mn}_{0.75}\text{MoO}_4$ nanoparticles.

With increasing scan rates in the CV profiles of all electrode materials, the oxidation and reduction peaks shifted towards higher and lower potentials, respectively, owing to the heightened polarization rate of the electrode materials. Transferring electrons and ions between the electrode and the electrolyte is a part of the oxidation and reduction reactions. At higher scan rates, the electrochemical reactions face limitations in their ability to accommodate these rapid changes. This results in a delay in the electrode's response to the potential changes, causing the oxidation and reduction peaks to shift. However, despite these shifts, the CV curve shapes remained consistent at higher potentials, underscoring the superior structural integrity and enhanced ion transport kinetics of the electrodes. Specifically, Fig. 8.5(e) illustrates the CV comparison at 10mV/s, highlighting that A3 exhibited a larger area than the other electrode materials. Furthermore, Fig. 8.5(f) presents a comparison graph depicting specific capacity against scan rate, unequivocally indicating that A3, attributed to its augmented surface area, achieved a higher specific capacity of 671.5Cg^{-1} (945.8Fg^{-1}) at 10mVs^{-1} compared to the remaining electrode materials. However, the decrease in the specific capacity of electrodes at higher scan rates in CV measurements is ascribed to reduced ion diffusion, slower kinetics, and increased polarization. Galvanostatic charging discharging (GCD) for all A1, A2, A3, and A4-based electrodes are shown in Fig. 8.6(a-d) within the potential window 0-0.42V. The near-symmetrical charging-discharging profile of all these electrodes, along with the presence of a plateau in the discharging curves, indicates their typical Faradic capacitive nature. Fig. 8.6(e) exhibits the GCD comparison of all electrodes and notably, the charging and discharging duration of the A3 electrode is longer than that of the A1, A2, and A4 electrodes. At 1Ag^{-1} , the A3 electrode exhibited a discharging time of 815 s, showcasing its impressive specific capacity of 789.5Cg^{-1} (1879.7Fg^{-1}). Fig. 8.6(f) shows the comparison graph of all electrodes between specific capacity at different current densities. On comparing with CV analysis and GCD results, it is clear that the A3 electrode performs in a better way and offers enhanced results owing to its mesoporous nature and enhanced surface area. However, the reduction in specific capacity at higher current densities in GCD may be ascribed to a combination of limited ion diffusion, increased polarization, and kinetic limitations.

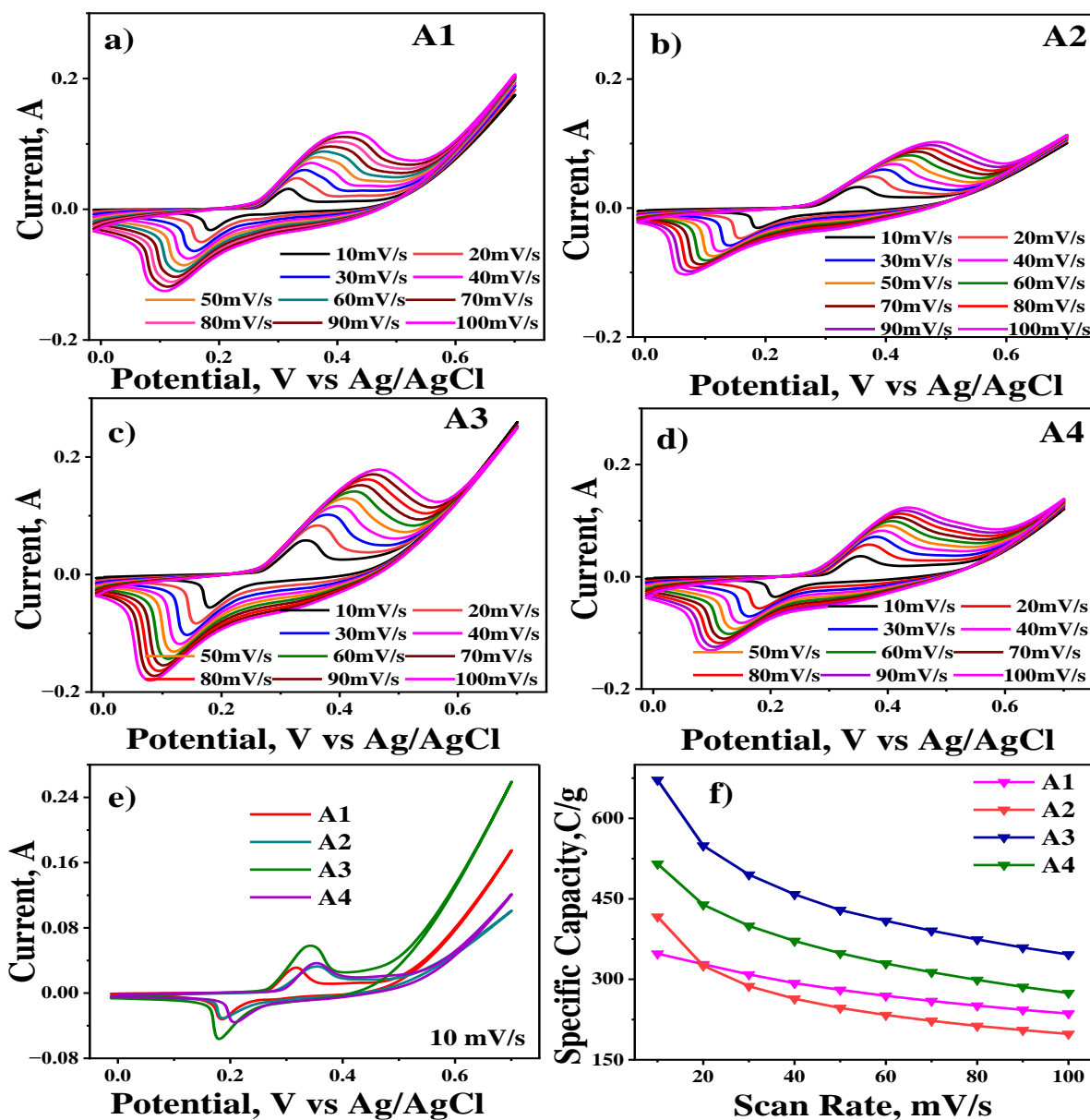


Fig. 8.5. a-d) The CV scans of electrodes prepared with $\text{Ni}_x\text{Mn}_{1-x}\text{MoO}_4$ at different values of x . e) The comparison of the CV scan of all electrodes at 10mV/s. f) The variation of specific capacity of these electrodes with scan rate.

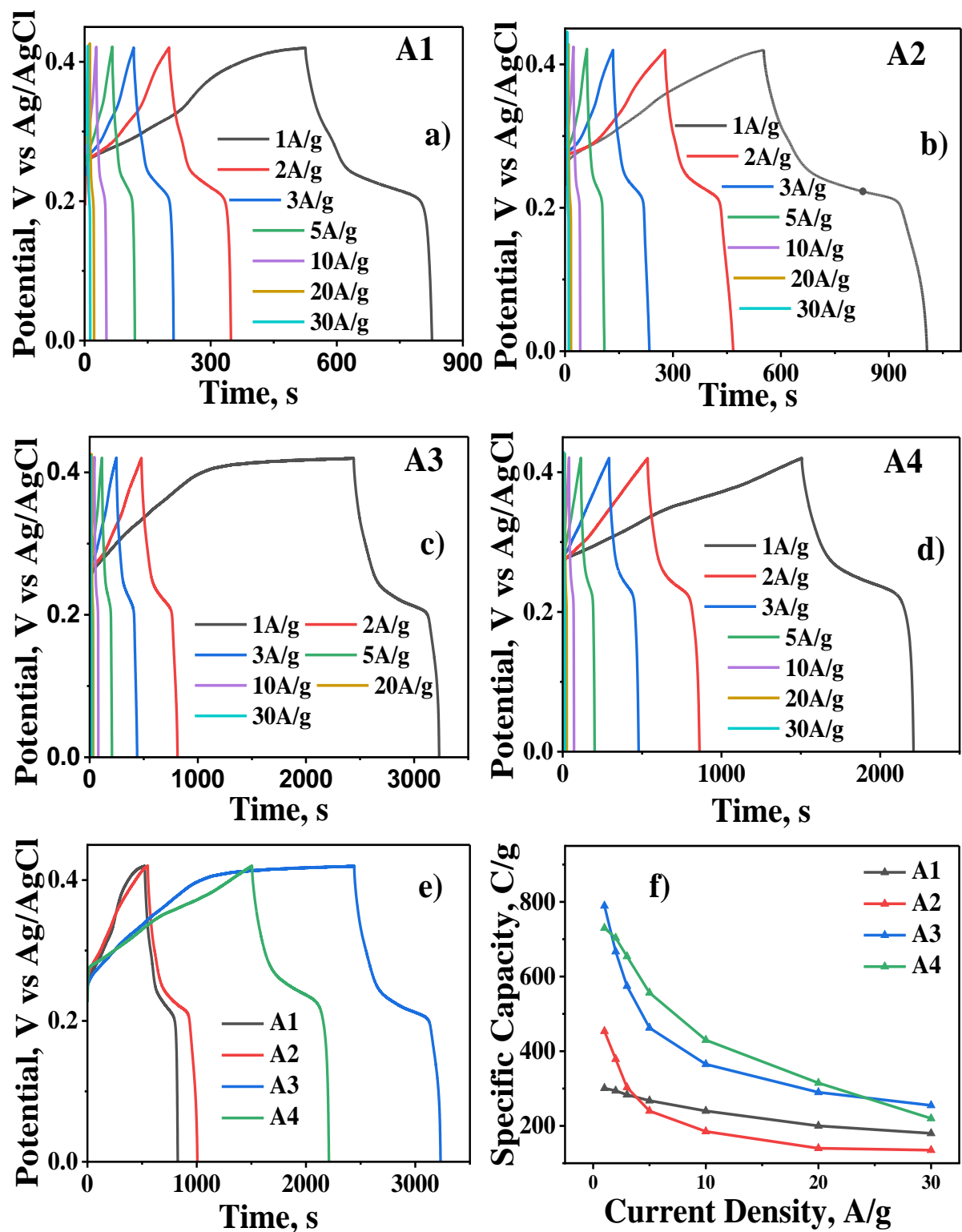


Fig. 8.6. a-d) The GCD curves of electrodes prepared with $\text{Ni}_x\text{Mn}_{1-x}\text{MoO}_4$ at different values of x . e) The comparison of GCD curves of all electrodes at 1 A/g. f) The variation of specific capacity of these electrodes with current density.

To further enhance electrochemical performance, electrochemical assessments of $\text{Ni}_{0.25}\text{Mn}_{0.75}\text{MoO}_4$ grown directly onto nickel foam ($\text{Ni}_{0.25}\text{Mn}_{0.75}\text{MoO}_4@\text{NF}$) were conducted, as depicted in Fig. 8.7 (a-d). The cyclic voltammetry (CV) analysis in Fig. 8.7(a), within the potential window of 0.01-0.7V, illustrates that the integrated area beneath the curve surpasses that of the binder-enriched A3 sample (Fig. 8.7(c)) across all scan rates. Consequently, the binder-free electrode demonstrates a notably higher specific capacity, registering 1039 Cg^{-1} at 10 mVs^{-1} , marking a 35.4% improvement compared to its binder-enriched counterpart. The specific capacity variations of the binder-free electrode at various scan rates are illustrated in Fig. 8.7(b). Comparable trends are observed in the galvanostatic charging-discharging profiles at various current densities, as presented in Fig. 8.7(c-d). The binder-free electrode showcases an extended discharging duration of 1297.5s and exhibits a significantly higher specific capacity of 1297.5 Cg^{-1} at 1 Ag^{-1} , demonstrating a notable 39.1% enhancement compared to the binder-enriched variant. The comparison of the specific capacity of the developed binder-enriched and binder-free $\text{Ni}_{0.25}\text{Mn}_{0.75}\text{MoO}_4@\text{NF}$ electrodes is done with the other reported electrodes prepared with similar material in Table 8.1. The augmented performance of the binder-free $\text{Ni}_{0.25}\text{Mn}_{0.75}\text{MoO}_4@\text{NF}$ can be noticed.

EIS was conducted within a three-electrode setup, revealing insightful Nyquist plots for the studied electrodes (Fig. 8.7(e)). Among the binder-enriched and the binder-free electrodes, the Nyquist plot of the binder-free electrode demonstrated a more pronounced and steeper slope than the binder-enriched electrode, signifying significantly reduced diffusion resistance within the binder-free electrode system. The equivalent circuit diagram shown in Fig. 8.7(e) features an arrangement comprising an equivalent resistance (R_s) in series with bulk and grain-boundary impedances, each composed of resistive and phase elements (R_B and CPE_B for bulk, R_{GB} and CPE_{GB} for grain boundaries). The impedance of the phase element is described by ω^{-N} , where ω represents angular frequency and N is a distribution factor [205]. The calculated values of various circuit components are detailed in Table 8.2. The relatively low R_s values observed in both binder-free and binder-enriched electrodes suggest minimal resistance contribution from the connecting leads or experimental setup in both configurations. Fitted values indicate increased ion movement restrictions at the grain boundaries compared to the more conducive charge transport in the bulk material. Furthermore, the detrimental impact of the binder on charge transport is evident from the significantly smaller R_B and R_{GB} values observed in the

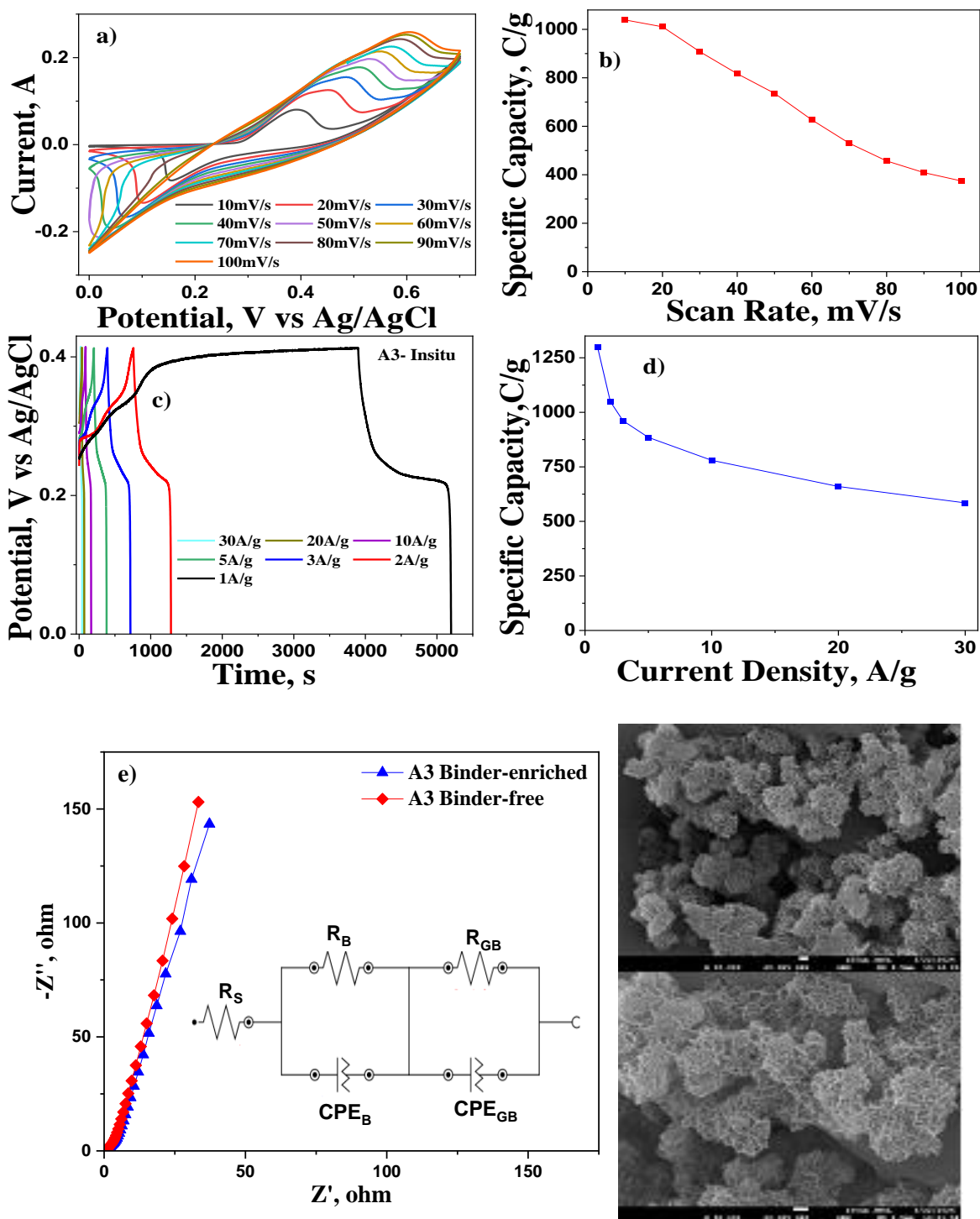


Fig. 8.7 a) The CV curves at different scan rates, b) the variation of specific capacity with scan rate. c) the GCD curves at different current densities, d) the variation of specific capacity with a current density of binder-free $\text{Ni}_{0.25}\text{Mn}_{0.75}\text{MoO}_4$ nanoparticles-based electrode. e) The EIS curves of binder-enriched and binder-free $\text{Ni}_{0.25}\text{Mn}_{0.75}\text{MoO}_4$ nanoparticles-based electrodes and their equivalent circuit. f) The FESEM images of $\text{Ni}_{0.25}\text{Mn}_{0.75}\text{MoO}_4$ nanoparticles directly grown on the nickel form.

Table 8.2. The fitted values of various components of the equivalent circuit of binder-enriched and binder-free electrodes.

Sample	R_s (Ω)	R_b (Ω)	R_{GB} (Ω)	CPE_b	CPE_{GB}	N_b	N_{GB}	Ionic conductivity (S/cm)
Binder-enriched	0.72	18.23	985	0.01893	0.01078	0.6	0.99	4.9×10^{-5}
Binder-free	0.92	5.02	785	0.01871	0.0066	0.62	0.91	6.3×10^{-5}

binder-free electrode. Ionic conductivities, calculated by combining bulk and grain boundary resistances, affirm the superior performance of the binder-free electrode over the binder-enriched counterpart. The fitted distribution factor values for bulk and grain boundaries of both electrodes suggest a tendency towards capacitive behavior in both impedance components. Furthermore, the electronic conductivity of binder-free and binder-enriched electrodes was measured using a four-probe setup. The measured values were 28.7 and 12.2 Scm^{-1} , respectively, which align well with the aforementioned findings. Additionally, the FESEM images (Fig. 8.7 (f)) of $\text{Ni}_{0.25}\text{Mn}_{0.75}\text{MoO}_4$ nanoparticles directly grown on the nickel foam displayed a mesoporous spherical morphology, clearly demonstrating the availability of an enhanced active surface area to facilitate electrochemical interactions. These distinctive observations imply high-rate charge-transfer capabilities and accelerated kinetics inherent in the binder-free $\text{Ni}_{0.25}\text{Mn}_{0.75}\text{MoO}_4$ electrode.

The comprehensive analysis encompassing CV, GCD, and EIS underscores the advantageous impact of incorporating nickel into $\text{Ni}_x\text{Mn}_{1-x}\text{MoO}_4$, significantly enhancing various aspects critical to electrochemical performance. The introduction of nickel has notably augmented conductivity, heightened redox activity, bolstered structural stability, and facilitated ion diffusion. This augmentation potentially triggers synergistic effects that collectively elevate the overall electrochemical efficiency. Furthermore, the direct synthesis of $\text{Ni}_{0.25}\text{Mn}_{0.75}\text{MoO}_4$ on nickel foam has notably bolstered electrode performance by circumventing the drawbacks associated with binders. Binders conventionally impede electron transfer and occupy space within the electrode, restraining direct contact between active material particles. They contribute additional weight and volume, diminishing the active material content per unit volume. In contrast, binder-free electrodes possess higher active material content. Moreover, these electrodes demonstrate reduced internal resistance, enhancing electron and ion mobility within the electrode architecture. As a consequence, binder-free electrodes exhibit amplified specific capacities, high-rate charge-transfer capabilities and accelerated kinetics.

8.3. An Asymmetric Device Analysis

The utilization of binder-enriched and binder-free $\text{Ni}_{0.25}\text{Mn}_{0.75}\text{MoO}_4\text{@NF}$ anode electrodes in real applications was scrutinized by developing their asymmetric supercapacitor devices. The mass loading of around 1 mg of active anode material per cm^2 of nickel foam was considered because it is often selected as a balance between maximizing electrode performance (capacitance, conductivity) and ensuring electrode stability for supercapacitor applications. The graphite-activated carbon (GAC) on Ni-foam was considered as a cathode for both devices. The GAC-based negative electrode slurry, composed of activated carbon, graphite fine powder, PVDF, and acetylene black in 1-Methyl-2-pyrrolidinone (NMP) at a weight-percentage ratio of 6:2:1:1, was prepared. The cathode was developed by depositing the slurry on approximately 1cm^2 of nickel foam and dried for 12 hours at 60°C , bearing a mass-loading of about 3 mg of active material on the nickel foam. A 3M KOH electrolyte was employed. The optimal potential window of 1.7V was deduced from the CV profiles of both devices in Fig.8.8(a) and Fig.8.9(a), recorded at 60 mV/s with varied potential. The CV scans at different rates for both devices are displayed in Fig.8.8(b) and 8.9(b). Both devices demonstrate stability within the voltage window of 0 to 1.7 V, which was deemed optimal for subsequent tests. The shape of the CV curves indicates contributions from both Faradic and double-layer mechanisms in the energy storage process. The shifting of redox peaks across scan rates (from 10 to 200mVs^{-1}) revealed alterations in charge storage mechanisms. The GCD curves (Fig.8.8(c) and 8.9(c)) demonstrated near-symmetrical profiles, attributed to reversible redox phenomena. Supercapacitor device utilizing binder-enriched $\text{Ni}_{0.25}\text{Mn}_{0.75}\text{MoO}_4$ electrodes displayed discharging durations of 198.5 s and a specific capacity of 198Cg^{-1} at 1Ag^{-1} , with a resultant energy density (E_g) of 46.7Whkg^{-1} at 850Wkg^{-1} . The robustness of the binder-free $\text{Ni}_{0.25}\text{Mn}_{0.75}\text{MoO}_4\text{@NF//GAC}$ configuration is evident as it demonstrates 47.3Whkg^{-1} at 8300Wkg^{-1} . Power density and energy density variations, shown in Fig. 8.8 (d) and 8.9(d), imply an inverse relationship between the two. To achieve a more accurate value, we have calculated energy density (E_i) through integration as shown in Fig. 8.8 (d) and 8.9(d). This comprehensive evaluation provides a detailed understanding of the device's energy storage capabilities under varying conditions. The device utilizing binder-enriched $\text{Ni}_{0.25}\text{Mn}_{0.75}\text{MoO}_4$ electrodes exhibited a maximum integral energy density (E_i) of 31.7Whkg^{-1} at a power density of 576.3Wkg^{-1} , whereas the binder-free device $\text{Ni}_{0.25}\text{Mn}_{0.75}\text{MoO}_4\text{@NF//GAC}$ displays an integral energy density (E_i) of 97.6Whkg^{-1} at a power density of 539Wkg^{-1} . The asymmetric device with

a binder-free electrode demonstrated remarkable cycle life, retaining 98.7% of its specific capacity over 10000 cycles, whereas the binder-enriched counterpart retained only 80.7%. Nyquist plots (Fig. 8.8(f) and 8.9(e)) of the binder-enriched supercapacitor pre- and post-10000 cycles indicated minimal structural and morphological degradation, while the binder-free asymmetric supercapacitor showed no degradation rather a possible enhancement is seen. The FESEM images of the binder-free $\text{Ni}_{0.25}\text{Mn}_{0.75}\text{MoO}_4\text{@NF}$ were captured after 10,000 cycles, and for reference, one image is shown in Fig. 8.9f). The image clearly demonstrates the morphological stability; however, some pore opening and slight broadening are observed compared to the images (Fig. 8.7(f)) taken before the galvanostatic charge-discharge (GCD) cycles due to continuous inward and outward motion of the electrolyte ions. The equivalent circuit of the device depicted in Fig. 8.9(g) closely resembles that plotted for the anodes in Fig. 8.7(f), with the notable addition of an inductor in the second impedance component. It should be noted that the values of various circuit components reflect the contributions of the anode, cathode, and electrolyte. The estimated values of the circuit components for the device fall within a similar range to those of the anode circuit. However, the presence of an inductive effect in the device circuit may be attributed to the restrictions imposed by the connecting leads or other external accessories used during measurements. The impedance analysis observations corroborate the GCD results of both devices. The influence of the binder on the device's electrochemical performance is clearly evident in these outcomes. The comparison between the current work and previously reported research is conducted through the Ragone plot depicted in Fig. 8.10 and Table 8.1. It's evident that the binder-free $\text{Ni}_{0.25}\text{Mn}_{0.75}\text{MoO}_4\text{//GAC}$ -based device has surpassed the electrochemical performance of all recently reported $\text{NiMoO}_4/\text{MnMoO}_4$ -based devices. This superior performance of binder-free device is attributed to enhanced conductivity, increased redox activity, improved structural stability, and facilitated ion diffusion after the optimized addition of nickel to manganese molybdate.

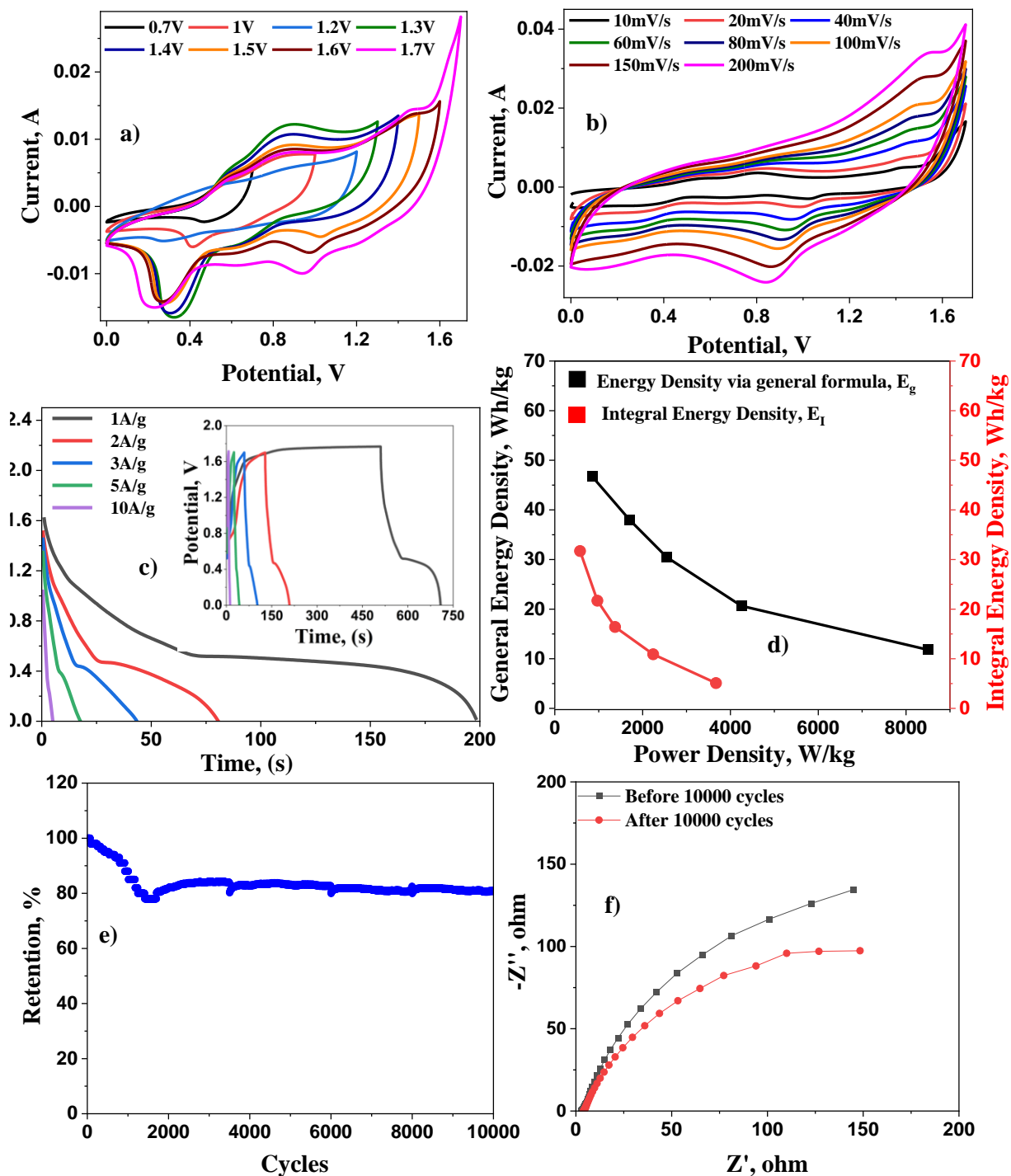


Fig. 8.8. The CV curves at various voltage windows **a)**, different scan rates **b)**, GCD curves at various current densities **c)**, power density and energy density variation **d)** with current density, percentage specific capacitance retention variation **e)** with cycle number, and Nyquist Plots **f)** of the binder-enriched $\text{Ni}_{0.25}\text{Mn}_{0.75}\text{MoO}_4@\text{NF} // \text{GAC}$ asymmetric device.

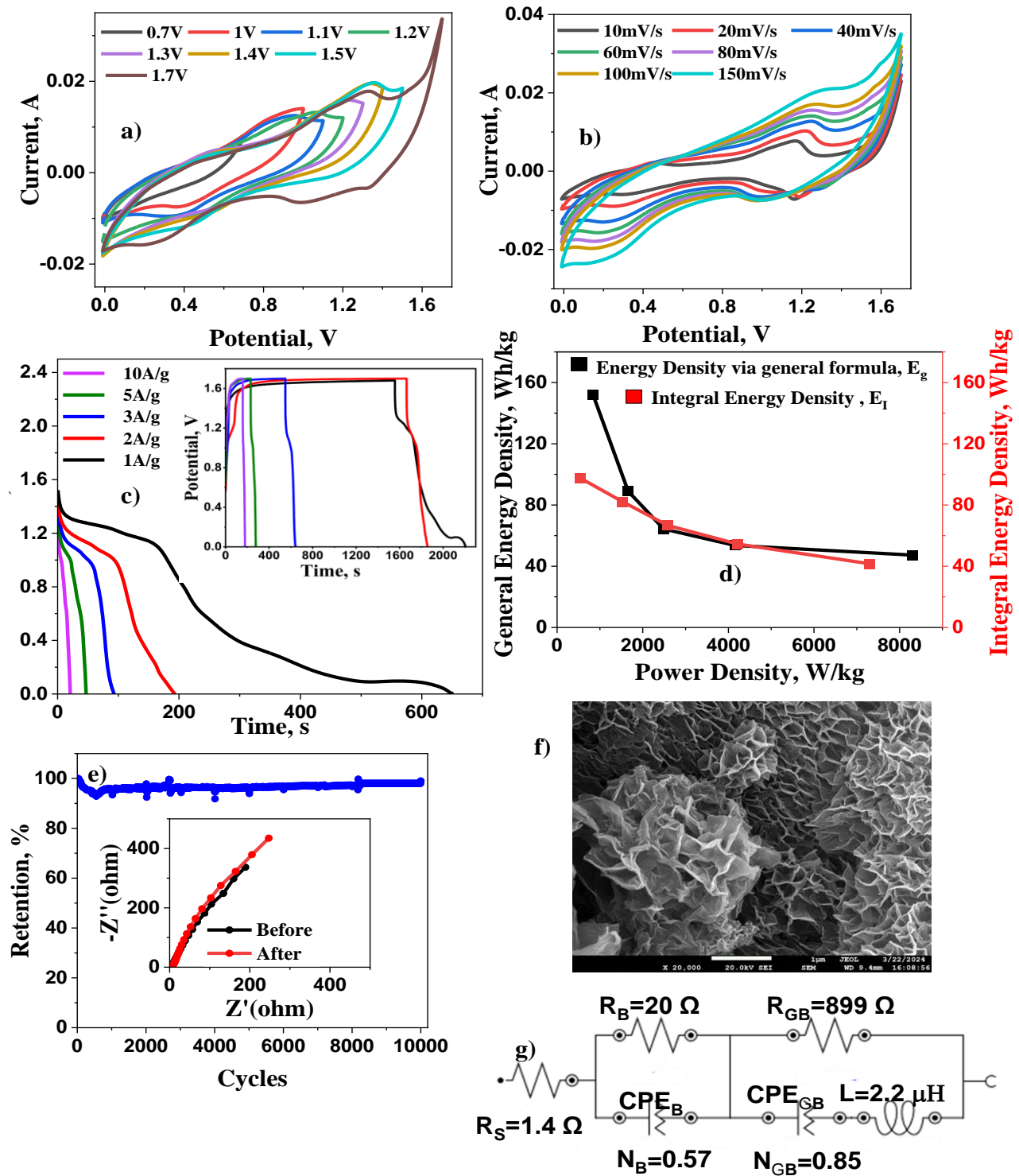


Fig. 8.9 The CV curves at various voltage windows **a)**, different scan rates **b)**, GCD curves at various current densities **c)**, power density and energy density variation **d)** with current density, percentage specific capacitance retention variation **e)** with cycle number, Nyquist Plots (inset) of the binder-free $\text{Ni}_{0.25}\text{Mn}_{0.75}\text{MoO}_4@\text{NF} // \text{GAC}$ asymmetric device. **f)** The FESEM image of the binder-free anode after 10000 cycles. **g)** The equivalent of the device.

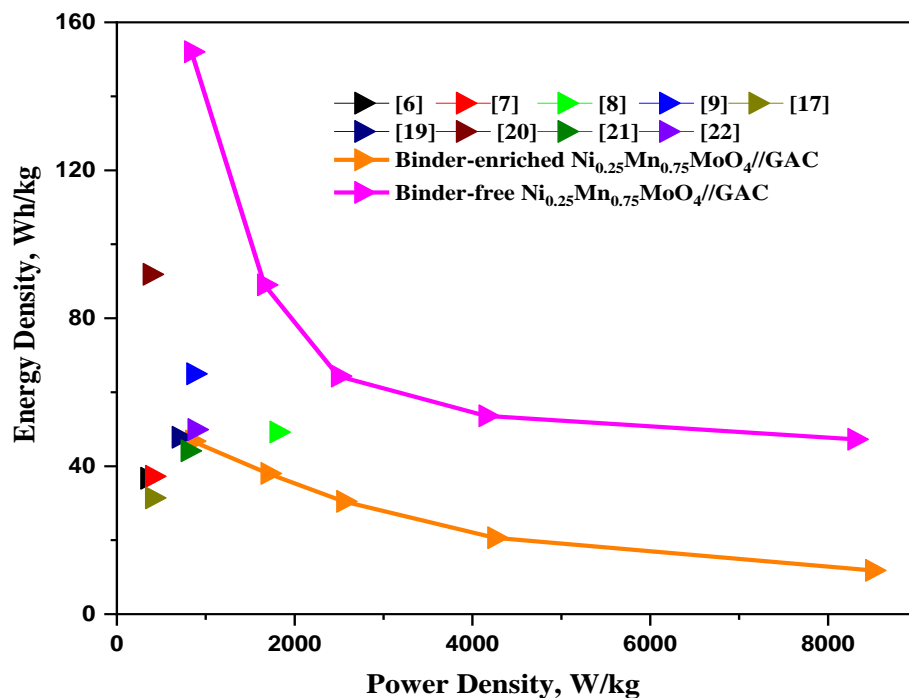


Fig. 8.10. The Ragone plot displaying the comparison of the present and the previously reported work.

Conclusion

In summary, this study underscores the promising role of elemental doping, particularly the synthesis of $\text{Ni}_{0.25}\text{Mn}_{0.75}\text{MoO}_4$, to address critical challenges in enhancing electrode material performance. The hydrothermal synthesis method led to the creation of mesoporous $\text{Ni}_{0.25}\text{Mn}_{0.75}\text{MoO}_4$ nanoparticles with diverse shapes and sizes in a nanoplate morphology, showcasing remarkable electrochemical properties. The direct growth of $\text{Ni}_{0.25}\text{Mn}_{0.75}\text{MoO}_4$ on Ni foam displayed a boosted specific capacity of 1297Cg^{-1} at 1Ag^{-1} , signifying its potential as a robust electrode material. The inclusion of nickel has possibly enhanced conductivity, increased redox activity, improved structural stability, and aided ion diffusion. Furthermore, the exceptional performance of the asymmetric supercapacitor utilizing binder-free $\text{Ni}_{0.25}\text{Mn}_{0.75}\text{MoO}_4@\text{NF}$ as the positive electrode highlighted an impressive energy density of 152Whkg^{-1} (97.6Whkg^{-1}) at a power density of 840Wkg^{-1} (539Wkg^{-1}), coupled with outstanding retention of 98.7% after 10000 cycles. These findings validate the significant promise of $\text{Ni}_{0.25}\text{Mn}_{0.75}\text{MoO}_4$ in advancing the development of future energy storage devices.

Chapter 9

Conclusions and Future Scope

This thesis systematically investigated the enhancement of MnMoO₄-based electrode materials for electrochemical capacitors through various strategic modifications, including mass loading optimization, calcination effects, compositing with carbonaceous materials and MoS₂, as well as Ni doping.

Initially, MnMoO₄ nanoribbons were synthesized via a one-step hydrothermal method, and electrodes were fabricated in situ with varying mass loadings. The electrode with a low mass loading (0.1 mg) exhibited exceptional electrochemical performance, achieving a high specific capacitance of 9000 F g⁻¹ at 5 A g⁻¹, with excellent retention of 72.5% after 1000 cycles at 50 A g⁻¹, highlighting its potential for high-performance supercapacitor applications.

Subsequently, the effect of calcination temperature on MnMoO₄ nanoparticles was explored. The nanoparticles, synthesized via a microwave-assisted method and calcinated at different temperatures, demonstrated optimal electrochemical performance at 500°C due to improved surface area and conductivity. The optimized electrode achieved a high specific capacitance of 3688.09 F g⁻¹ (1549 C g⁻¹) at 2 A g⁻¹.

To further enhance electrochemical performance, MnMoO₄ was composited with graphene oxide (GO) to evaluate their synergistic effects. The rGO@MnMoO₄ microrods, synthesized via a hydrothermal technique, exhibited significantly improved electrochemical properties. The controlled oxidation of GO, particularly with a 4-hour stirring duration (GO(G4)), resulted in the best synergistic effects. The optimized electrode demonstrated a high specific capacitance of 3092 F g⁻¹ (1299 C g⁻¹) at 2 A g⁻¹, attributed to the microporous MnMoO₄ structure, which increased the electroactive surface area, and rGO, which enhanced electrical conductivity.

Furthermore, to explore the combined effect of MnMoO₄ and MoS₂, a MoS₂@MnMoO₄ composite was synthesized using a two-step hydrothermal process. The composite, featuring granules and nanorods, exhibited enhanced energy storage capabilities by leveraging MoS₂'s high ionic conductivity and large surface area alongside MnMoO₄'s electrochemical durability. The optimized electrode achieved a high specific capacitance of 1720.2 F g⁻¹ (722.5 C g⁻¹) at 1 A g⁻¹, outperforming the individual components.

Additionally, the effect of elemental doping was investigated by incorporating Ni into MnMoO_4 to form a $\text{Ni}_x\text{Mn}_{1-x}\text{MoO}_4$ composite. The composite was synthesized via a hydrothermal method and exhibited a nanoplate and nanoparticle morphology. Optimization at different Ni concentrations revealed that the best-performing electrode, featuring a mesoporous nanoplate structure, achieved a high specific capacitance of 3089.2 F g^{-1} (1297 C g^{-1}) at 1 A g^{-1} . The incorporation of nickel contributed to enhanced conductivity, redox activity, and ion diffusion.

Additionally, a Ragone plot depicted in Fig. 9.1 illustrates the relationship between energy density and power density for all developed devices, providing valuable insight into their electrochemical performance. The analysis presented above, along with the Ragone plot in Fig. 9.1, demonstrates that elemental doping significantly enhances the performance of both the electrode and the supercapacitor device, leading to exceptional electrochemical properties.

In conclusion, these findings contribute significantly to the ongoing advancement of high-performance electrode materials for next-generation energy storage systems.

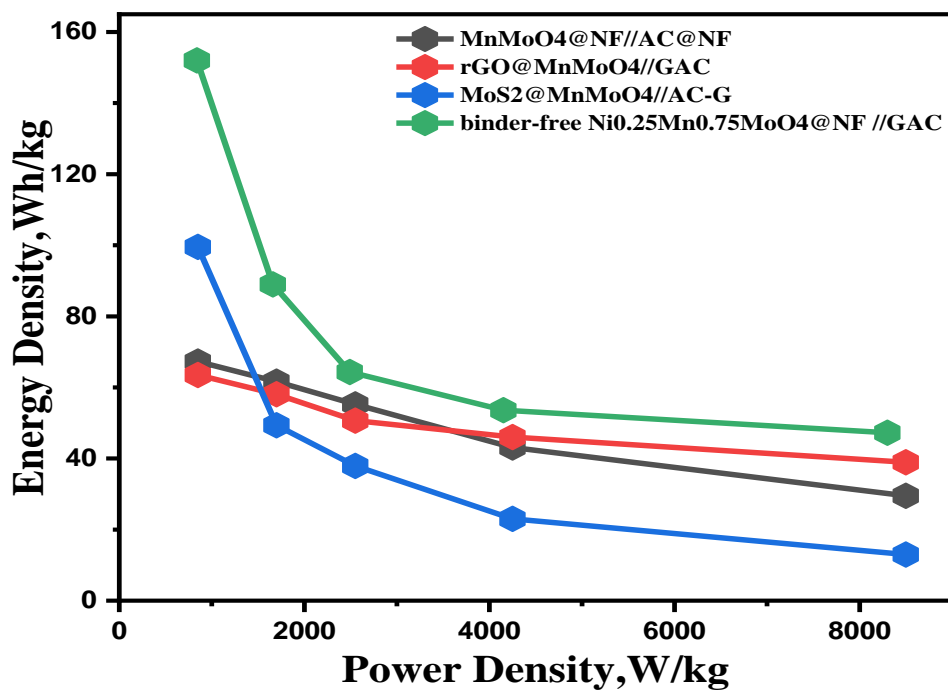


Fig. 9.1. Ragone Plot to compare the energy density of all asymmetric devices.

Metal molybdates hold significant potential for advancing both scientific research and industrial applications, particularly in the field of energy storage. Their versatile structural and electronic properties make them promising candidates for next-generation electrochemical capacitors and hybrid energy storage systems. Due to their ability to facilitate fast redox reactions, excellent electrochemical stability, and high theoretical capacities, metal molybdates can be effectively engineered to enhance energy storage performance. In this thesis, we focused on enhanced MnMoO_4 -based electrode materials for electrochemical capacitors by varying mass loadings, studied the calcination effect, compositing with carbonaceous or MoS_2 , and doping. However, compared to batteries, the supercapacitor technology is still in the early stages of research. The gap between supercapacitors and other energy storage devices can be further bridged by integrating fuel cell or battery-type electrodes with supercapacitor electrodes, enabling a combination of their respective characteristics. Numerous challenges need to be highlighted, ranging from synthesis to the development of devices. Here are some recommended future researches:

- More nanocomposites of MnMoO_4 with carbon materials or another conductive substrate can be developed to enhance conductivity in electrode material. Additionally, research can be done on some methods that can introduce or manipulate defects within the crystal structure of MnMoO_4 . So, the electrical conductivity of the electrode can be significantly improved.
- By using various molybdenum sources, research can focus on producing metal molybdate-supported perovskites materials known for excellent electronic properties, Pyrochlore oxides known for their stability, and MXenes 2D materials derived from layered carbides and nitrides with high electrical conductivity and diverse morphologies.
- Hybrid Halide perovskites are wonder materials with superior optoelectronic properties and mixed electronic conductivity. Therefore, these materials are good alternatives for energy storage devices.
- Different types of negative electrodes can be used to enhance the overall efficiency of supercapacitors instead of activated carbon and graphite-based activated carbon that we used in our research work

- Future research can focus on the design of supercapacitors like coin cells or cylindrical cells that can thoroughly or quantitatively evaluate the efficiency of electrochemical supercapacitors.
- Future research can focus on aligning the pore size of electrode materials with the ion size of the electrolyte to enhance the overall performance of supercapacitors. However, further fundamental experiments are needed to gain a comprehensive understanding of this relationship.
- Future research can also focus on different combinations in the fabrication of hybrid devices, especially by using battery or fuel cell electrodes with supercapacitor electrodes.

References

- [1] J.-M. Tarascon, “Key challenges in future Li-battery research,” *Philos. Trans. R. Soc. Math. Phys. Eng. Sci.*, vol. 368, no. 1923, pp. 3227–3241, Jul. 2010, doi: 10.1098/rsta.2010.0112.
- [2] S. Tanwar, A. Arya, A. Gaur, and A. L. Sharma, “Transition metal dichalcogenide (TMDs) electrodes for supercapacitors: a comprehensive review,” *J. Phys. Condens. Matter*, vol. 33, no. 30, p. 303002, Jul. 2021, doi: 10.1088/1361-648X/abfb3c.
- [3] P. A. Shinde, Q. Abbas, N. R. Chodankar, K. Ariga, M. A. Abdelkareem, and A. G. Olabi, “Strengths, weaknesses, opportunities, and threats (SWOT) analysis of supercapacitors: A review,” *J. Energy Chem.*, vol. 79, pp. 611–638, Apr. 2023, doi: 10.1016/j.jechem.2022.12.030.
- [4] I. Shaheen *et al.*, “Recent advancements in metal oxides for energy storage materials: Design, classification, and electrodes configuration of supercapacitor,” *J. Energy Storage*, vol. 72, p. 108719, Nov. 2023, doi: 10.1016/j.est.2023.108719.
- [5] D. A. Cullen *et al.*, “New roads and challenges for fuel cells in heavy-duty transportation,” *Nat. Energy*, vol. 6, no. 5, pp. 462–474, Mar. 2021, doi: 10.1038/s41560-021-00775-z.
- [6] O. Z. Sharaf and M. F. Orhan, “An overview of fuel cell technology: Fundamentals and applications,” *Renew. Sustain. Energy Rev.*, vol. 32, pp. 810–853, Apr. 2014, doi: 10.1016/j.rser.2014.01.012.
- [7] M. Winter and R. J. Brodd, “What Are Batteries, Fuel Cells, and Supercapacitors?,” *Chem. Rev.*, vol. 104, no. 10, pp. 4245–4270, Oct. 2004, doi: 10.1021/cr020730k.
- [8] D. Liu and G. Cao, “Engineering nanostructured electrodes and fabrication of film electrodes for efficient lithium ion intercalation,” *Energy Environ. Sci.*, vol. 3, no. 9, p. 1218, 2010, doi: 10.1039/b922656g.
- [9] X. Zhang, Q. Lu, H. Liu, K. Li, and M. Wei, “Nature-inspired design of NiS/carbon microspheres for high-performance hybrid supercapacitors,” *Appl. Surf. Sci.*, vol. 528, p. 146976, Oct. 2020, doi: 10.1016/j.apsusc.2020.146976.
- [10] Z. Sun, Y. Wang, Z. Chen, and X. Li, “Min-max game based energy management strategy for fuel cell/supercapacitor hybrid electric vehicles,” *Appl. Energy*, vol. 267, p. 115086, Jun. 2020, doi: 10.1016/j.apenergy.2020.115086.
- [11] C. Zhang *et al.*, “Unlocking the Electrocatalytic Activity of Chemically Inert Amorphous Carbon-Nitrogen for Oxygen Reduction: Discerning and Refactoring Chaotic Bonds,” *ChemElectroChem*, vol. 4, no. 6, pp. 1269–1273, Jun. 2017, doi: 10.1002/celc.201700106.
- [12] A. R. Dehghani-Sani, E. Tharumalingam, M. B. Dusseault, and R. Fraser, “Study of energy storage systems and environmental challenges of batteries,” *Renew. Sustain. Energy Rev.*, vol. 104, pp. 192–208, Apr. 2019, doi: 10.1016/j.rser.2019.01.023.
- [13] M. A. Abdelkareem, K. Elsaid, T. Wilberforce, M. Kamil, E. T. Sayed, and A. Olabi, “Environmental aspects of fuel cells: A review,” *Sci. Total Environ.*, vol. 752, p. 141803, Jan. 2021, doi: 10.1016/j.scitotenv.2020.141803.
- [14] U. S. Sani and I. H. Shanono, “A Review on Supercapacitors,” vol. 6, no. 2.
- [15] M. Mustaqeem *et al.*, “Rational design of metal oxide based electrode materials for high performance supercapacitors – A review,” *J. Energy Storage*, vol. 55, p. 105419, Nov. 2022, doi: 10.1016/j.est.2022.105419.
- [16] G. Wang, L. Zhang, and J. Zhang, “A review of electrode materials for electrochemical supercapacitors,” *Chem Soc Rev*, vol. 41, no. 2, pp. 797–828, 2012, doi: 10.1039/C1CS15060J.

- [17] K.-Y. Chan, B. Jia, H. Lin, N. Hameed, J.-H. Lee, and K.-T. Lau, "A critical review on multifunctional composites as structural capacitors for energy storage," *Compos. Struct.*, vol. 188, pp. 126–142, Mar. 2018, doi: 10.1016/j.compstruct.2017.12.072.
- [18] B. E. Conway and E. Gileadi, "Kinetic theory of pseudo-capacitance and electrode reactions at appreciable surface coverage," *Trans. Faraday Soc.*, vol. 58, p. 2493, 1962, doi: 10.1039/tf9625802493.
- [19] X. Zhang *et al.*, "Mechanically strong and highly conductive graphene aerogel and its use as electrodes for electrochemical power sources," *J. Mater. Chem.*, vol. 21, no. 18, p. 6494, 2011, doi: 10.1039/c1jm10239g.
- [20] J. Gamby, P. L. Taberna, P. Simon, J. F. Fauvarque, and M. Chesneau, "Studies and characterisations of various activated carbons used for carbon/carbon supercapacitors," *J. Power Sources*, vol. 101, no. 1, pp. 109–116, Oct. 2001, doi: 10.1016/S0378-7753(01)00707-8.
- [21] A. B. Fuertes, G. Lota, T. A. Centeno, and E. Frackowiak, "Templated mesoporous carbons for supercapacitor application," *Electrochimica Acta*, vol. 50, no. 14, pp. 2799–2805, May 2005, doi: 10.1016/j.electacta.2004.11.027.
- [22] J. Lin *et al.*, "3-Dimensional Graphene Carbon Nanotube Carpet-Based Microsupercapacitors with High Electrochemical Performance," *Nano Lett.*, vol. 13, no. 1, pp. 72–78, Jan. 2013, doi: 10.1021/nl3034976.
- [23] A. G. Pandolfo and A. F. Hollenkamp, "Carbon properties and their role in supercapacitors," *J. Power Sources*, vol. 157, no. 1, pp. 11–27, Jun. 2006, doi: 10.1016/j.jpowsour.2006.02.065.
- [24] M. F. El-Kady, V. Strong, S. Dubin, and R. B. Kaner, "Laser Scribing of High-Performance and Flexible Graphene-Based Electrochemical Capacitors," *Science*, vol. 335, no. 6074, pp. 1326–1330, Mar. 2012, doi: 10.1126/science.1216744.
- [25] L. L. Zhang and X. S. Zhao, "Carbon-based materials as supercapacitor electrodes," *Chem. Soc. Rev.*, vol. 38, no. 9, p. 2520, 2009, doi: 10.1039/b813846j.
- [26] P. R. Jothi *et al.*, "Synthesis and Characterization of α -NiMoO₄ Nanorods for Supercapacitor -Application," *Eur. J. Inorg. Chem.*, vol. 2015, no. 22, pp. 3694–3699, Aug. 2015, doi: 10.1002/ejic.201500410.
- [27] H. Yang, H. Xu, M. Li, L. Zhang, Y. Huang, and X. Hu, "Assembly of NiO/Ni(OH)₂/PEDOT Nanocomposites on Contra Wires for Fiber-Shaped Flexible Asymmetric Supercapacitors," *ACS Appl. Mater. Interfaces*, vol. 8, no. 3, pp. 1774–1779, Jan. 2016, doi: 10.1021/acsami.5b09526.
- [28] I. Hussain *et al.*, "Preserved crystal phase and morphology: Electrochemical influence of copper and iron co-doped cobalt oxide and its supercapacitor applications," *Electrochimica Acta*, vol. 340, p. 135953, Apr. 2020, doi: 10.1016/j.electacta.2020.135953.
- [29] H. Kashani, L. Chen, Y. Ito, J. Han, A. Hirata, and M. Chen, "Bicontinuous nanotubular graphene–polypyrrole hybrid for high performance flexible supercapacitors," *Nano Energy*, vol. 19, pp. 391–400, Jan. 2016, doi: 10.1016/j.nanoen.2015.11.029.
- [30] M. E. Abdelhamid and G. A. Snook, "Conducting Polymers and Their Application in Supercapacitor Devices," in *Encyclopedia of Polymer Science and Technology*, 3rd ed., H. F. Mark, Ed., Wiley, 2018, pp. 1–20. doi: 10.1002/0471440264.pst666.
- [31] A. Du Pasquier, A. Laforgue, P. Simon, G. G. Amatucci, and J.-F. Fauvarque, "A Nonaqueous Asymmetric Hybrid Li[sub 4]Ti[sub 5]O[sub 12]/Poly(fluorophenylthiophene)

- Energy Storage Device,” *J. Electrochem. Soc.*, vol. 149, no. 3, p. A302, 2002, doi: 10.1149/1.1446081.
- [32] M. Zhi, C. Xiang, J. Li, M. Li, and N. Wu, “Nanostructured carbon–metal oxide composite electrodes for supercapacitors: a review,” *Nanoscale*, vol. 5, no. 1, pp. 72–88, 2013, doi: 10.1039/C2NR32040A.
- [33] D. Wu *et al.*, “MnO₂/Carbon Composites for Supercapacitor: Synthesis and Electrochemical Performance,” *Front. Mater.*, vol. 7, p. 2, Feb. 2020, doi: 10.3389/fmats.2020.00002.
- [34] J. Yan, Z. Fan, T. Wei, W. Qian, M. Zhang, and F. Wei, “Fast and reversible surface redox reaction of graphene–MnO₂ composites as supercapacitor electrodes,” *Carbon*, vol. 48, no. 13, pp. 3825–3833, Nov. 2010, doi: 10.1016/j.carbon.2010.06.047.
- [35] Y.-C. Chung *et al.*, “Hydrothermal Synthesis of CuO/RuO₂/MWCNT Nanocomposites with Morphological Variants for High Efficient Supercapacitors,” *Catalysts*, vol. 12, no. 1, p. 23, Dec. 2021, doi: 10.3390/catal12010023.
- [36] J. Mannayil, M. M. S. Jayalekshmi, and M. K. Jayaraj, “PANI/MWCNT composite electrode for supercapacitor applications,” in *Low-Dimensional Materials and Devices 2018*, N. P. Kobayashi, A. A. Talin, A. V. Davydov, and M. S. Islam, Eds., San Diego, United States: SPIE, Sep. 2018, p. 25. doi: 10.1117/12.2320545.
- [37] L. Wan *et al.*, “Fabrication of core-shell NiMoO₄@MoS₂ nanorods for high-performance asymmetric hybrid supercapacitors,” *Int. J. Hydrog. Energy*, vol. 45, no. 7, pp. 4521–4533, Feb. 2020, doi: 10.1016/j.ijhydene.2019.12.057.
- [38] M. B. Askari *et al.*, “Construction of MnCo₂O₄/rGO hybrid nanostructures as promising electrode material for high-performance pseudocapacitors,” *J. Mater. Sci. Mater. Electron.*, vol. 32, no. 11, pp. 14863–14873, Jun. 2021, doi: 10.1007/s10854-021-06039-6.
- [39] Y. Zhou *et al.*, “High-performance hierarchical MnO₂/CNT electrode for multifunctional supercapacitors,” *Carbon*, vol. 184, pp. 504–513, Oct. 2021, doi: 10.1016/j.carbon.2021.08.051.
- [40] J. Bhagwan and J. I. Han, “Formation of MWCNT/LiCo₂O₄ nanoplates and their application for hybrid supercapacitor,” *Ceram. Int.*, vol. 50, no. 7, pp. 10676–10687, Apr. 2024, doi: 10.1016/j.ceramint.2023.12.382.
- [41] N. Yu, L. Gao, S. Zhao, and Z. Wang, “Electrodeposited PbO₂ thin film as positive electrode in PbO₂/AC hybrid capacitor,” *Electrochimica Acta*, vol. 54, no. 14, pp. 3835–3841, May 2009, doi: 10.1016/j.electacta.2009.01.086.
- [42] Y.-J. Hao, L. Wang, and Q.-Y. Lai, “Preparation and electrochemical performance of nano-structured Li₂Mn₄O₉ for supercapacitor,” *J. Solid State Electrochem.*, vol. 15, no. 9, pp. 1901–1907, Sep. 2011, doi: 10.1007/s10008-010-1206-6.
- [43] T. V. Thu *et al.*, “Graphene–MnFe₂O₄–polypyrrole ternary hybrids with synergistic effect for supercapacitor electrode,” *Electrochimica Acta*, vol. 314, pp. 151–160, Aug. 2019, doi: 10.1016/j.electacta.2019.05.042.
- [44] M. Ciszewski, D. Janas, and K. K. Koziol, “Copper-Decorated CNTs as a Possible Electrode Material in Supercapacitors,” *Batteries*, vol. 5, no. 3, p. 60, Sep. 2019, doi: 10.3390/batteries5030060.
- [45] X. Fu, “of the Requirement for the Degree”.
- [46] J.-S. Lee, S.-I. Kim, J.-C. Yoon, and J.-H. Jang, “Chemical Vapor Deposition of Mesoporous Graphene Nanoballs for Supercapacitor,” *ACS Nano*, vol. 7, no. 7, pp. 6047–6055, Jul. 2013, doi: 10.1021/nn401850z.

- [47] B. Li *et al.*, “Nitrogen-doped activated carbon for a high energy hybrid supercapacitor,” *Energy Environ. Sci.*, vol. 9, no. 1, pp. 102–106, 2016, doi: 10.1039/C5EE03149D.
- [48] Q. Cheng, J. Tang, J. Ma, H. Zhang, N. Shinya, and L.-C. Qin, “Graphene and carbon nanotube composite electrodes for supercapacitors with ultra-high energy density,” *Phys. Chem. Chem. Phys.*, vol. 13, no. 39, p. 17615, 2011, doi: 10.1039/c1cp21910c.
- [49] J. Wei, G. Lin, Y. Wang, X. He, C. Zhao, and X. Zhao, “Integrated carbon spheres on nickel foam as electrode for supercapacitors,” *Micro Nano Lett.*, vol. 8, no. 3, pp. 151–154, Mar. 2013, doi: 10.1049/mnl.2012.0885.
- [50] C.-C. Hu, W.-C. Chen, and K.-H. Chang, “How to Achieve Maximum Utilization of Hydrous Ruthenium Oxide for Supercapacitors,” *J. Electrochem. Soc.*, vol. 151, no. 2, p. A281, 2004, doi: 10.1149/1.1639020.
- [51] A. A. Kashale *et al.*, “Binder free 2D aligned efficient MnO₂ micro flowers as stable electrodes for symmetric supercapacitor applications,” *RSC Adv.*, vol. 7, no. 59, pp. 36886–36894, 2017, doi: 10.1039/C7RA05655A.
- [52] M. Huang, X. L. Zhao, F. Li, L. L. Zhang, and Y. X. Zhang, “Facile synthesis of ultrathin manganese dioxide nanosheets arrays on nickel foam as advanced binder-free supercapacitor electrodes,” *J. Power Sources*, vol. 277, pp. 36–43, Mar. 2015, doi: 10.1016/j.jpowsour.2014.12.005.
- [53] K. Liang, X. Tang, W. Hu, and Y. Yang, “Ultrafine V₂O₅ Nanowires in 3D Current Collector for High-Performance Supercapacitor,” *ChemElectroChem*, vol. 3, no. 5, pp. 704–708, May 2016, doi: 10.1002/celec.201500541.
- [54] A. Ali *et al.*, “Hydrothermally Synthesized Cobalt Oxide Nanowires on Nickel Foam for High-Performance Energy-Storage Applications,” *J. Electrochem. Soc.*, vol. 167, no. 10, p. 100509, Jun. 2020, doi: 10.1149/1945-7111/ab971f.
- [55] Q. Liu, Q. Yan, S. Wu, J. Wang, and H. Liu, “Ultrathin Porous NiO Nanoflake Arrays on Nickel Foam as Binder-free Electrodes for Supercapacitors,” *Electrochemistry*, vol. 84, no. 4, pp. 219–223, 2016, doi: 10.5796/electrochemistry.84.219.
- [56] G. Li, Z. Chang, T. Li, and K. Wang, “In situ growth of hexagonal prism-like Ni(OH)₂ microrods on nickel foam as binder-free electrodes,” *Ionics*, vol. 25, no. 12, pp. 5881–5888, Dec. 2019, doi: 10.1007/s11581-019-03171-6.
- [57] Y. Zhang, X. Xia, J. Kang, and J. Tu, “Hydrothermal synthesized porous Co(OH)₂ nanoflake film for supercapacitor application,” *Chin. Sci. Bull.*, vol. 57, no. 32, pp. 4215–4219, Nov. 2012, doi: 10.1007/s11434-012-5291-z.
- [58] D. Cai *et al.*, “Iron Oxide Nanoneedles Anchored on N-Doped Carbon Nanoarrays as an Electrode for High-Performance Hybrid Supercapacitor,” *ACS Appl. Energy Mater.*, vol. 3, no. 12, pp. 12162–12171, Dec. 2020, doi: 10.1021/acsaem.0c02238.
- [59] M. Rajesh *et al.*, “Expedition and eco-friendly hydrothermal polymerization of PEDOT nanoparticles for binder-free high performance supercapacitor electrodes,” *RSC Adv.*, vol. 6, no. 111, pp. 110433–110443, 2016, doi: 10.1039/C6RA22958A.
- [60] K. Wang, J. Huang, and Z. Wei, “Conducting Polyaniline Nanowire Arrays for High Performance Supercapacitors,” *J. Phys. Chem. C*, vol. 114, no. 17, pp. 8062–8067, May 2010, doi: 10.1021/jp9113255.
- [61] H. Zhang, G. Cao, Z. Wang, Y. Yang, Z. Shi, and Z. Gu, “Growth of Manganese Oxide Nanoflowers on Vertically-Aligned Carbon Nanotube Arrays for High-Rate Electrochemical Capacitive Energy Storage,” *Nano Lett.*, vol. 8, no. 9, pp. 2664–2668, Sep. 2008, doi: 10.1021/nl800925j.

- [62] R. K. Sharma, A. C. Rastogi, and S. B. Desu, "Manganese oxide embedded polypyrrole nanocomposites for electrochemical supercapacitor," *Electrochimica Acta*, vol. 53, no. 26, pp. 7690–7695, Nov. 2008, doi: 10.1016/j.electacta.2008.04.028.
- [63] H.-P. Cong, X.-C. Ren, P. Wang, and S.-H. Yu, "Flexible graphene–polyaniline composite paper for high-performance supercapacitor," *Energy Environ. Sci.*, vol. 6, no. 4, p. 1185, 2013, doi: 10.1039/c2ee24203f.
- [64] Z. Zhu, G. Wang, M. Sun, X. Li, and C. Li, "Fabrication and electrochemical characterization of polyaniline nanorods modified with sulfonated carbon nanotubes for supercapacitor applications," *Electrochimica Acta*, vol. 56, no. 3, pp. 1366–1372, Jan. 2011, doi: 10.1016/j.electacta.2010.10.070.
- [65] H. Pang *et al.*, "Microwave-assisted synthesis of NiS₂ nanostructures for supercapacitors and cocatalytic enhancing photocatalytic H₂ production," *Sci. Rep.*, vol. 4, no. 1, p. 3577, Jan. 2014, doi: 10.1038/srep03577.
- [66] Y. Ji *et al.*, "A facile template-free approach for the solid-phase synthesis of CoS₂ nanocrystals and their enhanced storage energy in supercapacitors," *RSC Adv*, vol. 4, no. 91, pp. 50220–50225, 2014, doi: 10.1039/C4RA08614G.
- [67] M. Acerce, D. Voiry, and M. Chhowalla, "Metallic 1T phase MoS₂ nanosheets as supercapacitor electrode materials," *Nat. Nanotechnol.*, vol. 10, no. 4, pp. 313–318, Apr. 2015, doi: 10.1038/nnano.2015.40.
- [68] K.-J. Huang, J.-Z. Zhang, and Y. Fan, "One-step solvothermal synthesis of different morphologies CuS nanosheets compared as supercapacitor electrode materials," *J. Alloys Compd.*, vol. 625, pp. 158–163, Mar. 2015, doi: 10.1016/j.jallcom.2014.11.137.
- [69] Z. Pu, Q. Liu, C. Tang, A. M. Asiri, and X. Sun, "Ni₂P nanoparticle films supported on a Ti plate as an efficient hydrogen evolution cathode," *Nanoscale*, vol. 6, no. 19, pp. 11031–11034, Aug. 2014, doi: 10.1039/C4NR03037K.
- [70] E. G. Da Silveira Firmiano *et al.*, "Supercapacitor Electrodes Obtained by Directly Bonding 2D MoS₂ on Reduced Graphene Oxide," *Adv. Energy Mater.*, vol. 4, no. 6, p. 1301380, Apr. 2014, doi: 10.1002/aenm.201301380.
- [71] H. Huo, Y. Zhao, and C. Xu, "3D Ni₃S₂ nanosheet arrays supported on Ni foam for high-performance supercapacitor and non-enzymatic glucose detection," *J. Mater. Chem. A*, vol. 2, no. 36, p. 15111, Jul. 2014, doi: 10.1039/C4TA02857K.
- [72] Q. Wang *et al.*, "Morphology evolution of urchin-like NiCo₂O₄ nanostructures and their applications as pseudocapacitors and photoelectrochemical cells," *J. Mater. Chem.*, vol. 22, no. 40, p. 21647, 2012, doi: 10.1039/c2jm34705a.
- [73] Y. Zhao, L. Hu, S. Zhao, and L. Wu, "Preparation of MnCo₂O₄@Ni(OH)₂ Core–Shell Flowers for Asymmetric Supercapacitor Materials with Ultrahigh Specific Capacitance," *Adv. Funct. Mater.*, vol. 26, no. 23, pp. 4085–4093, Jun. 2016, doi: 10.1002/adfm.201600494.
- [74] B. Liu *et al.*, "New Energy Storage Option: Toward ZnCo₂O₄ Nanorods/Nickel Foam Architectures for High-Performance Supercapacitors," *ACS Appl. Mater. Interfaces*, vol. 5, no. 20, pp. 10011–10017, Oct. 2013, doi: 10.1021/am402339d.
- [75] Y. Wang, P. He, W. Lei, F. Dong, and T. Zhang, "Novel FeMoO₄/graphene composites based electrode materials for supercapacitors," *Compos. Sci. Technol.*, vol. 103, pp. 16–21, Oct. 2014, doi: 10.1016/j.compscitech.2014.08.009.

- [76] L.-Q. Mai, F. Yang, Y.-L. Zhao, X. Xu, L. Xu, and Y.-Z. Luo, "Hierarchical MnMoO₄/CoMoO₄ heterostructured nanowires with enhanced supercapacitor performance," *Nat. Commun.*, vol. 2, no. 1, p. 381, Jul. 2011, doi: 10.1038/ncomms1387.
- [77] Q. Liao, N. Li, S. Jin, G. Yang, and C. Wang, "All-Solid-State Symmetric Supercapacitor Based on Co₃O₄ Nanoparticles on Vertically Aligned Graphene," *ACS Nano*, vol. 9, no. 5, pp. 5310–5317, May 2015, doi: 10.1021/acs.nano.5b00821.
- [78] D. Guo *et al.*, "NiMoO₄ nanowires supported on Ni foam as novel advanced electrodes for supercapacitors," *J. Mater. Chem. A*, vol. 1, no. 32, p. 9024, 2013, doi: 10.1039/c3ta11487b.
- [79] K. Xu *et al.*, "Hierarchical mesoporous NiCo₂O₄@MnO₂ core-shell nanowire arrays on nickel foam for aqueous asymmetric supercapacitors," *J. Mater. Chem. A*, vol. 2, no. 13, p. 4795, 2014, doi: 10.1039/c3ta14647b.
- [80] X. Feng *et al.*, "Self-assembly of 3D hierarchical MnMoO₄/NiWO₄ microspheres for high-performance supercapacitor," *J. Alloys Compd.*, vol. 763, pp. 801–807, Sep. 2018, doi: 10.1016/j.jallcom.2018.06.025.
- [81] Y. Jiang and J. Liu, "Definitions of Pseudocapacitive Materials: A Brief Review," *ENERGY Environ. Mater.*, vol. 2, no. 1, pp. 30–37, Mar. 2019, doi: 10.1002/eem2.12028.
- [82] A. Mendhe and H. S. Panda, "A review on electrolytes for supercapacitor device," *Discov. Mater.*, vol. 3, no. 1, p. 29, Oct. 2023, doi: 10.1007/s43939-023-00065-3.
- [83] J. Feng, Y. Wang, Y. Xu, Y. Sun, Y. Tang, and X. Yan, "Ion regulation of ionic liquid electrolytes for supercapacitors," *Energy Environ. Sci.*, vol. 14, no. 5, pp. 2859–2882, 2021, doi: 10.1039/D0EE04002A.
- [84] S. S. Shah and Md. A. Aziz, "Properties of Electrode Materials and Electrolytes in Supercapacitor Technology," *J. Chem. Environ.*, pp. 1–45, Feb. 2024, doi: 10.56946/jce.v3i1.309.
- [85] L. Li *et al.*, "Flexible double-cross-linked cellulose-based hydrogel and aerogel membrane for supercapacitor separator," *J. Mater. Chem. A*, vol. 6, no. 47, pp. 24468–24478, 2018, doi: 10.1039/C8TA07751G.
- [86] C. Y. Bon *et al.*, "Flexible poly(vinyl alcohol)-ceramic composite separators for supercapacitor applications," *J. Ind. Eng. Chem.*, vol. 68, pp. 173–179, Dec. 2018, doi: 10.1016/j.jiec.2018.07.043.
- [87] E. G. Calvo, F. Lufrano, P. Staiti, A. Brigandì, A. Arenillas, and J. A. Menéndez, "Optimizing the electrochemical performance of aqueous symmetric supercapacitors based on an activated carbon xerogel," *J. Power Sources*, vol. 241, pp. 776–782, Nov. 2013, doi: 10.1016/j.jpowsour.2013.03.065.
- [88] N. R. Chodankar, D. P. Dubal, G. S. Gund, and C. D. Lokhande, "Flexible all-solid-state MnO₂ thin films based symmetric supercapacitors," *Electrochimica Acta*, vol. 165, pp. 338–347, May 2015, doi: 10.1016/j.electacta.2015.02.246.
- [89] A. Bello, F. Barzegar, D. Momodu, J. Dangbegnon, F. Taghizadeh, and N. Manyala, "Symmetric supercapacitors based on porous 3D interconnected carbon framework," *Electrochimica Acta*, vol. 151, pp. 386–392, Jan. 2015, doi: 10.1016/j.electacta.2014.11.051.
- [90] Q. Xie *et al.*, "Sandwich-like nitrogen-enriched porous carbon/graphene composites as electrodes for aqueous symmetric supercapacitors with high energy density," *Electrochimica Acta*, vol. 189, pp. 22–31, Jan. 2016, doi: 10.1016/j.electacta.2015.12.087.

- [91] M. Manuraj, K. V. Kavya Nair, K. N. N. Unni, and R. B. Rakhi, "High performance supercapacitors based on MoS₂ nanostructures with near commercial mass loading," *J. Alloys Compd.*, vol. 819, p. 152963, Apr. 2020, doi: 10.1016/j.jallcom.2019.152963.
- [92] D. P. Dubal, A. D. Jagadale, and C. D. Lokhande, "Big as well as light weight portable, Mn₃O₄ based symmetric supercapacitive devices: Fabrication, performance evaluation and demonstration," *Electrochimica Acta*, vol. 80, pp. 160–170, Oct. 2012, doi: 10.1016/j.electacta.2012.06.124.
- [93] M. R. Waikar *et al.*, "Electrochemical performance of Polyaniline based symmetrical energy storage device," *Mater. Sci. Semicond. Process.*, vol. 120, p. 105291, Dec. 2020, doi: 10.1016/j.mssp.2020.105291.
- [94] A. Kumar, A. Sanger, A. Kumar, Y. K. Mishra, and R. Chandra, "Performance of High Energy Density Symmetric Supercapacitor Based on Sputtered MnO₂ Nanorods," *ChemistrySelect*, vol. 1, no. 13, pp. 3885–3891, Aug. 2016, doi: 10.1002/slct.201600757.
- [95] O. Gerard, A. Numan, S. Krishnan, M. Khalid, R. Subramaniam, and R. Kasi, "A review on the recent advances in binder-free electrodes for electrochemical energy storage application," *J. Energy Storage*, vol. 50, p. 104283, Jun. 2022, doi: 10.1016/j.est.2022.104283.
- [96] S. Najib and E. Erdem, "Current progress achieved in novel materials for supercapacitor electrodes: mini review," *Nanoscale Adv.*, vol. 1, no. 8, pp. 2817–2827, 2019, doi: 10.1039/C9NA00345B.
- [97] M. Kim and J. Kim, "Development of high power and energy density microsphere silicon carbide–MnO₂ nanoneedles and thermally oxidized activated carbon asymmetric electrochemical supercapacitors," *Phys. Chem. Chem. Phys.*, vol. 16, no. 23, p. 11323, 2014, doi: 10.1039/c4cp01141d.
- [98] C. Zhang, L. Xie, W. Song, J. Wang, G. Sun, and K. Li, "Electrochemical performance of asymmetric supercapacitor based on Co₃O₄/AC materials," *J. Electroanal. Chem.*, vol. 706, pp. 1–6, Oct. 2013, doi: 10.1016/j.jelechem.2013.07.032.
- [99] M. Cheng, S. Duan, H. Fan, X. Su, Y. Cui, and R. Wang, "Core@shell CoO@Co₃O₄ nanocrystals assembling mesoporous microspheres for high performance asymmetric supercapacitors," *Chem. Eng. J.*, vol. 327, pp. 100–108, Nov. 2017, doi: 10.1016/j.cej.2017.06.042.
- [100] J. Huang *et al.*, "Asymmetric supercapacitors based on β-Ni(OH)₂ nanosheets and activated carbon with high energy density," *J. Power Sources*, vol. 246, pp. 371–376, Jan. 2014, doi: 10.1016/j.jpowsour.2013.07.105.
- [101] H. Kim *et al.*, "High-Performance Hybrid Supercapacitor Based on Graphene-Wrapped Li₄Ti₅O₁₂ and Activated Carbon," *ChemElectroChem*, vol. 1, no. 1, pp. 125–130, Jan. 2014, doi: 10.1002/celec.201300186.
- [102] R. Arian, A. M. Zardkhoshoui, and S. S. Hosseiny Davarani, "Rational Construction of Core-Shell Ni–Mn–Co–S@Co(OH)₂ Nanoarrays toward High-Performance Hybrid Supercapacitors," *ChemElectroChem*, vol. 7, no. 13, pp. 2816–2825, Jul. 2020, doi: 10.1002/celec.202000611.
- [103] A. Muzaffar and M. B. Ahamed, "Iron molybdate and manganese dioxide microrods as a hybrid structure for high-performance supercapacitor applications," *Ceram. Int.*, vol. 45, no. 3, pp. 4009–4015, Feb. 2019, doi: 10.1016/j.ceramint.2018.11.078.

- [104] H.-J. Kim *et al.*, “A Comprehensive Review of Li-Ion Battery Materials and Their Recycling Techniques,” *Electronics*, vol. 9, no. 7, p. 1161, Jul. 2020, doi: 10.3390/electronics9071161.
- [105] D. H. Nagaraju, Q. Wang, P. Beaujuge, and H. N. Alshareef, “Two-dimensional heterostructures of V_2O_5 and reduced graphene oxide as electrodes for high energy density asymmetric supercapacitors,” *J Mater Chem A*, vol. 2, no. 40, pp. 17146–17152, 2014, doi: 10.1039/C4TA03731F.
- [106] L. Lai *et al.*, “Controllable synthesis of reduced graphene oxide/nickel hydroxide composites with different morphologies for high performance supercapacitors,” *J. Alloys Compd.*, vol. 820, p. 153120, Apr. 2020, doi: 10.1016/j.jallcom.2019.153120.
- [107] A. I. Abdel-Salam, S. Y. Attia, F. I. El-Hosiny, M. A. Sadek, S. G. Mohamed, and M. M. Rashad, “Facile one-step hydrothermal method for NiCo₂S₄/rGO nanocomposite synthesis for efficient hybrid supercapacitor electrodes,” *Mater. Chem. Phys.*, vol. 277, p. 125554, Feb. 2022, doi: 10.1016/j.matchemphys.2021.125554.
- [108] D. Yi, F. Hui, Z. Fengjun, F. Youchun, and Z. Qicai, “Preparation of MnMoO₄·XH₂O (X=0.9, 1.5) by a Microemulsion Method under Different Manganese Precursors and Analysis of Their Band-gap Energy,” *Rare Met. Mater. Eng.*, vol. 46, no. 1, pp. 68–72, Jan. 2017, doi: 10.1016/S1875-5372(17)30079-6.
- [109] L. Zhang *et al.*, “Fabrication of Metal Molybdate Micro/Nanomaterials for Electrochemical Energy Storage,” *Small*, vol. 13, no. 33, p. 1700917, Sep. 2017, doi: 10.1002/sml.201700917.
- [110] M. Isacfranklin *et al.*, “Hydrothermal Method–Derived MnMoO₄ Crystals: Effect of Cationic Surfactant on Microstructures and Electrochemical Properties,” *ChemistrySelect*, vol. 5, no. 26, pp. 7728–7733, Jul. 2020, doi: 10.1002/slct.202001384.
- [111] L. Huang, J. Xiang, W. Zhang, C. Chen, H. Xu, and Y. Huang, “3D interconnected porous NiMoO₄ nanoplate arrays on Ni foam as high-performance binder-free electrode for supercapacitors,” *J. Mater. Chem. A*, vol. 3, no. 44, pp. 22081–22087, 2015, doi: 10.1039/C5TA05644F.
- [112] S. Peng, L. Li, H. B. Wu, S. Madhavi, and X. W. (David) Lou, “Controlled Growth of NiMoO₄ Nanosheet and Nanorod Arrays on Various Conductive Substrates as Advanced Electrodes for Asymmetric Supercapacitors,” *Adv. Energy Mater.*, vol. 5, no. 2, p. 1401172, Jan. 2015, doi: 10.1002/aenm.201401172.
- [113] M. Yao, Z. Hu, Y. Liu, and P. Liu, “A novel synthesis of size-controllable mesoporous NiMoO₄ nanospheres for supercapacitor applications,” *Ionics*, vol. 22, no. 5, pp. 701–709, May 2016, doi: 10.1007/s11581-015-1587-8.
- [114] L. An, T. Ma, Y. Nie, and J. Wang, “Study of Nd-NiMoO₄ Nanocomposites Prepared by Sol–Gel Method and Their Capacitive Properties,” *Coatings*, vol. 14, no. 3, p. 330, Mar. 2024, doi: 10.3390/coatings14030330.
- [115] X. Feng *et al.*, “Heterostructure arrays of NiMoO₄ nanoflakes on N-doping of graphene for high-performance asymmetric supercapacitors,” *J. Alloys Compd.*, vol. 816, p. 152625, Mar. 2020, doi: 10.1016/j.jallcom.2019.152625.
- [116] C. Teng *et al.*, “Synthesis of coaxial carbon@NiMoO₄ composite nanofibers for supercapacitor electrodes,” *RSC Adv.*, vol. 8, no. 57, pp. 32979–32984, 2018, doi: 10.1039/C8RA05912H.
- [117] M. Minakshi, T. Watcharatharapong, S. Chakraborty, and R. Ahuja, “A combined theoretical and experimental approach of a new ternary metal oxide in molybdate composite

- for hybrid energy storage capacitors,” *APL Mater.*, vol. 6, no. 4, p. 047701, Apr. 2018, doi: 10.1063/1.4994750.
- [118] J. Wang, J. Chang, L. Wang, and J. Hao, “One-step and low-temperature synthesis of CoMoO₄ nanowire arrays on Ni foam for asymmetric supercapacitors,” *Ionics*, vol. 24, no. 12, pp. 3967–3973, Dec. 2018, doi: 10.1007/s11581-018-2552-0.
- [119] L. Liu, D. Dai, B. Yang, B. Li, and X. Liu, “Green preparation of CoMoO₄ nanoparticles through a mechanochemical method for energy storage applications,” *New J. Chem.*, vol. 46, no. 48, pp. 23369–23378, 2022, doi: 10.1039/D2NJ04351C.
- [120] H. Long, T. Liu, W. Zeng, Y. Yang, and S. Zhao, “CoMoO₄ nanosheets assembled 3D-frameworks for high-performance energy storage,” *Ceram. Int.*, vol. 44, no. 2, pp. 2446–2452, Feb. 2018, doi: 10.1016/j.ceramint.2017.10.216.
- [121] J. Li *et al.*, “Synthesis of monodispersed CoMoO₄ nanoclusters on the ordered mesoporous carbons for environment-friendly supercapacitors,” *J. Alloys Compd.*, vol. 810, p. 151841, Nov. 2019, doi: 10.1016/j.jallcom.2019.151841.
- [122] M.-C. Liu, L.-B. Kong, C. Lu, X.-M. Li, Y.-C. Luo, and L. Kang, “Facile fabrication of CoMoO₄ nanorods as electrode material for electrochemical capacitors,” *Mater. Lett.*, vol. 94, pp. 197–200, Mar. 2013, doi: 10.1016/j.matlet.2012.12.057.
- [123] Y.-P. Gao, K.-J. Huang, C.-X. Zhang, S.-S. Song, and X. Wu, “High-performance symmetric supercapacitor based on flower-like zinc molybdate,” *J. Alloys Compd.*, vol. 731, pp. 1151–1158, Jan. 2018, doi: 10.1016/j.jallcom.2017.10.161.
- [124] P. Sivakumar, L. Kulandaivel, J. Park, C. J. Raj, R. Ramesh, and H. Jung, “Rational design and fabrication of one-dimensional hollow cuboid-like FeMoO₄ architecture as a high performance electrode for hybrid supercapacitor,” *Ceram. Int.*, vol. 48, no. 19, pp. 29144–29151, Oct. 2022, doi: 10.1016/j.ceramint.2022.05.064.
- [125] L. Gurusamy, L. Karuppasamy, S. Anandan, C.-H. Liu, and J. J. Wu, “Recent advances on metal molybdate-based electrode materials for supercapacitor application,” *J. Energy Storage*, vol. 79, p. 110122, Feb. 2024, doi: 10.1016/j.est.2023.110122.
- [126] L. H. D. S. Lacerda and M. A. San-Miguel, “Unraveling the MnMoO₄ polymorphism: a comprehensive DFT investigation of α , β , and ω phases,” *J. Mater. Sci.*, vol. 57, no. 22, pp. 10179–10196, Jun. 2022, doi: 10.1007/s10853-022-07277-7.
- [127] M. Jang, T. J. R. Weakley, and K. M. Doxsee, “Aqueous Crystallization of Manganese(II) Group 6 Metal Oxides,” *Chem. Mater.*, vol. 13, no. 2, pp. 519–525, Feb. 2001, doi: 10.1021/cm000754c.
- [128] S. Lei, K. Tang, Q. Liu, Z. Fang, Q. Yang, and H. Zheng, “Preparation of manganese molybdate rods and hollow olive-like spheres,” *J. Mater. Sci.*, vol. 41, no. 15, pp. 4737–4743, Aug. 2006, doi: 10.1007/s10853-006-0044-5.
- [129] C. Zhang *et al.*, “Manganese molybdate nanoflakes on silicon microchannel plates as novel nano energetic material,” *R. Soc. Open Sci.*, vol. 4, no. 12, p. 171229, Dec. 2017, doi: 10.1098/rsos.171229.
- [130] Z. Zhu *et al.*, “Mini-review: progress on micro/nanoscale MnMoO₄ as an electrode material for advanced supercapacitor applications,” *Mater. Chem. Front.*, vol. 5, no. 20, pp. 7403–7418, 2021, doi: 10.1039/D1QM00914A.
- [131] K. K. Purushothaman, M. Cuba, and G. Muralidharan, “Supercapacitor behavior of α -MnMoO₄ nanorods on different electrolytes,” *Mater. Res. Bull.*, vol. 47, no. 11, pp. 3348–3351, Nov. 2012, doi: 10.1016/j.materresbull.2012.07.027.

- [132] L. Wang *et al.*, “Synthesis of 3D α -MnMoO₄ hierarchical architectures for high-performance supercapacitor applications,” *CrystEngComm*, vol. 18, no. 48, pp. 9286–9291, 2016, doi: 10.1039/C6CE02051H.
- [133] S. M. Babulal *et al.*, “Synthesis of MnMoO₄ Nanorods by a Simple Co-Precipitation Method in Presence of Polyethylene Glycol for Pseudocapacitor Application,” *Int. J. Electrochem. Sci.*, vol. 15, no. 7, pp. 7053–7063, Jul. 2020, doi: 10.20964/2020.07.90.
- [134] S. Jayasubramaniyan, S. Balasundari, P. A. Rayjada, N. Satyanarayana, and P. Muralidharan, “Microwave hydrothermal synthesis of α -MnMoO₄ nanorods for high electrochemical performance supercapacitors,” *RSC Adv.*, vol. 8, no. 40, pp. 22559–22568, 2018, doi: 10.1039/C8RA02751J.
- [135] B. Senthilkumar, R. K. Selvan, D. Meyrick, and M. Minakshi, “Synthesis and Characterization of Manganese Molybdate for Symmetric Capacitor Applications,” *Int. J. Electrochem. Sci.*, vol. 10, no. 1, pp. 185–193, Jan. 2015, doi: 10.1016/S1452-3981(23)04985-4.
- [136] R. Sheng, J. Hu, X. Lu, W. Jia, J. Xie, and Y. Cao, “Solid-state synthesis and superior electrochemical performance of MnMoO₄ nanorods for asymmetric supercapacitor,” *Ceram. Int.*, vol. 47, no. 11, pp. 16316–16323, Jun. 2021, doi: 10.1016/j.ceramint.2021.02.211.
- [137] P. Prabakaran *et al.*, “Construction of hierarchical MnMoO₄ nanostructures on Ni foam for high-performance asymmetric supercapacitors,” *Surf. Interfaces*, vol. 40, p. 103086, Aug. 2023, doi: 10.1016/j.surf.2023.103086.
- [138] S. B. Patil, B. Kishore, M. K. Nagaraj, N. Ganganagappa, and U. Velu, “Mesoporous MnMoO₄ Nanorods for Enhanced Electrochemical Performance,” *ChemistrySelect*, vol. 3, no. 26, pp. 7490–7495, Jul. 2018, doi: 10.1002/slct.201800803.
- [139] Y. Cao *et al.*, “MnMoO₄ · 4H₂O nanoplates grown on a Ni foam substrate for excellent electrochemical properties,” *J Mater Chem A*, vol. 2, no. 48, pp. 20723–20728, 2014, doi: 10.1039/C4TA04019H.
- [140] G. K. Veerasubramani, K. Krishnamoorthy, R. Sivaprakasam, and S. J. Kim, “Sonochemical synthesis, characterization, and electrochemical properties of MnMoO₄ nanorods for supercapacitor applications,” *Mater. Chem. Phys.*, vol. 147, no. 3, pp. 836–842, Oct. 2014, doi: 10.1016/j.matchemphys.2014.06.028.
- [141] X. Mu *et al.*, “A high energy density asymmetric supercapacitor from ultrathin manganese molybdate nanosheets,” *Electrochimica Acta*, vol. 211, pp. 217–224, Sep. 2016, doi: 10.1016/j.electacta.2016.06.072.
- [142] Y. Liu *et al.*, “Uniform P-Doped MnMoO₄ Nanosheets for Enhanced Asymmetric Supercapacitors Performance,” *Molecules*, vol. 29, no. 9, p. 1988, Apr. 2024, doi: 10.3390/molecules29091988.
- [143] Y. Lu *et al.*, “Electrospun porous MnMoO₄ nanotubes as high-performance electrodes for asymmetric supercapacitors,” *J. Solid State Electrochem.*, vol. 22, no. 3, pp. 657–666, Mar. 2018, doi: 10.1007/s10008-017-3781-2.
- [144] T. Watcharatharapong *et al.*, “Effect of Transition Metal Cations on Stability Enhancement for Molybdate-Based Hybrid Supercapacitor,” *ACS Appl. Mater. Interfaces*, vol. 9, no. 21, pp. 17977–17991, May 2017, doi: 10.1021/acsami.7b03836.
- [145] D. Ghosh, S. Giri, Md. Moniruzzaman, T. Basu, M. Mandal, and C. K. Das, “ α MnMoO₄ /graphene hybrid composite: high energy density supercapacitor electrode material,” *Dalton Trans*, vol. 43, no. 28, pp. 11067–11076, 2014, doi: 10.1039/C4DT00672K.

- [146] B. Saravanakumar, S. P. Ramachandran, G. Ravi, V. Ganesh, A. Sakunthala, and R. Yuvakkumar, "Transition mixed-metal molybdates (MnMoO_4) as an electrode for energy storage applications," *Appl. Phys. A*, vol. 125, no. 1, p. 6, Jan. 2019, doi: 10.1007/s00339-018-2309-7.
- [147] G. Harichandran, P. Divya, S. Radha, and J. Yesuraj, "Facile and controllable CTAB-assisted sonochemical synthesis of one-dimensional MnWO_4 nanorods for supercapacitor application," *J. Mol. Struct.*, vol. 1199, p. 126931, Jan. 2020, doi: 10.1016/j.molstruc.2019.126931.
- [148] M. Moussa *et al.*, "Self-Assembly and Cross-Linking of Conducting Polymers into 3D Hydrogel Electrodes for Supercapacitor Applications," *ACS Appl. Energy Mater.*, vol. 3, no. 1, pp. 923–932, Jan. 2020, doi: 10.1021/acsaem.9b02007.
- [149] R. Thangappan, R. Dhinesh Kumar, and R. Jayavel, "Synthesis, structural and electrochemical properties of Mn-MoO_4 /graphene nanocomposite electrode material with improved performance for supercapacitor application," *J. Energy Storage*, vol. 27, p. 101069, Feb. 2020, doi: 10.1016/j.est.2019.101069.
- [150] D. Merum *et al.*, "Pseudocapacitive Performance of Freestanding $\text{Ni}_3\text{V}_2\text{O}_8$ Nanosheets for High Energy and Power Density Asymmetric Supercapacitors," *ACS Appl. Energy Mater.*, vol. 5, no. 5, pp. 5561–5578, May 2022, doi: 10.1021/acsaem.1c03754.
- [151] H. Cao, N. Wu, Y. Liu, S. Wang, W. Du, and J. Liu, "Facile synthesis of rod-like manganese molybdate crystallines with two-dimensional nanoflakes for supercapacitor application," *Electrochimica Acta*, vol. 225, pp. 605–613, Jan. 2017, doi: 10.1016/j.electacta.2017.01.021.
- [152] Y. Zhang *et al.*, "Microwave-assisted green synthesis of manganese molybdate nanorods for high-performance supercapacitor," *Ionics*, vol. 25, no. 9, pp. 4361–4370, Sep. 2019, doi: 10.1007/s11581-019-02991-w.
- [153] X. Mu *et al.*, "Construction of Hierarchical CNT/rGO-Supported MnMoO_4 Nanosheets on Ni Foam for High-Performance Aqueous Hybrid Supercapacitors," *ACS Appl. Mater. Interfaces*, vol. 9, no. 41, pp. 35775–35784, Oct. 2017, doi: 10.1021/acsaami.7b09005.
- [154] Y. Chen *et al.*, "Facile-synthesized NiCo_2O_4 @ MnMoO_4 with novel and functional structure for superior performance supercapacitors," *Appl. Surf. Sci.*, vol. 452, pp. 413–422, Sep. 2018, doi: 10.1016/j.apsusc.2018.05.026.
- [155] H. Peng *et al.*, "Ultrathin α - MnO_2 Nanosheets Wrapped on Acanthosphere-like Microspheres with Highly Reversible Performance for Energy Storage," *Electrochimica Acta*, vol. 247, pp. 745–753, Sep. 2017, doi: 10.1016/j.electacta.2017.07.055.
- [156] Y. Lv *et al.*, "Three-dimensional interconnected MnCo_2O_4 nanosheets@ MnMoO_4 nanosheets core-shell nanoarrays on Ni foam for high-performance supercapacitors," *Chem. Eng. J.*, vol. 336, pp. 64–73, Mar. 2018, doi: 10.1016/j.cej.2017.11.049.
- [157] S. Chen *et al.*, "Growth of CuCo_2O_4 @ MnMoO_4 core/shell nanosheet arrays for high energy density asymmetric supercapacitors," *Electrochimica Acta*, vol. 341, p. 135893, May 2020, doi: 10.1016/j.electacta.2020.135893.
- [158] Y. Li *et al.*, "Manganese-doped nickel molybdate nanostructures for high-performance asymmetric supercapacitors," *Chem. Eng. J.*, vol. 372, pp. 452–461, Sep. 2019, doi: 10.1016/j.cej.2019.04.167.
- [159] Z. Xie *et al.*, "Synthesis of core-shell structured Ni_3S_2 @ MnMoO_4 nanosheet arrays on Ni foam for asymmetric supercapacitors with superior performance," *J. Alloys Compd.*, vol. 874, p. 159860, Sep. 2021, doi: 10.1016/j.jallcom.2021.159860.

- [160] J. Huang, X. Qian, X. An, X. Li, and J. Guan, "Double in situ fabrication of PPY@MnMoO₄/cellulose fibers flexible electrodes with high electrochemical performance for supercapacitor applications," *Cellulose*, vol. 27, no. 10, pp. 5829–5843, Jul. 2020, doi: 10.1007/s10570-020-03154-1.
- [161] J. Bhagwan, Sk. K. Hussain, B. N. V. Krishna, and J. S. Yu, "Facile synthesis of MnMoO₄@MWCNT and their electrochemical performance in aqueous asymmetric supercapacitor," *J. Alloys Compd.*, vol. 856, p. 157874, Mar. 2021, doi: 10.1016/j.jallcom.2020.157874.
- [162] R. Thangappan, R. Dhinesh Kumar, and R. Jayavel, "Synthesis, structural and electrochemical properties of Mn-MoO₄/graphene nanocomposite electrode material with improved performance for supercapacitor application," *J. Energy Storage*, vol. 27, p. 101069, Feb. 2020, doi: 10.1016/j.est.2019.101069.
- [163] S. Jayasubramaniyan *et al.*, "Hydrothermal synthesis of novel Mn_{1/3}Ni_{1/3}Co_{1/3}MoO₄ on reduced graphene oxide with a high electrochemical performance for supercapacitors," *J. Alloys Compd.*, vol. 778, pp. 900–912, Mar. 2019, doi: 10.1016/j.jallcom.2018.11.187.
- [164] Md. W. Ahmad, S. Anand, K. Shalini, M. Ul-Islam, D.-J. Yang, and A. Choudhury, "MnMoO₄ nanorods-encapsulated carbon nanofibers hybrid mat as binder-free electrode for flexible asymmetric supercapacitors," *Mater. Sci. Semicond. Process.*, vol. 136, p. 106176, Dec. 2021, doi: 10.1016/j.mssp.2021.106176.
- [165] H. Li and H. Xuan, "Hierarchical design of Ni(OH)₂/MnMoO₄ composite on reduced graphene oxide/Ni foam for high-performances battery-supercapacitors hybrid device," *Int. J. Hydrog. Energy*, vol. 46, no. 77, pp. 38198–38211, Nov. 2021, doi: 10.1016/j.ijhydene.2021.09.083.
- [166] X. Wei, Y. Li, H. Peng, C. Liu, Y. Zhang, and P. Xiao, "Core-shell NiCo₂S₄@MnMoO₄ as an Advanced Electrode Material for High-performance Electrochemical Energy Storage," *ChemElectroChem*, vol. 4, no. 10, pp. 2634–2642, Oct. 2017, doi: 10.1002/celec.201700483.
- [167] A. Singh and A. K. Ojha, "Designing vertically aligned porous NiCo₂O₄@MnMoO₄ Core@Shell nanostructures for high-performance asymmetric supercapacitors," *J. Colloid Interface Sci.*, vol. 580, pp. 720–729, Nov. 2020, doi: 10.1016/j.jcis.2020.07.062.
- [168] C. Guo, Y. Meng, D. Yu, L. Liu, X. Zhao, and X. Liu, "Synthesis of the sandwich-type MnMoO₄@NiMoO₄@Mn₂O₃ core-shell nanostructured materials and their application in the high-performance battery-supercapacitor hybrid devices," *J. Alloys Compd.*, vol. 932, p. 167686, Jan. 2023, doi: 10.1016/j.jallcom.2022.167686.
- [169] J. Lin *et al.*, "Hybrid hollow spheres of carbon@Co_xNi_{1-x}MoO₄ as advanced electrodes for high-performance asymmetric supercapacitors," *Nanoscale*, vol. 11, no. 7, pp. 3281–3291, 2019, doi: 10.1039/C8NR09497G.
- [170] J. Yuan *et al.*, "Mn-Doped NiMoO₄ Mesoporous Nanorods/Reduced Graphene Oxide Composite for High-Performance All-Solid-State Supercapacitor," *ACS Appl. Energy Mater.*, vol. 3, no. 2, pp. 1794–1803, Feb. 2020, doi: 10.1021/acsaem.9b02238.
- [171] Y. Zhong *et al.*, "Controllable synthesis of Ni_{1-x}Co_xMoO₄ with tunable morphologies for high-performance asymmetric supercapacitors," *J. Alloys Compd.*, vol. 850, p. 156734, Jan. 2021, doi: 10.1016/j.jallcom.2020.156734.
- [172] A. A. Bunaciu, E. G. Udriștioiu, and H. Y. Aboul-Enein, "X-Ray Diffraction: Instrumentation and Applications," *Crit. Rev. Anal. Chem.*, vol. 45, no. 4, pp. 289–299, Oct. 2015, doi: 10.1080/10408347.2014.949616.

- [173] L. D. Whittig and W. R. Allardice, "X-Ray Diffraction Techniques," in *SSSA Book Series*, A. Klute, Ed., Madison, WI, USA: Soil Science Society of America, American Society of Agronomy, 2018, pp. 331–362. doi: 10.2136/sssabookser5.1.2ed.c12.
- [174] "International Journal of Engineering and Technical Research (IJETR)," *Raman Spectrosc.*, vol. 6, no. 1, 2016.
- [175] C. Berthomieu and R. Hienerwadel, "Fourier transform infrared (FTIR) spectroscopy," *Photosynth. Res.*, vol. 101, no. 2–3, pp. 157–170, Sep. 2009, doi: 10.1007/s11120-009-9439-x.
- [176] A. A. Ismail, F. R. Van De Voort, and J. Sedman, "Chapter 4 Fourier transform infrared spectroscopy: Principles and applications," in *Techniques and Instrumentation in Analytical Chemistry*, vol. 18, Elsevier, 1997, pp. 93–139. doi: 10.1016/S0167-9244(97)80013-3.
- [177] R. S. Prabhu, R. Priyanka, M. Vijay, and G. R. K. Vikashini, "Field Emission Scanning Electron Microscopy (Fesem) with A Very Big Future in Pharmaceutical Research," *Int. J. Pharm. Biol. Sci.*.
- [178] A. Mayeen, L. K. Shaji, A. K. Nair, and N. Kalarikkal, "Morphological Characterization of Nanomaterials," in *Characterization of Nanomaterials*, Elsevier, 2018, pp. 335–364. doi: 10.1016/B978-0-08-101973-3.00012-2.
- [179] A. Datar, S. Yoon, L.-C. Lin, and Y. G. Chung, "Brunauer–Emmett–Teller Areas from Nitrogen and Argon Isotherms Are Similar," *Langmuir*, vol. 38, no. 38, pp. 11631–11640, Sep. 2022, doi: 10.1021/acs.langmuir.2c01390.
- [180] J. D. Andrade, "X-ray Photoelectron Spectroscopy (XPS)," in *Surface and Interfacial Aspects of Biomedical Polymers*, J. D. Andrade, Ed., Boston, MA: Springer US, 1985, pp. 105–195. doi: 10.1007/978-1-4684-8610-0_5.
- [181] G. Greczynski and L. Hultman, "X-ray photoelectron spectroscopy: Towards reliable binding energy referencing," *Prog. Mater. Sci.*, vol. 107, p. 100591, Jan. 2020, doi: 10.1016/j.pmatsci.2019.100591.
- [182] T. L. Barr, "Recent advances in x-ray photoelectron spectroscopy studies of oxides," *J. Vac. Sci. Technol. Vac. Surf. Films*, vol. 9, no. 3, pp. 1793–1805, May 1991, doi: 10.1116/1.577464.
- [183] P. Song, A. C. Fisher, J. D. Wadhawan, J. J. Cooper, H. J. Ward, and N. S. Lawrence, "A mechanistic study of the EC' mechanism – the split wave in cyclic voltammetry and square wave voltammetry," *RSC Adv.*, vol. 6, no. 74, pp. 70237–70242, 2016, doi: 10.1039/C6RA08723J.
- [184] P. T. Kissinger and W. R. Heineman, "Cyclic voltammetry," *J. Chem. Educ.*, vol. 60, no. 9, p. 702, Sep. 1983, doi: 10.1021/ed060p702.
- [185] Yu. M. Vol'fkovich and T. M. Serdyuk, "[No title found]," *Russ. J. Electrochem.*, vol. 38, no. 9, pp. 935–959, 2002, doi: 10.1023/A:1020220425954.
- [186] H.-K. Song, Y.-H. Jung, K.-H. Lee, and L. H. Dao, "Electrochemical impedance spectroscopy of porous electrodes: the effect of pore size distribution," *Electrochimica Acta*, vol. 44, no. 20, pp. 3513–3519, Jun. 1999, doi: 10.1016/S0013-4686(99)00121-8.
- [187] H. Shao, Z. Lin, K. Xu, P.-L. Taberna, and P. Simon, "Electrochemical study of pseudocapacitive behavior of Ti3C2Tx MXene material in aqueous electrolytes," *Energy Storage Mater.*, vol. 18, pp. 456–461, Mar. 2019, doi: 10.1016/j.ensm.2018.12.017.
- [188] B. Guan, W. Sun, and Y. Wang, "Carbon-Coated MnMoO4 Nanorod for High-Performance Lithium-Ion Batteries," *Electrochimica Acta*, vol. 190, pp. 354–359, Feb. 2016, doi: 10.1016/j.electacta.2016.01.008.

- [189] Z. Xu *et al.*, “High-Energy-Density Asymmetric Supercapacitor Based on a Durable and Stable Manganese Molybdate Nanostructure Electrode for Energy Storage Systems,” *ACS Appl. Energy Mater.*, vol. 3, no. 6, pp. 5393–5404, Jun. 2020, doi: 10.1021/acsaem.0c00393.
- [190] I. Kanesaka, H. Hashiba, and I. Matsuura, “Polarized Raman spectrum and normal coordinate analysis of α -MnMoO₄,” *J. Raman Spectrosc.*, vol. 19, no. 3, pp. 213–218, May 1988, doi: 10.1002/jrs.1250190312.
- [191] H. Wang, D. Tran, J. Qian, F. Ding, and D. Losic, “MoS₂/Graphene Composites as Promising Materials for Energy Storage and Conversion Applications,” *Adv. Mater. Interfaces*, vol. 6, no. 20, p. 1900915, Oct. 2019, doi: 10.1002/admi.201900915.
- [192] M. Saraf, K. Natarajan, and S. M. Mobin, “Emerging Robust Heterostructure of MoS₂ – rGO for High-Performance Supercapacitors,” *ACS Appl. Mater. Interfaces*, vol. 10, no. 19, pp. 16588–16595, May 2018, doi: 10.1021/acsami.8b04540.
- [193] B. E. Conway, “Transition from ‘Supercapacitor’ to ‘Battery’ Behavior in Electrochemical Energy Storage,” *J. Electrochem. Soc.*, vol. 138, no. 6, pp. 1539–1548, Jun. 1991, doi: 10.1149/1.2085829.
- [194] Z. Xu *et al.*, “Interconnected network of ultrafine MnO₂ nanowires on carbon cloth with weed-like morphology for high-performance supercapacitor electrodes,” *Electrochimica Acta*, vol. 268, pp. 340–346, Apr. 2018, doi: 10.1016/j.electacta.2018.02.138.
- [195] M. I. A. Abdel Maksoud *et al.*, “Advanced materials and technologies for supercapacitors used in energy conversion and storage: a review,” *Environ. Chem. Lett.*, vol. 19, no. 1, pp. 375–439, Feb. 2021, doi: 10.1007/s10311-020-01075-w.
- [196] S. Jabeen, P. Kumar, S. Sharma, and K. S. Samra, “Binder-free MnMoO₄ nanoribbons on Ni-foam for high performance electrochemical energy storage devices,” *Mater. Lett.*, vol. 324, p. 132741, Oct. 2022, doi: 10.1016/j.matlet.2022.132741.
- [197] H. Farsi, S. Moghiminia, H. Raissi, A. Riley, and Z. Li, “The effects of electrolyte on the capacitive behavior of nanostructured molybdenum oxides,” *J. Chem. Technol. Biotechnol.*, vol. 94, no. 12, pp. 3800–3805, Dec. 2019, doi: 10.1002/jctb.6166.
- [198] F. Nti, D. A. Anang, and J. I. Han, “Facile room temperature synthesis and application of MnMoO₄·0.9H₂O as supercapacitor electrode material,” *Mater. Lett.*, vol. 217, pp. 146–150, Apr. 2018, doi: 10.1016/j.matlet.2018.01.072.
- [199] A. V. Rane, K. Kanny, V. K. Abitha, and S. Thomas, “Methods for Synthesis of Nanoparticles and Fabrication of Nanocomposites,” in *Synthesis of Inorganic Nanomaterials*, Elsevier, 2018, pp. 121–139. doi: 10.1016/B978-0-08-101975-7.00005-1.
- [200] P. G. Jamkhande, N. W. Ghule, A. H. Bamer, and M. G. Kalaskar, “Metal nanoparticles synthesis: An overview on methods of preparation, advantages and disadvantages, and applications,” *J. Drug Deliv. Sci. Technol.*, vol. 53, p. 101174, Oct. 2019, doi: 10.1016/j.jddst.2019.101174.
- [201] S. H. Jhung, T. Jin, Y. K. Hwang, and J. Chang, “Microwave Effect in the Fast Synthesis of Microporous Materials: Which Stage Between Nucleation and Crystal Growth is Accelerated by Microwave Irradiation?,” *Chem. – Eur. J.*, vol. 13, no. 16, pp. 4410–4417, May 2007, doi: 10.1002/chem.200700098.
- [202] G. Harichandran, S. Radha, P. Divya, and J. Yesuraj, “Facile morphology-controlled synthesis of nanostructured MnMoO₄ nanorods as an advance electrode material for supercapacitor application,” *J. Mater. Sci. Mater. Electron.*, vol. 31, no. 2, pp. 1646–1653, Jan. 2020, doi: 10.1007/s10854-019-02681-3.

- [203] H. Fu, M. Wang, Q. Ma, M. Wang, X. Ma, and Y. Ye, “MnMoO₄-S nanosheets with rich oxygen vacancies for high-performance supercapacitors,” *Nanoscale Adv.*, vol. 4, no. 12, pp. 2704–2712, 2022, doi: 10.1039/D2NA00148A.
- [204] Y. Xu *et al.*, “Hierarchical three-dimensional NiMoO₄-anchored rGO/Ni foam as advanced electrode material with improved supercapacitor performance,” *J. Mater. Sci.*, vol. 53, no. 11, pp. 8483–8498, Jun. 2018, doi: 10.1007/s10853-018-2171-1.
- [205] M. Saraf, K. Natarajan, and S. M. Mobin, “Microwave assisted fabrication of a nanostructured reduced graphene oxide (rGO)/Fe₂O₃ composite as a promising next generation energy storage material,” *RSC Adv.*, vol. 7, no. 1, pp. 309–317, 2017, doi: 10.1039/C6RA24766K.
- [206] M. Farshadnia, A. A. Ensafi, K. Z. Mousaabadi, B. Rezaei, and M. Demir, “Facile synthesis of NiTe₂-Co₂Te₂@rGO nanocomposite for high-performance hybrid supercapacitor,” *Sci. Rep.*, vol. 13, no. 1, p. 1364, Jan. 2023, doi: 10.1038/s41598-023-28581-5.
- [207] O. Rabbani, S. Ghasemi, and S. R. Hosseini, “Sonochemical assisted synthesis of manganese–nickel molybdate/reduced graphene oxide nanohybrid for energy storage,” *J. Alloys Compd.*, vol. 840, p. 155665, Nov. 2020, doi: 10.1016/j.jallcom.2020.155665.
- [208] S. H. Aboutalebi *et al.*, “Comparison of GO, GO/MWCNTs composite and MWCNTs as potential electrode materials for supercapacitors,” *Energy Environ. Sci.*, vol. 4, no. 5, p. 1855, 2011, doi: 10.1039/c1ee01039e.
- [209] U. A. Méndez-Romero, S. A. Pérez-García, X. Xu, E. Wang, and L. Licea-Jiménez, “Functionalized reduced graphene oxide with tunable band gap and good solubility in organic solvents,” *Carbon*, vol. 146, pp. 491–502, May 2019, doi: 10.1016/j.carbon.2019.02.023.
- [210] S. Tamang, S. Rai, M. K. Mondal, N. K. Bhattacharyya, B. P. Swain, and J. Biswas, “Microwave-assisted reduction of graphene oxide using Artemisia vulgaris extract for supercapacitor application,” *J. Mater. Sci. Mater. Electron.*, vol. 34, no. 7, p. 575, Mar. 2023, doi: 10.1007/s10854-023-09995-3.
- [211] X. H. Yau, F. W. Low, C. S. Khe, C. W. Lai, S. K. Tiong, and N. Amin, “An investigation of the stirring duration effect on synthesized graphene oxide for dye-sensitized solar cells,” *PLOS ONE*, vol. 15, no. 2, p. e0228322, Feb. 2020, doi: 10.1371/journal.pone.0228322.
- [212] S. Pei, Q. Wei, K. Huang, H.-M. Cheng, and W. Ren, “Green synthesis of graphene oxide by seconds timescale water electrolytic oxidation,” *Nat. Commun.*, vol. 9, no. 1, p. 145, Jan. 2018, doi: 10.1038/s41467-017-02479-z.
- [213] M. Kashif *et al.*, “Reaction-Time-Dependent Opto-Electrical Properties of Graphene Oxide,” *Crystals*, vol. 12, no. 9, p. 1303, Sep. 2022, doi: 10.3390/cryst12091303.
- [214] M. Sieradzka, C. Ślusarczyk, W. Biniaś, and R. Fryczkowski, “The Role of the Oxidation and Reduction Parameters on the Properties of the Reduced Graphene Oxide,” *Coatings*, vol. 11, no. 2, p. 166, Jan. 2021, doi: 10.3390/coatings11020166.
- [215] Mohd Akhair S.S. *et al.*, “Effect of graphene oxide with controlled stirring time,” *Chem. Eng. Trans.*, vol. 56, pp. 709–714, Apr. 2017, doi: 10.3303/CET1756119.
- [216] A. C. Reynosa-Martínez *et al.*, “Effect of the degree of oxidation of graphene oxide on As(III) adsorption,” *J. Hazard. Mater.*, vol. 384, p. 121440, Feb. 2020, doi: 10.1016/j.jhazmat.2019.121440.

- [217] R. Liu *et al.*, “Fundamentals, advances and challenges of transition metal compounds-based supercapacitors,” *Chem. Eng. J.*, vol. 412, p. 128611, May 2021, doi: 10.1016/j.cej.2021.128611.
- [218] J. Cherusseri, N. Choudhary, K. Sambath Kumar, Y. Jung, and J. Thomas, “Recent trends in transition metal dichalcogenide based supercapacitor electrodes,” *Nanoscale Horiz.*, vol. 4, no. 4, pp. 840–858, 2019, doi: 10.1039/C9NH00152B.
- [219] T. Wang, H. C. Chen, F. Yu, X. S. Zhao, and H. Wang, “Boosting the cycling stability of transition metal compounds-based supercapacitors,” *Energy Storage Mater.*, vol. 16, pp. 545–573, Jan. 2019, doi: 10.1016/j.ensm.2018.09.007.
- [220] A. L. Patterson, “The Scherrer Formula for X-Ray Particle Size Determination,” *Phys. Rev.*, vol. 56, no. 10, pp. 978–982, Nov. 1939, doi: 10.1103/PhysRev.56.978.
- [221] M. Cheng *et al.*, “Restoration of graphene from graphene oxide by defect repair,” *Carbon*, vol. 50, no. 7, pp. 2581–2587, Jun. 2012, doi: 10.1016/j.carbon.2012.02.016.
- [222] K. N. Kudin, B. Ozbas, H. C. Schniepp, R. K. Prud’homme, I. A. Aksay, and R. Car, “Raman Spectra of Graphite Oxide and Functionalized Graphene Sheets,” *Nano Lett.*, vol. 8, no. 1, pp. 36–41, Jan. 2008, doi: 10.1021/nl071822y.
- [223] M. D. P. Lavin-Lopez, A. Romero, J. Garrido, L. Sanchez-Silva, and J. L. Valverde, “Influence of Different Improved Hummers Method Modifications on the Characteristics of Graphite Oxide in Order to Make a More Easily Scalable Method,” *Ind. Eng. Chem. Res.*, vol. 55, no. 50, pp. 12836–12847, Dec. 2016, doi: 10.1021/acs.iecr.6b03533.
- [224] T. F. Emiru and D. W. Ayele, “Controlled synthesis, characterization and reduction of graphene oxide: A convenient method for large scale production,” *Egypt. J. Basic Appl. Sci.*, vol. 4, no. 1, pp. 74–79, Mar. 2017, doi: 10.1016/j.ejbas.2016.11.002.
- [225] K. Zhou *et al.*, “Ultrathin MoO₃ nanocrystals self-assembled on graphene nanosheets via oxygen bonding as supercapacitor electrodes of high capacitance and long cycle life,” *Nano Energy*, vol. 12, pp. 510–520, Mar. 2015, doi: 10.1016/j.nanoen.2015.01.017.
- [226] A. B. Appiagyei *et al.*, “Rational design of sucrose-derived graphitic carbon coated MnMoO₄ for high performance asymmetric supercapacitor,” *J. Energy Storage*, vol. 58, p. 106383, Feb. 2023, doi: 10.1016/j.est.2022.106383.
- [227] B. Purty, R. B. Choudhary, A. Biswas, and G. Udayabhanu, “Chemically grown mesoporous f-CNT/ α -MnO₂/PI nanocomposites as electrode materials for supercapacitor application,” *Polym. Bull.*, vol. 76, no. 4, pp. 1619–1640, Apr. 2019, doi: 10.1007/s00289-018-2458-z.
- [228] J. Wen *et al.*, “Flexible coaxial-type fiber solid-state asymmetrical supercapacitor based on Ni₃S₂ nanorod array and pen ink electrodes,” *J. Power Sources*, vol. 324, pp. 325–333, Aug. 2016, doi: 10.1016/j.jpowsour.2016.05.087.
- [229] Z. Xie *et al.*, “Synthesis of hierarchical Ni₃S₂@NiMoO₄ core-shell nanosheet arrays on Ni foam for high-performance asymmetric supercapacitors,” *J. Energy Storage*, vol. 44, p. 103459, Dec. 2021, doi: 10.1016/j.est.2021.103459.
- [230] J. Xu *et al.*, “Fabrication of hierarchical MnMoO₄·H₂O@MnO₂ core-shell nanosheet arrays on nickel foam as an advanced electrode for asymmetric supercapacitors,” *Chem. Eng. J.*, vol. 334, pp. 1466–1476, Feb. 2018, doi: 10.1016/j.cej.2017.11.085.
- [231] Y. Yuan *et al.*, “Three-Dimensional NiCo₂O₄@MnMoO₄ Core-Shell Nanoarrays for High-Performance Asymmetric Supercapacitors,” *Langmuir*, vol. 33, no. 40, pp. 10446–10454, Oct. 2017, doi: 10.1021/acs.langmuir.7b01966.

- [232] S. Jabeen, P. Kumar, and K. S. Samra, "Boosting the electrochemical characteristics of MnMoO₄ nanoparticles for supercapacitor applications," *J. Appl. Electrochem.*, vol. 54, no. 6, pp. 1435–1445, Jun. 2024, doi: 10.1007/s10800-023-02034-3.
- [233] J. Yesuraj, V. Elumalai, M. Bhagavathiachari, A. S. Samuel, E. Elaiyappillai, and P. M. Johnson, "A facile sonochemical assisted synthesis of α -MnMoO₄/PANI nanocomposite electrode for supercapacitor applications," *J. Electroanal. Chem.*, vol. 797, pp. 78–88, Jul. 2017, doi: 10.1016/j.jelechem.2017.05.019.
- [234] J. M. Soon and K. P. Loh, "Electrochemical Double-Layer Capacitance of MoS₂ Nanowall Films," *Electrochem. Solid-State Lett.*, vol. 10, no. 11, p. A250, 2007, doi: 10.1149/1.2778851.
- [235] S. S. Singha *et al.*, "Mn incorporated MoS₂ nanoflowers: A high performance electrode material for symmetric supercapacitor," *Electrochimica Acta*, vol. 338, p. 135815, Apr. 2020, doi: 10.1016/j.electacta.2020.135815.
- [236] K. S. Kumar, N. Choudhary, Y. Jung, and J. Thomas, "Recent Advances in Two-Dimensional Nanomaterials for Supercapacitor Electrode Applications," *ACS Energy Lett.*, vol. 3, no. 2, pp. 482–495, Feb. 2018, doi: 10.1021/acsenergylett.7b01169.
- [237] J. Xiao, D. Choi, L. Cosimbescu, P. Koech, J. Liu, and J. P. Lemmon, "Exfoliated MoS₂ Nanocomposite as an Anode Material for Lithium Ion Batteries," *Chem. Mater.*, vol. 22, no. 16, pp. 4522–4524, Aug. 2010, doi: 10.1021/cm101254j.
- [238] T. Wang, S. Chen, H. Pang, H. Xue, and Y. Yu, "MoS₂-Based Nanocomposites for Electrochemical Energy Storage," *Adv. Sci.*, vol. 4, no. 2, p. 1600289, Feb. 2017, doi: 10.1002/advs.201600289.
- [239] S. Chen, Z. Zhang, W. Zeng, J. Chen, and L. Deng, "Construction of NiCo₂S₄@NiMoO₄ Core-Shell Nanosheet Arrays with Superior Electrochemical Performance for Asymmetric Supercapacitors," *ChemElectroChem*, vol. 6, no. 2, pp. 590–597, Jan. 2019, doi: 10.1002/celec.201800970.
- [240] S. Asaithambi *et al.*, "Synthesis and characterization of various transition metals doped SnO₂@MoS₂ composites for supercapacitor and photocatalytic applications," *J. Alloys Compd.*, vol. 853, p. 157060, Feb. 2021, doi: 10.1016/j.jallcom.2020.157060.
- [241] P. Salarizadeh, M. B. Askari, K. Hooshyari, and H. Saeidfirozeh, "Synergistic effect of MoS₂ and Fe₃O₄ decorated reduced graphene oxide as a ternary hybrid for high-performance and stable asymmetric supercapacitors," *Nanotechnology*, vol. 31, no. 43, p. 435401, Oct. 2020, doi: 10.1088/1361-6528/aba1bd.
- [242] X. Yang, L. Zhao, and J. Lian, "Arrays of hierarchical nickel sulfides/MoS₂ nanosheets supported on carbon nanotubes backbone as advanced anode materials for asymmetric supercapacitor," *J. Power Sources*, vol. 343, pp. 373–382, Mar. 2017, doi: 10.1016/j.jpowsour.2017.01.078.
- [243] H. Zhang *et al.*, "Facile and scalable fabrication of MnO₂ nanocrystallines and enhanced electrochemical performance of MnO₂/MoS₂ inner heterojunction structure for supercapacitor application," *J. Power Sources*, vol. 450, p. 227616, Feb. 2020, doi: 10.1016/j.jpowsour.2019.227616.
- [244] M. Iqbal, N. G. Saykar, A. Arya, I. Banerjee, P. S. Alegaonkar, and S. K. Mahapatra, "High-performance supercapacitor based on MoS₂@TiO₂ composite for wide range temperature application," *J. Alloys Compd.*, vol. 883, p. 160705, Nov. 2021, doi: 10.1016/j.jallcom.2021.160705.

- [245] C. Zhao *et al.*, “Electrostatic force-driven anchoring of Ni(OH)₂ nanocrystallites on single-layer MoS₂ for high-performance asymmetric hybrid supercapacitors,” *Electrochimica Acta*, vol. 320, p. 134591, Oct. 2019, doi: 10.1016/j.electacta.2019.134591.
- [246] D. Wang *et al.*, “Kelp-like structured NiCo₂S₄-C-MoS₂ composite electrodes for high performance supercapacitor,” *J. Alloys Compd.*, vol. 735, pp. 1505–1513, Feb. 2018, doi: 10.1016/j.jallcom.2017.11.249.
- [247] A. Mohammadi, S. E. Moosavifard, A. Goljanian Tabrizi, M. M. Abdi, and G. Karimi, “Nanoporous CuCo₂S₄ Microspheres: A Novel Positive Electrode for High-Performance Hybrid Energy Storage Devices,” *ACS Appl. Energy Mater.*, vol. 2, no. 1, pp. 627–635, Jan. 2019, doi: 10.1021/acsaem.8b01651.
- [248] A. Rafique *et al.*, “Binder Free and Flexible Asymmetric Supercapacitor Exploiting Mn₃O₄ and MoS₂ Nanoflakes on Carbon Fibers,” *Nanomaterials*, vol. 10, no. 6, p. 1084, May 2020, doi: 10.3390/nano10061084.
- [249] D. Chen *et al.*, “Hierarchical core-shell structural NiMoO₄@NiS₂/MoS₂ nanowires fabricated *via* an *in situ* sulfurization method for high performance asymmetric supercapacitors,” *J. Mater. Chem. A*, vol. 7, no. 38, pp. 21759–21765, 2019, doi: 10.1039/C9TA07731F.
- [250] C.-R. Yang, Y.-P. Chang, and S.-F. Tseng, “Synthesis of flower-like Mn-Co-MoS₂ compounds for high-performance asymmetric supercapacitors,” *Int. J. Adv. Manuf. Technol.*, vol. 128, no. 7–8, pp. 3661–3671, Oct. 2023, doi: 10.1007/s00170-023-12190-7.
- [251] T. N. Y. Khawula, K. Raju, P. J. Franklyn, I. Sigalas, and K. I. Ozoemena, “Symmetric pseudocapacitors based on molybdenum disulfide (MoS₂)-modified carbon nanospheres: correlating physicochemistry and synergistic interaction on energy storage,” *J. Mater. Chem. A*, vol. 4, no. 17, pp. 6411–6425, 2016, doi: 10.1039/C6TA00114A.
- [252] M. R. and G. Raina, “Hydrothermally synthesized 2H-MoS₂ under optimized conditions – A structure and morphology analysis,” *Phys. Scr.*, vol. 97, no. 12, p. 125808, Dec. 2022, doi: 10.1088/1402-4896/ac9d6f.
- [253] C. Sekar, R. K. Selvan, S. T. Senthilkumar, B. Senthilkumar, and C. Sanjeeviraja, “Combustion synthesis and characterization of spherical α -MnMoO₄ nanoparticles,” *Powder Technol.*, vol. 215–216, pp. 98–103, Jan. 2012, doi: 10.1016/j.powtec.2011.09.016.
- [254] M. R. Pallavolu, A. N. Banerjee, R. R. Nallapureddy, and S. W. Joo, “Urea-assisted hydrothermal synthesis of MnMoO₄/MnCO₃ hybrid electrochemical electrode and fabrication of high-performance asymmetric supercapacitor,” *J. Mater. Sci. Technol.*, vol. 96, pp. 332–344, Jan. 2022, doi: 10.1016/j.jmst.2021.05.025.
- [255] J. Guo *et al.*, “Structure–property relationships of novel microwave dielectric ceramics with low sintering temperatures: (Na_{0.5x}Bi_{0.5x}Ca_{1-x})MoO₄,” *Dalton Trans*, vol. 43, no. 31, pp. 11888–11896, 2014, doi: 10.1039/C4DT00838C.
- [256] H. F. Hasmin, C. Imawan, and V. Fauzia, “The Role of Temperature in the Hydrothermal Synthesis on the Structural and Morphological Properties of MoS₂,” *J. Phys. Conf. Ser.*, vol. 1951, no. 1, p. 012014, Jun. 2021, doi: 10.1088/1742-6596/1951/1/012014.
- [257] A. Gigot *et al.*, “Mixed 1T–2H Phase MoS₂/Reduced Graphene Oxide as Active Electrode for Enhanced Supercapacitive Performance,” *ACS Appl. Mater. Interfaces*, vol. 8, no. 48, pp. 32842–32852, Dec. 2016, doi: 10.1021/acsaami.6b11290.
- [258] M. Wang, H. Fei, P. Zhang, and L. Yin, “Hierarchically Layered MoS₂/Mn₃O₄ Hybrid Architectures for Electrochemical Supercapacitors with Enhanced Performance,”

- Electrochimica Acta*, vol. 209, pp. 389–398, Aug. 2016, doi: 10.1016/j.electacta.2016.05.078.
- [259] P. Hutar *et al.*, “Highly Crystalline MoS₂ Thin Films Fabricated by Sulfurization,” *Phys. Status Solidi B*, vol. 256, no. 12, p. 1900342, Dec. 2019, doi: 10.1002/pssb.201900342.
- [260] Q. Lin *et al.*, “Molybdenum disulfide with enlarged interlayer spacing decorated on reduced graphene oxide for efficient electrocatalytic hydrogen evolution,” *J. Mater. Sci.*, vol. 55, no. 15, pp. 6637–6647, May 2020, doi: 10.1007/s10853-020-04478-w.
- [261] H. Wei, J. Yang, Y. Zhang, Y. Qian, and H. Geng, “Rational synthesis of graphene-encapsulated uniform MnMoO₄ hollow spheres as long-life and high-rate anodes for lithium-ion batteries,” *J. Colloid Interface Sci.*, vol. 524, pp. 256–262, Aug. 2018, doi: 10.1016/j.jcis.2018.03.100.
- [262] Z. Gu and X. Zhang, “NiCo₂O₄ @MnMoO₄ core–shell flowers for high performance supercapacitors,” *J. Mater. Chem. A*, vol. 4, no. 21, pp. 8249–8254, 2016, doi: 10.1039/C6TA02746F.
- [263] S. E. Moosavifard, J. Shamsi, and M. Ayazpour, “2D high-ordered nanoporous NiMoO₄ for high-performance supercapacitors,” *Ceram. Int.*, vol. 41, no. 1, pp. 1831–1837, Jan. 2015, doi: 10.1016/j.ceramint.2014.09.130.
- [264] J. Sun, C. Xu, and H. Chen, “A review on the synthesis of CuCo₂O₄-based electrode materials and their applications in supercapacitors,” *J. Materiomics*, vol. 7, no. 1, pp. 98–126, Jan. 2021, doi: 10.1016/j.jmat.2020.07.013.
- [265] P. Sun, C. Wang, W. He, P. Hou, and X. Xu, “One-Step Synthesis of 3D Network-like Ni_xCo_{1-x}MoO₄ Porous Nanosheets for High Performance Battery-type Hybrid Supercapacitors,” *ACS Sustain. Chem. Eng.*, vol. 5, no. 11, pp. 10139–10147, Nov. 2017, doi: 10.1021/acssuschemeng.7b02143.
- [266] Y. Wang *et al.*, “Facile solvothermal synthesis of novel MgCo₂O₄ twinned-hemispheres for high performance asymmetric supercapacitors,” *J. Alloys Compd.*, vol. 818, p. 152905, Mar. 2020, doi: 10.1016/j.jallcom.2019.152905.
- [267] Y. Liu *et al.*, “Nanosheet-assembled porous MnCo₂O_{4.5} microflowers as electrode material for hybrid supercapacitors and lithium-ion batteries,” *J. Colloid Interface Sci.*, vol. 627, pp. 815–826, Dec. 2022, doi: 10.1016/j.jcis.2022.07.105.
- [268] F. K. Nsaif, J. S. Mohammed, I. A. Mohammed, and K. A. Jasim, “Preparation and Study the Structural Properties for Compound Tl_{0.9}Hg_{0.1}Sr₂Ca₂Cu₃O_{8+δ} Using the Modified Scherer Equation,” *IOP Conf. Ser. Mater. Sci. Eng.*, vol. 1258, no. 1, p. 012008, Oct. 2022, doi: 10.1088/1757-899X/1258/1/012008.
- [269] R. W. Cranston and F. A. Inkley, “17 The Determination of Pore Structures from Nitrogen Adsorption Isotherms,” in *Advances in Catalysis*, vol. 9, Elsevier, 1957, pp. 143–154. doi: 10.1016/S0360-0564(08)60163-7.
- [270] K. S. W. Sing and R. T. Williams, “Physisorption Hysteresis Loops and the Characterization of Nanoporous Materials,” *Adsorpt. Sci. Technol.*, vol. 22, no. 10, pp. 773–782, Dec. 2004, doi: 10.1260/0263617053499032.
- [271] P. Dubey, N. Kaurav, R. S. Devan, G. S. Okram, and Y. K. Kuo, “The effect of stoichiometry on the structural, thermal and electronic properties of thermally decomposed nickel oxide,” *RSC Adv.*, vol. 8, no. 11, pp. 5882–5890, 2018, doi: 10.1039/C8RA00157J.
- [272] H. Sun *et al.*, “Sonochemical synthesis of battery-type ZnCo₂O₄ electrode material with huge specific surface area for advanced hybrid supercapacitors,” *J. Energy Storage*, vol. 76, p. 109780, Jan. 2024, doi: 10.1016/j.est.2023.109780.

List of Publications

1. **Shakra Jabeen**, Prashant Kumar, Seema Sharma, and Kawaljeet Singh Samra. "Binder-free MnMoO₄ nanoribbons on Ni-foam for high performance electrochemical energy storage devices." *Materials Letters* 324 (2022): 132741. **I.F= 3, SJR=0.6**
2. **Shakra Jabeen**, Prashant Kumar, and Kawaljeet Singh Samra. "Boosting the electrochemical characteristics of MnMoO₄ nanoparticles for supercapacitor applications." *Journal of Applied Electrochemistry* (2023): 1-11. **I.F= 2.9, SJR=0.49**
3. **Shakra Jabeen**, Prashant Kumar, and Kawaljeet Singh Samra. "Optimizing electrochemical performance: Investigating the influence of oxidation of graphene oxide in rGO@ MnMoO₄." *Journal of Alloys and Compounds* 981 (2024): 173673. **I.F= 6.2, SJR=1.1**
4. **Shakra Jabeen**, Prashant Kumar, Sandeep Sheokand, and Kawaljeet Singh Samra. "Mesoporous Ni doped MnMoO₄ nanoparticles for high performance asymmetric supercapacitors." *Journal of Energy Storage* 93 (2024): 112464. **I.F= 9.4, SJR=1.6**
5. **Shakra Jabeen**, Prashant Kumar, and Kawaljeet Singh Samra. "Elevated Charge-Storage Kinetics of Mesoporous MoS₂@MnMoO₄ heterostructures for Advanced Hybrid Supercapacitors". Submitted.

Other Publications

1. Kumar, Prashant, Seema Sharma, **Shakra Jabeen**, and Kawaljeet Singh Samra. "Hybrid microwave annealing assisted synthesis of MoS₂-RGO nanostructures: Optimization and characterization for application in supercapacitors." *Electrochimica Acta* 426 (2022): 140738.
2. Sheokand, Sandeep, Prashant Kumar, **Shakra Jabeen**, and Kawaljeet Singh Samra. "3D highly porous microspherical morphology of NiO nanoparticles for supercapacitor application." *Journal of Solid State Electrochemistry* 27, no. 3 (2023): 727-738.
3. Nisar, Faiziya, Prashant Kumar, **Shakra Jabeen**, and Kawaljeet Singh Samra. "One-pot, facile and microwave-assisted timesaving-synthesis of Co₃O₄@ CuO nanocomposite for enhanced energy-storage application." *Chemical Physics Letters* 829 (2023): 140748.

4. KP, Jithul, Prashant Kumar, **Shakra Jabeen**, and Kawaljeet Singh Samra. "Facile synthesis and optimization of CuO/Cu (OH) ₂ nanostructures on Cu-foil for an energy storage application." *Russian Journal of Applied Chemistry* 95, no. 11 (2022): 1723-1737.